An investigation into the formation of the lower Main Zone in the Eastern Limb of the Bushveld Complex, South Africa

By
Chantelle Estelle Clark – Halkett
23031957

Submitted in partial fulfillment of the requirements for the degree
M.Sc.: Geology
In the Faculty of Natural & Agricultural Sciences
University of Pretoria

2010

Declaration

I, Chantelle Estelle Clark-Halkett declare that the thesis/dissertation, which I hereby submit for the degree M.Sc.: Geology at the University of Pretoria, is my own work and has not previously been submitted by me for a degree at this or any other tertiary institution.

Signature:……
Date:……

Declaration of Originality

Full names of student:……...

Student number:……

Declaration

1. I understand what plagiarism is and am aware of the University's policy in this regard.
2. I declare that this……. (E.g. essay, report, project, assignment, dissertation, thesis, etc.), is my own original work. Where other people's work has been used (either from a printed source, Internet or any other source), this has been properly acknowledged and referenced in accordance with departmental requirements.
3. I have not used work previously produced by another student or any other person to hand in as my own.
4. I have not allowed, and will not allow, anyone to copy my work with the intention of passing it off as his or her own work.

Signature of Student:……

Signature of Supervisor……

Acknowledgements

I acknowledge the support and help I have received from my supervisor, Dr. R.J. Roberts. I want to thank Prof. R.W.K Merkle for the use of the XRF and XRD data obtained by Honors students and Mr. Peter Graser for his help and time on the Microprobe Analyses. I also acknowledge the support of the other members of the Department of Geology.

Abstract

The Main Zone is dominated by medium – grained, homogeneous gabbronorite, and anorthosites. The plagioclase compositions of the core is $((Na_{(0.227 – 0.353)}, K_{(0.012 – 0.046)}, Ca_{(0.651 – 0.777)}) Al_{(1.630 – 1.752)} Si_{(2.183 – 2.345)} O_8)$ and at the rim is $((Na_{(0.189 – 0.371)}, K_{(0.005 – 0.108)}, Ca_{(0.651 – 0.777)}) Al_{(1.630 – 1.752)} Si_{(2.183 – 2.345)} O_8)$. The composition of orthopyroxene is $((Mg_{(0.660 – 0.808)}, Fe_{(0.206 – 0.309)}, Ca_{(0.007 – 0.081)}) Si_{(0.960 – 1.037)} O_3)$ and the compositions of clinopyroxene is $((Mg_{(0.229 – 0.678)}, Fe_{(0.092 – 0.427)}, Ca_{(0.012 – 0.475)} Si_{(0.776 – 1.012)} O_3)$. The Mg# and An# varies with depth, where plagioclase increase in concentration the An# increases and the Mg# decreases. The variations in magma compositions are attributed to interlayering of different lithologies which are the result of fractional crystallisation in the magma chamber. This is supported by linear trends of the major and trace element bivariant plots. The magmatic event forming the Main Zone resulted in lateral expansion of the sheet – like magma chamber. The Main Zone formed through two magmas; first magma forming the lower Main Zone and the second magma, intruded the Main Zone at the level of the Pyroxenite Marker, forming the upper Main Zone.

Contents

List of Tables

List of Figures

CHAPTER 1: INTRODUCTION

1.1. Introduction

Many models have been proposed for the Main Zone (MZ) of the Bushveld Igneous Complex (BIC), but there is still controversy between the scientific communities. Within the BIC, the world's largest layered intrusion, situated in the northern part of South Africa, the Main Zone is the largest recognised subdivision, consisting of a pile of magmatic cumulates between 3 and 5 km in thickness (Eales & Cawthorn, 1996). Though the MZ does not host major economic deposits like the Upper Zone and Lower Zone, the MZ, as the most voluminous part of the BIC, is an important part of the BIC as a while.

Mineralogical data obtained from two boreholes located on the Eastern Limb will give a comprehensive understanding of the processes involved in the formation of the MZ. This study's main aim is to investigate geochemical data throughout a large portion of the MZ as well as to review some of the ideas on how the MZ formed. As opposed to previous studies (e.g. Kruger, 1994) which tackled the issue of magma recharge in the BIC via isotopic studies, this study aims to use mineralogical and geochemical data to investigate the magmatic history of the MZ.

1.2. Petrology of a Layered Intrusion

Fractional crystallisation is one of the most important processes in the crystallisation of igneous magmas. As a layered intrusion cools over many thousands of years the crystals will form according to the physical conditions in the melt and the composition of that melt (Bowen, 1928). The textures of a layered intrusion are frequently explained by the cumulus model (Wager et al., 1960 and Irvine, 1982). According to this model the rocks are the result of interaction between the melt and solid phases. The cumulus crystals represent early precipitates from a melt dominated system. Post cumulus crystals represent crystallisation from intercumulus liquid in the pores of the cumulus framework (Irvine, 1982).

The challenge to identify parental magma composition in a large layered igneous complex becomes menacing and contentious when there is evidence for addition of later magmas that have a different composition from the first (Cawthorn, 2007). The characteristic horizontal layering in these complexes might be attributed to simple gravitationally induced crystal settling but the processes involved in formation of a large igneous intrusion is much more complex; such as temperature gradients, change in density due to cooling of magma. Density variation can also be due to crystal fractionation or a change in magma chemistry (influx of a new magma or crustal contamination).

Mineral composition and Sr-isotopic data can be evaluated to identify an injection of magma. If the mineral composition changes abruptly there is an influx of magma, but if the changes are gradual the processes involved in formation is normal fractional crystallisation. If Sr-ratio changes abruptly there is an influx of magma or crustal contamination. However, isotopic changes should be accompanied by mineralogical changes if an influx of magma has occurred, and the absence of mineralogical change accompanying an isotopic shift may indicate that the isotopic ratios have been altered in a post-cumulus event.

Despite the intensive investigations conducted on mafic and ultramafic intrusions, especially in the last decade or so, no agreement has been reached on the origin of the layering that is such a striking feature of these rocks. It is suggested that large layered mafic intrusions, like the Bushveld Complex, illustrate processes of melt percolation and metasomatism of a pre-existing cumulate assemblage by that melt.

Many of these ideas have already been applied to the BIC, though there is little consensus on which processes occurred during the formation of the BIC. In the MZ, it has been theorised that the lower MZ crystallised from small injections of primitive liquid and simultaneous the leucocratic upper MZ crystallised from a combination of intruded MZ magma and residual liquid which remained after the major separation of the footwall mafic phases (Eales et al., 1986). Eales et al., (1986) also suggested that the layered

gabbronorite of the MZ may contain some pyroxenites and anorthosites, therefore representing crystallisation products of a progressive blend of residual magma from the underlying Merensky Reef (MR), Platreef and the Bastard Reef.

The incompatible trace element ratios and the initial Sr and Nd isotopic composition of the MZ resemble those of the tholeiitic basalt rather than the high Mg andesitic basalt magma (Kruger, 1994). Kruger (2005) provided interpretative evidence suggesting that the MZ was affected by numerous influxes of magma with contrasting isotopic compositions. The lower MZ would have crystallised during the 'Integration Stage', which is the process of magma addition and is reflected in 1) changes of initial $^{87}Sr/^{86}Sr$, 2) the mineralogy of the rocks, as well as 3) erosional unconformities that are evident in the stratigraphy. The upper MZ would then be part of the 'Differentiation Stage '. During this stage, the evolution of the magma chamber occurred as a closed system, except for the single, very large and final, influx that occurred at the position of the Pyroxenite Marker

Cawthorn and Walraven (1998) suggested that the MZ formed by the crystallisation of consecutive injections of magma. The injections of magma occurred at intervals closely spaced in time, so consequently the preceding magma did not have sufficient time to cool and differentiate before the addition of a new magma. These authors also invoked the argument that a vast amount of mafic magma was ejected as lava from the magma chamber. No mafic lavas are known above (or peripheral to) the Rooiberg Group and hence there is no field evidence to support magma ejection.

In another line of research, Lundgaard et al., (2006) recognised an increase in trapped liquid content along the line of the Eastern Limb of the Bushveld. This study recognised an enrichment of P, Zr and Rb in the Stoffberg area, which may indicate that the MZ magma was formed after 90% of an initial magma had crystallised through fractional crystallisation. The explanation favoured for the lateral increase in incompatible trace elements is that the magma was progressively more differentiated towards the south.

However, the initial Sr-isotopic ratios are constant at Stoffberg, and there is therefore no evidence for the influx of magma into the MZ magma chamber in this area.

There are thus several contradictory lines of evidence for the formation of the MZ. Whereas isotopic evidence in some studies suggests the lower portion of the MZ has formed through multiple injections of magma, isotopic and trace element evidence from other studies argues that the MZ is a single fractionally crystallising batch of magma. The current study aims to evaluate these competing ideas using mineralogical data from a portion of the Eastern Limb of the Bushveld.

1.3. The Bushveld Complex (BIC)

The BIC located in the northern parts of South Africa (Figure 1), is the largest layered mafic intrusion emplaced into a stable cratonic setting on Earth (Tegner et al., 2006). Gravimetric data indicate that the RLS of the BIC covers an area of at least 65 000km^2 (Cawthorn and Webb, 2001). The BIC contains the largest resources of PGE on earth and most of the world's vanadium (V) and titanium (Ti) (Barnes et al., 2004). The Rustenburg Layered Suite (RLS) outcrops in four discrete areas (normally referred to as "limbs"): Northern, Western, South-Eastern and Eastern Limbs (Eales and Cawthorn, 1996).

The BIC was emplaced into the upper crust at 2550– 2060 Ma (Nelson et al., 1999), in several major magma recharge events (Cawthorn and Walraven, 1998). The BIC intruded into a very thick package of intracratonic chemical and clastic sedimentary rocks, the Transvaal Supergroup (Cawthorn and Webb, 2001) which forms the floor and roof of the BIC. The Transvaal Supergroup intruded by the BIC includes a dolomitic and banded ironstone sequence known as the Chuniespoort Group, the Pretoria Group with an alternating quartzite and shale package and the Rooiberg Group which exhibit an upper basaltic and acidic volcanic sequence (Cheney and Twist, 1992).

The BIC consists of a ~6.5 km thick sequence of mafic and ultramafic rocks (Tegner et al., 2006) subdivided into three groups of rocks, namely the Lebowa Granite Suite, the Rashoop Granophyre Suite, and the RLS (Cawthorn et al., 2005). According to Eales and Cawthorn (1996) the sheer volume of the BIC suggests that it probably evolved by accretion of consecutive batches of magma. The overall tendency towards more differentiated rocks is distinctive of a closed-system with some magma loss; the trace element behaviour in the BIC supports this hypothesis (Maier et al., 2001).

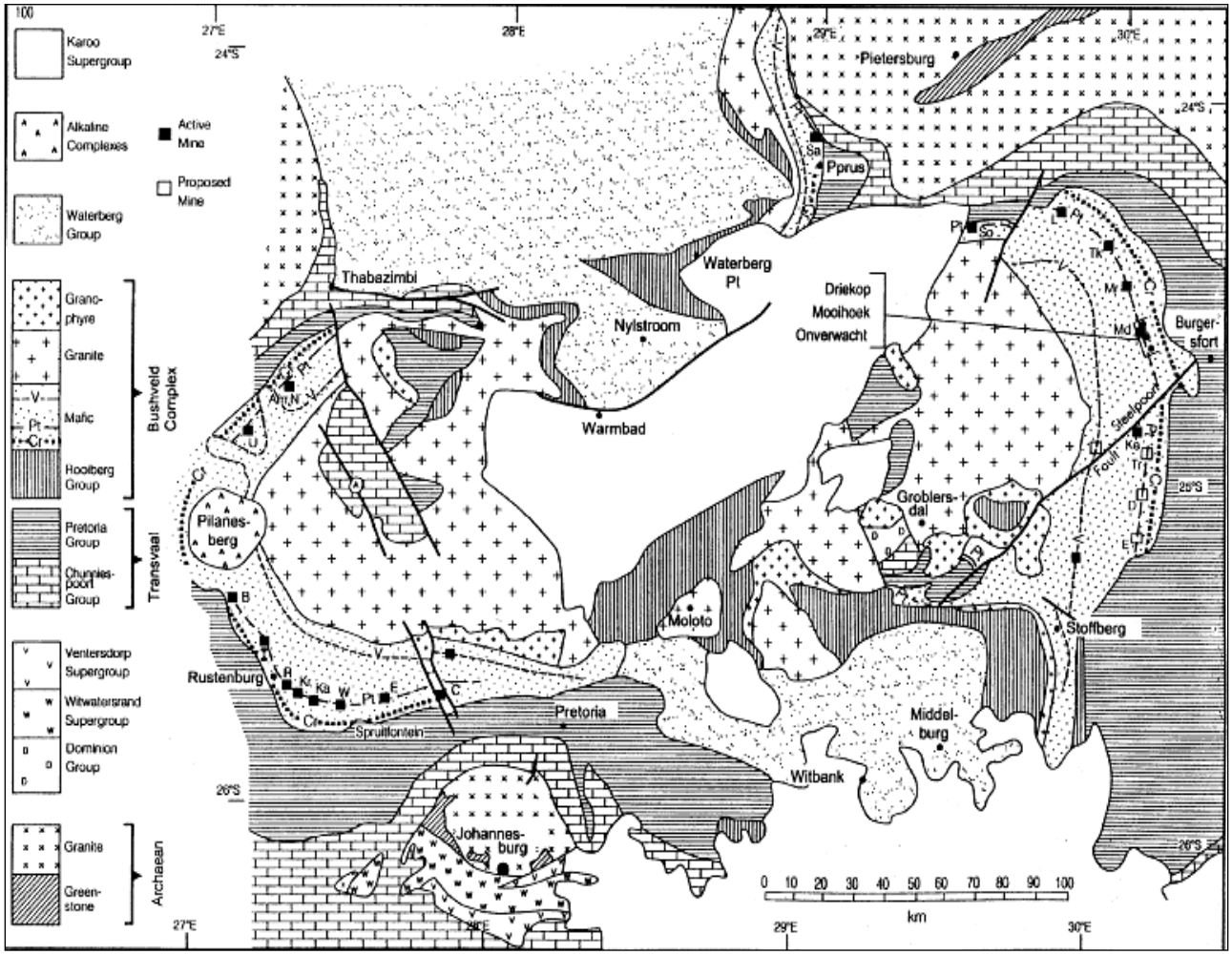

Figure 1: Geological map of the northern parts of South Africa, indicating where the Bushveld Complex outcrops (Cawthorn et al., 2005).

1.4. The Rustenburg Layered Suite (RLS)

The RLS (Figure 2) is subdivided into five zones (Hall, 1932). From bottom to top, the igneous complex features rocks evolving from peridotites and pyroxenites to gabbros, and finally to diorites and rare granites (Maier et al., 2001). The basal Marginal Zone (MRZ) ranges in thickness from 0m– 800m, and consists of medium-grained, heterogeneous norites and pyroxenites, representing composite sills or rapidly cooled derivatives of parental magmas (Eales and Cawthorn, 1996). This is commonly considered as a chilled magma, where assimilation of country rock occurred.

The Lower Zone (LZ) is found above the MRZ, and is poorly exposed and not continuous throughout the entire intrusion. The LZ is a ~1700 m thick succession of alternating layers of bronzitite, dunite and harzburgite (Cameron, 1978), where the layering is produced by repetitive magma additions (Kruger, 1992). The LZ is also characterised by the absence of chromite layers, as compared to the overlying Critical Zone.

The Critical Zone (CZ); (~1800 m) features chromite layers and cumulus plagioclase, The CZ is subdivided into a lower CZ and an upper CZ. Some of these layers contain the world's largest mineralisation of chromite and PGEs. The lower CZ consists of a series of cyclic units of chromitites, harzburgite and pyroxenites. The chromitite layers are referred to as Lower Group (LG) 1 to 7 and Middle Group (MG) 1. At the base of the upper CZ the appearance of plagioclase as a cumulus phase occurs in an anorthosite layer just above the MG-2 chromitite. In most areas, the upper CZ consists of cyclic units of chromitite, pyroxenite and norite. Some contain anorthosite as the upper unit and not all contain chromitite. The PGE-bearing reefs occur in the 100 m to 300 m thick stratigraphy between the Upper Group chromite 1 (UG1) and the MZ. The Merensky Reef, a platiniferous layer at the top of the CZ, is one of the economic layers with a near-constant grade of PGE (5- 8 g/t) over a near-constant thickness (40- 120 cm); (Barnes and Maier, 2002). The mineralisation contained by the MR occurs within very distinctive sequences, but is not restricted to explicit rock types (Cawthorn and Webb, 2001). The increase in initial Sr ratio at the MR level is considered to represent a magma influx (Kruger, 1994).

Above the CZ is the MZ which is the focus area of this project and will be discussed separately.

The Upper Zone (UZ) caps the RLS succession, and is characterised by a heterogeneous sequence of ~1700 m thick rocks which evolves upward from norites to gabbros, diorites and minor felsic intrusions. All rock types contain titaniferous magnetite (von Gruenewaldt, 1973). The UZ contains cumulus magnetitite and between 20 and 30 layers of monomineralic magnetitite. This zone also contains apatite above a certain level (Cawthorn and Walsh, 1988). The presence of apatite indicates a high concentration of phosphorous, which is consistent with the UZ forming from an evolved melt, rich in incompatible elements.

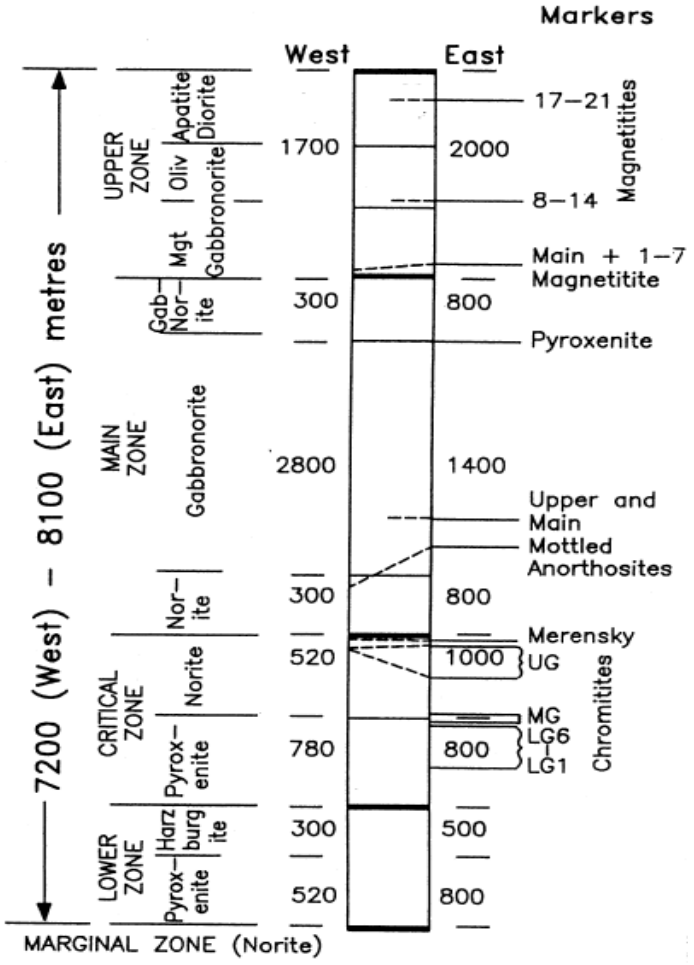

Figure 2: Stratigraphy of the Bushveld Complex according to *Cawthorn and Lee, 1998*.

1.5. Connectivity between the Western and Eastern Limbs

The Western Limb can be described as a semicircular arc from Thabazimbi through Rustenburg to Pretoria, and the Eastern Limb is a mirror image of the Western Limb and stretches from north of Burgersfort to Belfast (Cawthorn and Webb, 2001). Throughout the years there has been a great deal of debate on whether these two limbs are connected or not (Figure 3).

The similarities between the Western and Eastern Limbs are characterised by the occurrence of atypical sequences, which are not the normal consequence of magma fractionation, which are recognised in both limbs. These include the chromitite layers as well as the platiniferous MR of the CZ. The MR is very important due to the fact that it resembles a transition zone where the MZ magma intruded. The Pyroxenite Marker of the MZ and the Main Magnetitite layer (1.0% vanadium) of the UZ are also nonconforming sequences. The base of the UZ is defined as the lowest level at which cumulus magnetite first appears (Cawthorn and Molyneux, 1986).

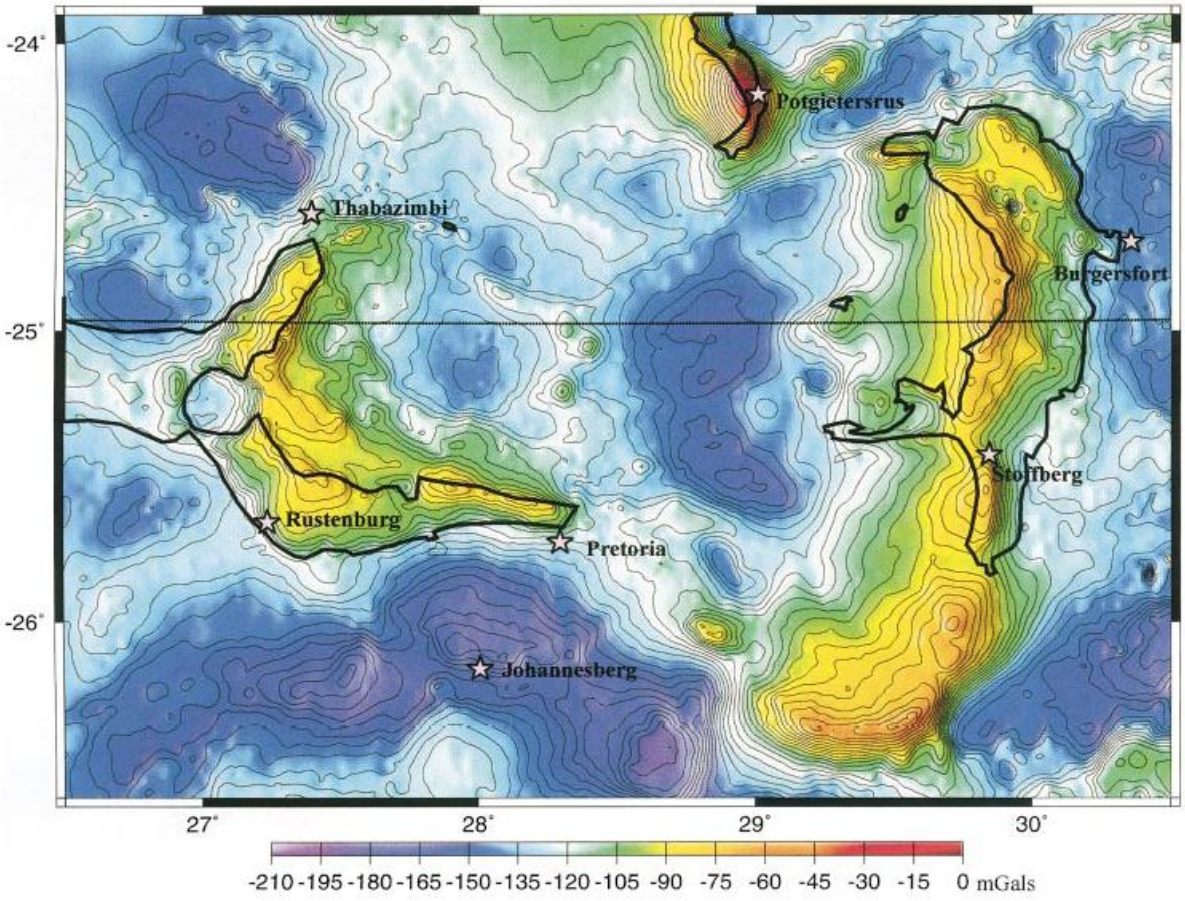

Figure 3: Gravity map of the Bushveld Complex (Cawthorn and Webb, 2001).

The MG chromitites are well developed in both the Western and Eastern Limbs. There is a virtually indistinguishable and complex sequence of several, closely-spaced chromititite layers which have been named MG 1- 4. The MG-2 layer is geochemical important because at this level cumulus plagioclase first appears in the entire sequence (Cawthorn and Webb, 2001). The UG 1 chromitite is distinct as it splits into a number of thin layers and re-joins, enclosing lenses of anorthosite. The UG 2 is mined on the Western Limb and Eastern Limb for PGE's.

The Pyroxenite Marker in the upper parts of the MZ has a distinctive $^{87}Sr/^{86}Sr$ ratio in relation to the lower parts of the MZ, according to Sharpe (1985) and von Gruenewaldt (1973) this represent the addition of a new magma. The UZ has exactly the same $^{87}Sr/^{86}Sr$ ratio in both the limbs. The formation of the Pyroxenite Marker and the UZ occurred in one single magmatic event in the Western and Eastern Limbs (Cawthorn and Webb, 2001). Therefore the Eastern and Western Limbs must be connected.

The principle of differentiation and phase diagrams predict that a comparable sequence of cumulus rocks should form from similar magma bodies without them having to be physically connected but these previously mentioned nonconforming sequences require extraordinary magmatic processes. The formation of the six characteristic layers to form at the same time in two different magma chambers 200- 300 km apart seems unlikely (Cawthorn and Webb, 2001).

1.6. The Main Zone (MZ)

The MZ is situated between the upper CZ (just above the Merensky Reef) and the lower UZ. It is situated roughly 4.2 km above the floor of the RLS in the Eastern Limb. The MZ is dominated by medium-grained, homogeneous gabbronorite, anorthosite and minor norites (Eales and Cawthorn, 1996). The major minerals are cumulus plagioclase that is often myrmekitic, orthopyroxene, minor clinopyroxene and large oikocrysts of inverted pigeonite (Lundgaard et al., 2006).

The magmatic event which formed the MZ resulted in lateral expansion of the sheet-like magma chamber (Kruger, 2005). There is substantial lateral variation in the thickness of the MZ in the BIC. In the Eastern Limb, the MZ is about 2860 m thick at Thornhill in the north, 3940 m thick at Roossenekal and 1080- 1440 m thick in the Stoffberg area. In the Western Limb the Main Zone's thickness can be up to ~3.4 km. Despite these thickness variations, the notable similarities between the layered sequences of the Eastern and Western Limbs, as well as gravimetric data suggest that these limbs formed within a single lopolithic intrusion (Cawthorn and Webb, 2001) thus making the MZ the largest possible single magma recharge event of the BIC.

Previous studies subdivided the MZ into different sub zones. Subdivision of a layered intrusion is normally based on the appearance and disappearance of cumulus minerals; minerals that nucleate and grow freely from the main body. The crystallisation of these minerals controls the path of differentiation in the magma chamber (Lundgaard et al., 2006). Von Gruenewaldt (1973) subdivided the Main Zone into subzones A, B and C

from base to the top of stratigraphic unit. This subdivision was based on the compositional variation of the Ca-poor pyroxenes (Table 1). Mitchell (1990) and Kruger (1990) subdivided the MZ into a lower and upper part based on the initial $^{87}Sr/^{86}Sr$ values. The lower MZ comprises of norites, gabbronorites, minor anorthosite and pyroxenite. The overlying upper MZ contains gabbronorites with variable compositions of pyroxene and plagioclase (Kruger, 1990). The transition between the lower and upper MZ is characterised by ~2000 m layer of orthopyroxenite; the Pyroxenite Marker (Mitchell, 1990).

Table 1: Von Gruenewaldt (1973) subdivided the MZ.

Subzone	Rock type	Thickness (m)
C	gabbronorite – norite at base of this unit the Pyroxenite Marker	700 - 800
B	homogeneous gabbronorite with pigeonite (now inverted to orthopyroxene) primary orthopyroxene as Ca-poor pyroxene	1000
A	gabbronorite, anorthosite and norites	1200

In this study we will be focussing on the subdivision of Nex et al., (1998). According to Nex et al., (1998) (Table 2) the MZ can be subdivided into five subzones (A- E) based on the appearance of inverted pigeonite and primary orthopyroxene. Subzone A comprises of mainly norites and lesser gabbronorite (Lundgaard et al., 2006). Subzone B hosts equigranular gabbronorites. The transition between subzone B and subzone C is characterised with the coexistence of three pyroxenes; primary orthopyroxene, inverted pigeonite and clinopyroxene. Subzone C contains homogeneous gabbronorite with cumulus plagioclase, minor clinopyroxene and large oikocrysts of inverted pigeonite (Lundgaard et al., 2006). It is suggested that the pigeonite was inverted to orthopyroxene during cooling (Nex et al., 1998). The transition zone between subzone C and D is a thick layer ~2000 m of orthopyroxenite, generally known as the Pyroxenite Marker (Lombard, 1934). The Pyroxenite Marker was produced by the disappearance of pigeonite and the reappearance of orthopyroxene (Lundgaard et al., 2006). Subzone D is distinguished

based on the reappearance of orthopyroxene. Subzone E is composed of gabbronorites and is characterised by the reappearance of inverted pigeonite (Nex et al., 1998).

Table 2: Subdivision of the Main Zone according to Nex et al. (1998).

Subzone	Rock type	Properties
E	gabbronorite	inverted pigeonite
D	gabbronorite	reappearance of orthopyroxene
Transition between C-D	Pyroxenite Marker; orthopyroxenite layer of 2m thick.	
C	homogeneous gabbronorite with cumulus plagioclase and minor clinopyroxene	large oikocrysts of inverted pigeonite
Transition between B-C	coexistence of three pyroxenes; primary orthopyroxene, inverted pigeonite and clinopyroxene	
B	equigranular gabbronorite	
A	norites, gabbronorite	

1.7. Chemical evolution of a large layered intrusion

It has been suggested that the RLS crystallised from at least three distinct magma types (Cawthorn and McCarthy, 1981; Sharpe, 1981; Eales and Cawthorn, 1996). The absence of intraplutonic quenching, which is the addition of magma significantly hotter than that resident in the chamber, indicates that the replenishing of magma must have occurred before the previous magma cooled and differentiate significantly. According to Figure 4 the initial Sr-isotope data (Kruger and Marsh, 1982; Sharpe, 1985; Kruger, 1994) at the base of the LZ records the lowest Sr ratio (0.7048) with greater variability up in the section. The CZ is also highly variable with a sudden increase at the level of the MR from 0.7065 to 0.7075. The initial Sr-ratio in the lower part of the MZ varies between 0.7075 and 0.7090. The accretion of the LZ, CZ and lower MZ formed from small batches of magma, with mafic compositions evolving by fractional crystallisation and crystal

separation, this forms a succession of ultramafic cumulates, norites and anorthosites. The mixing of recharged magmas with residual magmas in the chamber forms different cycles separated by chromitite layers.

The middle and upper parts of the MZ has a fairly constant initial Sr-isotope ratio of 0.7085. This resembles a single batch of magma with a more felsic composition that evolved by in- situ crystallisation with little crystal settling. At the Pyroxenite Marker there is a sudden shift in initial Sr ratio (0.7073) and this value remains throughout the UZ of the RLS. Kruger, (1994) suggested that the Sr-isotope ratios from the LZ to the lower MZ represents an open-system 'Integration Stage' with a number of magma influxes, whereas the upper MZ to UZ is a closed-system ' Differentiation Stage' where the evolution of the magmas were dominated by fractional crystallisation with possible additions of new magma or in situ contamination.

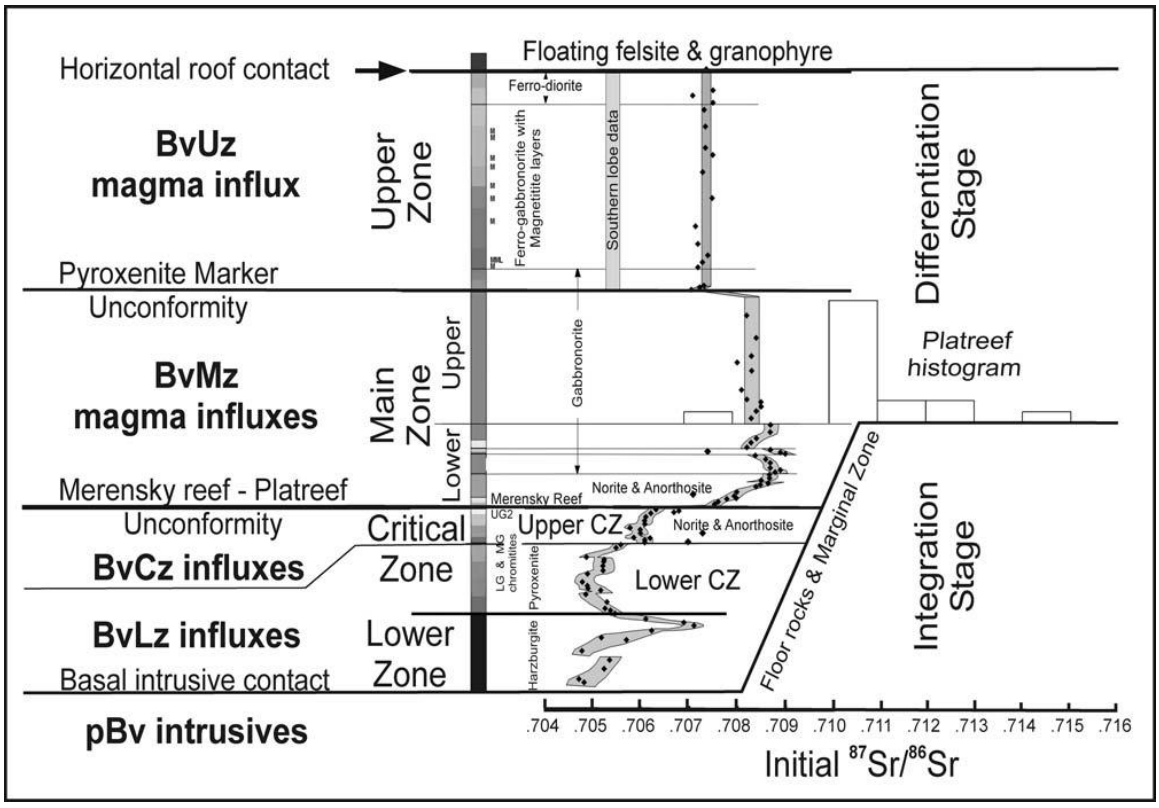

Figure 4: Stratigraphic and isotopic summary (Kruger, 2005). The isotope profile is from Kruger (1994).

According to Ariskin and Yaroshevsky (2006) magma will differentiate if the material is affected by change, chemical or physical. The magmatic melts serve as the transporting medium. A prerequisite for crystallisation is temperature, pressure and chemical composition. . The change in composition of the magma can be due to an influx of new magma or due to crustal contamination. They also suggested that during cooling of magma the mechanical motion must obey Stokes Law of crystal settling. The mechanical motion may be due to infiltration and/or expulsion of intercumulus melts, or a combination of both. These conditions can generate heterogeneity in a homogenous magma system.

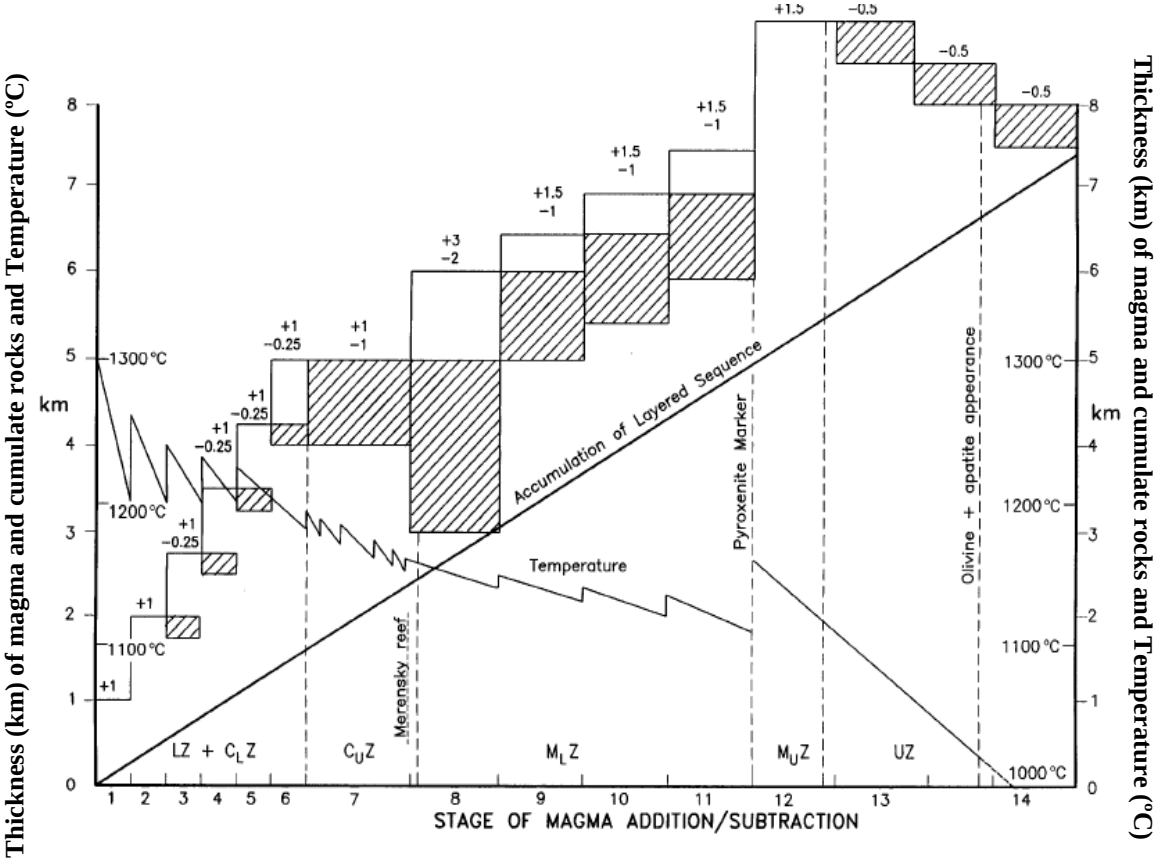

Figure 5: Diagrammatic model for the filling and crystallisation of the BIC (Cawthorn and Walraven, 1998). The numbers indicate thickness of magma added and/or subtracted in km.

The model of Cawthorn and Walraven, (1998), (Figure 5) describes how much magma was added at a time, how much crystallisation took place and how much magma was erupted for each stage of the calculation. The first stages (1- 6) represent the formation of the LZ and lower CZ. Stage 7 is the formation of the upper CZ with eight identical

repetitive additions of 1 km of primitive magma and removal of 1km of residual magma (Cawthorn and Walraven, 1998). The possibility of a 4km magma producing only 2.5 km thick succession of rock requires that 1.5 km of the residual magma was lost from the chamber (Cawthorn and Walraven, 1998).

Data indicate that much of the magmatic activity represented by the Rooiberg-Loskop-Bushveld Complex succession occurred within 3- 5 Ma (Table 3). The mafic/ultramafic portion, the RLS represents a magma chamber that has been replenished numerous times (Figure 4) while it cooled and crystallised (Kruger et al., 1987).

Table 3: Various components of the BIC display recent age dating (Harmer and Armstrong, 2000).

Lithstratigraphic Unit	Age (Ma± 95%)
Loskop Formation	2057.2 ± 3.8
Lebowa Granite Suite	2053.4 ± 3.9 , 2054.2 ± 2.8, 2057.5 ± 4.2
Rustenburg Layered Suite	2054.4 ± 2.8, 2054.5 ± 1.5
Rashoop Granophyre Suite Rooiberg Group	2061.8 ± 5.5 2057.3 ± 2.8

1.8. Models proposed for layering

To devise a model for a mafic-ultramafic layered intrusion we must account for the processes that are involved during crystallisation of the magma. The understanding of cumulus rocks and igneous layering imagines them to have formed by the igneous equivalent of processes that formed clastic sedimentary rocks. Any model for the crystallisation must be able to explain the coeval phase, cryptic and modal layering. The "large-scale or small-scale" layering must correspond to the mineralogy; consequently the sequence of minerals forming must change if the composition changes when the magma is cooling. The layering in the BIC is still controversial and there are several models that have been proposed for the interlaying. Some of the models for layering will be reviewed in this paper.

The chemical composition and mineralogy of the source region state a fundamental control over the chemistry of magmatic rocks. The major and trace element composition of a melt is determined by the type of melting process and the degree of partial melting, even though the composition of the melt can considerably change on the way to the surface. The composition of the source is directly affected by the mixing processes in the source region. Magma chamber processes regularly adjust the chemical composition of the primary magma through different processes; partial melting of the source, fractional crystallisation, magma mixing, contamination or a dynamic mixture of several of these processes.

The mechanism for magmatic differentiation is to separate the crystals from the liquid in a magma body and this process is generally referred to as fractional crystallisation. The easiest way to separate out crystals from the liquid is by gravitational crystal settling, but this process is still under scrutiny.

1.) Gravity settling by Wager (1963):

Gravity separation of crystals from liquid normally involves sinking of crystals due to their density. However flotation may be the process if density of the crystals is less than the density of the liquid. The deposition of a single sequence of rocks involves the settling of denser crystals beneath the lighter ones, due to compaction of accumulated crystals, the late differentiated liquid will therefore be expelled from the system. Convective overturn of the whole cooling unit will remove the liquid and rehomogenise the system interrupting the crystal settling, this process will repeat itself periodically (Wager et al., 1960). Therefore each cycle would be more evolved as a result of the removal of the phases in the rhythmic unit.

McBirney and Noyes (1979) argued against the importance of crystal settling due to the low probability of static conditions existing in the magma chamber. Convection occurring within the magma chamber will be highly turbulent and the crystals will remain in suspension (Sparks et al., 1985). The plagioclase crystals are less dense than the iron-rich magmas from which they crystallise and should therefore float (McBirney and Noyes,

1979). Jackson (1961) came across this problem when he discovered that the grains of olivine and pyroxene in graded layers of the Stillwater Complex are not hydraulically equivalent and concluded that the minerals must have nucleated and grown in-situ. Density is a vital aspect in the progress of "adcumulate" textures in which numerous, large crystals of plagioclase have grown far beyond the compositional liquidus proportions of the magma in which they are alleged to have nucleated (Tait et al., 1984 and Sparks et al., 1985). This argumentative statement led to a different idea of the processes involved in magmatic differentiation.

2.) Oscillations across the cotectic (Harker, 1909; Wager, 1959; Maaloe, 1978):

According to Harker (1909), Wagner (1959), and Maaloe (1978) the layering of rocks can be ascribed to liquid compositions that are displaced across the cotectic liquid line of descent by a variety of processes. These processes comprises of convective overturn, magma mixing, assimilation of country rocks, gain or loss of volatiles or changes in the temperature. When the displacement of the liquid composition from the cotectic occurs, crystallisation of the phase corresponding to the liquidus, that is adjacent to the cotectic, will bring the composition of the liquid back to the cotectic again. Therefore the liquid path meanders across the liquidus during cooling, which lead to the formation of alternating layers.

On larger scale, meters to tens of meters, cyclic layering has been attributed to the refluxing of the chamber with new batches of primitive magma (Cambell, 1977 and Irvine, 1980). Each unit records the influx of a new pulse of magma with subsequent mixing with the more differentiated magma chamber. During replenishment the hotter, denser and more primitive magma forms a layer at the base of the chamber. When the layer at the base of chamber cools and crystallises by exchanging heat with the more fractionated residual magma chamber the density will be reduced in relation to the overlying layer and mixing will thereafter occur (Sparks and Huppert, 1984).

3.) Compaction by McBirney (1995):

The weight of the overlying crystal mush can compress the cumulate mass in the floor of the chamber. According to Coats (1936), crystals of differing sizes and densities tend to sort themselves in crude layers as they consolidate under the force of gravity. Compaction develops layering as a resultant of recrystallisation, mechanical sorting, or a combination of the two. Compression results in ejection of highly enriched residual liquids into the magma chamber (Mathez et al., 1997). The expelled intercumulus liquids might react with other liquid-mineral mixture resulting in the replacement of the original liquid-mineral mixture. The process is known as the secondary replacement (Winter, 2001). Compaction, expulsion, and convective rise of less dense intercumulus liquid are significant processes in the advancement of cumulus assemblages and later liquids. The forces accountable for this sorting are not well understood but they seem to be associated to particles organising themselves according to their drag coefficients in a viscous fluid.

1.9. Previous models for formation of the Main Zone

Many models have been proposed for the MZ of the BIC, but there is still controversy between the scientific communities. The broad variations in magma compositions are attributed to interlayering of different lithologies which can be the result of fractional crystallisation in the magma chamber. Identifying a parental magma composition is challenging when there is evidence for addition of later magmas that have a different composition from the initial magma as in the RLS.

Eales et al., (1986) suggested that the lower MZ crystallised from small injections of primitive liquid and the leucocratic upper part (subzone A of MZ) crystallised from combination of intruded MZ magma and residual liquid which remained after major separation of the footwall mafic phases. He also suggested that the layered gabbronorite may contain some pyroxenites and anorthosites therefore representing crystallisation products of a progressive blend of residual magma from the underlying MR, Platreef and the Bastard Reef. According to Eales et al., (1986) proposed that if magma was intermittently added during crystallisation and mixed with a significant volume of

residual magma complementary to the upper Critical Zone's cumulate rocks; the Sr-isotopic ratio would steadily increase upwards throughout the entire lower MZ.

According to Sharpe (1985) the BIC is considered to have formed from repeated additions of magmas which were linked to a central magma source. Two main parental magmas gave rise to the RLS (Eales, 2002). The first a high-Mg andesite (B1) forming the LZ and lower CZ and the second a low-Titholeiitic basalt (B2 and B3) which formed the MZ and UZ (Harmer and Sharpe, 1985). Harmer and Sharpe (1985) proposed a tholeiitic magma composition, with 9% MgO, for the base of the MZ. Following is some of the proposed parental magma compositions for the MZ of the BIC (Table 4).

Table 4: Compositions of proposed parental magmas (Modified after Cawthorn et al., 2007). *LOD* (limit of detection).

	1. (wt %)	**2. (wt %)**	**3. (wt %)**	**4. (wt %)**
SiO_2	50.70	51.58	50.28	51.35
TiO_2	0.41	0.46	0.82	0.14
Al_2O_3	16.03	16.04	15.50	21.99
FeO_{tot}	9.14	9.70	12.53	4.87
MnO	0.17	0.19	0.19	0.09
MgO	9.21	7.57	5.88	6.72
CaO	11.14	10.95	10.84	12.07
Na_2O	2.52	1.85	2.87	2.09
K_2O	0.23	0.34	0.27	0.27
P_2O_5	0.08	0.05	0.09	0.01
	1. (ppm)	**2. (ppm)**	**3. (ppm)**	**4. (ppm)**
Cr	205	459	208	260
Sr	324	335	311	267
Ni	162	135	105	136
Zr	20,26	31	115	24
Ba	*LOD*	*LOD*	245	103
Rb	7	4	6	8

1. Harmer and Sharpe (1985), **2.** Maier et al., (2001), **3.** Cawthorn et al. (1981, 2005) and **4.** Average rock analysis for this study (PK206 + TW632)

Maier et al., (2001) proposed magma compositions with 8% MgO for the MZ (Table 4). According to Maier et al., (2001) the B2 and B3 magmas are more primitive and has relatively steep rare earth element (REE; normalized La/Yb = 5– 12) patterns. The MZ magma was formed through higher degrees (40– 50%) of contamination with the

depleted magma forming as a result of the first partial melting event. This MZ magma had lower silica and lower MgO content, which is consistent with higher degrees of contamination. This transformation occurs at level of the Merensky Reef which is the transition zone between the CZ and MZ (Maier et al., 2001).

Harris et al., (2005) concluded through O-isotope data, that the amount of contamination must have been between 40% and 50%, to form the MZ. The change between plagioclase and pyroxene concentration is significant lower between the Pyroxenite Marker and the MZ-UZ contact in the Northern Limb than above the Pyroxenite Marker. This lower plagioclase – pyroxene concentration is due to the higher closure temperature in relation to the oxygen diffusion in the rocks therefore indicating an input of new magma at the Pyroxenite Marker.

Kruger (2005) compiled Sr-isotopic data that indicates that the RLS magma chamber filled in two different stages. The Integration Stage (LZ, CZ and lower MZ) was affected by numerous influxes of magma with contrasting isotopic compositions. The larger influxes correspond to the boundaries of the zones and subzones which are marked by isotopic shifts. The accretion of the LZ, CZ and lower MZ formed from small batches of magma, with mafic compositions evolving by fractional crystallisation and crystal separation, this forms a succession of ultramafic cumulates, norites and anorthosites.

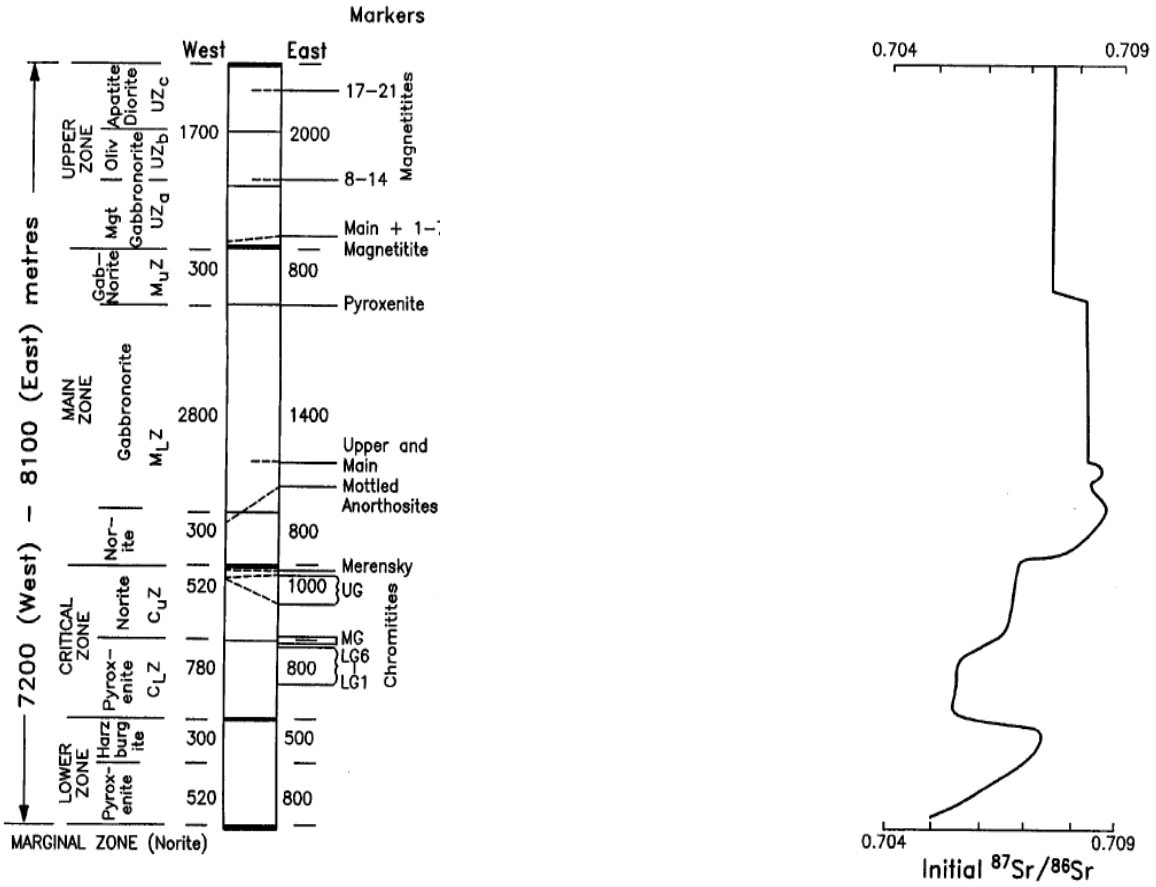

Figure 6: Stratigraphy of the Rustenburg Layered Suite correlated to the initial $^{87}Sr/^{86}Sr$ ratio for whole-rock and plagioclase separates (Kruger, 1994).

Previous studies of strontium (Sr) isotopic data indicate that a magma forming the lower MZ was intruded into the BIC at the level of the MR (Kruger and Marsh, 1982; Kruger, 1994). The initial Sr-ratio in the lower part of the MZ varies between 0.7075 and 0.7090.

The upper MZ and UZ are part of the Differentiation Stage where there were no major influxes of magma except for the magma addition which terminated the upper MZ. The upper MZ formed by fractional crystallisation. The middle and upper parts of the MZ has a fairly constant initial Sr-isotope ratio of 0.7085. This resembles a single batch of magma with a more felsic composition that evolved by in- situ crystallisation with little crystal settling.

Obtaining data from a sill in the Western Limb of the BIC Cawthorn and McCarthy (1981) proposed a parental magma to the MZ which comprises of 6% MgO (Table 4).

Cawthorn et al., (2005) proposed that by considering the values for Cr and Sr concentrations in the MZ we can identify the parental magma composition. He reported a Cr concentration of 208ppm which is similar to the reported values of Sharpe (1981) and Maier et al. (2001). According to Cawthorn et al., (2005) the similarity of the data does not explain the decrease in Cr in the pyroxenes near the base of the MZ (Figure 7).

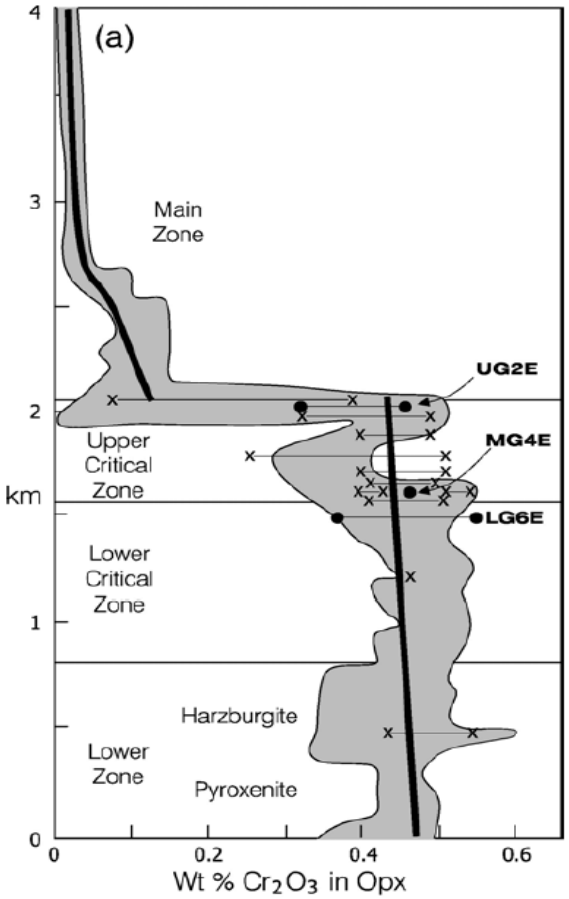

Figure 7: Cr contents in orthopyroxene from the Bushveld Complex (Cawthorn et al., 2005).

The Sr concentrations reported by Cawthorn and McCarthy (1981), Sharpe (1981) and Maier et al. (2001) are +/- 350 ppm. All the compositions proposed for the parental magma are crude due to the assumption that the composition of the magma from which the minerals formed was identical to the new magma added (Cawthorn et al., 2005). The Cr content in PK 206 and TW 632 is higher and the Sr content is lower than reported by Cawthorn and McCarthy (1981), Sharpe (1981) and Maier et al. (2001).

Lundgaard et al., (2006) proposed that the gabbronorites in the lower MZ display normal fractionation trends in mineral compositions and in initial Sr-isotopic ratios. He also recognized lateral variations in Mg# of orthopyroxenes and incompatible trace-element concentrations. Enrichment of P, Zr and Rb in the Stoffberg area with stratigraphic height indicates that the MZ magma crystallised from 50% to 80% fractional crystallisation and does not reflect an influx of magma into the magma chamber.

Lundgaard et al., (2006) recognised a southward increase in trapped liquid content, due to rapid heat loss at the margins of the RLS. Modelling of Rayleigh fractional crystallisation of whole-rock trace element concentration suggested more than 60- 80% crystallisation is required to account for the Y, Ti and Ba enrichment. The enrichment of P, Zr and Rb in the Stoffberg area indicate that the MZ magma crystallised from 90% fractional crystallisation. The only explanation for the lateral increase in incompatible trace elements is that the magma was progressively more differentiated towards the south. The initial Sr-isotopic ratios are constant at Stoffberg therefore there is no influx of magma into the magma chamber.

1.10. Aims and Objectives

This study main aim is to investigate geochemical data of the MZ obtained from two boreholes (PK 206 and TW 632) located on the Eastern Limb of the BIC. The geochemical data involves : 1) petrographic study to obtain an overview of the types of rocks of the lower MZ, 2) CIPW and XRD data evaluation to get an idea on what types of minerals are present in the rocks, 3) major and trace element studies to evaluate the chemical variation in the two boreholes as well as to determine which processes were active in the magma at the time of the formation of the lower MZ, 4) Electron Probe Microanalysis (EPM) of core and rim plagioclase, orthopyroxene and clinopyroxene to determine all mineralogical variation within the lower MZ. This study will also review some ideas on the formation of the MZ.

CHAPTER 2: METHODOLOGY

2.1. Location of the study area

This study focuses on the MZ of the RLS's Eastern Limb. The samples were taken from two boreholes: 1) TW 632 (~700 m) from Twickenham farm, which is situated 40 km north of the town Burgersfort and 80km from the Polokwane smelters, 2) PK 206 (~800 m) collected from Paschaskraal (also known as Ga-Phasha) north of the Twickenham farm (Figure 8). The boreholes were provided by Anglo Platinum Exploration services.

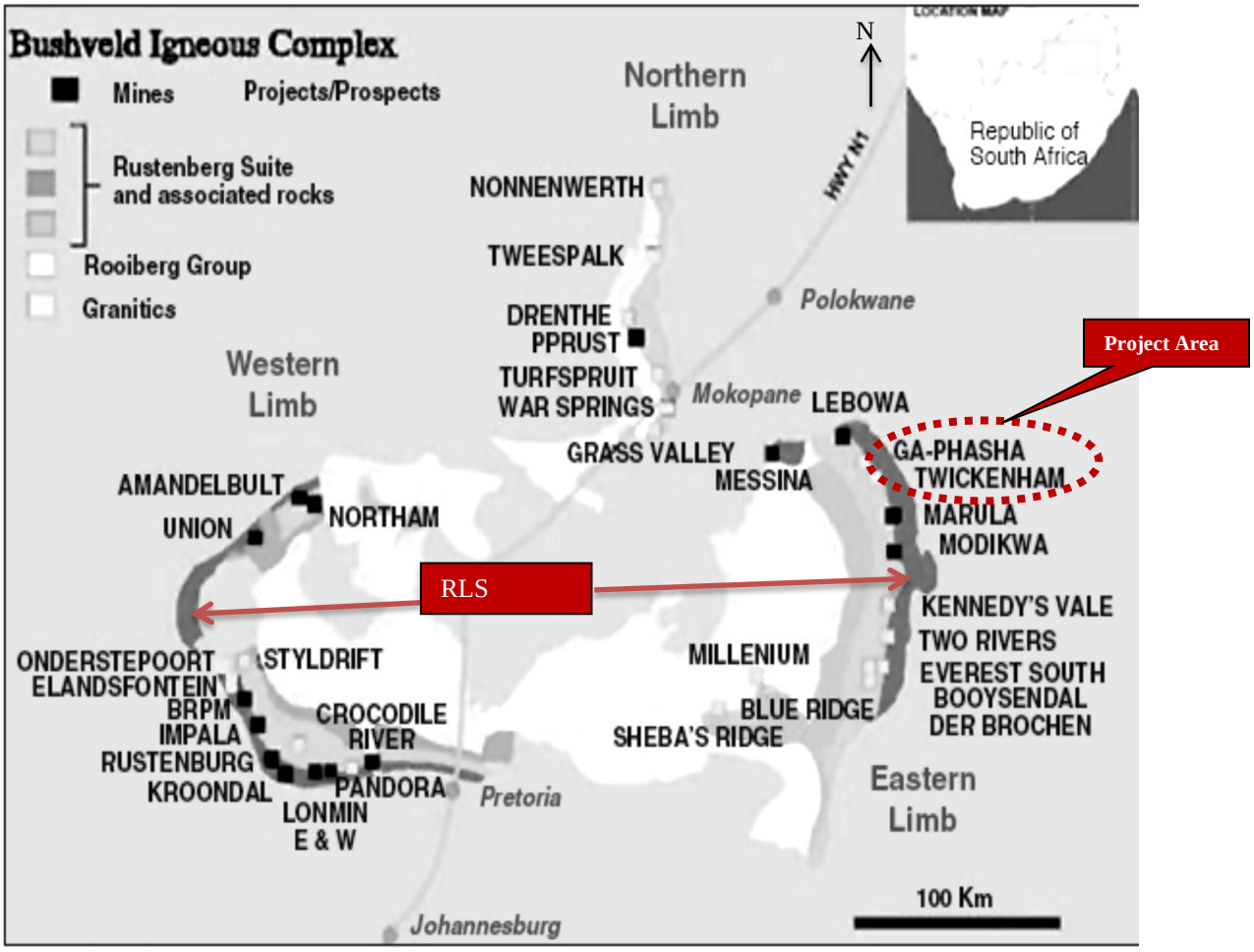

Figure 8: Map of the Eastern Bushveld Complex showing the location of study area, courtesy of Anglo Platinum.

2.2. Sampling

Borehole Paschaskraal (PK 206) was sampled at 10m intervals from the lowermost part of the MZ in subzone A just above the Bastard Reef. The samples were named PAS 1 (at the bottom of the borehole just above the Bastard Reef) to PAS 40 (at the top of the borehole; Table 5).

Borehole Twickenham (TW 632) was also sampled at 10m intervals from the lowermost part of the MZ in subzone A just above the Bastard Reef. The samples were given appropriate names TW 1 (at the bottom of the borehole just above the Bastard Reef) to TW 28 (at the top of the borehole; Table 6).

All the rock analysis for the two boreholes PK 206 and TW 632 was carried out at the Stoneman Laboratory at the University of Pretoria.

2.3. Sample Preparation

Each of the 68 samples was cut into two pieces, with one half analysed and the other half kept for reference. Thin sections were prepared for 28 samples using only a quarter of each cut sample. The other three-quarters of each core were crushed into a 1- 2 cm aggregate using a carbon-steel jaw crusher. The samples were then milled to a particle size of <75 µm with a tungsten carbide milling vessel. Pure quartz was milled in between each sample, assuring accuracy and no contamination. The milling vessel was also cleaned and dried with acetone between samples.

Table 5: Samples taken from Paschaskraal farm (PK 206).

Depth (m) Below Surface	Samples	Rock Type
0	PAS 40	Mottled Anorthosite
-9.91	PAS 39	Spotted Anorthosite
-30.18	PAS 38	Gabbronorite
-60.84	PAS 37	Gabbronorite
-69.73	PAS 36	Gabbronorite
-90.05	PAS 35	Spotted Anorthosite
-99.87	PAS 34	Gabbronorite
-109.77	PAS 33	Gabbronorite
-119.98	PAS 32	Gabbronorite
-139.9	PAS 31	Anorthosite
-180.15	PAS 30	Gabbronorite
-209.84	PAS 29	Gabbronorite
-230.32	PAS 28	Spotted Anorthosite
-240.22	PAS 27	Anorthosite
-280.11	PAS 26	Gabbronorite
-294.12	PAS 25	Gabbronorite
-300.24	PAS 24	Gabbronorite
-340.08	PAS 23	Gabbronorite
-349.96	PAS 22	Anorthosite
-369.99	PAS 21	Anorthosite
-390.02	PAS 20	Gabbronorite
-399.95	PAS 19	Gabbronorite
-419.43	PAS 18	Gabbronorite
-419.69	PAS 17	Gabbronorite
-429.96	PAS 16	Gabbronorite
-470.02	PAS 15	Gabbronorite
-479.84	PAS 14	Gabbronorite
-489.98	PAS 13	Gabbronorite
-530.2	PAS 12	Gabbronorite
-539.82	PAS 11	Gabbronorite
-560	PAS 10	Gabbronorite
-580.22	PAS 9	Gabbronorite
-600.16	PAS 8	Gabbronorite
-619.84	PAS 7	Gabbronorite
-650.87	PAS 6	Gabbronorite
-680.17	PAS 5	Gabbronorite
-700.11	PAS 4	Mottled Anorthosite
-730.19	PAS 3	Gabbronorite
-751.29	PAS 2	Gabbronorite
-760.24	PAS 1	Gabbronorite

Table 6: Samples taken from Twickenham farm (TW 632).

Depth (m) Below Surface	Samples	Rock Type
0	TW 28	Gabbronorite
-19.34	TW 27	Spotted Anorthosite
-40.2	TW 26	Mottled Anorthosite
-40.23	TW 25	Mottled Anorthosite
-71.5	TW 24	Gabbronorite
-91.26	TW 23	Gabbronorite
-115.86	TW 22	Gabbronorite
-124.2	TW 21	Mottled Anorthosite
-134.17	TW 20	Anorthosite
-183.9	TW 19	Gabbronorite
-242.22	TW 18	Gabbronorite
-249.89	TW 17	Gabbronorite
-258.91	TW 16	Gabbronorite
-262.32	TW 15	Gabbronorite
-344.06	TW 14	Gabbronorite
-372.41	TW 13	Gabbronorite
-392.68	TW 12	Gabbronorite
-428.72	TW 11	Gabbronorite
-448.42	TW 10	Gabbronorite
-468.17	TW 9	Gabbronorite
-498.59	TW 8	Gabbronorite
-528.72	TW 7	Gabbronorite
-548.57	TW 6	Gabbronorite
-578.33	TW 5	Gabbronorite
-608.6	TW 4	Gabbronorite
-638.7	TW 3	Gabbronorite
-668.74	TW 2	Gabbronorite
-688.05	TW 1	Mottled Anorthosite

2.4. X-Ray Fluorescence Spectroscopy (XRF)

XRF was used to analyse the major and trace elements. Three grams of each sample powder was weighed and dried at 100 ^{o}C overnight before being roasted at 1000 ^{o}C for a second to determine the Loss On ignition value. After adding 1g sample to 6g $Li_2B_4O_7$, the samples were fused into a glass bead. Major element analysis was conducted on the fused bead using the ARL9400XP+ spectrometer. Another aliquot of the sample was pressed in a powder briquette for trace element analysis. The XRF spectrometer was

calibrated with certified reference materials. The NBSGSC fundamental parameter program was used for matrix correction of major elements and the Rh Compton ratio method was used for the trace elements.

2.5. X-Ray Diffraction (XRD)

XRD was used to identify the different phases within the samples. The samples were prepared for XRD analysis using a back loading preparation method. They were analysed with a PANalytical X'Pert Pro powder diffractometer with X'Celerator detector and variable divergence- and receiving slits with Fe filtered Co-K_α radiation. The phases were identified using X'Pert Highscore plus software. The relative phase amounts in weight percentages were estimated using the Rietveld method (Autoquan Program). Amorphous phases, if present, were not taken into account in the quantification. Errors are on the 3 sigma level.

2.6. Thin section preparation

28 Samples were selected from the two boreholes; 15 from PK 206 and 13 from TW 632. The initial borehole samples were split into halves where 5cm of each sample was taken for polished thin sections. The preparation involves cutting, trimming, grinding, mounting, embedding, regrinding, impregnation, regrinding, and polishing, final polishing with 0.5 micron diamond paste. All samples were reground and repolished (to 3 mm) after the initial processes.

2.7. Electron Probe Microanalysis (EPM)

The quantitative electron microprobe analyses were performed using a CAMECA SX 100. The acceleration voltage was 20 kV and the beam current was 20 nA. Counting times were 20 seconds on peak position and 10 seconds on each background (pers. com. P. Graser).

Table 7: X-ray lines, spectrometer crystals and standards that were used.

X-ray Lines	Spectrometer Crystals	Standards
SiKα	TAP	KP Garnet
CaKα	PET	KP Garnet
AlKα	TAP	KP Garnet
MgKα	TAP	Diopside
FeKα	LLIF	KP Garnet
MnKα	LLIF	Rhodonite
TiKα	PET	Rutile
KKα	PET	KP Hornblende
NaKα	LTAP	KP Hornblende
CrKα	PET	Chromite
NiKα	LLIF	Olivine

CHAPTER 3: BOREHOLE STRATIGRAPHY AND PETROGRAPHY

3.1. Petrography of borehole core PK 206

The Paschaskraal boreholes consist of a succession of gabbronorites with infrequent anorthosites (Figure 9). Generally all the rocks contain about 52 wt% – 95 wt% plagioclase, and orthopyroxene and clinopyroxene in the ratio of 2:1.

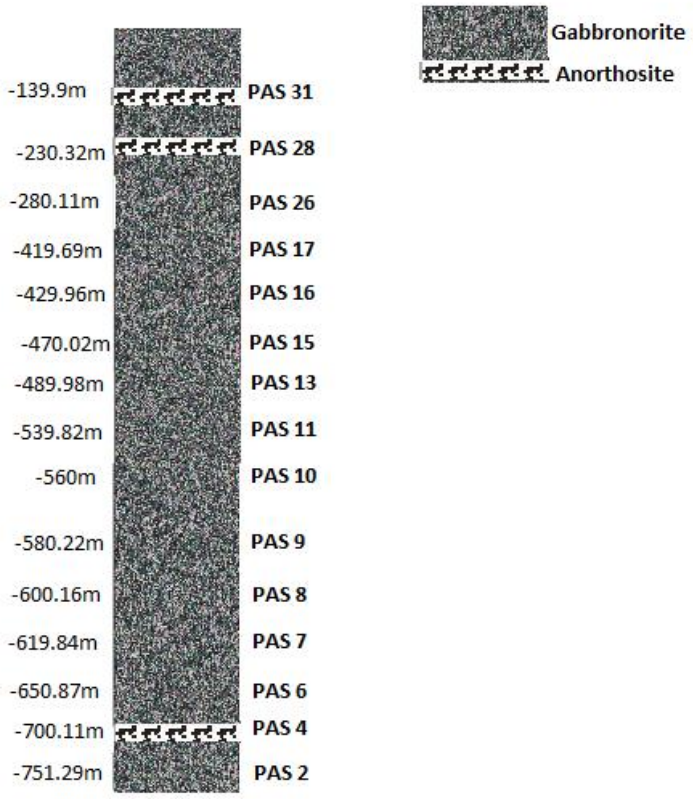

Figure 9: Borehole log for thin sections (PK 206).

The gabbronorites are coarse grained, basic igneous rocks containing mainly orthopyroxene, clinopyroxene and lesser plagioclase. Gabbronorites (Figure 10) are differentiated from anorthosites by having a lower concentration of plagioclase, therefore looking darker than the plagioclase-rich anorthosites. Anorthosite is dominated by plagioclase feldspar (>90 wt %) and lesser amounts of clinopyroxene and orthopyroxene crystals. Two different anorthosites are observed, namely mottled anorthosite and spotted anorthosites (Figure 11). According to van Zyl (1970), the spots and mottles are due to accumulation of orthopyroxene.

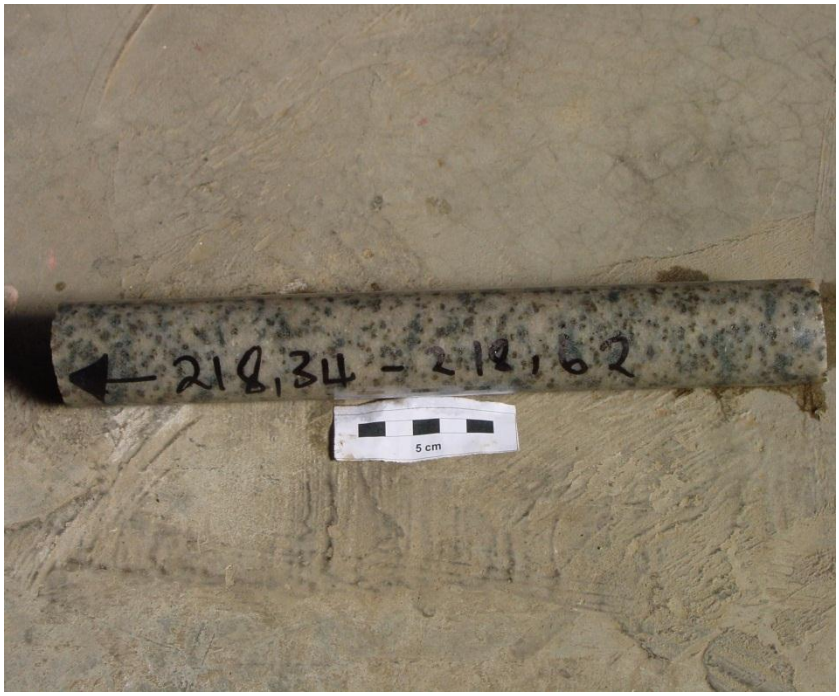

Figure 10: Gabbronorite (PAS 12).

.

Figure 11: Spotted Anorthosite (PAS 28).

Gabbronorites (PAS 2, PAS 6, PAS 7, PAS 8, PAS 9, PAS 10, PAS 11, PAS 13, PAS 15, PAS 16, PAS 17 and PAS 26):

In gabbronorites (Figure 12) plagioclase minerals form small and euhedral to large and subhedral or anhedral crystals. The plagioclase (plag) exhibits Albite and Carlsbad twinning. Oikocrysts of orthopyroxene (opx) and clinopyroxene (cpx) enclose euhedral pre-existing plagioclase crystals. According to Nex et al., (2002) the inclusions of plagioclase within pyroxene (px) have a more primitive composition than cumulus plagioclase.

The opx in gabbronorite is normally subhedral or anhedral, and most grains are subrounded. Orthopyroxene may also occur as elongated crystals with grain sizes ranging from 1-4mm. The anhedral clinopyroxene crystals vary in sizes from 1-2 mm. A number of pyroxene crystals show lamellar texture; for example Figure 12h shows orthopyroxene phenocrysts with clinopyroxene lamellas. According to van Zyl (1970) the observed variation in modal ratios of orthopyroxene and clinopyroxene (2:1) is a reaction relationship where cpx has grown at the expense of opx. Alteration of cpx to chlorite (Figure 12b) and alteration of opx to serpentine or talc (Figure 12g) are visible in the thin sections. Little or no zoning has been found within the pyroxenes. Nex et al., (2002) interpreted this as being due to rapid diffusion and re-equilibration of divalent components particularly Fe^{2+} and Mg^{2+} within the pyroxenes.

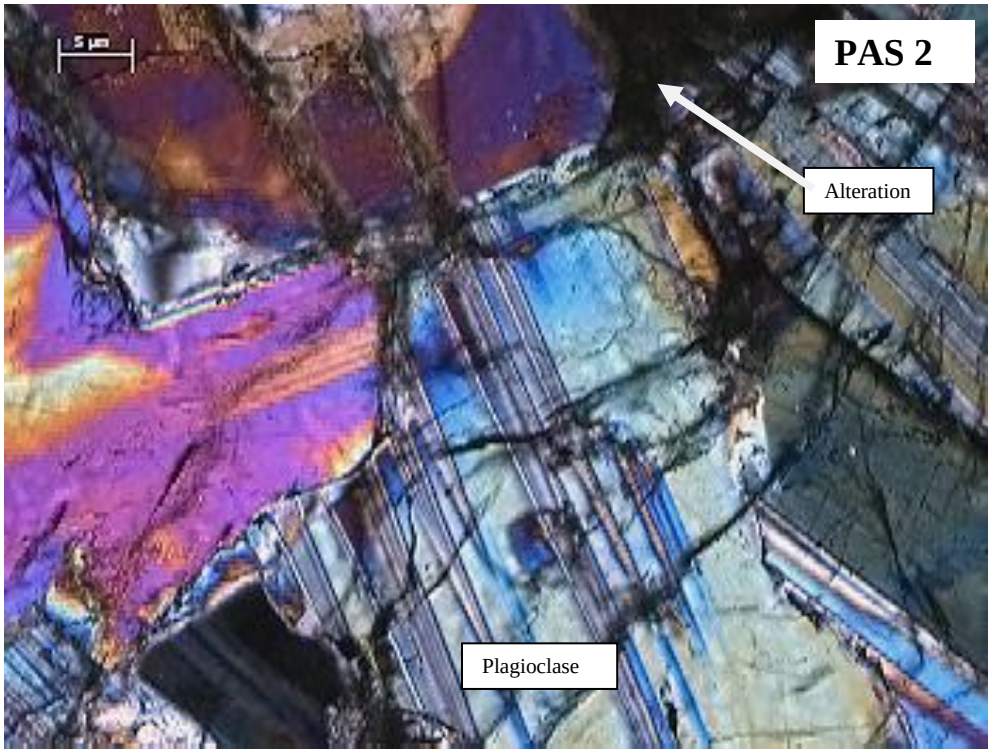

Figure 12a: (PAS 2) Subhedral plagioclase crystals showing albite twinning, the plagioclase crystals overlap each other. +/- 30% anhedral pyroxene present in the rock consist of more orthopyroxene than clinopyroxene.

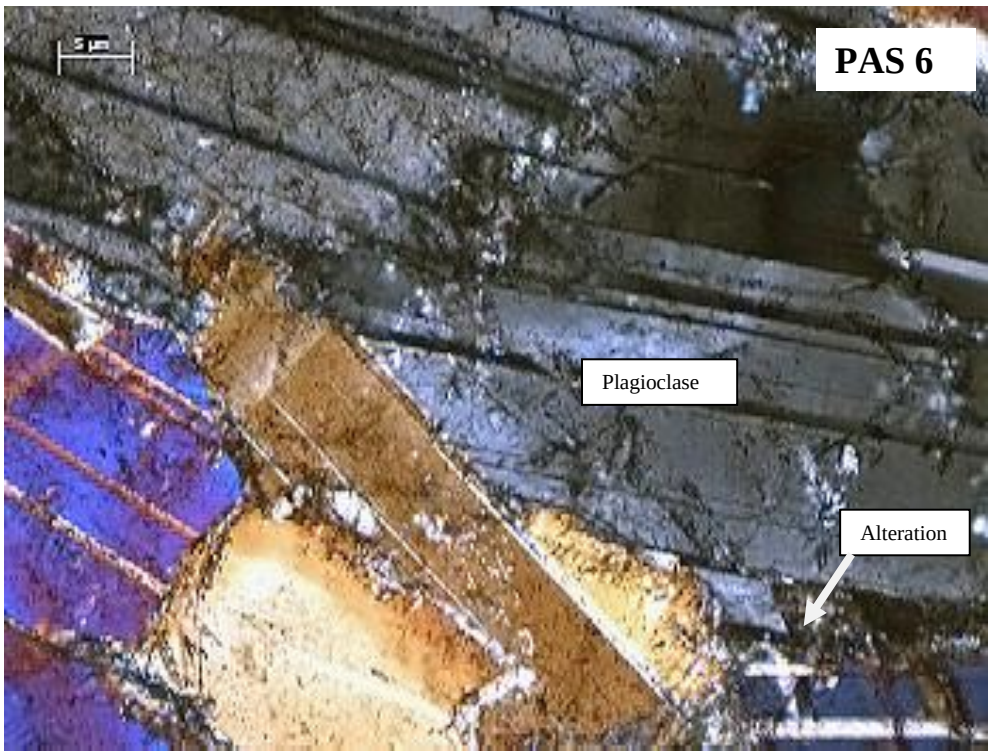

Figure 12b: (PAS 6) Large subhedral plagioclase crystals and smaller anhedral plagioclase crystals with saussuritization at the edges. Chlorite alteration visible which is a product of clinopyroxene and talc alteration which is product of orthopyroxene.

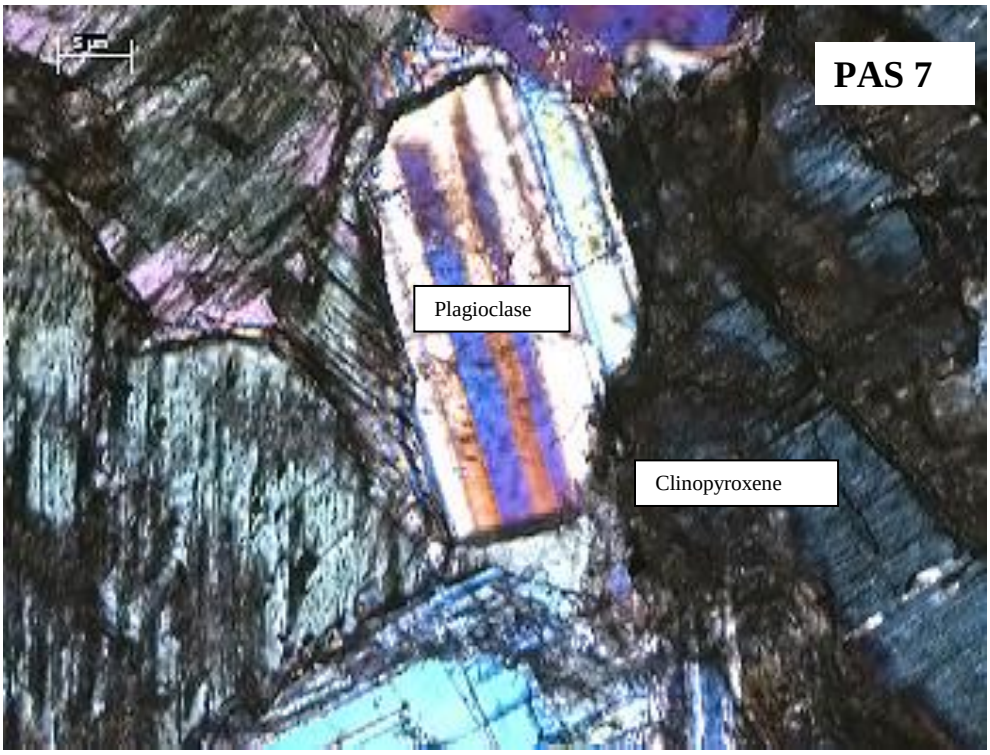

Figure 12c: (PAS 7) Anhedral, rounded plagioclase crystals enclosed by clinopyroxene. Clinopyroxene shows exsolution lamellae of orthopyroxene.

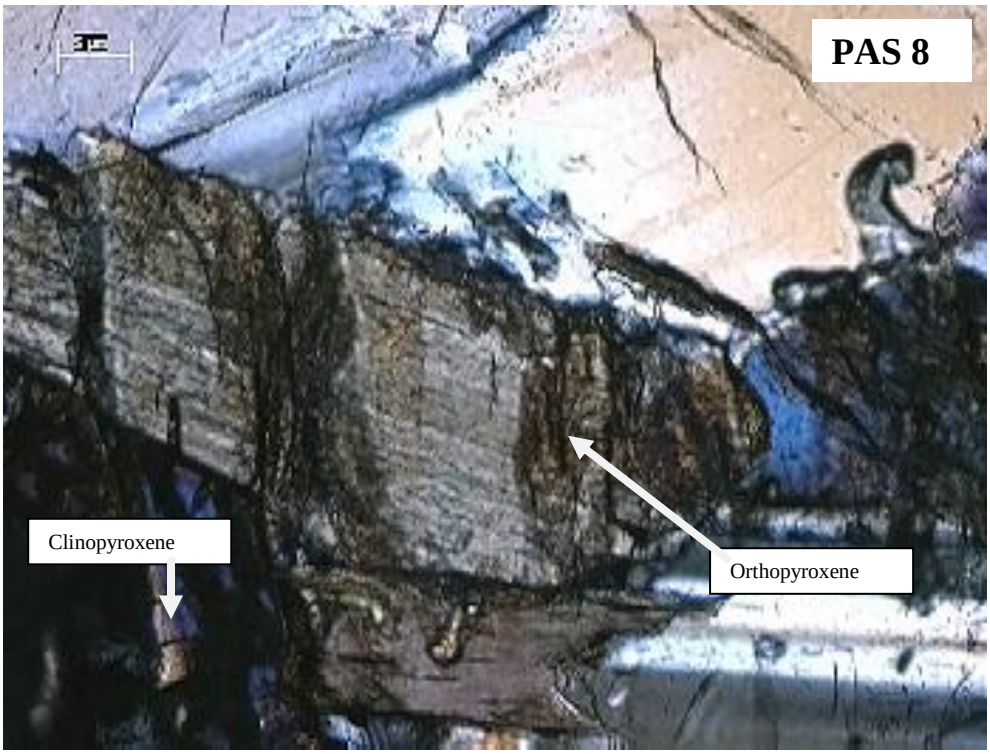

Figure 12d: (PAS 8) Pyroxenes are enclosed by large subhedral plagioclase matrix.

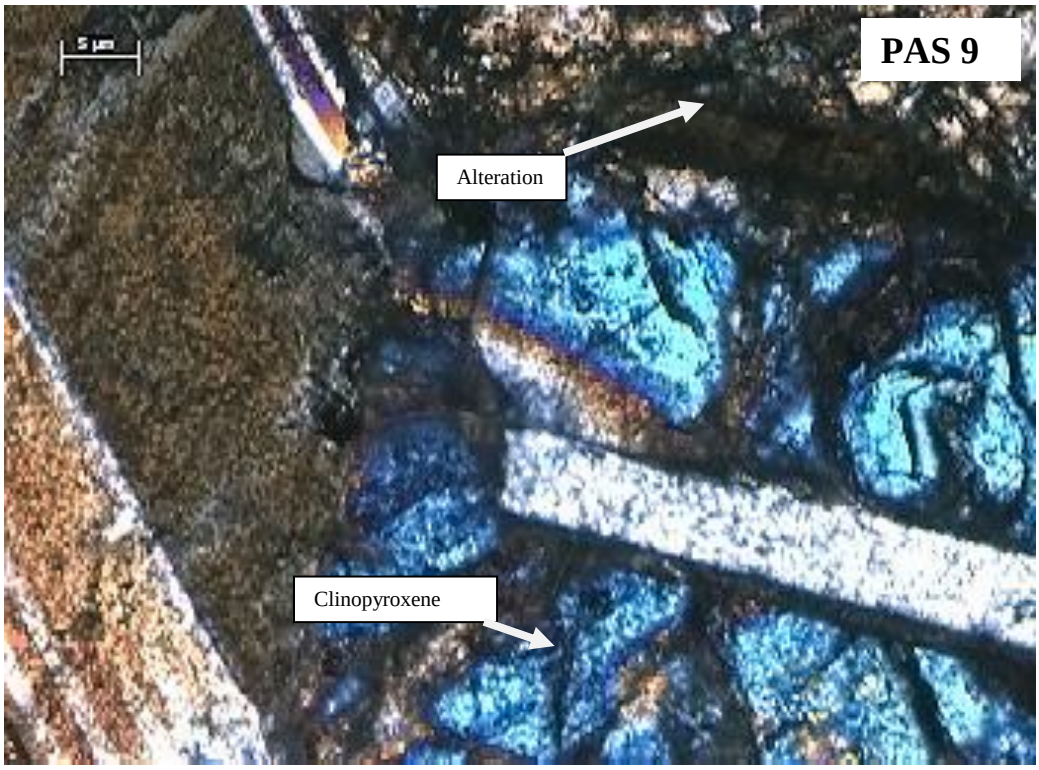

Figure 12e: (PAS 9) Subhedral to anhedral plagioclase enclosed by an anhedral clinopyroxene.

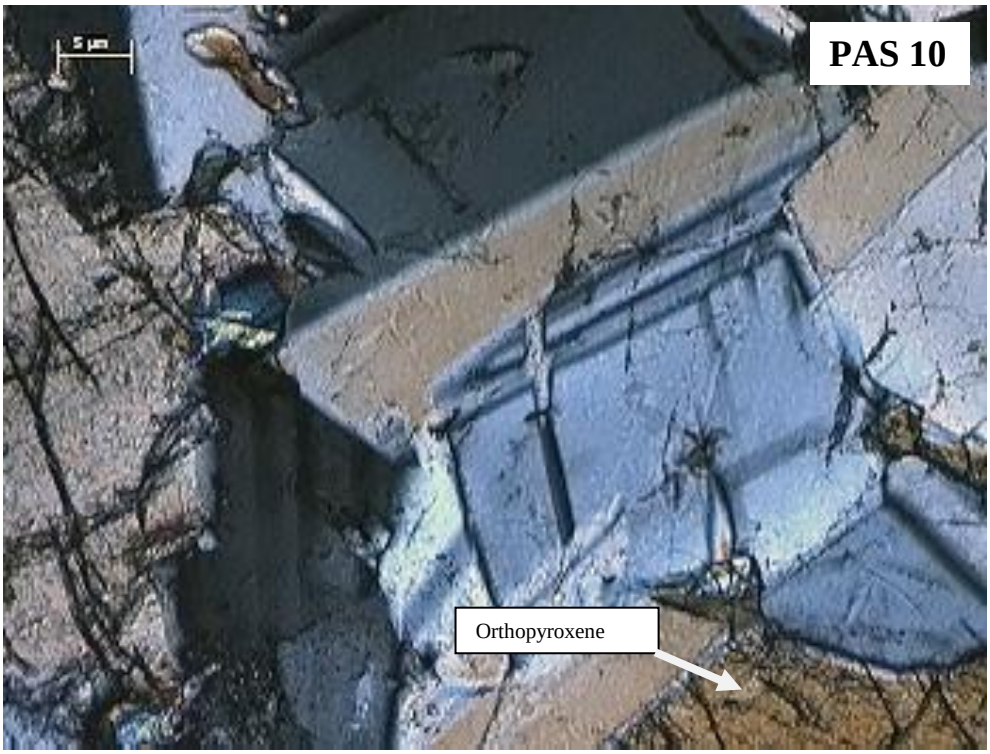

Figure 12f: (PAS 10) Orthopyroxene enclosed by large anhedral plagioclase.

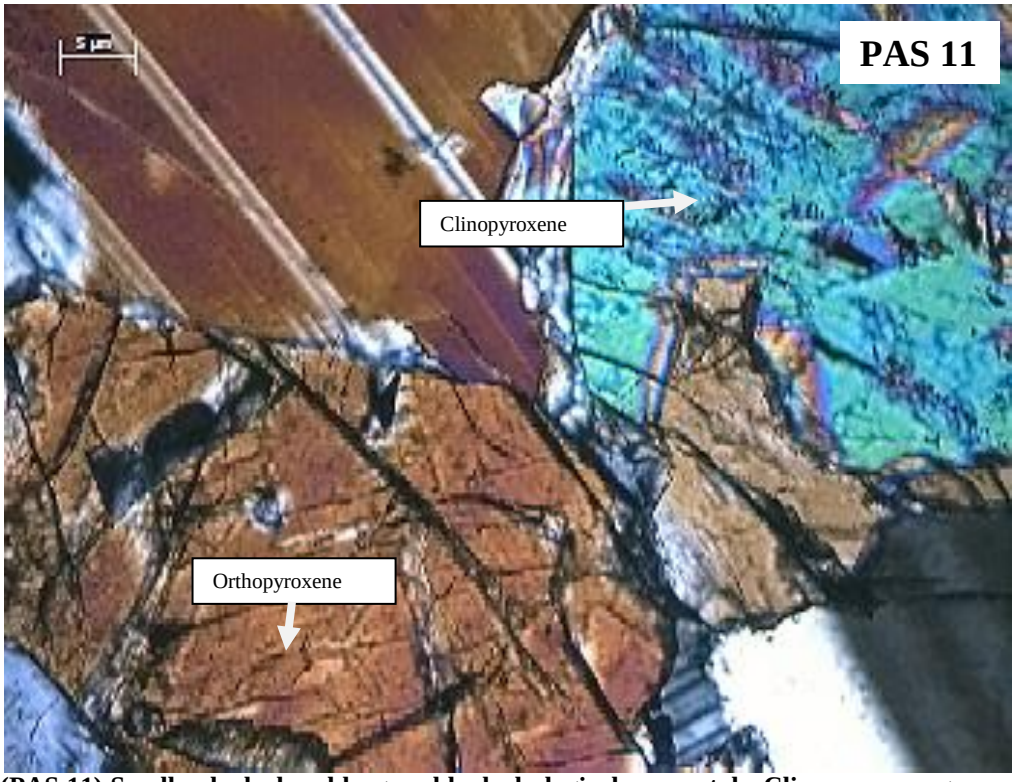

Figure 12g: (PAS 11) Small euhedral and large subhedral plagioclase crystals. Clinopyroxene grown at expense of orthopyroxene, due to some of the orthopyroxene having lamellae of clinopyroxene. Talc is visible in small amounts which indicate the alteration of orthopyroxene.

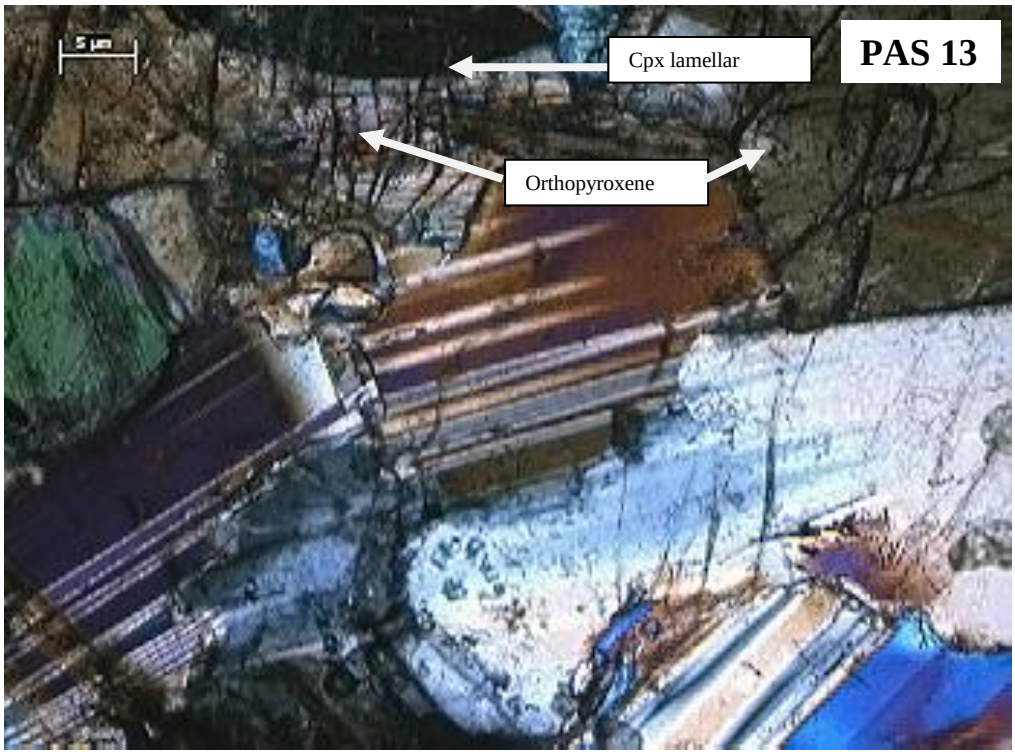

Figure 12h: (PAS 13) Large orthopyroxenes (3mm) are subhedral to anhedral with exsolution lamellae of small anhedral clinopyroxene. Talc is also visible in small amounts thus indicating orthopyroxene has been altered. Pyroxene encloses the plagioclase therefore the plagioclase crystals formed first.

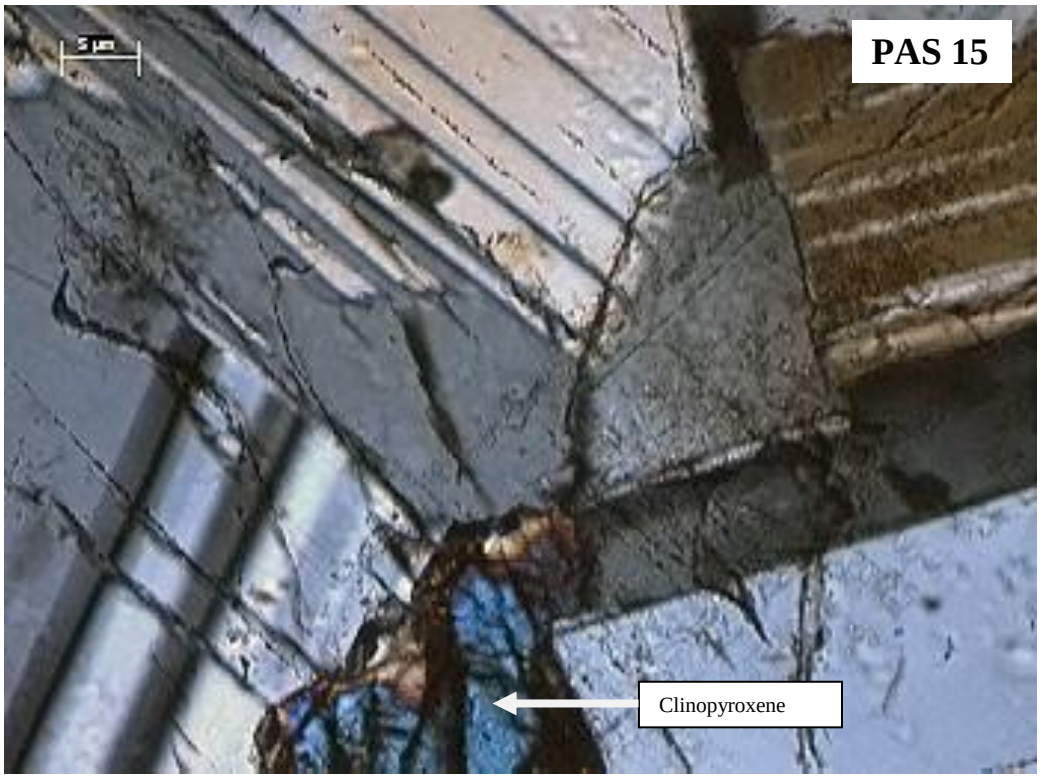

Figure 12i: (PAS 15) Large subhedral, rounded plagioclase showing albite and Carlsbad twinning (+/-45%). Clinopyroxene encloses plagioclase crystals. The more abundant subhedral orthopyroxene has exsolution lamellae of euhedral plagioclase.

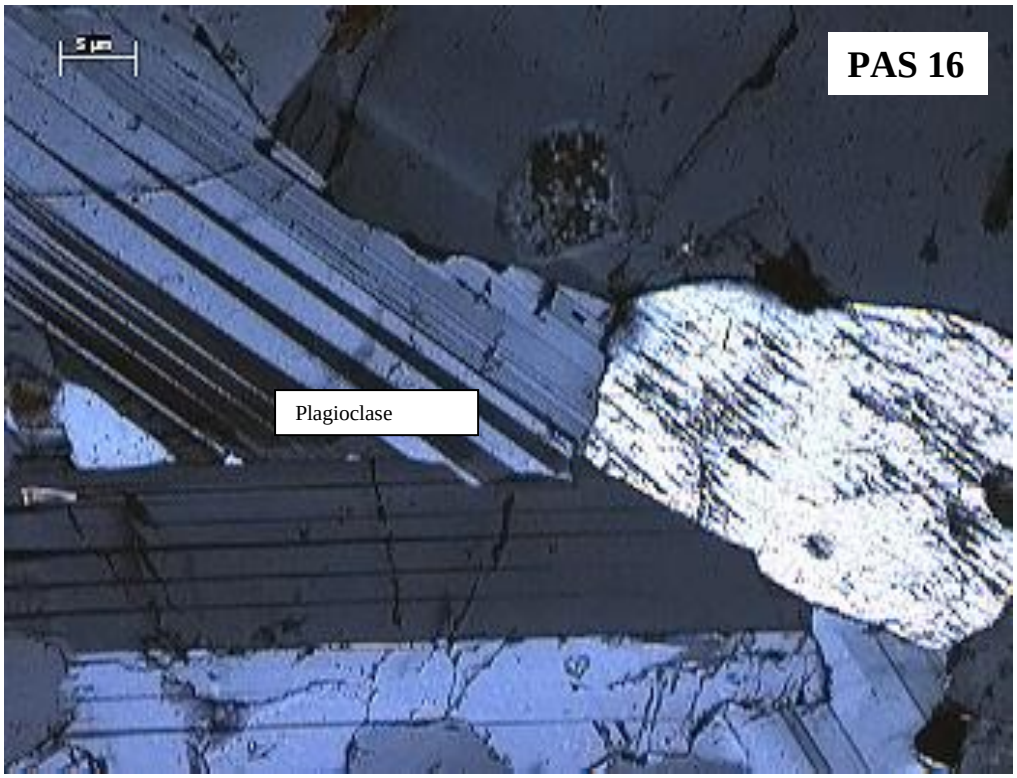

Figure 12j: (PAS 16) Elongated large, subhedral plagioclase crystals showing albite twinning. Small traces of talc are an alteration product of orthopyroxene. Clinopyroxene has interstitial plagioclase.

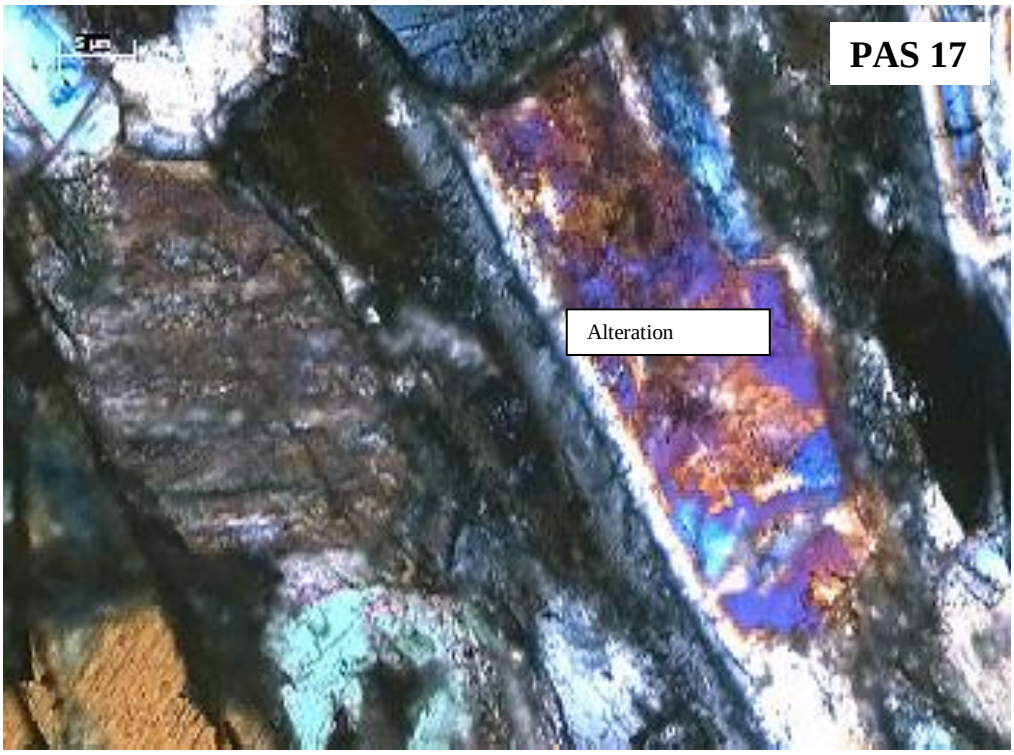

Figure 12k: (PAS 17) Anhedral plagioclase crystals. The anhedral orthopyroxene are more abundant than the clinopyroxene. Small traces of talc are visible which is the alteration product of orthopyroxene.

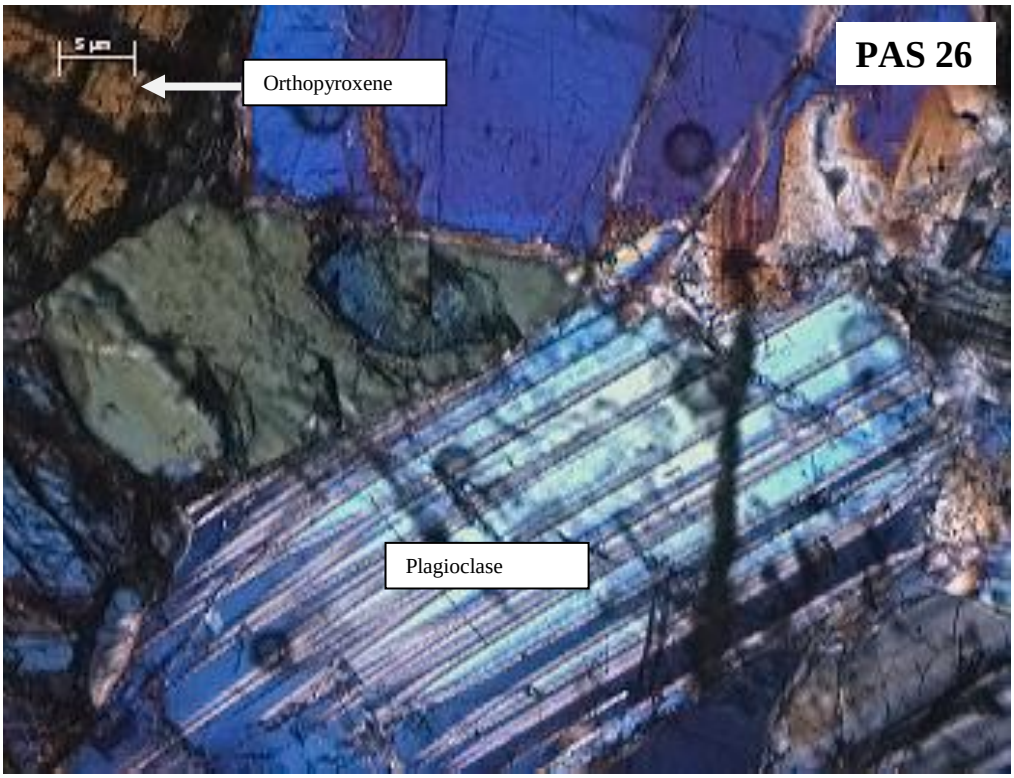

Figure 12 l: (PAS 26) Large subhedral plagioclase crystal shows albite and some Carlsbad twinning. The small anhedral orthopyroxene (1mm) are more abundant than the medium (2.5mm) clinopyroxene. Small traces of talc are visible which is the alteration product of orthopyroxene.

Anorthosites (PAS 4, PAS 28 and PAS 31):

Anorthosite rocks show both large (~3 mm) subhedral plagioclase crystals and small (~0.5 mm) euhedral plagioclase crystals. The elongated plag crystals make up >90 wt% of the rock. The plagioclase crystals exhibit Albite and Carlsbad twinning. The px in anorthosite contribute ~10 wt% of the rock and is interstitial, growing in the spaces between plagioclase crystals. Orthopyroxene is more dominant than cpx (Figure 13). The subhedral to anhedral opx are light brown and the cpx crystals are light green in colour and anhedral.

.

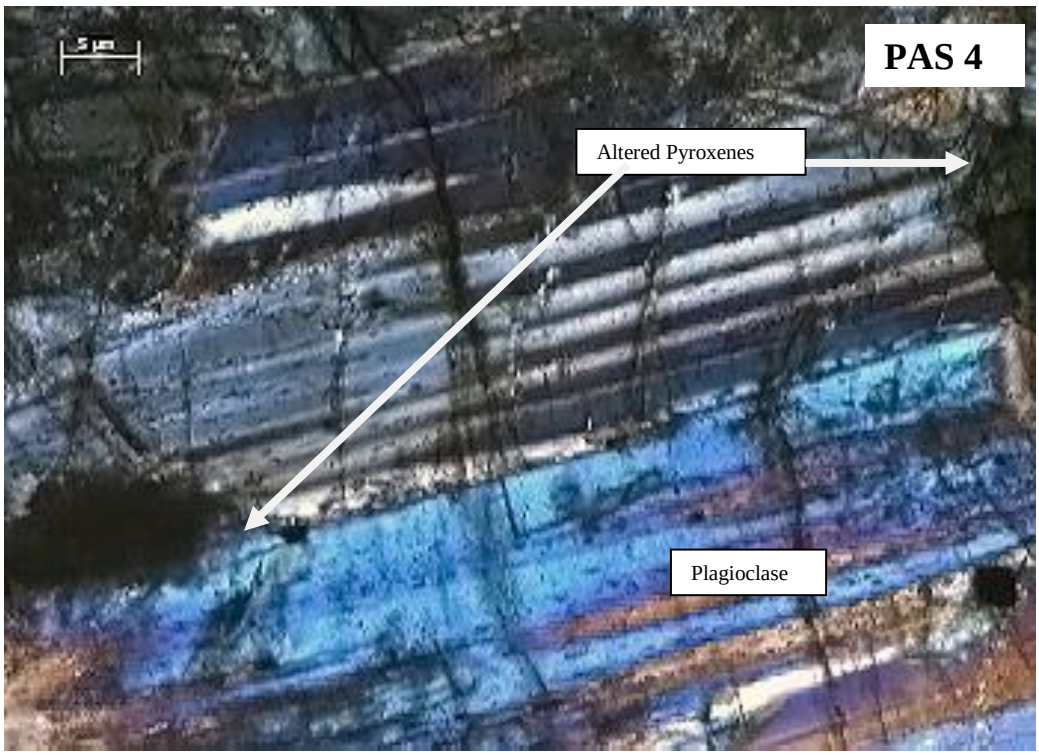

Figure 13a: (PAS 4) Poikilitic elongated orthopyroxene with inclusions of euhedral plagioclase and exsolution lamellae of clinopyroxene. The rock comprises of more orthopyroxene than clinopyroxene and +/- 85% plagioclase.

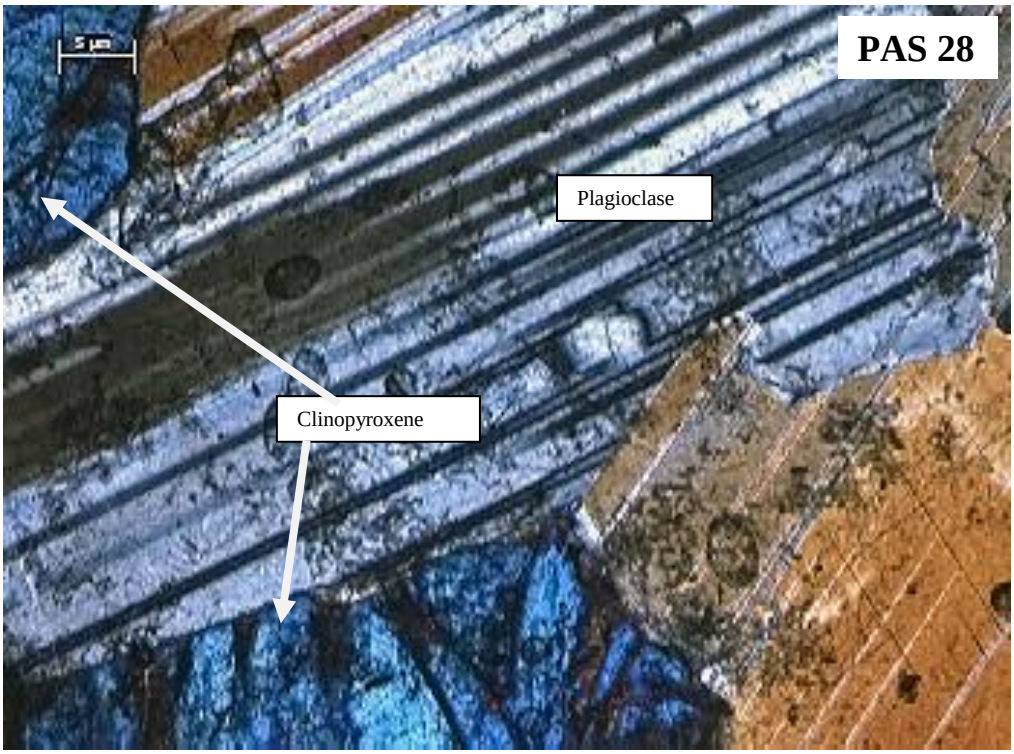

Figure 13b: (PAS 28) Large subhedral, elongated plagioclase crystals (>4mm) show albite twinning and in some cases Carlsbad twinning.

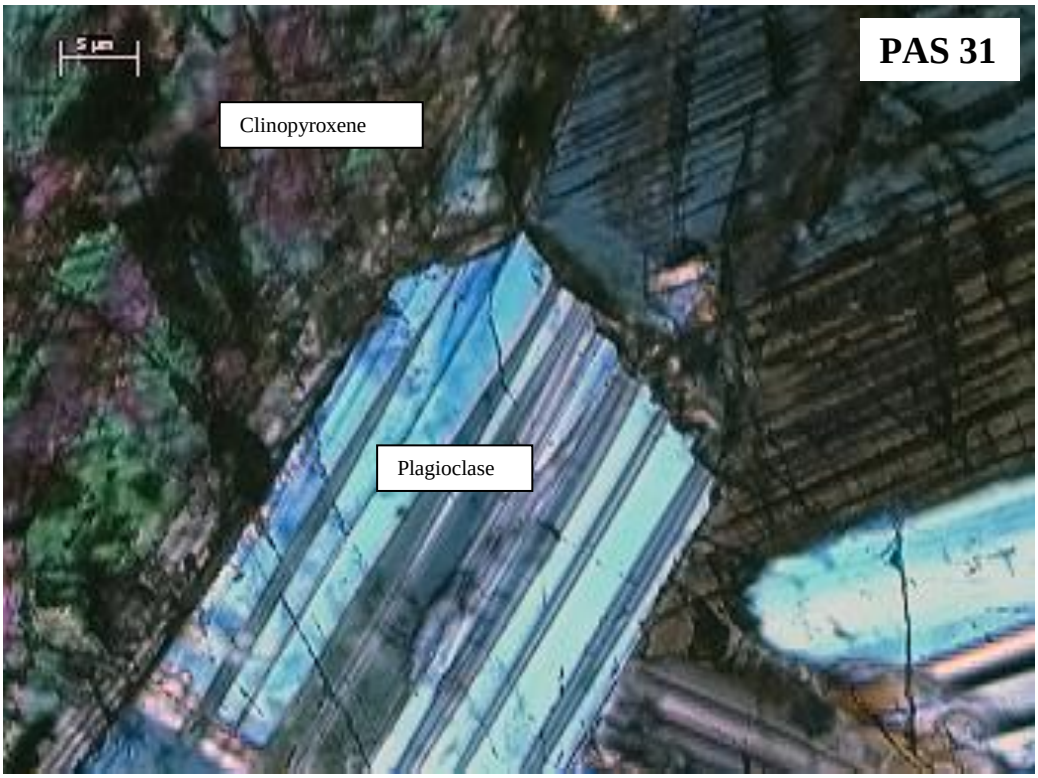

Figure 13c: (PAS 31) Large subhedral plagioclase (4mm) crystals showing albite twinning. The large anhedral pyroxenes consist of +/-5% clinopyroxene and +/- 15% orthopyroxene. The pyroxenes are enclosed by plagioclase crystals.

3.2. Petrography of borehole core TW 632

The Twickenham borehole contains mostly gabbronorites with infrequent anorthosites (Figure 14). All rocks contain about 44 wt% - 93 wt% plagioclase and orthopyroxene and clinopyroxene in the ratio of 2:1.

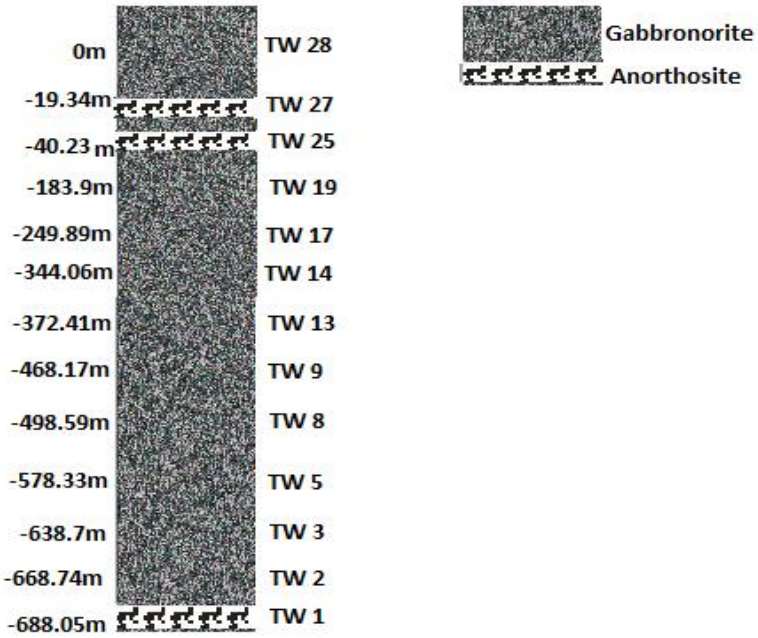

Figure 14: Borehole log for thin sections (TW 632).

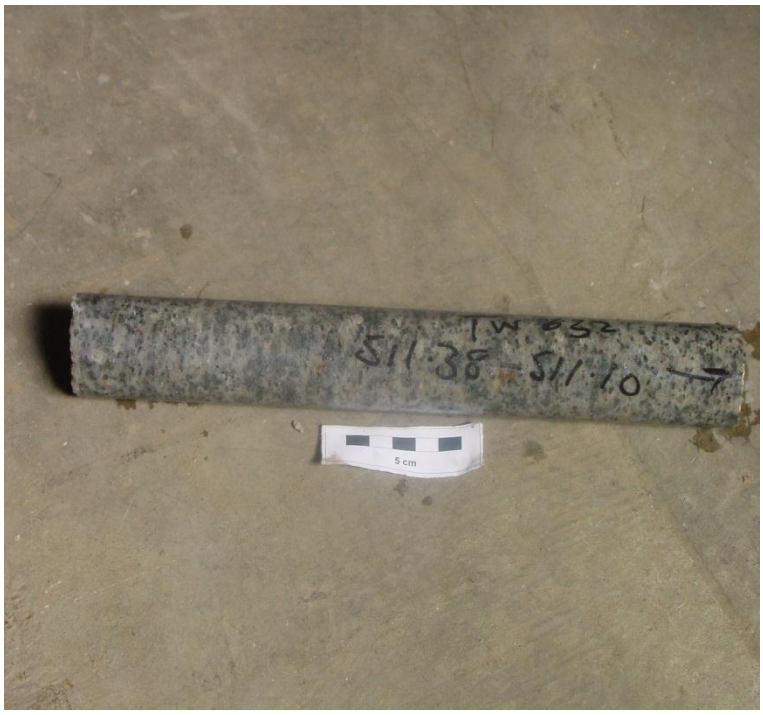

Figure 15: Gabbronorite (TW 19).

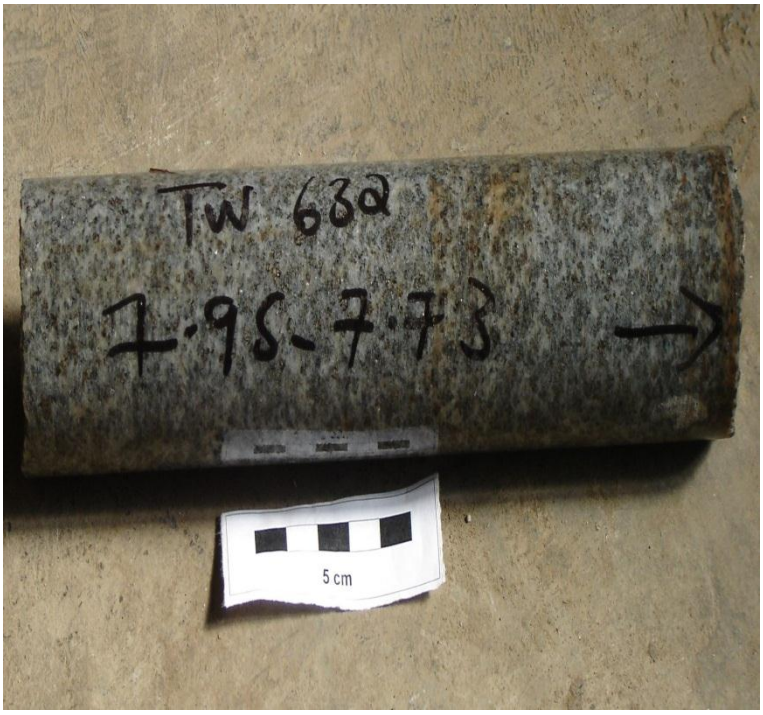

Figure 16: Mottled Anorthosite (TW 1).

Gabbronorites (TW 2, TW 3, TW 5, TW 8, TW 9, TW 13, TW 14, TW 17, TW 19 AND TW 28):

The gabbronorites are medium (~2 mm) to coarse (~5 mm) grained (Figure 17), with plagioclase crystals ranging from small and euhedral to large and subhedral or anhedral. The plagioclase crystals (plag) exhibit Albite and Carlsbad twinning. Plagioclase occurs as inclusions in large (>5 mm) pyroxene crystals, thus indicating the plagioclase crystals formed first.

Euhedral opx and smaller subhedral cpx make up ~10 wt% of the rock. Chlorite is an alteration by-product of clinopyroxene and talc and serpentine are alteration by-products of orthopyroxene.

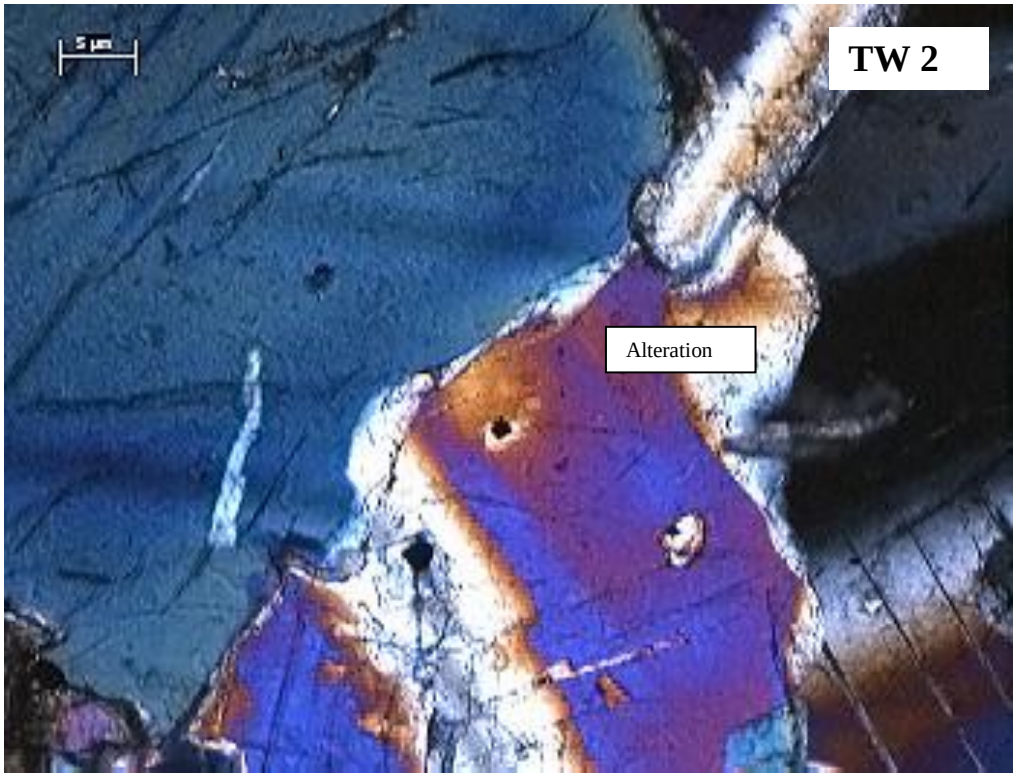

Figure 17a: (TW 2) Plagioclase crystals show Albite and Carlsbad twinning. The rock has an equigranular texture, and comprises of +/-90% plagioclase, +/-8% clinopyroxene and +/-3% orthopyroxene.

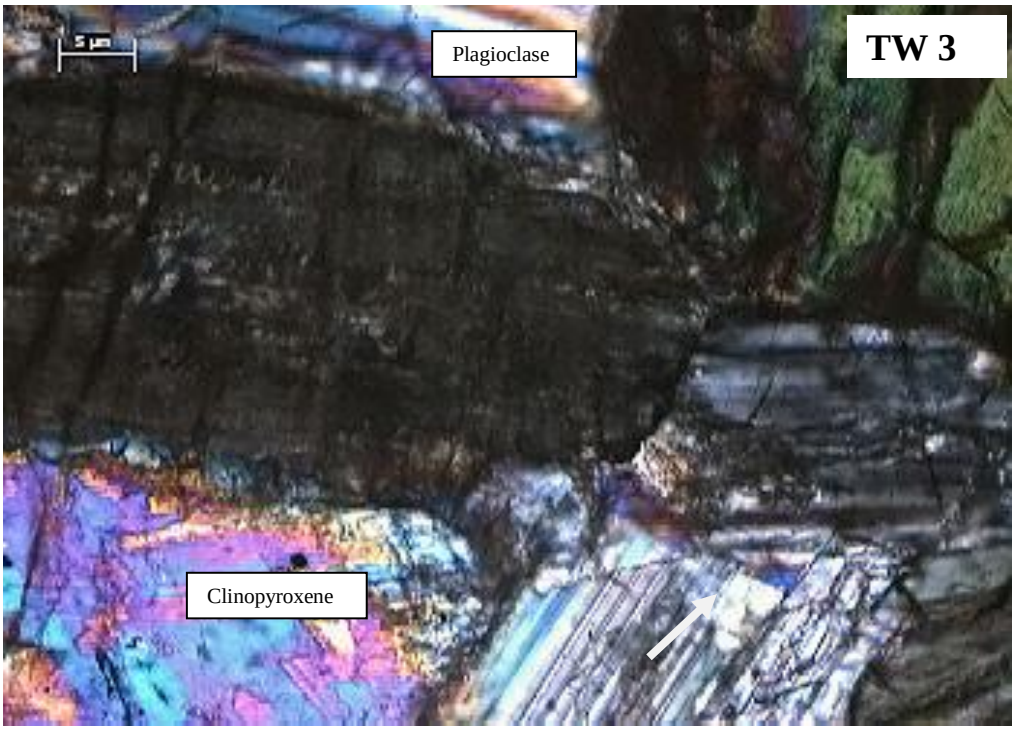

Figure 17b: (TW 3) Medium to coarse grained (2-4mm) rock containing elongated plagioclase crystals, showing Albite and Carlsbad twinning. Plagioclase occurs as inclusions in the pyroxenes. Orthopyroxene and clinopyroxene also present but orthopyroxene more abundant than clinopyroxene.

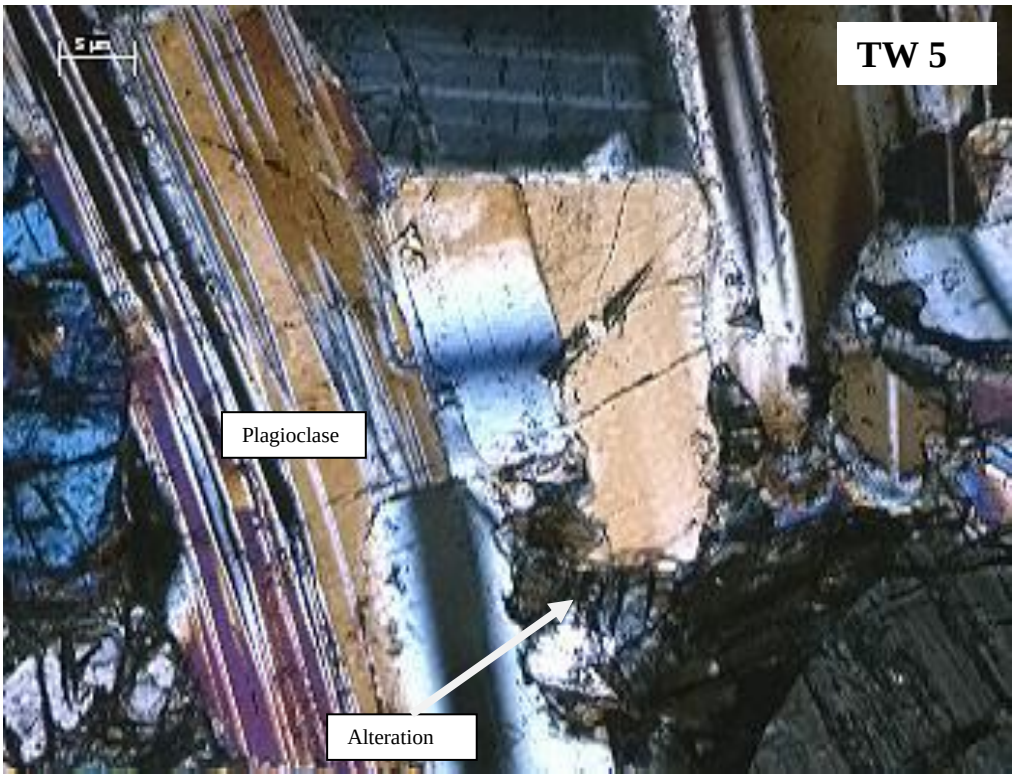

Figure 17c: (TW 5) Medium to coarse grained (2-4mm) rock containing elongated plagioclase crystals, showing Albite and Carlsbad twinning. Plagioclase crystals occur as inclusions in the pyroxenes. Orthopyroxene and clinopyroxene also present but orthopyroxene more abundant than clinopyroxene.

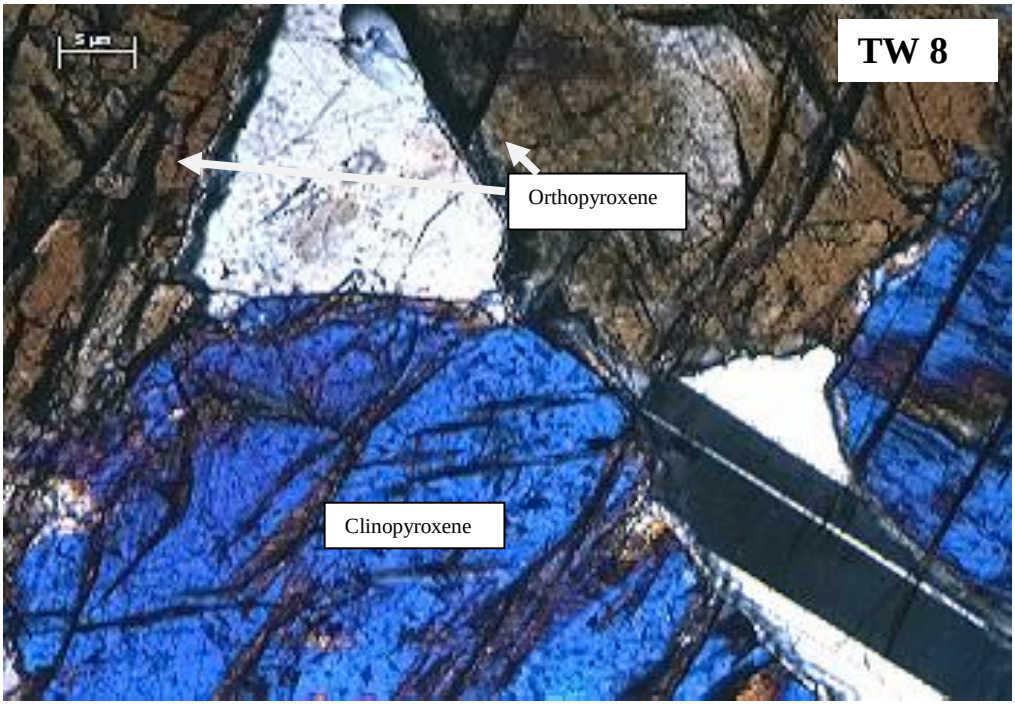

Figure 17d: (TW 8) Medium to coarse grained (2-4mm) rock containing elongated plagioclase crystals, showing Albite and Carlsbad twinning. The plagioclase crystals are enveloped by pyroxene crystals. Orthopyroxene and clinopyroxene also present but orthopyroxene more abundant than clinopyroxene.

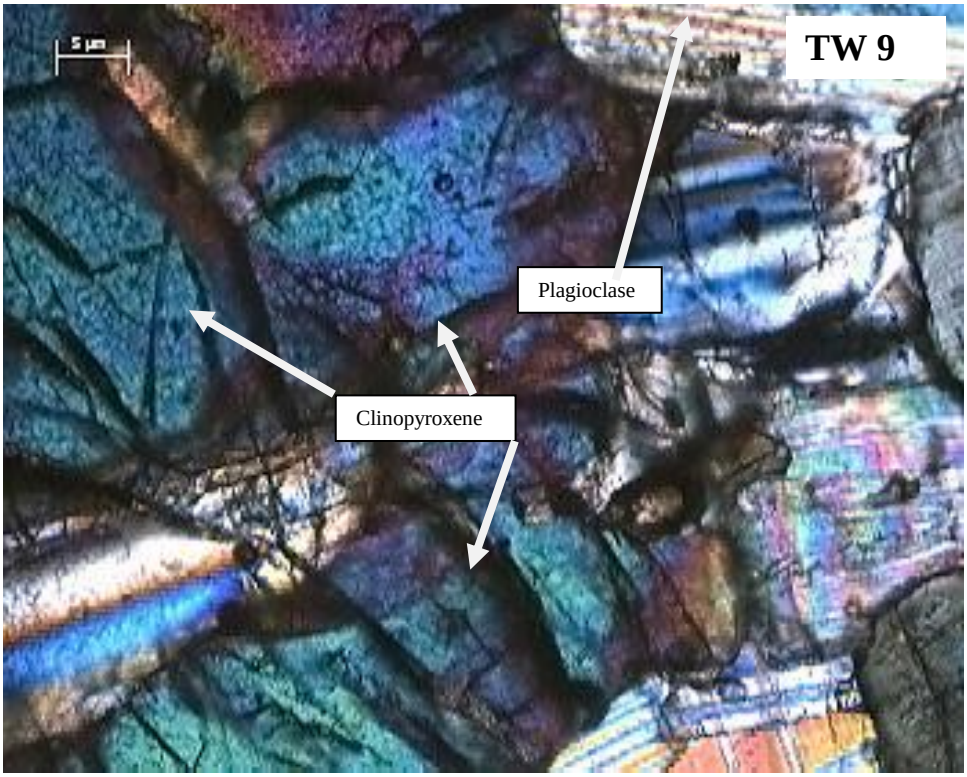

Figure 17e: (TW 9) Medium to coarse grained (2-4mm) rock containing elongated plagioclase crystals, showing Albite and Carlsbad twinning. There are plagioclase inclusions in the pyroxenes. Orthopyroxene and clinopyroxene also present but orthopyroxene more abundant than clinopyroxene.

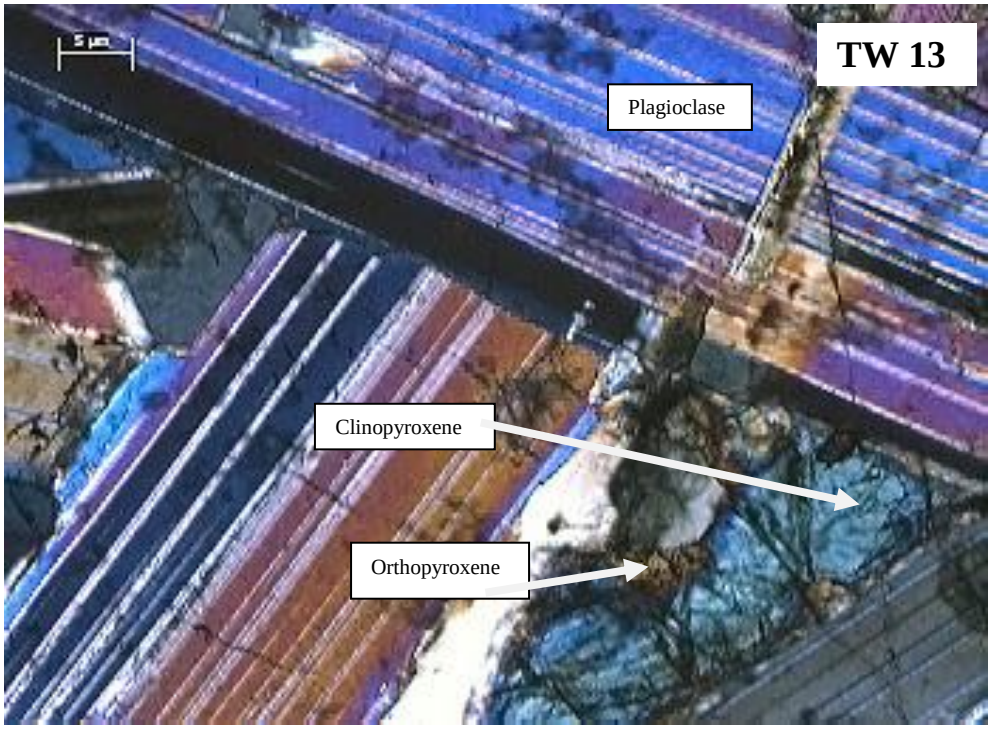

Figure 17f: (TW 13) Medium to coarse grained (2-4mm) rock containing elongated plagioclase crystals, showing Albite and Carlsbad twinning. There are plagioclase inclusions in the pyroxenes. Orthopyroxene and clinopyroxene also present but orthopyroxene more abundant than clinopyroxene.

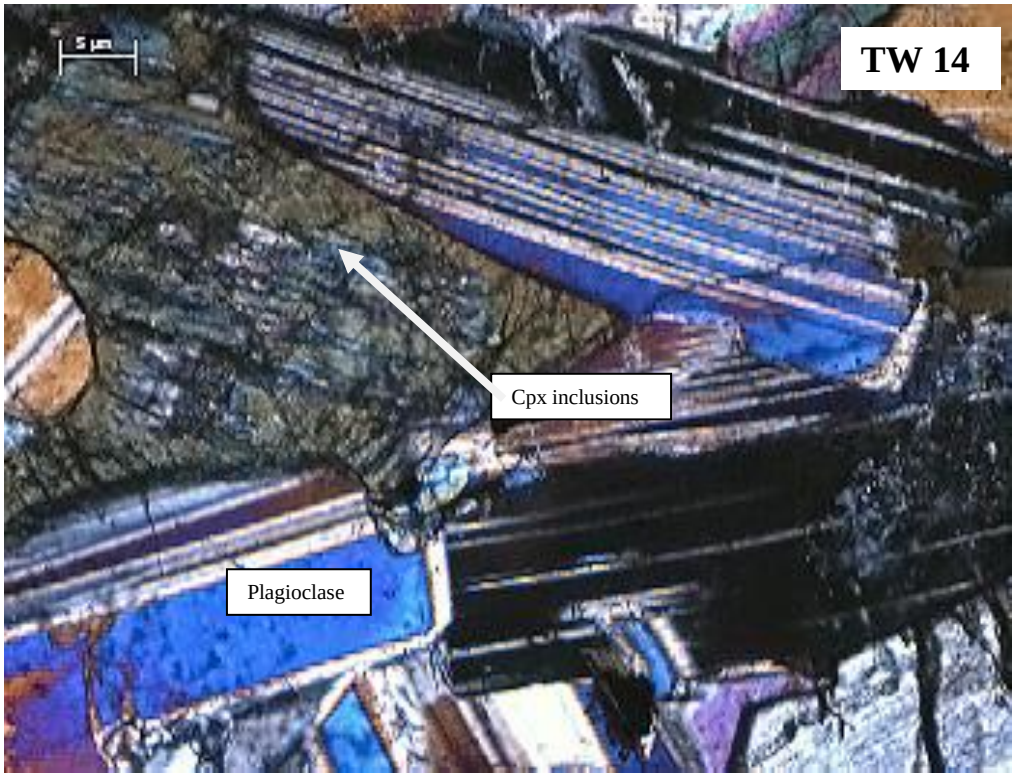

Figure 17g: (TW 14) Medium grained (1-2mm) plagioclase showing Carlsbad and albite twinning. Euhedral orthopyroxene and medium grained, subhedral clinopyroxene crystals are present. Chlorite is an alteration product of clinopyroxene.

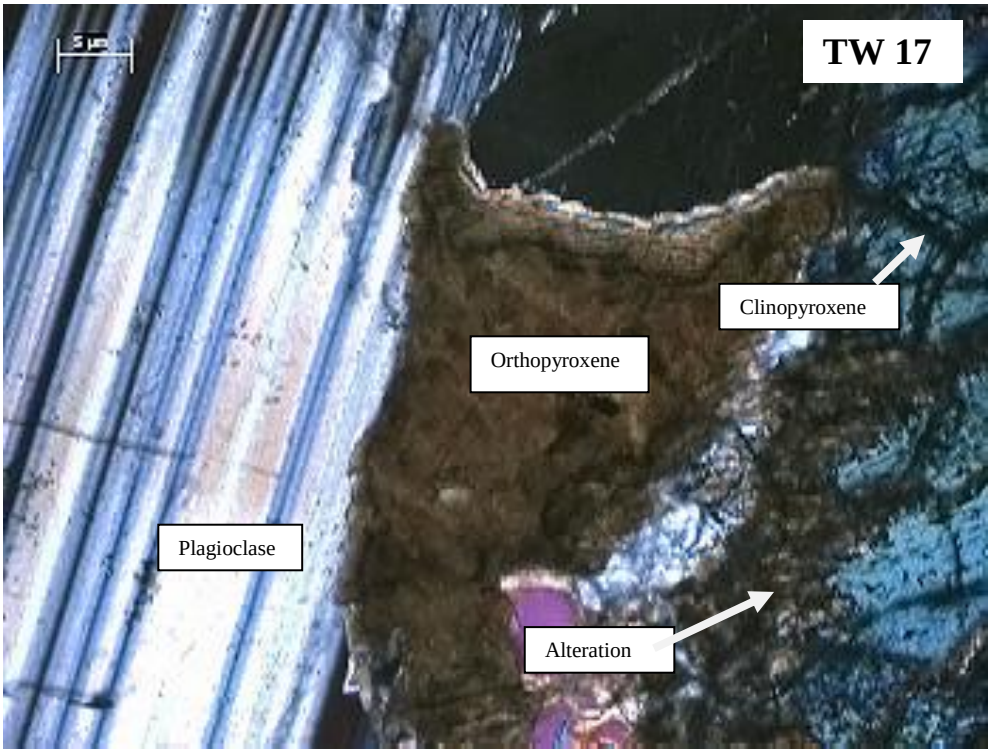

Figure 17h: (TW 17) Medium grained (1-2mm) plagioclase showing Carlsbad and albite twinning. Euhedral orthopyroxene and medium grained, subhedral clinopyroxene crystals are present. Chlorite is an alteration product of clinopyroxene.

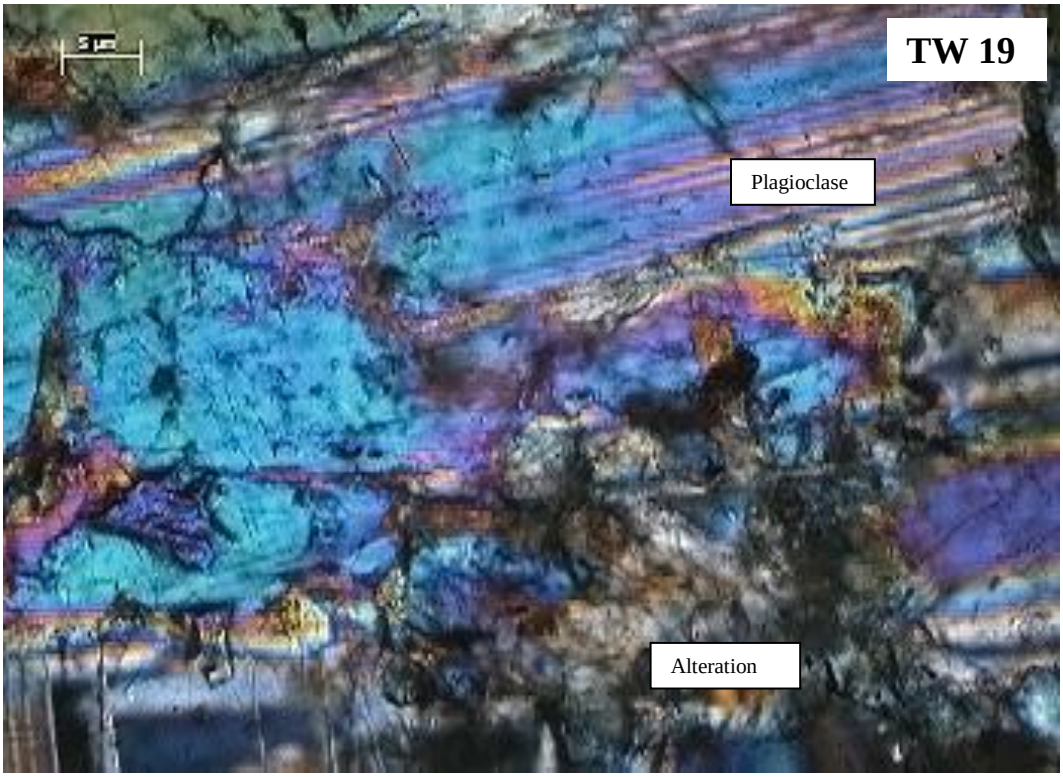

Figure 17i: (TW 19) Medium grained (1-2mm) plagioclase showing Carlsbad and albite twinning. Large, euhedral orthopyroxene and medium grained, subhedral clinopyroxene crystals are present.

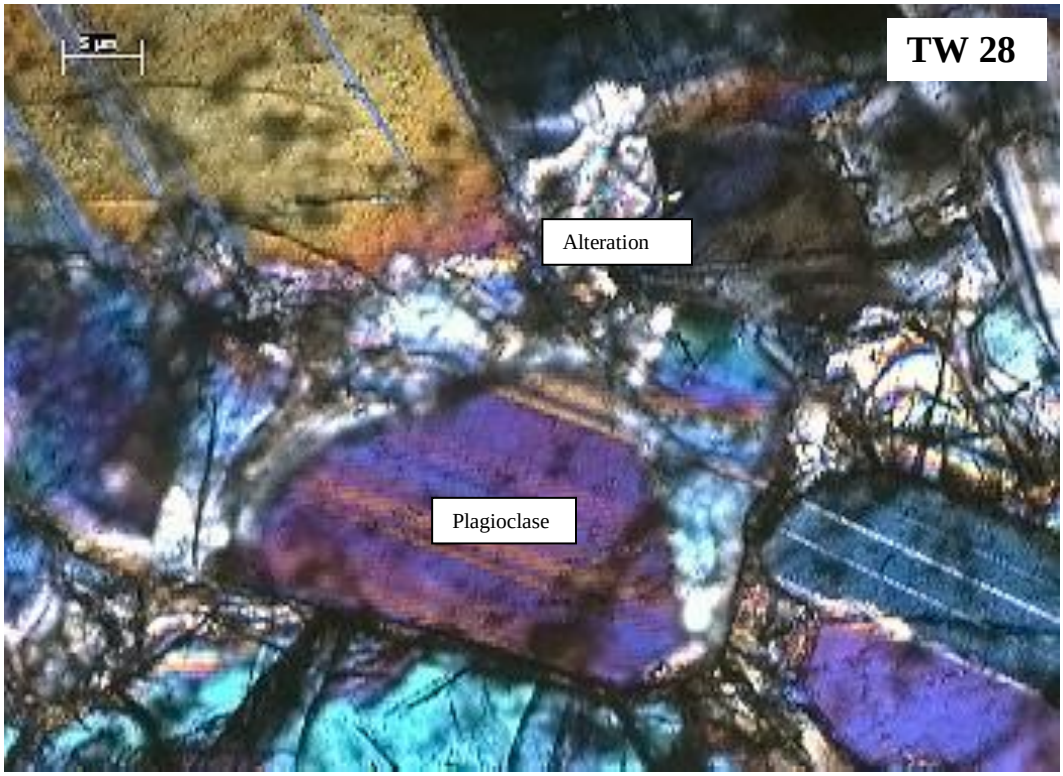

Figure 17j: (TW 28) Larger euhedral orthopyroxene with smaller subhedral clinopyroxene. There is visible alteration of clinopyroxene to chlorite.

Anorthosites (TW 1, TW 25 AND TW 27):

Anorthosite is composed almost entirely of feldspar with small quantities of ferromagnesian minerals (pyroxenes). Plagioclase crystals exhibit grain sizes that range between 2- 4 mm. They also show signs of Carlsbad, Pericline (Figure 18b) and Albite twinning. The px in anorthosite contribute ~10 wt% of the rock and are interstitial. Clinopyroxene are the dominant ferromagnesian minerals in the anorthosites.

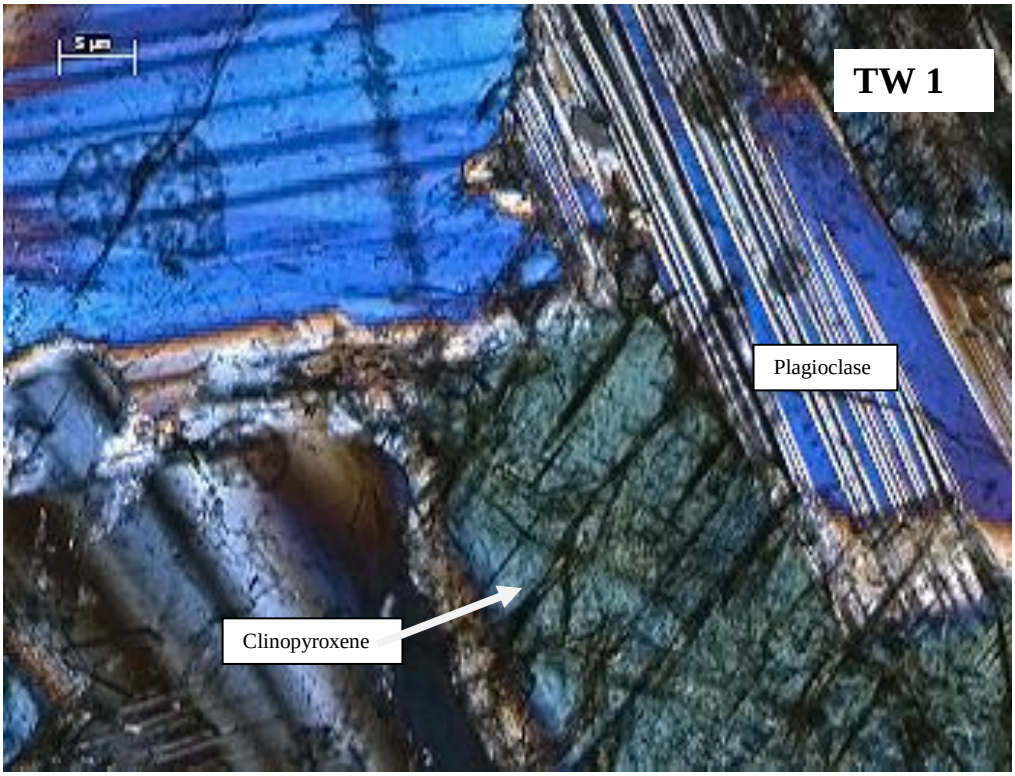

Figure 18a: (TW 1) Subhedral plagioclase crystals. Orthopyroxene and clinopyroxene also present but orthopyroxene more abundant than clinopyroxene.

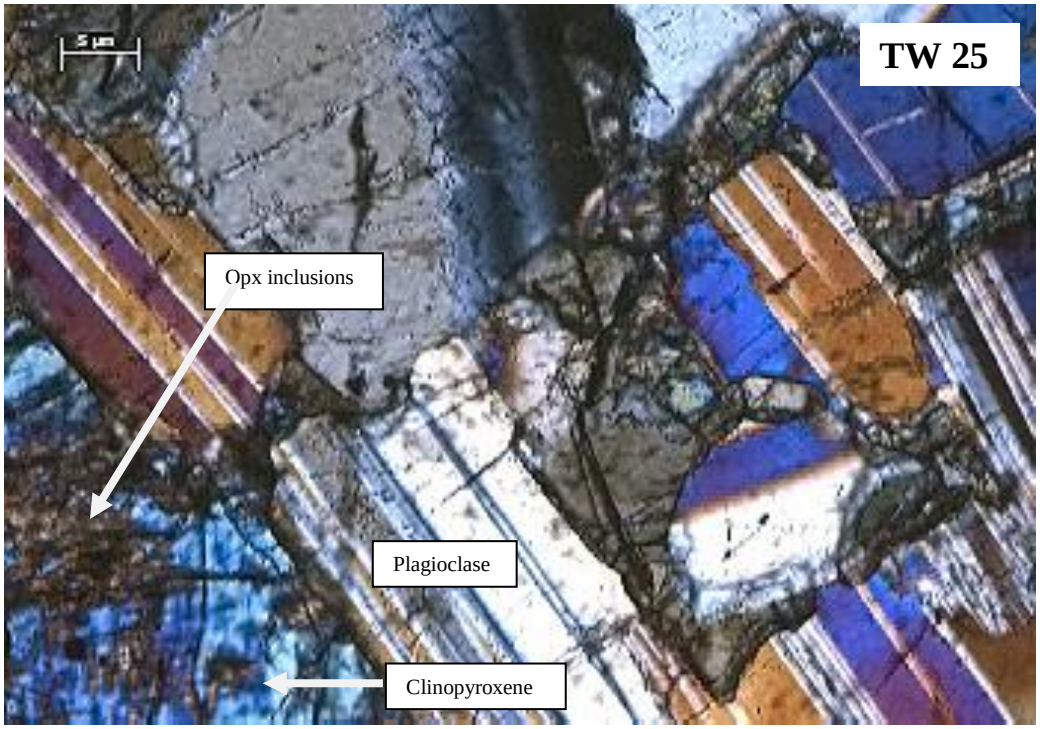

Figure 18b: (TW 25) Plagioclase crystals are euhedral showing Carlsbad and Albite twinning. Plagioclase crystals are in mutual contact with each other, indicating that the plagioclase grew prior to the solidification of the interstitial liquid. The small grained clino – and -orthopyroxenes have interstitial oxides.

Figure 18c: (TW 27) Plagioclase crystals are euhedral showing albite and Carlsbad twinning. Orthopyroxene and clinopyroxenes range from anhedral to subhedral. Clinopyroxene envelopes plagioclase laths, thus indicating clinopyroxene formed later than the plagioclase. The rock is fine grained with +/-70% plagioclase and +/-10% pyroxene with more clinopyroxene than orthopyroxene.

CHAPTER 4: GEOCHEMICAL RESULTS

4.1. CIPW and XRD data

The CIPW norm (Table 8 and Table 9) is the most commonly used mineral classification scheme. The CIPW scheme is designed to present a normalised mineralogy for a geochemical analysis, and is intended to allow comparison of rocks from different locations. The CIPW of a rock may substantially differ from the observed mineralogy due to a few simplifying assumptions: 1) the magma from which the minerals crystallised is considered anhydrous and thus biotite and hornblende are not permitted, and, 2) no account is taken for minor solid solution of elements such as Ti/Al, Fe/Mg. The major rock type observed throughout the two boreholes studied is gabbronorite with minor anorthosite (Figure 19). The normative mineralogy is given due to the small variation in ratio between the orthopyroxene and clinopyroxene in the thin sections; thus the CIPW norm may be more informative than an estimation of pyroxene content and composition derived from optical mineralogy.

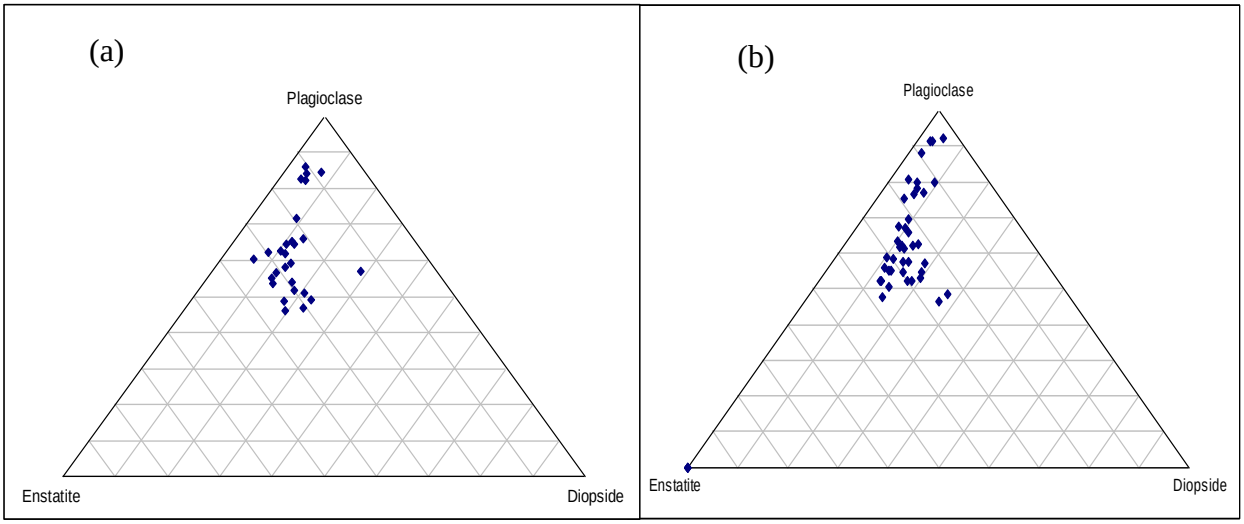

Figure 19: Triplot of the normative mineralogy (Plagioclase and Pyroxene) showing the different rock types of borehole (a) PK 206 (Paschaskraal) and (b) TW 632 (Twickenham).

The amount of quartz (Q) is low with values ranging from 0- 7.42 wt%, with a few samples containing no quartz at all (PAS 40, TW 25 and TW 27). The XRD data indicate

that the previously mentioned samples contain small amounts of quartz 1.01, 2.22 and 2.18 respectfully. The low amount of quartz in the boreholes reflects the magmas original composition.

Table 8a: Gabbronorite rocks displaying mineral variation (CIPW data).

	Average (wt %)	Std. Dev. (wt %)	Std. Dev.*100 (wt %)	Rel. Std. Dev. (wt %)	Max. (wt %)	Min. (wt %)
Q	4.91	1.76	176.06	35.90	7.42	0.57
Or	1.62	0.36	35.87	22.14	2.92	0.96
Ab	17.14	3.36	335.86	19.60	26.91	11.86
An	47.65	7.69	768.79	16.14	65.76	36.49
plagioclase	64.79	10.79	1079.39	16.66	90.68	48.35
Hy(MS)	8.04	4.48	447.53	55.63	19.28	0.53
pyroxene	15.01	5.23	523.10	34.85	23.81	0.44
Ol(MS)	23.06	8.17	816.75	35.42	35.14	4.54
Il	0.00	0.01	0.67	425.96	0.04	0.00
Hm	0.22	0.06	6.32	28.76	0.31	0.07
Tn	5.31	1.42	142.07	26.74	7.56	1.61
Pf	0.07	0.07	6.73	90.69	0.28	0.00

Table 8b: Anorthosite rocks displaying mineral variation (CIPW data).

	Average (wt %)	Std. Dev. (wt %)	Std. Dev.*100 (wt %)	Rel. Std. Dev. (wt %)	Max. (wt %)	Min. (wt %)
Q	2.39	2.17	216.69	90.67	5.84	0.00
Or	1.74	0.59	58.72	33.69	2.95	0.88
Ab	20.79	2.65	264.61	12.73	25.88	16.75
An	60.53	8.95	894.78	14.79	72.67	46.04
plagioclase	81.31	10.55	1054.53	12.97	92.92	62.78
Ne	0.11	0.30	30.39	267.50	1.04	0.00
Wo	0.21	0.71	70.94	346.43	2.56	0.00
Di(MS)	5.76	4.08	408.29	70.88	16.90	0.99
Hy(MS)	5.14	5.28	528.03	102.66	15.08	0.00
pyroxene	10.90	7.37	736.67	67.56	25.21	1.42
Ol(MS)	0.10	0.26	25.79	250.99	0.82	0.00
Il	0.12	0.06	6.29	52.83	0.23	0.04
Hm	2.91	1.47	147.41	50.64	5.40	1.21
Tn	0.16	0.16	16.14	102.06	0.60	0.00
Pf	0.00	0.01	0.89	274.87	0.03	0.00
Ap	0.04	0.06	5.78	158.88	0.21	0.00

Table 9a: Mineral variations of gabbronorite rocks (XRD data). (Units = Weight Fraction).

	Average	Std. Dev.	Std. Dev.*100	Rel. Std. Dev.	Max.	Min.
Biotite	3.54	2.86	285.65	80.71	10.50	0.00
Calcite	1.90	0.60	59.96	31.63	4.46	0.95
Chlorite	0.45	1.48	148.38	328.09	8.62	0.00
Diopside	11.76	4.47	446.47	37.96	23.45	2.37
Enstatite	22.89	6.29	628.55	27.46	32.72	1.70
Magnetite	0.79	0.99	98.50	125.35	2.88	0.00
Hornblende	0.25	0.87	86.77	350.50	5.79	0.00
Lizardite	0.06	0.28	27.77	469.04	1.30	0.00
Microcline	1.82	0.82	81.92	45.04	3.54	0.00
Plagioclase	51.73	9.32	931.71	18.01	75.60	36.41
Prehnite	2.44	1.34	134.26	54.99	4.06	0.00
Quartz	2.63	1.96	195.75	74.43	15.17	0.47
Talc	1.35	1.42	142.30	105.20	5.02	0.00

Table 9b: Mineral variations of anorthosite rocks (XRD data). (Units = Weight Fraction).

	Average	Std. Dev.	Std. Dev.*100	Rel. Std. Dev.	Max.	Min.
Biotite	1.31	2.04	203.76	156.05	7.81	0.00
Calcite	2.13	0.64	63.64	29.84	2.52	0.00
Chlorite	0.32	0.87	86.71	272.17	3.02	0.00
Diopside	6.84	5.48	547.38	80.05	23.45	2.51
Enstatite	13.57	5.72	572.04	42.17	23.81	4.92
Magnetite	0.36	0.62	62.16	171.31	1.71	0.00
Hornblende	0.08	0.28	28.33	374.17	1.06	0.00
Microcline	2.22	0.70	69.54	31.29	3.21	0.61
Plagioclase	68.66	9.84	984.05	14.33	82.86	47.10
Prehnite	3.28	1.80	180.41	54.94	5.24	0.83
Quartz	2.98	1.23	122.54	41.19	5.33	1.01
Talc	0.37	0.64	63.85	172.90	2.18	0.00

The orthoclase (Or) values range from 0.88- 2.95 wt% according to the CIPW calculations. The XRD data obtained indicate that the K-feldspars ($KAlSi_3O_8$) are limited to microcline, the triclinic feldspar, instead of orthoclase, the monoclinic feldspar. This is an indication that the magma cooled slowly at considerable depth.

Plagioclase feldspars form at elevated temperatures and have a complete solid solution series from pure albite (Ab) to pure anorthosite (An). The albite values range from $Ab_{11.86\text{-}26.91}$ and the anorthosite values range from $An_{72.67\text{-}36.49}$ according to the CIPW norm, which is not a true estimation of the mineralogy. CIPW normative calculations do

not account for solid solution of elements. Plagioclase minerals are abundant in all the rocks of the MZ, and as a general rule the lower the percentage of SiO_2, the greater the percentage of darker minerals and the more calcic the plagioclase.

The pyroxene group is subdivided into orthopyroxene (opx): enstatite ($MgSiO_3$), ferrosilite ($FeSiO_3$) and pigeonite $Ca_{0.25}(Mg,Fe)_{1.75}Si_2O_6$ and clinopyroxene (cpx): diopside ($CaMgSi_2O_6$), hedenbergite ($CaFeSi_2O_6$) and augite $(Ca,Na)(Mg,Fe,Al)(Si,Al)_2O_6)$. The CIPW calculations cannot account for the relationship between Mg and Fe. The hypersthene (Hy) indicates the amount of opx and diopside (Di) is the amount of cpx. The XRD data is a better estimation for the pyroxenes with opx values ranging from 1.7- 32.72 and the cpx ranging from 2.37- 22.28.

Olivine (Ol) occurs in low concentrations (0- 0.82) and is a high temperature mineral. A few samples in the middle and top portion of borehole PK 206 contain trace amounts of magnetite (0.91- 2.88), hematite (1.21- 7.56), ilmenite (0.04- 0.31) and titanite (0– 0.60) but these minerals are in low abundance and may only reflect magmatic segregation.

Apatite (Ap) accounts 0.02 wt% on average for the rocks in the two boreholes. The calcite values according to the XRD data, range from 0.98- 4.46 wt% and will be incorporated into the Ca-rich pyroxenes.

4.2. Major Element Geochemistry

In a layered intrusive complex, whole rock major element chemistry simply reflects the cumulus mineralogy (Cawthorn and Webb 2001). Cawthorn (1982) has shown that unless a cumulus mineral is abundant in a rock its composition may be significantly changed towards the low – temperature end member by post cumulus reequilibration with trapped liquid. The extent of this change is proportional to the amount of trapped liquid and inversely related to the proportion of the cumulus phase.

Major element data can also be used to construct variation diagrams and scatter plots, which are used to indicate the interrelationship between elements. The mineralogy and crystallisation within a magma chamber are largely controlled by the concentration of major elements. The major elements (Table 10) also control density, viscosity and diffusivity of magmas and rocks (Winter, 2001); thus major element data is used to observe evolutionary trends within the magma chamber.

Table 10: Major element data.

	Average (wt %)	Std. Dev. (wt %)	Max. (wt %)	Min. (wt %)
SiO_2	51.35	1.21	53.22	48.43
TiO_2	0.14	0.04	0.26	0.04
Al_2O_3	22.00	4.01	30.88	15.93
Fe_2O_3	4.87	1.71	7.48	1.20
MnO	0.09	0.03	0.14	0.02
MgO	6.72	3.03	11.05	0.26
CaO	12.07	1.40	16.11	10.03
Na_2O	2.10	0.41	3.12	1.39
K_2O	0.28	0.070	0.49	0.15
P_2O_5	0.01	0.01	0.09	0.00
Cr_2O_3	0.05	0.02	0.12	0.00
NiO	0.02	0.01	0.05	0.00
V_2O_5	0.01	0.01	0.02	0.00
ZrO_2	0.01	0.00	0.01	0.00
LOI	0.18	0.51	3.08	-0.16
Total	99.90	0.72	101.21	97.97

Harker diagrams (Figure 20 - 28), on which two selected variables are plotted, can give a good description of how the magma evolved.

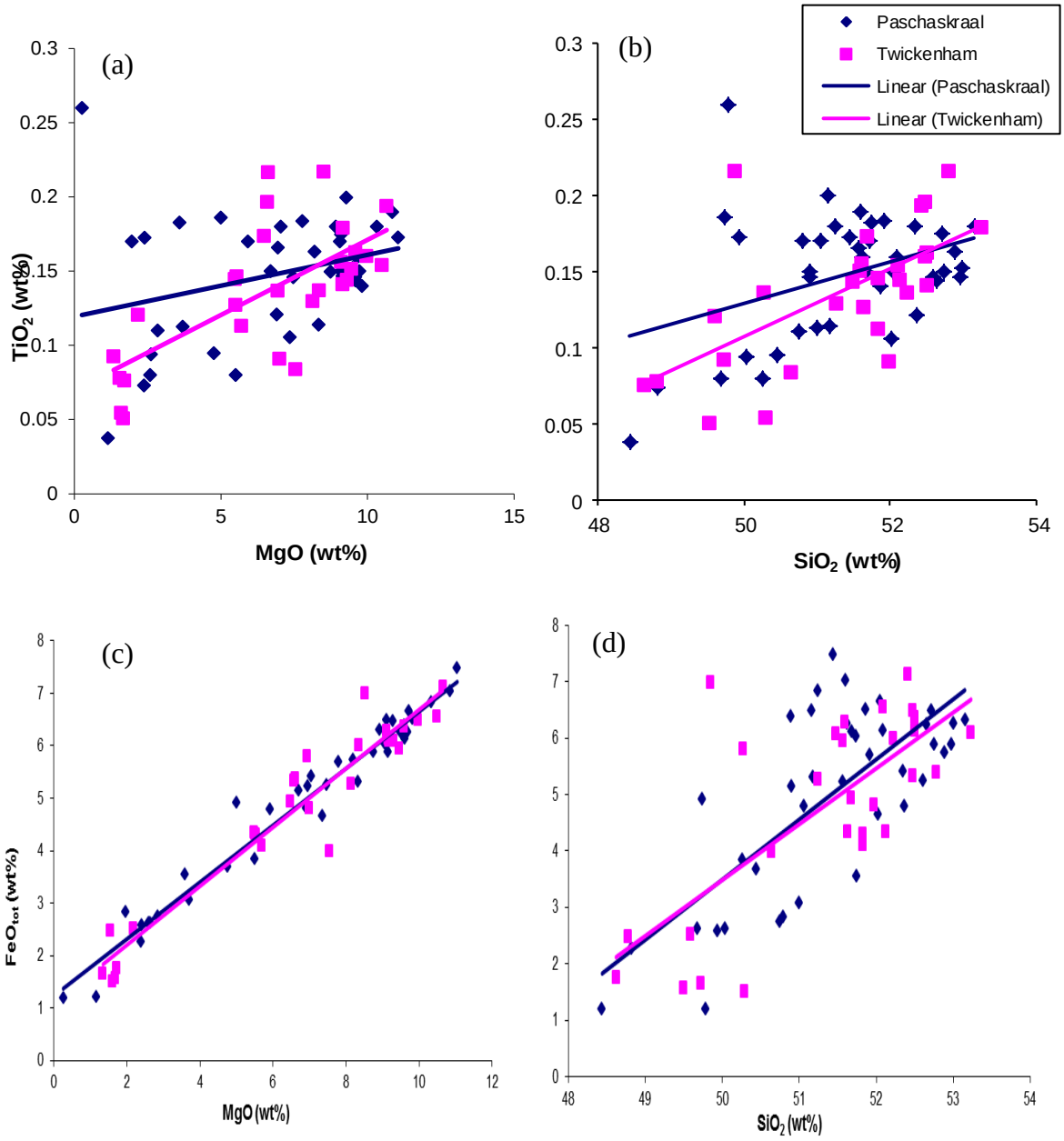

Figure 20: (a) TiO_2 (wt %) vs MgO (wt %), (b) TiO_2 (wt %) vs SiO_2 (wt %), (c) FeO_{tot} (wt %) vs MgO (wt %), (d) FeO_{tot} (wt %) vs SiO_2 (wt %).

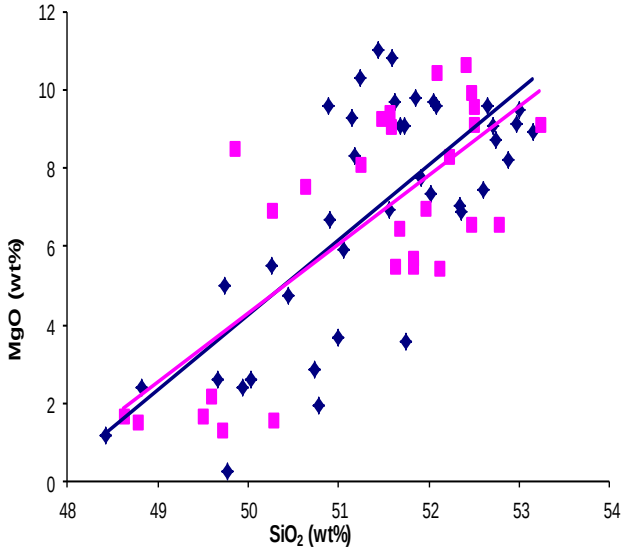

Figure 21: (a) MgO (wt %) vs SiO_2 (wt %).

The TiO_2 concentration varies from 0.04- 1.70 wt%, but is fairly constant throughout the two boreholes. The TiO_2 slightly increases with increasing SiO_2. There is a good correlation between the two boreholes and this supports the idea that the rocks crystallised from the same magma. Ti can substitute for Mg and will fractionate into the more mafic pyroxenes rather than into the felsic plagioclase minerals. There is an inverse correlation of TiO_2 in relation to Fe_2O_3 and MgO with a few exceptions at -99.87 m, -120 m, -180.15 m, -468.17 m and -638.7 m where lower TiO_2 correlates with higher MgO and Fe_2O_3 concentrations.

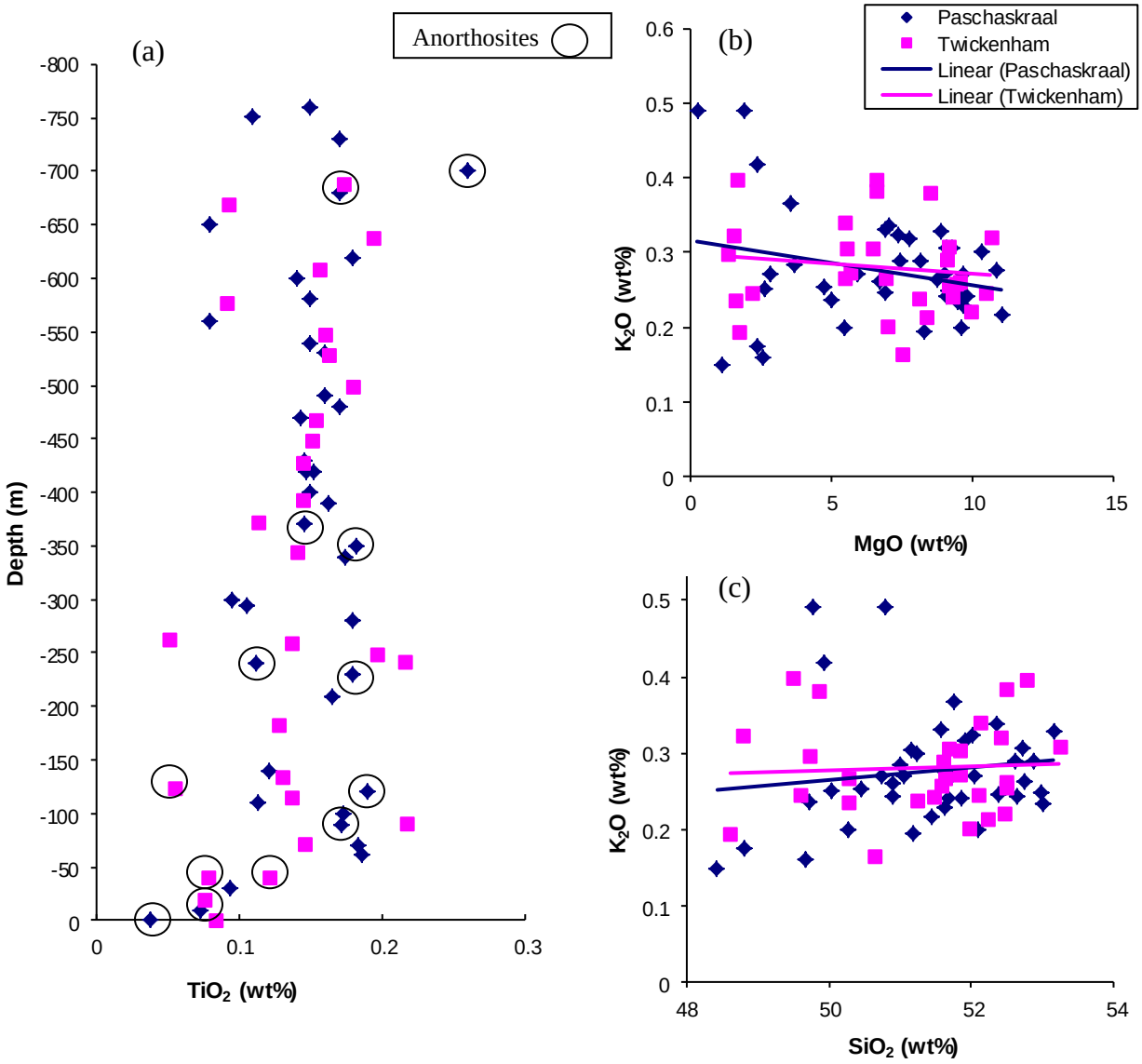

Figure 22: (a) Variation of TiO_2 (wt %) with Depth (m), (b) K_2O (wt %) vs MgO (wt %) and (c) K_2O (wt %) vs SiO_2 (wt %).

There is a slight decrease in K_2O from the bottom to the top of the boreholes but it remains constant at (0.15– 0.49 wt%) in relation to the SiO_2 concentration. K_2O decreases with increasing MgO owing to the compatibility of K with plagioclase.

The P_2O_5 values are constant throughout the boreholes (ranging from 0– 0.15 wt%) with only one significant increase, at -700 m. The P_2O_5 increases with increasing SiO_2. This is directly correlated to the concentration of apatite minerals throughout the MZ. The

constant V_2O_5 (0- 0.06 wt%) concentration increases with increasing SiO_2 concentration. The stable ZrO_2 (0- 0.01 wt%) value decreases with increasing SiO_2 concentration due to the compatibility of Zr and plagioclase, this would be expected.

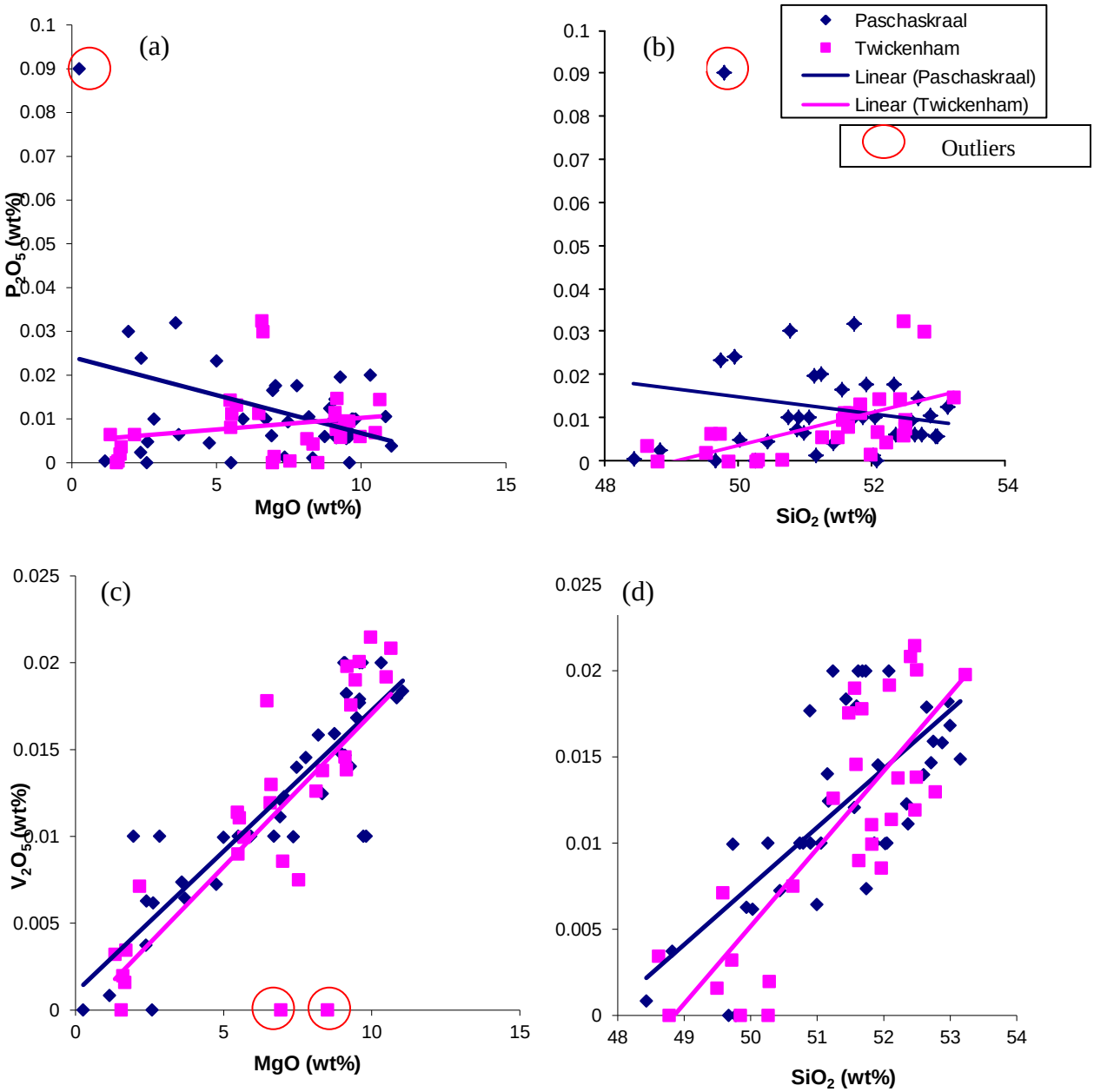

Figure 23: (a) P_2O_5 (wt %) vs MgO (wt %), (b) P_2O_5 (wt %) vs SiO_2 (wt %), (c) V_2O_5 (wt %) vs MgO (wt %) and (d) V_2O_5 (wt %) vs SiO_2 (wt %).

The anorthosite rocks are mainly composed of plagioclase feldspar, and thus these rocks are rich in Al and dependant on the composition of plagioclase. The Al_2O_3 concentration varies from 16.42- 30.87 wt% in PK 206 and 13.02– 29.58 wt% in TW 632. The

decreases with increasing SiO_2 content, which indicates the fractionation of the Al_2O_3 into the plagioclase phases, owing to Al having an affinity for plagioclase.

CaO varies from 10.03– 15.60 wt% in the PK 206 borehole and from 10.25– 16.11wt% in the TW 632 borehole. CaO decreases with increasing SiO_2, owing to the Ca affinity between plagioclase minerals and Ca. The Ca-poor pyroxene minerals that are in the MZ are thus late stage forming minerals.

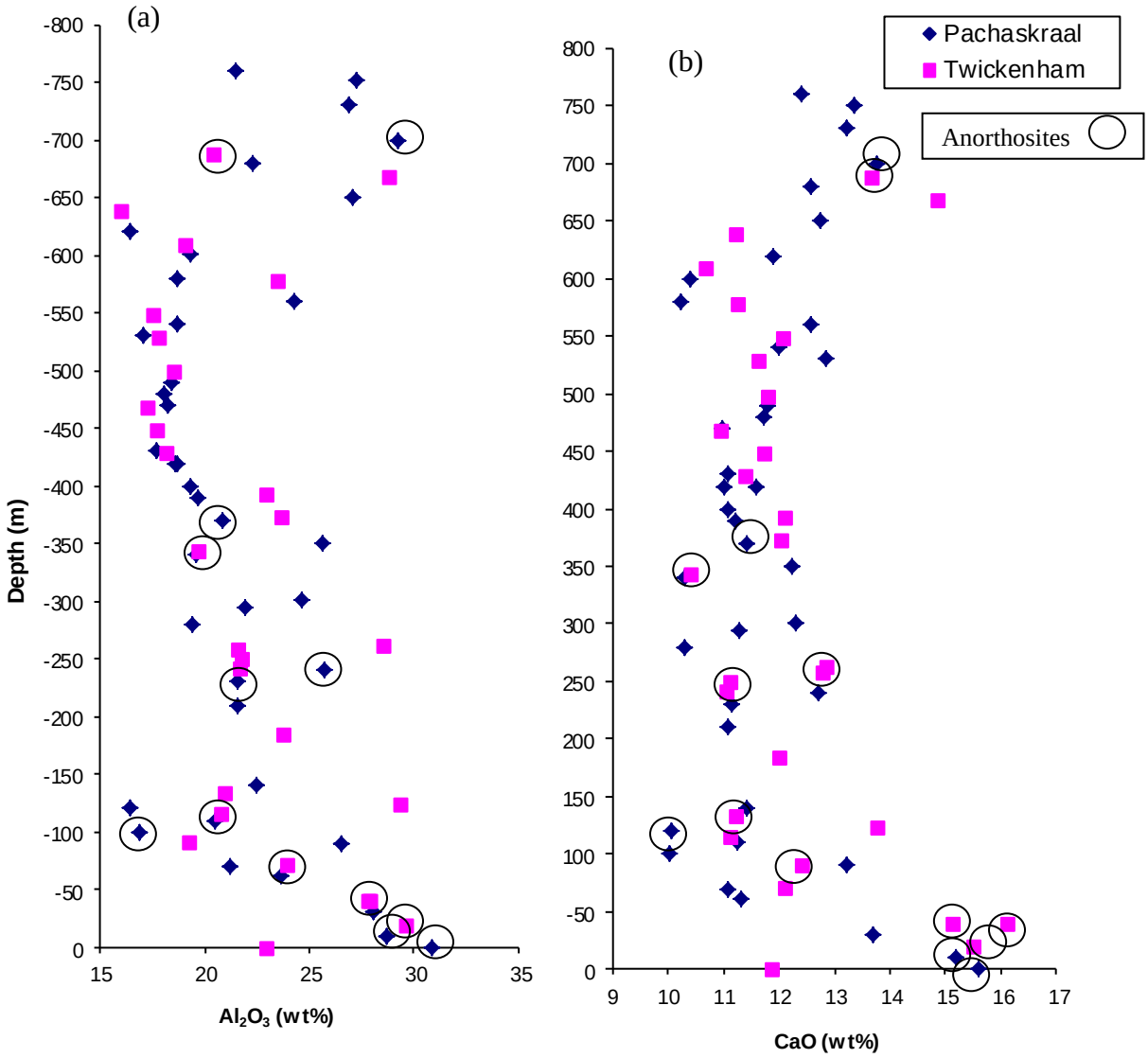

Figure 24: (a) Variation Al_2O_3 (wt %) with Depth (m) and (b) Variation CaO (wt%) with Depth (m).

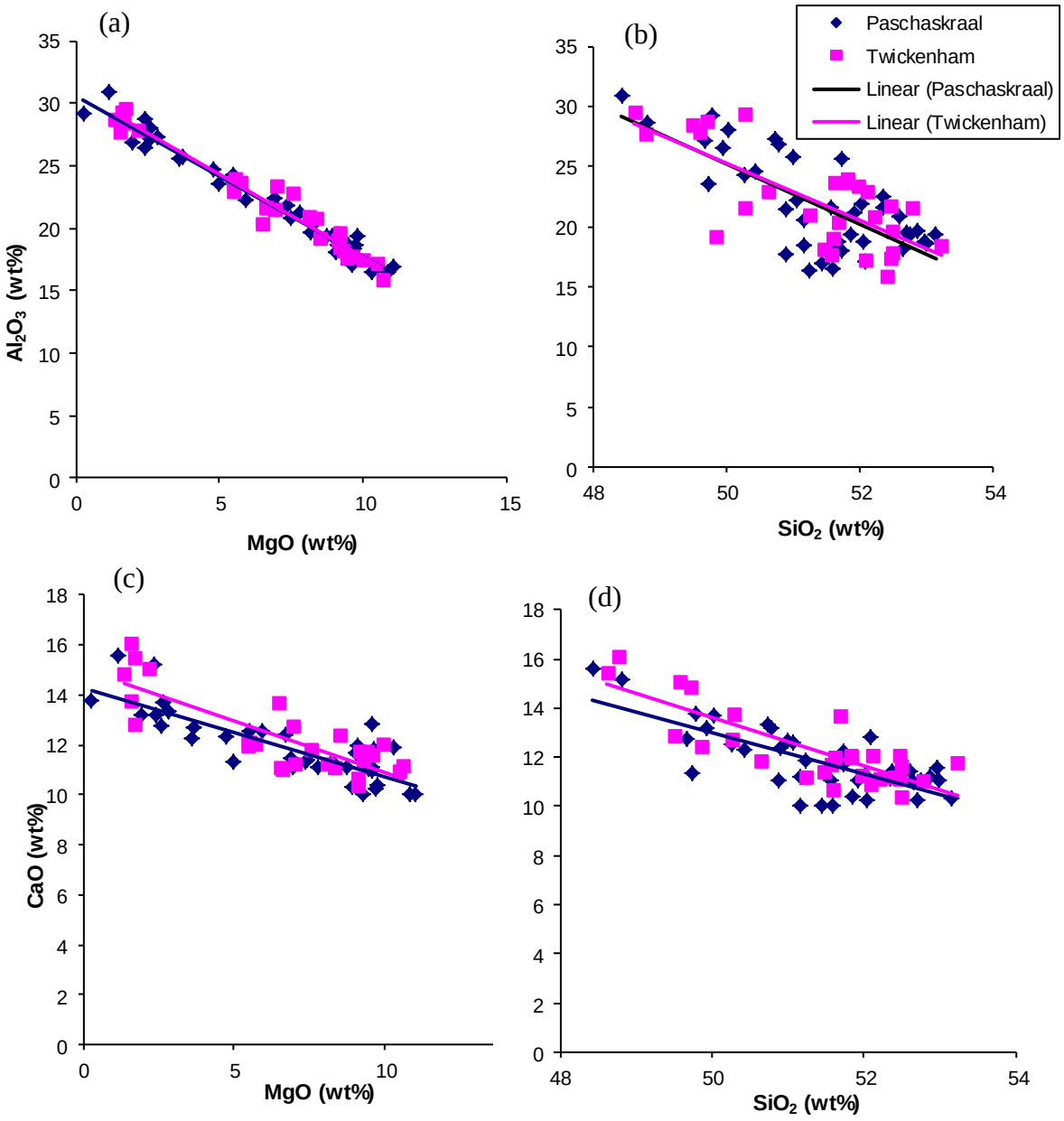

Figure 25: (a) Al_2O_3 (wt %) vs MgO (wt %), (b) Al_2O_3 (wt %) vs SiO_2 (wt %), (c) CaO (wt %) vs MgO (wt %) and (d) CaO (wt %) vs SiO_2 (wt %).

Na_2O concentrations (1.39– 3.12 wt%) decrease with increasing SiO_2 and is incorporated into the plagioclase minerals. Na has an affinity to the more felsic minerals. Na_2O decreases with increasing MgO concentration. As with the Al_2O_3 and CaO, the Na elements will be incorporated into the felsic plagioclase minerals.

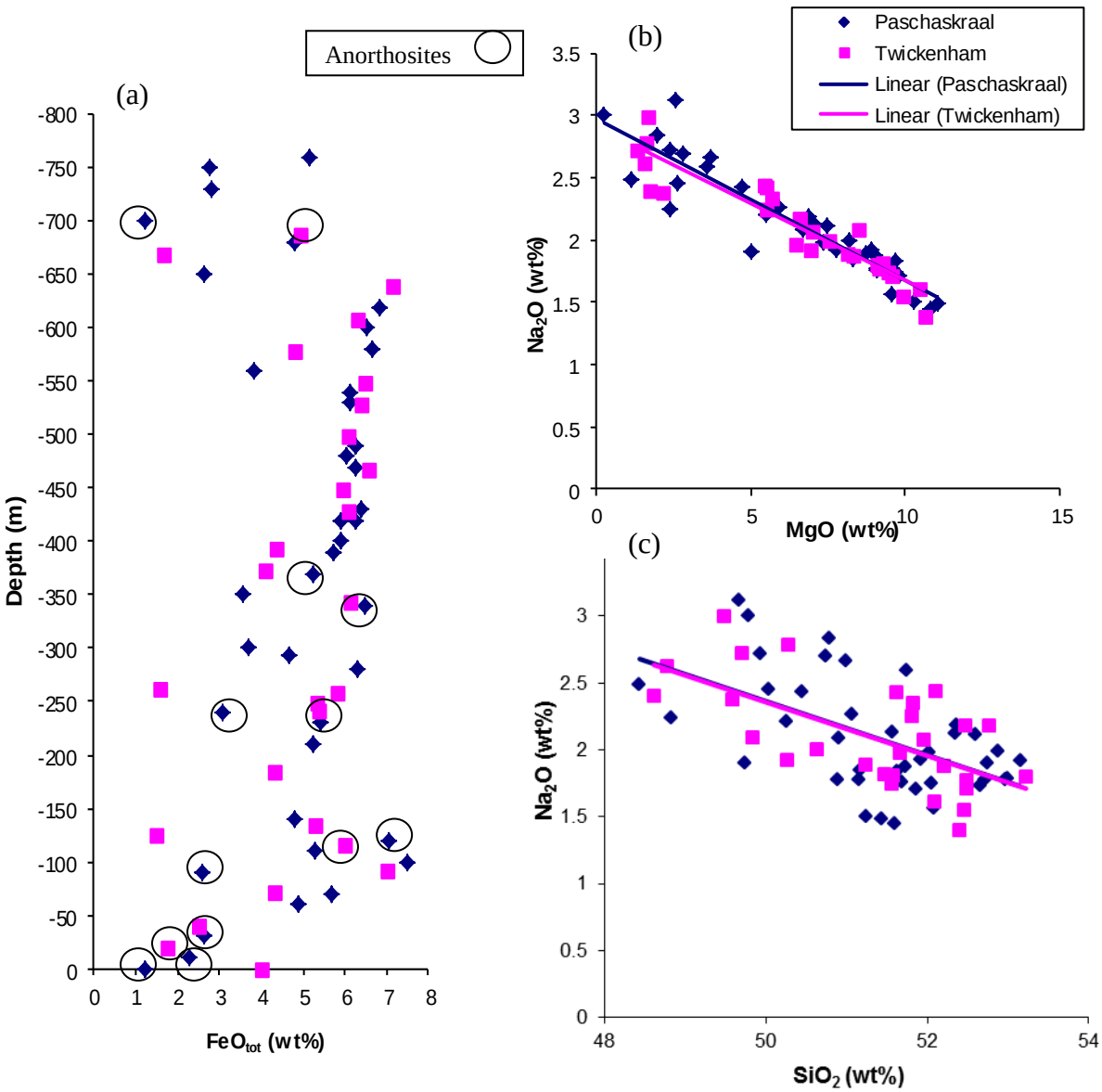

Figure 26: (a) Variation FeOtot (wt%) with Depth (m), (b) Na_2O (wt %) vs MgO (wt %) and (c) Na_2O (wt %) vs SiO_2 (wt %).

The MgO (0.26- 11.04 wt%) also increases with increasing SiO_2. The MgO concentration increases due to the fractionation of Mg into the initial crystallisation phases. The MnO concentration varies between 0.02 wt% and 0.23 wt%. The MnO increases with increasing SiO_2 as well as with increasing MgO. Mn has an affinity for Fe and therefore will be incorporated into the pyroxene minerals. The higher concentrations of FeO_{tot} (1.20- 15.56 wt%) in anorthosites indicates the presence of magnetite. Cr_2O_3 (0- 0.12 wt%) and NiO concentration varies between 0 wt% and 0.05 wt%. These heavier

elements can substitute for Fe, Mn, Mg and Ti thus they can fractionate into the pyroxene minerals.

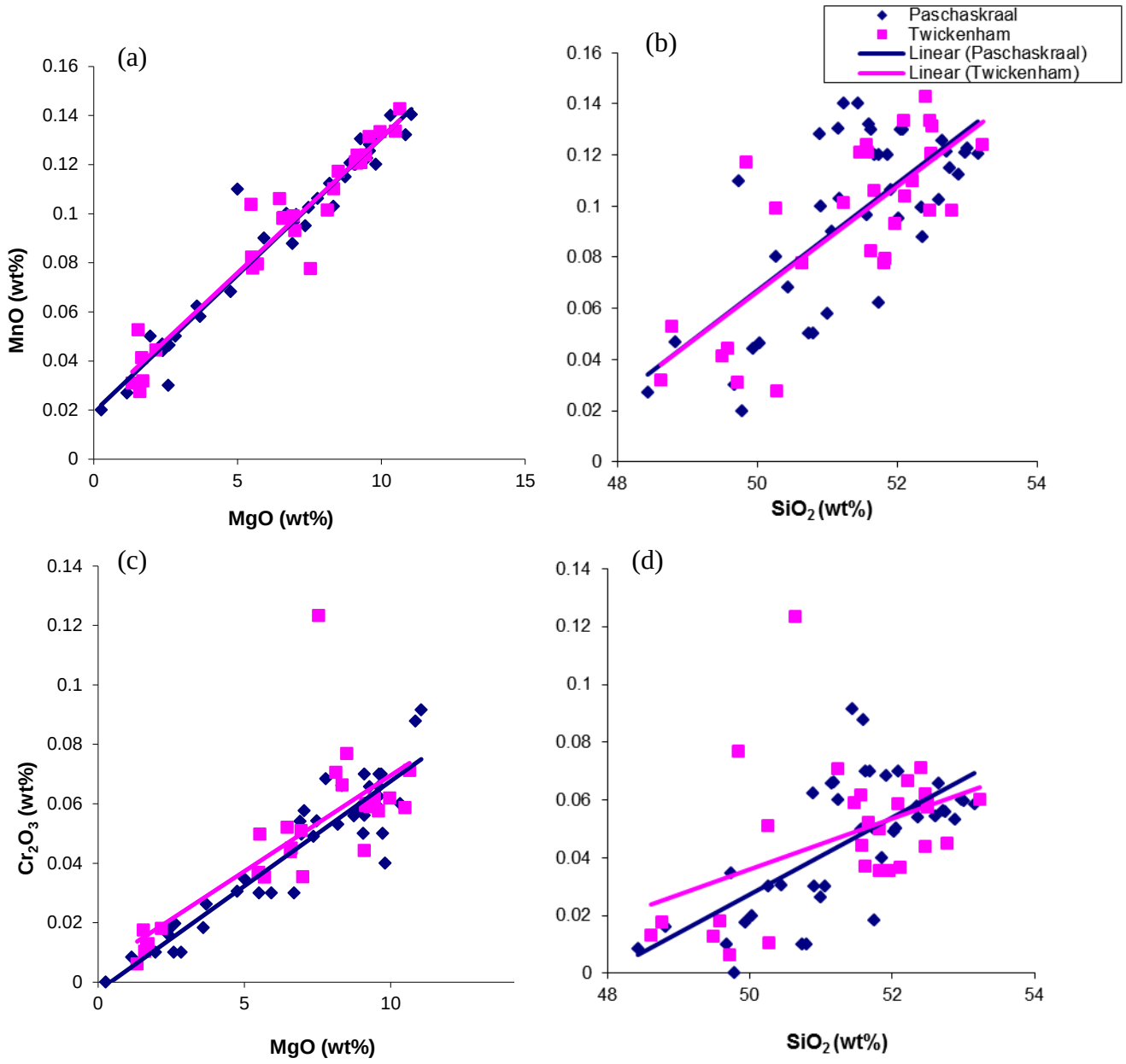

Figure 27: (a) MnO (wt %) vs MgO (wt %), (b) MnO (wt %) vs SiO_2 (wt %), (c) Cr_2O_3 (wt %) vs MgO (wt %) and (d) Cr_2O_3 (wt %) vs SiO_2 (wt %).

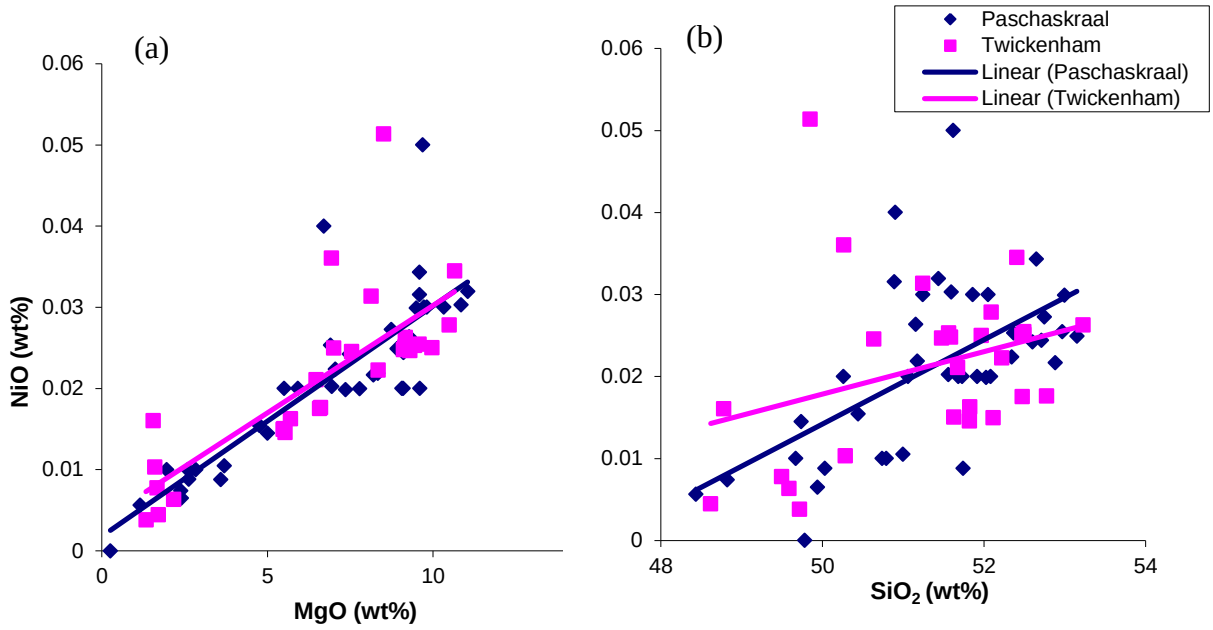

Figure 28: (a) NiO (wt %) vs MgO (wt %) and (b) NiO (wt %) vs SiO_2 (wt %).

4.3. Trace Element Geochemistry

Trace element concentration (Table 11) is used in an equivalent way to the major element concentrations, and can indicate evolutionary trends. Trace element patterns (incompatible elements and rare earth elements) exhibit systematic variations, including small-scale cyclic changes indicative of the presence of cumulus crystals and intercumulus liquid derived from different magmas. The trace element patterns are indicative of transient associations between distinct magma layers. Ratios of incompatible trace elements present a basis for establishing a connection between mafic cumulates and possible parental magmas.

Table 11: Trace element data.

	Average (ppm)	Std. Dev. (ppm)	Max. (ppm)	Min. (ppm)
As	5	2	12	3
Cu	14	4	34	5
Ga	15	2	21	12
Mo	1	LOD	2	1
Nb	2	LOD	4	2
Ni	136	62	231	12
Pb	5	3	13	3
Rb	8	3	16	3
Sr	267	46	356	187
Th	3	LOD	5	3
U	3	LOD	3	3
W*	133	60	269	29
Y	7	2	11	4
Zn	39	11	71	17
Zr	25	6	38	11
Cl*	101	111	576	8
Co	46	13	76	20
Cr	260	144	711	7
F*	585	160	973	100
S*	182	281	1852	16
Sc	12	6	23	1
V	70	33	134	17
Cs	9	LOD	9	9
Ba	103	18	164	77
La	11	3	17	5
Ce	5	1	8	5

Values for elements indicated with an * should be considered semi-quantitative.

The As concentrations average at 5 ppm and is relatively constant throughout the two boreholes. Cu concentrations throughout PK 206 and TW 632 are relatively constant (14 ppm), which is a good indication that no distinct crystallisation of sulphide or PGE rich zones occurred. The concentration of Ga is also very consistent (average of 15 ppm); however between 0– 110 m a remarkable change in Ga occurs in the PK 206 borehole. This change is most likely due to the higher concentration of Ga in the anorthosite rocks. The variation of Ni with depth (m) is highly variable (12 ppm – 231 ppm) but again there is an increasing trend up to -600 m with a gradual deceasing trend downwards thereafter. The W increases with height due to the increase of plagioclase. The concentration of Co increases in the lower MZ up until a depth of -600 m where it gradually starts to decrease.

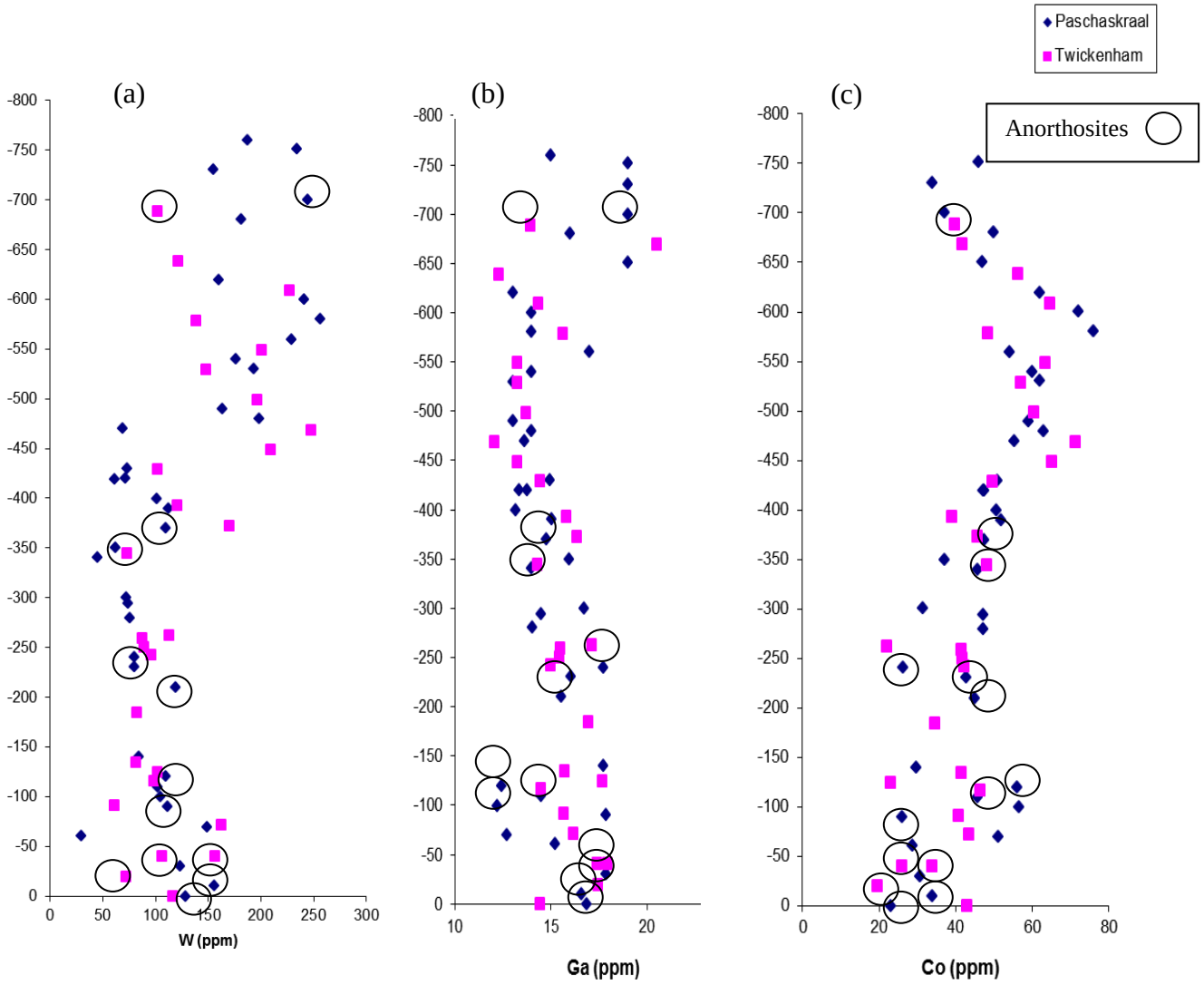

Figure 29: (a) Variation W (ppm) with Depth (m), (b) Variation Ga (ppm) with Depth (m) and (c) Variation Co (ppm) with Depth (m).

The chalcophiles are nearly all constant throughout the two boreholes, with the exception of Zn (17– 71 ppm) which increases from 0m to -600 m and then gradually decrease below -600 m. The concentration of Zn increases slightly during crystallisation thus at -600 m the crystallisation stops and a possible magma influx occurs.

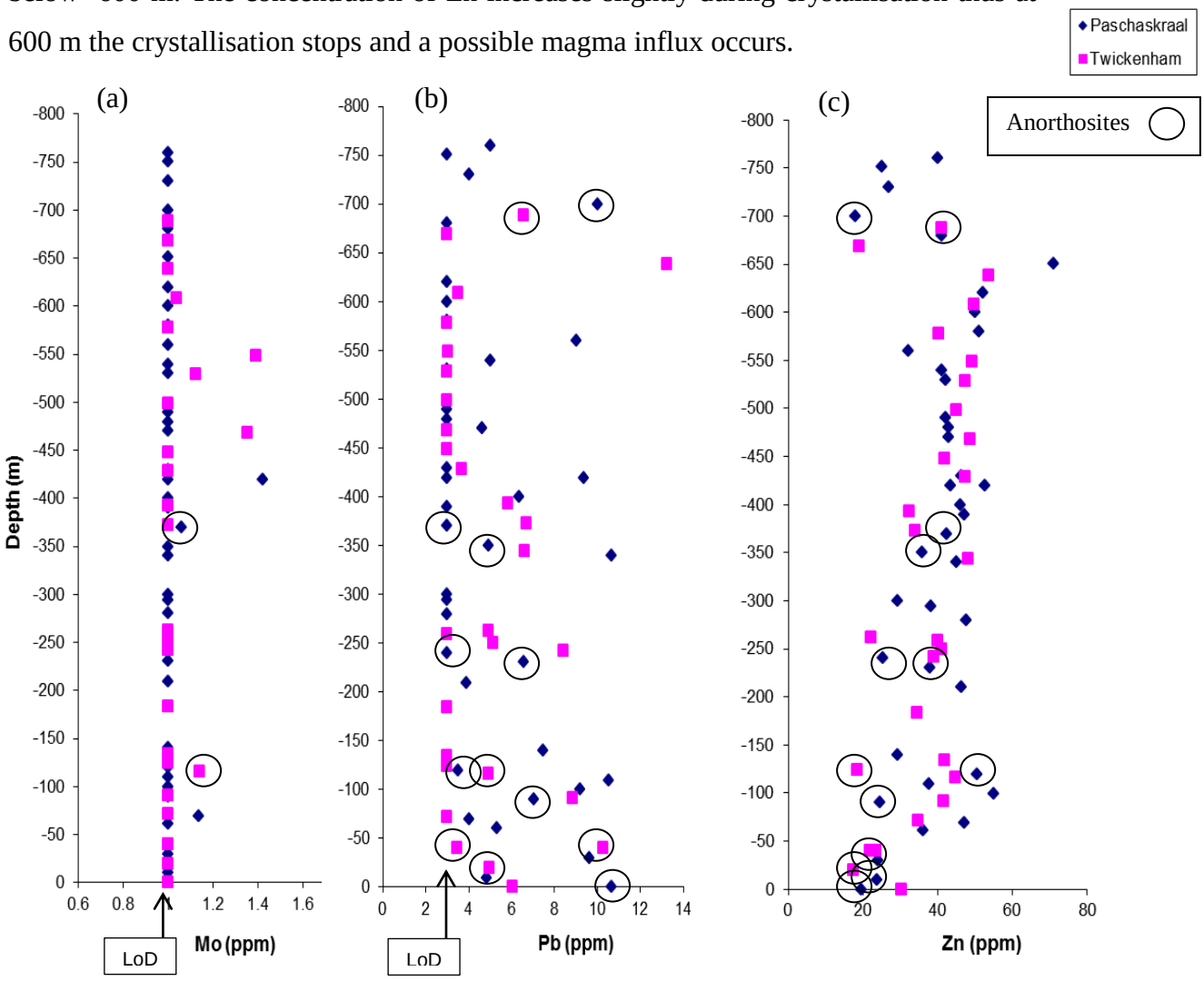

Figure 30: (a) Variation Mo (ppm) with Depth (m), (b) Variation Pb (ppm) with Depth (m) and (c) Variation Zn (ppm) with Depth (m).

The Nb, Th and U concentration are relatively constant, with a detection limit of 2 ppm, 3 ppm and 3 ppm respectfully. The Sr concentrations initially decrease from 0 m to -600 m. Below -600 m the Sr values increases. Y has a slight increase with height but is near constant due to its incompatibility. Cr concentrations increase between 0m and -550 m, below -550 m to -750 m the Cr concentration decreases. The average concentration of Cr in the MZ is 2 ppm. The V and Sc seem to have

the same geochemical trend as Cr, with initial increase in concentration followed by a decrease.

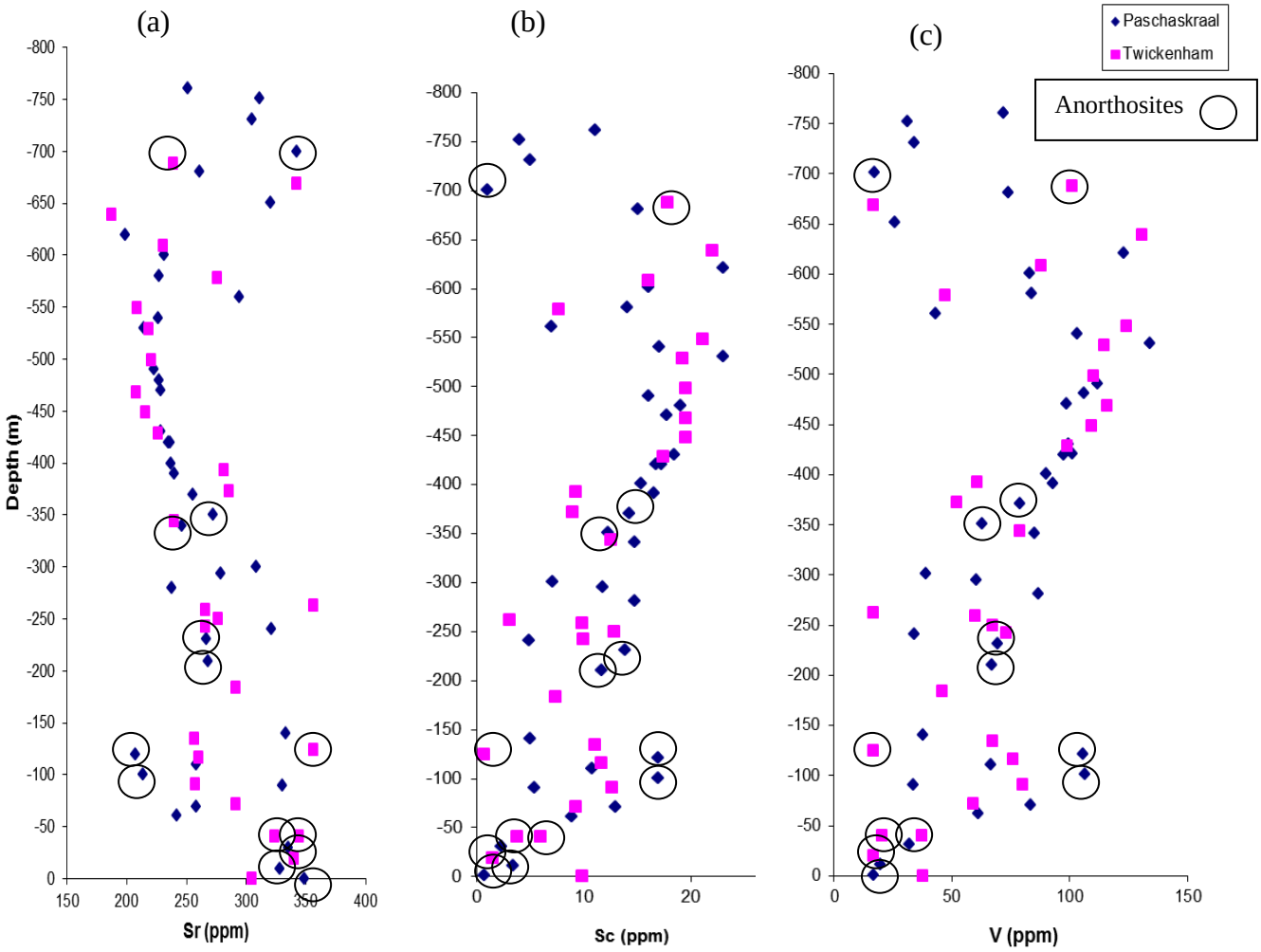

Figure 31 (a) Variation Sr (ppm) with Depth (m), (b) Variation Sc (ppm) with Depth (m) and (c) Variation V (ppm) with Depth (m).

The Cl concentration has a constant increase in relation to depth. Higher concentrations are visible at -50 m and at -650 m, which may be due to an increase in interstitial apatite concentration. The concentrations of Ba and Rb have unique trends; between 0 m and -250 m the value increases. For the next 400 m the value decreases slightly and below -650 m the concentrations increases. Sc and V concentration indicate an abrupt change in concentration of plagioclase at a depth of -500 m.

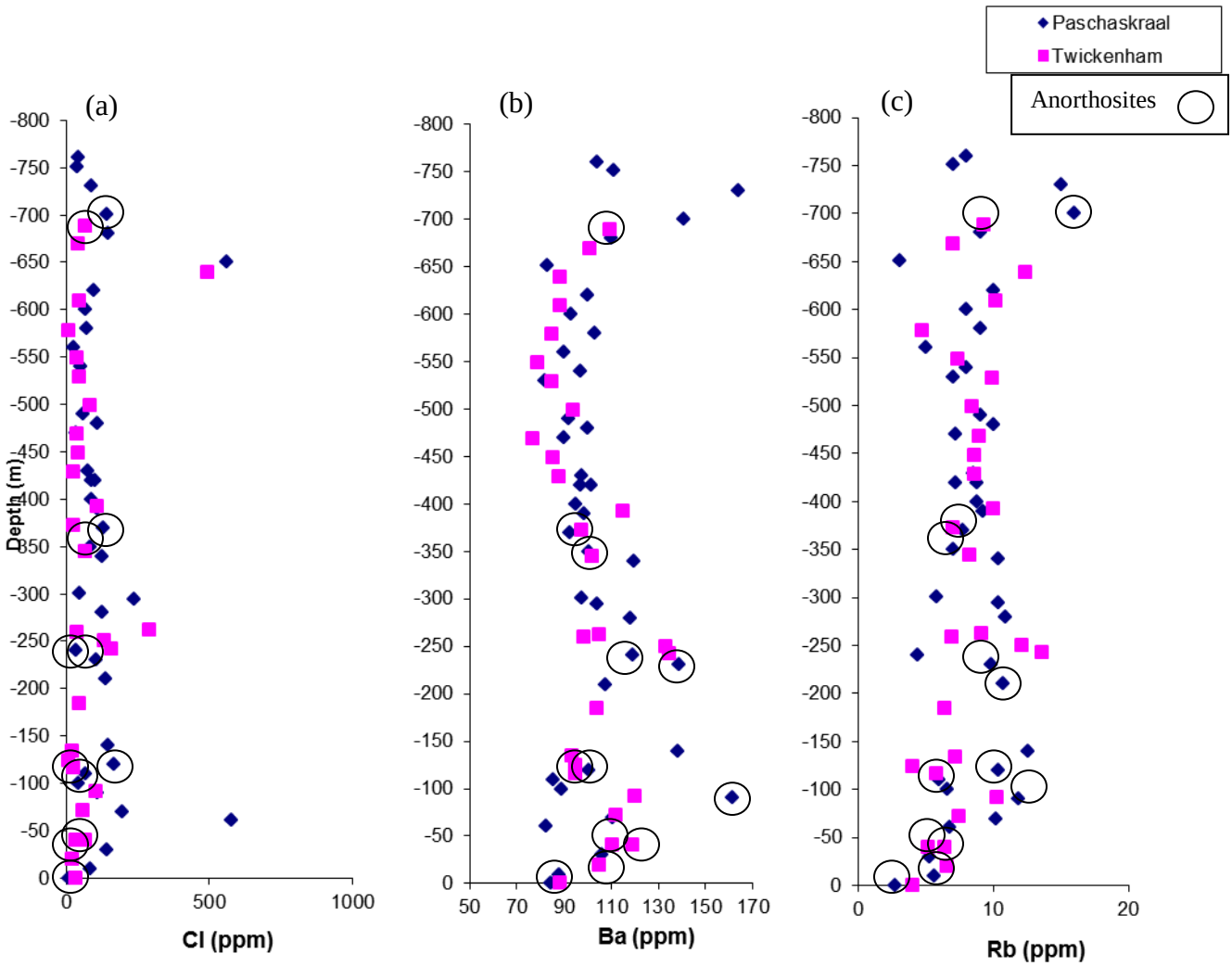

Figure 32: (a) Variation Cl (ppm) with Depth (m), (b) Variation Ba (ppm) with Depth (m) and (c) Variation Rb (ppm) with Depth (m).

La concentration increases between 0 m to -200 m and gradually decreases below this depth. Ce concentration is below the detection limit of 5 ppm thus no trend could be observed.

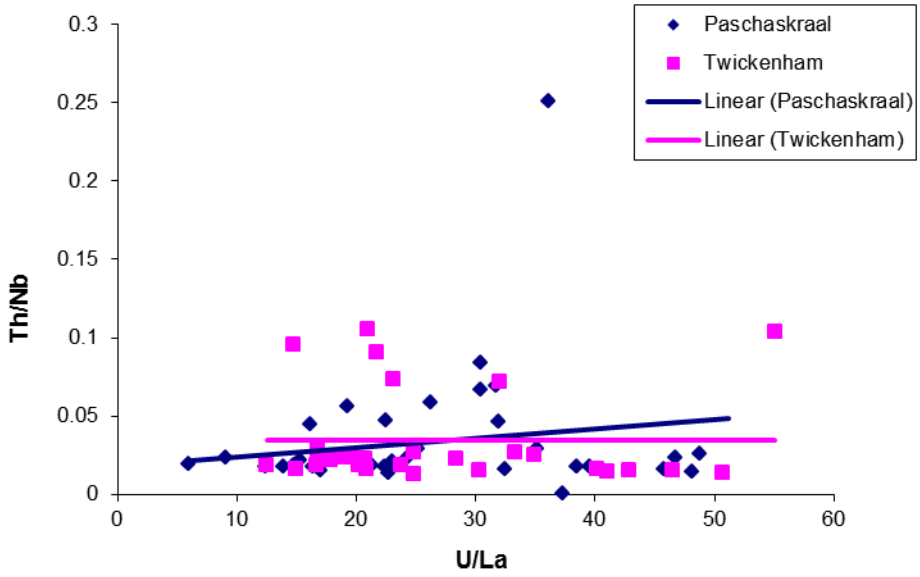

Figure 33: Th (ppm)/Nb (ppm) vs U (ppm)/La (ppm).

There is a good correlation between the two boreholes in terms of their Th/Nb vs U/La ratios. This is an indication that the lower MZ that was sampled formed from the same parental magma.

4.4. Mineral Compositions

The electron microprobe determines in - situ elemental composition and distribution for minerals on a microscopic scale. Data was obtained for 99 (core) plagioclase crystals and 97 (rim) plagioclase crystals. 82 data points selected for orthopyroxene and 65 analyses for clinopyroxene crystals.

The composition of core plagioclase crystals varies slightly with respect to all the major elements (Table 12).The plagioclase varies between 22.7- 35.3 wt% Na, which trend toward the end - member albite ($(Na_{(0.227 - 0.353)}, K_{(0.012 - 0.046)})\ Al_{(1.630 - 1.752)}, Si_{(2.183 - 2.345)}\ O_8$). The calcium (Ca) concentration at the core of the plagioclase crystals varies

between 65.1- 77.7 wt%, trending toward end – member anorthite ($Ca_{(0.651 - 0.777)}$ $Al_{(1.630 - 1.752)}$ $Si_{(2.183 - 2.345)}$ O_8).

Table 12: Core Plagioclase.

	Average (wt %)	Std. Dev. (wt %)	Std. Dev.*100 (wt %)	Rel. Std. Dev. (wt %)	Max. (wt %)	Min. (wt %)
Na	0.299	0.026	2.571	8.605	0.353	0.227
Mg	0.001	0.002	0.164	140.503	0.014	0.000
Al	1.677	0.024	2.412	1.438	1.752	1.630
Si	2.276	0.035	3.490	1.533	2.345	2.183
K	0.023	0.005	0.513	22.324	0.046	0.012
Ca	0.707	0.027	2.683	3.796	0.777	0.651
Ti	0.001	0.001	0.083	70.294	0.005	0.000
Cr	0.000	0.000	0.041	141.032	0.001	0.000
Mn	0.000	0.001	0.050	148.301	0.002	0.000
Fe	0.011	0.002	0.209	19.189	0.019	0.008
Ba	0.000	0.000	0.031	136.784	0.001	0.000
An#	0.687	0.027	2.714	3.950	0.765	0.627

The An# (Ca/Ca + Na +K) content varies between 62.7- 76.5 wt%, thus the plagioclase crystallised from an evolved magma at lower temperatures. In the Paschaskraal (PK 206) borehole the An# shows three distinct changes; a decrease between -139.9 m and -429.96 m, an increase between -429.96 m to -650.87 m, and a decrease between -650.87 m and -751.29 m. In the Twickenham borehole (TW 632) the An# have four distinct cycles; increasing from 0 m to -40.2 m, where the An# is higher due to the presence of anorthosites (TW 17 and TW 25).The second cycle decreases in value between -40.2 m to -468.17 m which changes to a third cycle with increasing An# between -468.17 m to -638.7 m. The final cycle decreases at -638.7 m to -668.74 m (Figure 34a).

The plagioclase composition (Table 13) at the rim of the crystals varies to some extent. The Na concentrations vary between 18.9- 37.1 wt%, again trending toward the end - member albite ($Na_{(0.189 - 0.371)}$, $K_{(0.005 - 0.108)}$) $Al_{(1.551 - 1.783)}$, $Si_{(2.141 - 2.389)}$ O_8). The calcium (Ca) concentration at the rim of the plagioclase crystals varies between 62.4- 82.0 wt%, which is the end – member anorthite ($Ca_{(0.651 - 0.777)}$ $Al_{(1.630 - 1.752)}$ $Si_{(2.183 - 2.345)}$ O_8).

Table 13: Rim Plagioclase.

	Average (wt %)	Std. Dev. (wt %)	Std. Dev.*100 (wt %)	Rel. Std. Dev. (wt %)	Max. (wt %)	Min. (wt %)
Na	0.300	0.036	3.629	12.100	0.371	0.189
Mg	0.002	0.005	0.520	334.001	0.051	0.000
Al	1.683	0.038	3.797	2.256	1.783	1.551
Si	2.282	0.044	4.443	1.947	2.389	2.141
K	0.023	0.010	1.028	45.148	0.108	0.005
Ca	0.709	0.038	3.796	5.351	0.820	0.624
Ti	0.001	0.001	0.096	82.556	0.007	0.000
Cr	0.000	0.000	0.037	174.859	0.002	0.000
Mn	0.000	0.000	0.043	136.642	0.002	0.000
Fe	0.011	0.004	0.412	36.136	0.039	0.008
Ba	0.000	0.000	0.032	142.485	0.001	0.000
An#	0.687	0.038	3.756	5.463	0.804	0.622

There is a slightly larger variation in An# (Ca/Ca + Na +K) content between 62.2 wt% and 80.4 wt%. In the PK 206 borehole, An# has constant values at between -139.9 m and -280.11 m. The An# value decreases between -280.11 m and -489.98 m. A third distinct cycle in An# starts at the depth of -489.98 m to -700.11 m and above -700.11 m the values are constant. In the TW 632 borehole there are four cycles with distinct changes in the An#; increase at 0- 40.2 m, a decrease between -40.2 m and -249.89 m, an increase from -249.89 m to -578.33 m and the last cycle has a decrease in An# between -578.33 m to -688.05 m (Figure 34b).

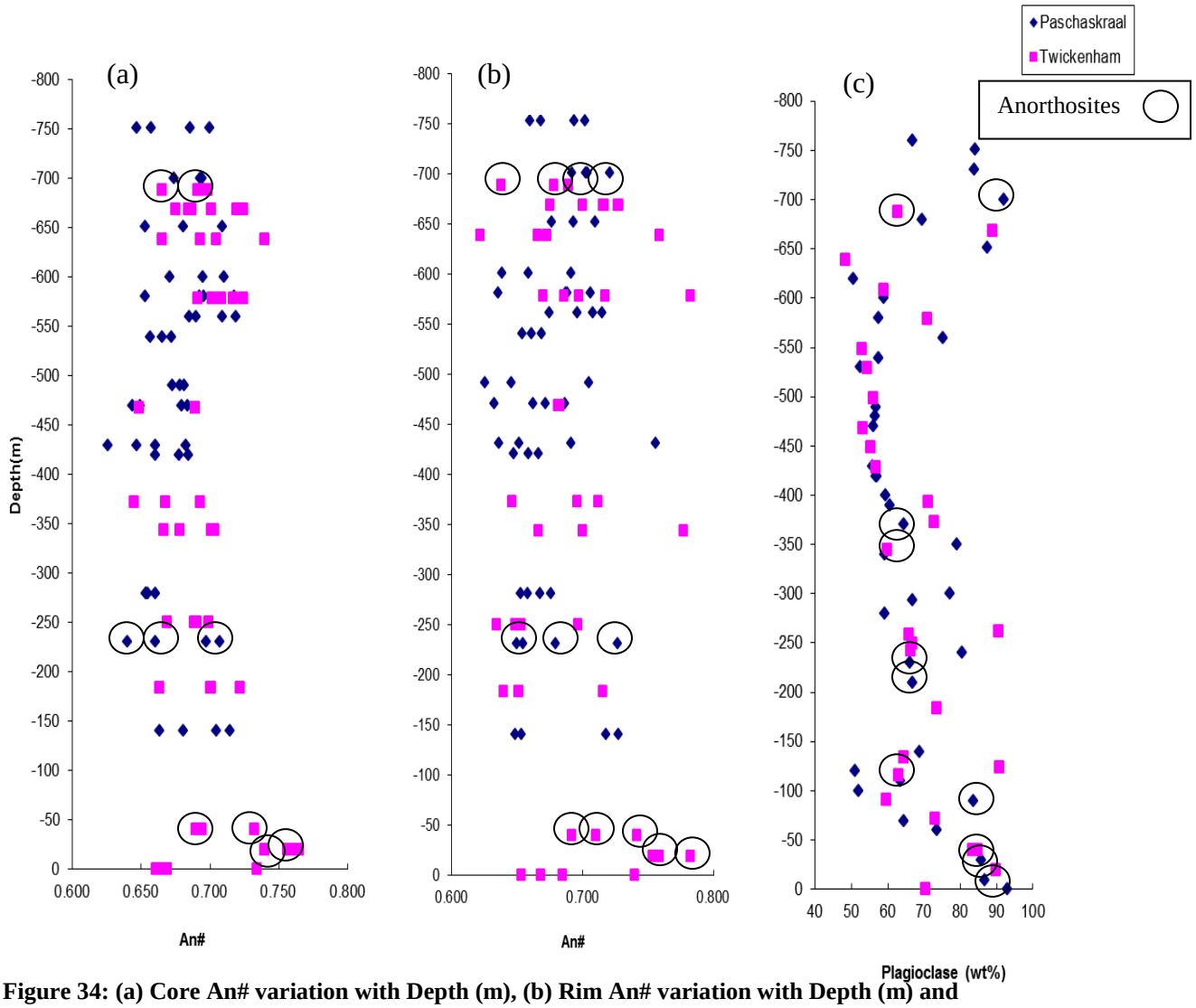

Figure 34: (a) Core An# variation with Depth (m), (b) Rim An# variation with Depth (m) and (c) Plagioclase (CIPW) variation with Depth (m).

The composition of orthopyroxene crystals vary slightly throughout the different boreholes (Table 14). The range of composition for Mg is between 66.0 wt% and 80.8 wt% whereas the range of Fe is between 20.6 wt% and 30.9 wt%. The Calcium (Ca) concentration is significant due to inverted pigeonite present in the MZ at the transition zone between subzones B and C, subzone C and subzone E (Nex et al., 1998). The Ca concentration varies between 0.7 wt% and 8.1 wt%. The composition of the orthopyroxene is ($Mg_{(0.660 - 0.808)}$, $Fe_{(0.206 - 0.309)}$, $Ca_{(0.007 - 0.081)}$) $Si_{(0.960 - 1.037)}$ O_3. The Mg# (Mg/Mg + Fe) content ranges between 68.8 wt% and 79.1 wt%.

Table 14: Orthopyroxene.

	Average (wt %)	Std. Dev. (wt %)	Std. Dev.*100 (wt %)	Rel. Std. Dev. (wt %)	Max. (wt %)	Min. (wt %)
Na	0.001	0.000	0.041	61.786	0.002	0.000
Mg	0.714	0.028	14.485	20.295	0.808	0.660
Al	0.018	0.003	0.710	39.998	0.033	0.014
Si	1.009	0.015	3.354	3.325	1.037	0.960
K	0.000	0.001	0.051	247.899	0.004	0.000
Ca	0.027	0.014	20.305	746.102	0.081	0.007
Ti	0.004	0.007	1.967	491.962	0.067	0.001
Cr	0.002	0.001	0.123	64.630	0.007	0.001
Mn	0.006	0.001	0.153	27.424	0.007	0.004
Fe	0.271	0.021	8.096	29.871	0.309	0.206
Ba	0.000	0.000	0.010	128.180	0.001	0.000
Mg#	0.725	0.022	4.735	6.534	0.791	0.688

Table 15: Clinopyroxene.

	Average (wt %)	Std. Dev. (wt %)	Std. Dev.*100 (wt %)	Rel. Std. Dev. (wt %)	Max. (wt %)	Min. (wt %)
Na	0.008	0.005	0.454	54.048	0.014	0.000
Mg	0.465	0.105	10.517	22.610	0.678	0.229
Al	0.030	0.025	2.542	84.604	0.214	0.009
Si	0.972	0.040	4.030	4.147	1.012	0.776
K	0.000	0.000	0.050	239.072	0.003	0.000
Ca	0.349	0.185	18.460	52.822	0.475	0.012
Ti	0.011	0.026	2.551	240.854	0.163	0.001
Cr	0.003	0.001	0.129	47.781	0.006	0.000
Mn	0.004	0.002	0.192	45.748	0.011	0.002
Fe	0.170	0.099	9.929	58.234	0.427	0.092
Ba	0.000	0.000	0.009	149.013	0.000	0.000
Mg#	0.747	0.076	7.583	10.150	0.819	0.536

The compositions of clinopyroxene vary slightly throughout the different boreholes (Table 15). The concentration for Mg is between 22.9 wt% and 67.8 wt% and the range of Fe is between 9.2 wt% and 42.7 wt%. The Ca concentration varies between 1.2 wt% and 47.5 wt%. The composition of the orthopyroxene is (Mg $_{(06.229 - 0.678)}$, Fe $_{(0.092 - 0.427)}$, Ca $_{(0.012 - 0.475)}$) Si $_{(0.776 - 1.012)}$ O_3. The Mg# (Mg/Mg + Fe) ranges between 53.6 wt% and 81.9 wt%.

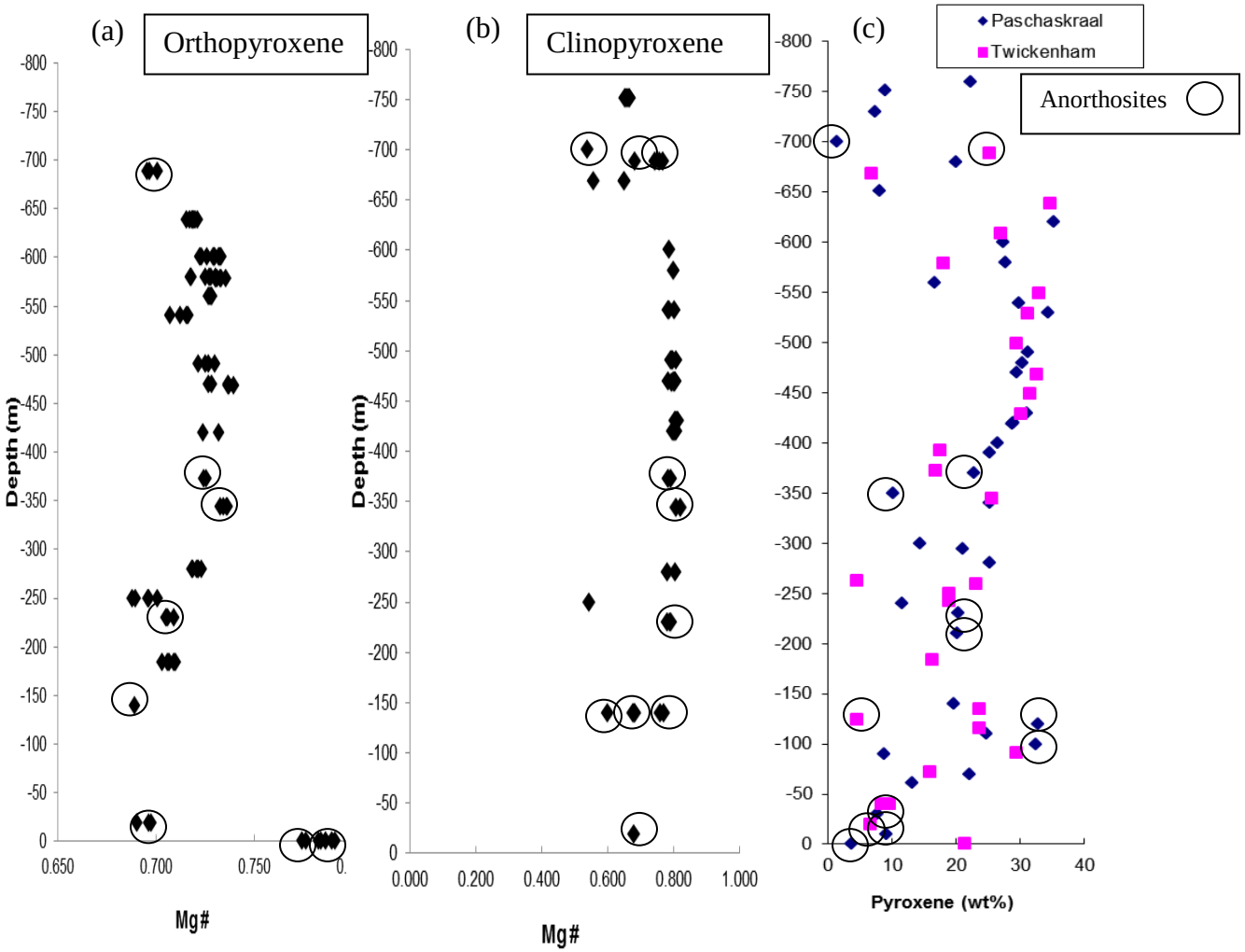

Figure 35: (a) Opx Mg# variation with Depth (m), (b) Cpx Mg# variation with Depth (m) and (c) Pyroxene (CIPW) variation with Depth (m).

CHAPTER 5: DISCUSSION

5.1. Identifying fractional crystallisation and magma influx

As a layer intrusion cools over many thousands of years the crystals will form according to the physical conditions in the melt and the composition of that melt (Bowen, 1928).In a layered intrusion such as the RLS, the resultant pile of cumulate rocks records this history of crystallisation in the chemistry of the minerals present. The major element geochemistry of the MZ displays variation with stratigraphic depth throughout boreholes PK 206 and TW 632, which need to be explained in terms of processes within the magma chamber. There are two possible mechanisms that might have generated the variations observed in this study. The first mechanism is fractional crystallisation and crystal accumulation, and the second mechanism could involve influx of new, primitive magmas.

Wager et al., (1960) proposed that the An content of plagioclase decreases with increasing differentiation from An_{77} to An_{30} within the Skaergaard Intrusion, reflecting that the Skaergaard Intrusion formed from one crystallising magma. Plagioclase compositions are an important factor due to the slow diffusive exchange between CaAl and NaSi in plagioclase (Morse, 1984). This characteristic of plagioclase preserves primary compositions of the melt in the cores of the grains.

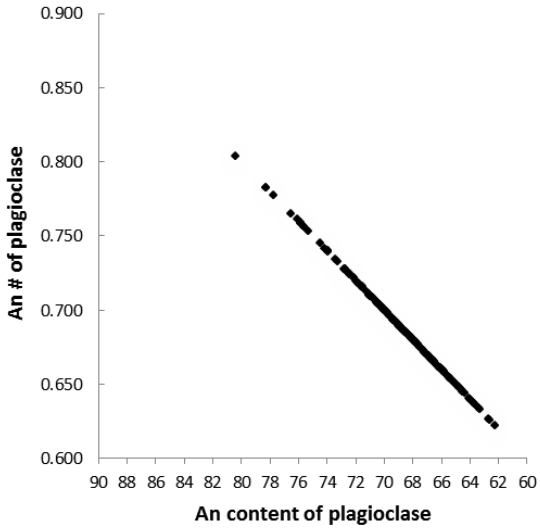

Figure 36: An content of plagioclase plotted as a function of An# of plagioclase.

In data collected in this study, there is an overall decrease in the An content of plagioclase with increasing differentiation from An_{80} to An_{62} within the PK 206 and TW 632 boreholes. The data obtained in this study can be correlated with the Wager et al., (1960) data from Skaergaard, and it is readily apparent that the two data sets show identical trends, consequently implying that the lower MZ possibly formed from a single magma.

The bivariant diagrams for this study (Figure 20– 28) show linear trends and the elements compare well with each other, thus indicating differentiation by fractional crystallisation (Figure 37 (i)).

To identify new magma influxes into a large igneous intrusion we have to look at the An content of plagioclase. If the new magma is more primitive, a reversal in An content may be observed. The reversal can be abrupt (Figure 37 (iii)) signifying an immediate mixing and homogenization of the new and residual magmas or it can represent emplacement of the new magma under the residual magma with no mixing. The reversal can be gradual (Figure 37 (iv)) consequently indicating slow addition of magma (Cawthorn and Ashwal, 2009). If the added magma was more differentiated the An content could have forward jumps (Figure 37 (v) and (vi)).

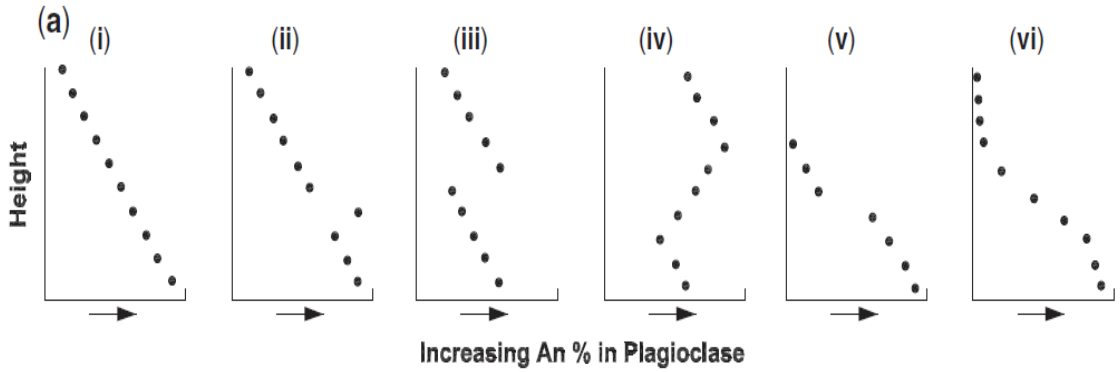

Figure 37: Possible trends of An content in plagioclase as a function of height (Cawthorn and Ashwal, 2009).

The variation of An content of plagioclase with depth (m) through the boreholes PK 206 and TW 632 indicate gradual variations. These variations are caused by a change in magma composition (chemical or mineralogical) and not an influx of new primitive magma. The Mg# of the pyroxenes (Figure 35a, b) and An# of plagioclase (Figure 34a, b) indicates variation which is attributed to fractional crystallisation.

The compositional layering of the gabbronorites within the MZ is important in understanding of the processes working within the magma chamber. These different variations in composition within a relatively homogenous sequence of rocks display evidence of layering, of primary and secondary origin (Nex et al., 1998). Reversals in cryptic mineral composition and changes in initial Sr isotope ratio indicate whether there has been addition of magmas superimposed on the overall differentiation trend.

The cyclic units within a mafic-ultramafic layered intrusion can be roughly classified into three major types, namely: (a) no basal reversals, (b) cryptic basal reversals and (c) phase, modal and cryptic reversals. A basal reversal refers to a rock interval above the base of a cyclic unit that displays mineral crystallisation sequences and compositional trends that are contradictory to those predicted by phase equilibria considerations (Campbell, 1977 and Latypov 2003).

(a) Cyclic units with no basal reversals:

The compositional variation from the base to the top indicates a decrease in whole-rock MgO, Ni and in Mg# of the cumulus orthopyroxene. Cyclic units exhibiting these types of compositional variations are expected to have formed purely through the combination of fractional crystallisation and periodic magma replenishment (Latypov et al., 2007). A good example of cyclic units lacking basal reversals are the upper CZ of the BIC (Naldrett, 1989) (Figure 38).

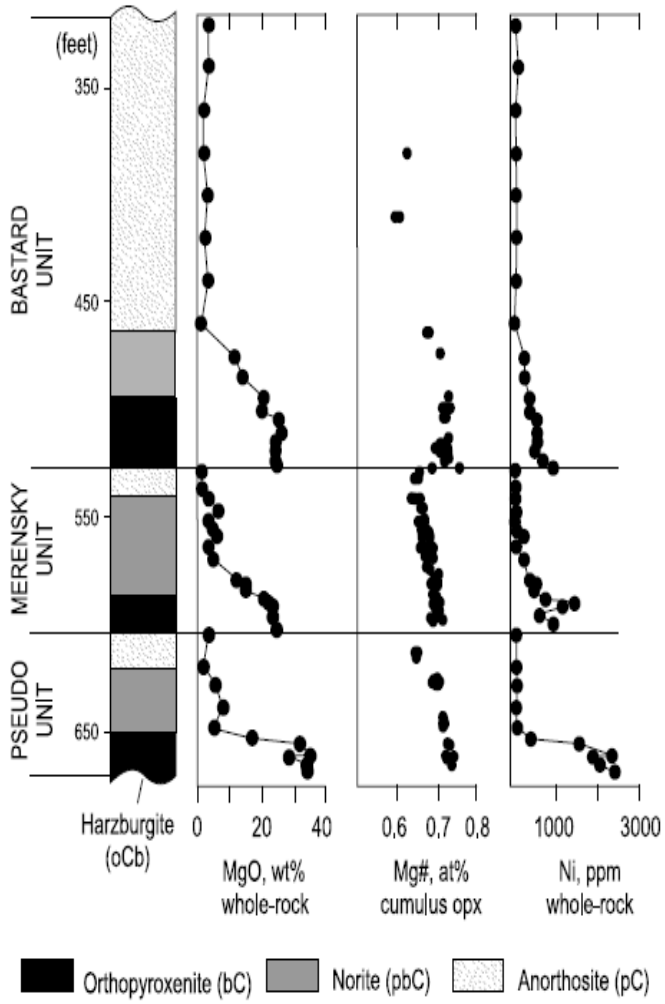

Cumulate abbreviations:
o = olivine
p = plagioclase
a = clinopyroxene
b = orthopyroxene
c = chromite
C = cumulate

Figure 38: Cyclic units with no basal reversals (modified after Naldrett, 1989) (Latypov et al., 2007).

In the PK 206 and TW 632 boreholes the whole-rock MgO ranges from 0.26- 11.04 wt%. The concentration of the MgO (Figure 39a) increases throughout the two boreholes from top of borehole (0 m) to a depth of -638.7 m, with a decreasing trend in the TW 632 borehole from 0 m to -40.2 m due to the presence of anorthosites. From a depth of +/- -640 m to +/- -700 m the MgO concentration decreases and below -700 m there is an increase in MgO concentration within the PK 206 borehole. The Mg# reflects the fractionation of Mg into the pyroxene minerals (Figure 39b). The Ni concentration trend is identical to the MgO concentration trend (Figure 39c). The small chemical variations within the lower MZ is due to normal fractional crystallisation rather than magma influxes.

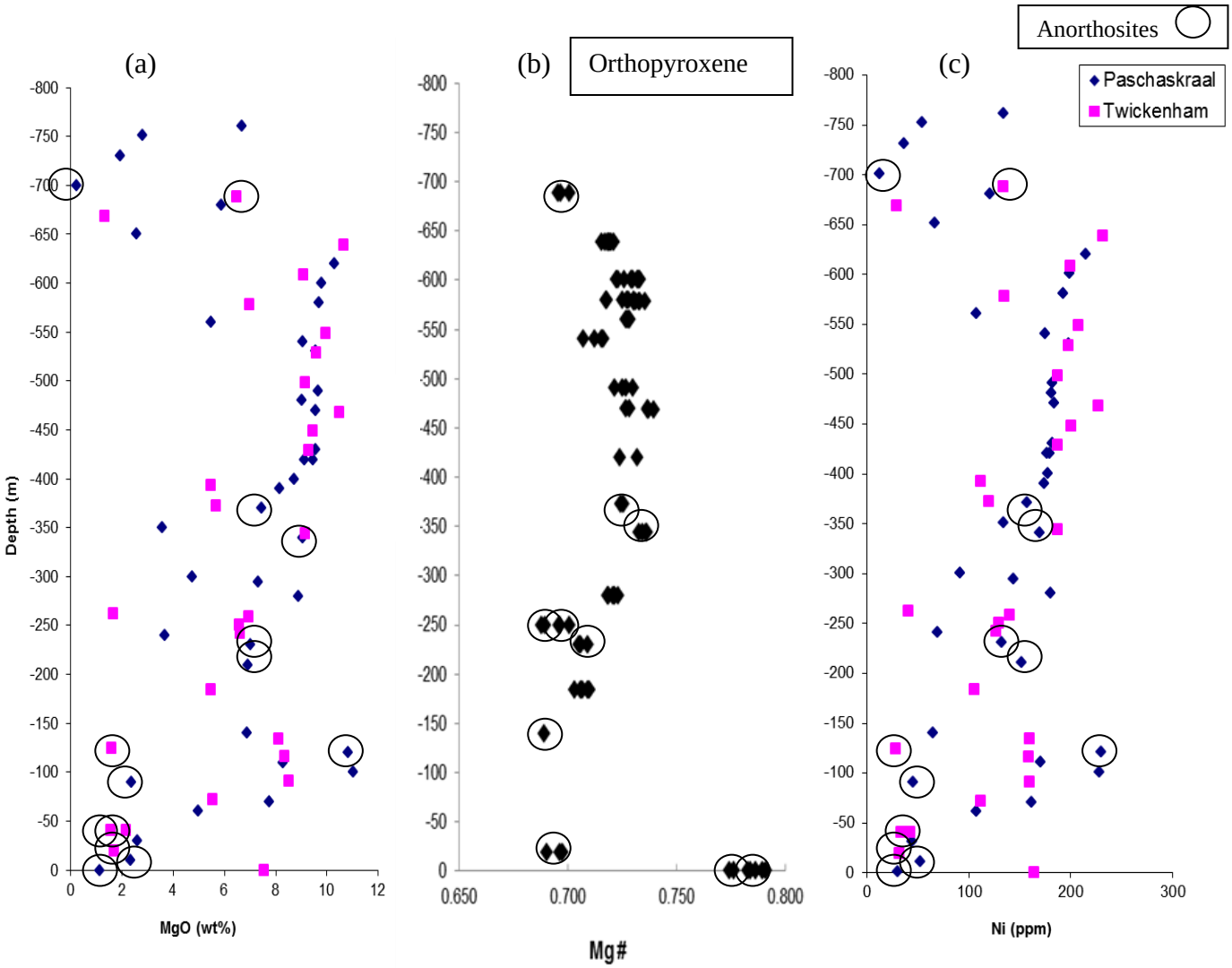

Figure 39: (a)Variation MgO (wt %) with Depth (m), (b) Variation Mg# of orthopyroxene with Depth (m) and (c) Variation Ni (ppm) with Depth (m).

(b) Cyclic units with cryptic basal reversals:

The compositional variation of cryptic basal reversals is discussed in terms of whole-rock Mg#, Ni and Cr contents. The crossover maximum of whole-rock Mg# is higher in stratigraphy than the whole-rock Ni content. The whole-rock Cr concentration variations are very distinct. The Ni content indicates a systematic initial increase followed by a gradual decrease throughout the most of the stratigraphic unit (Latypov et al., 2007). A good example of cyclic units with basal reversals is the Muskox intrusion (Irvine, 1980) (Figure 40). These compositional variations visible within the Muskox intrusion are a post magmatic feature. Therefore at the base of the stratigraphic unit there was an influx of new magma which caused the reversal in trends.

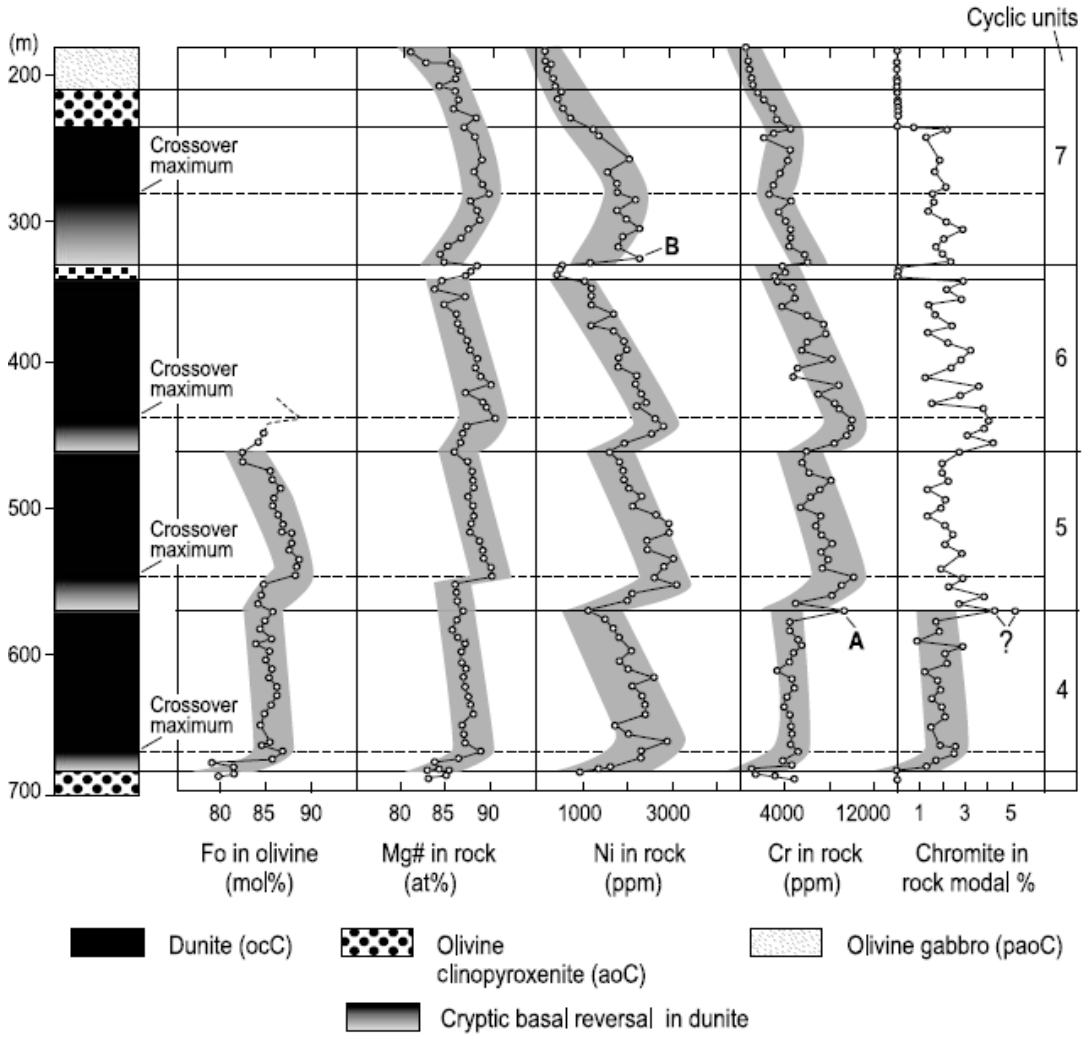

Figure 40: Cyclic units with cryptic basal reversals (modified after Irvine, 1980) (Latypov et al., 2007).

In PK 206 and TW 632 boreholes the whole-rock Mg# (Figure 39a) has very distinctive variation through the stratigraphic unit. The whole-rock Mg# increases from the top (0 m) to a depth of -638.7 m and decreases between depths of +/- -640 m and +/- -700 m. The decreasing trend in the two boreholes indicates the presence of anorthosite or an increase in plagioclase content. The variation in Ni (Figure 39c) and Cr (Figure 41b) is identical to the whole-rock Mg#. Below -700 m the Mg#, Ni and Cr increases.

When correlating the data obtained from this study, to the model proposed by Latypov et al., (2007) modified after Irvine (1980) the whole-rock Mg# maximum value must be higher than the Ni (ppm) maximum value in the stratigraphy. The data from this project indicates maximum whole-rock Mg# at a depth of -638.7m and the maximum Ni (ppm) is at the same depth in the TW 632 borehole. The whole-rock Mg# maximum and the Ni

(ppm) maximum are at a depth of -619.84 m in the PK 206 borehole. Thus there is no indication that the lower part of the MZ has cryptic basal reversals as the Muskox intrusion.

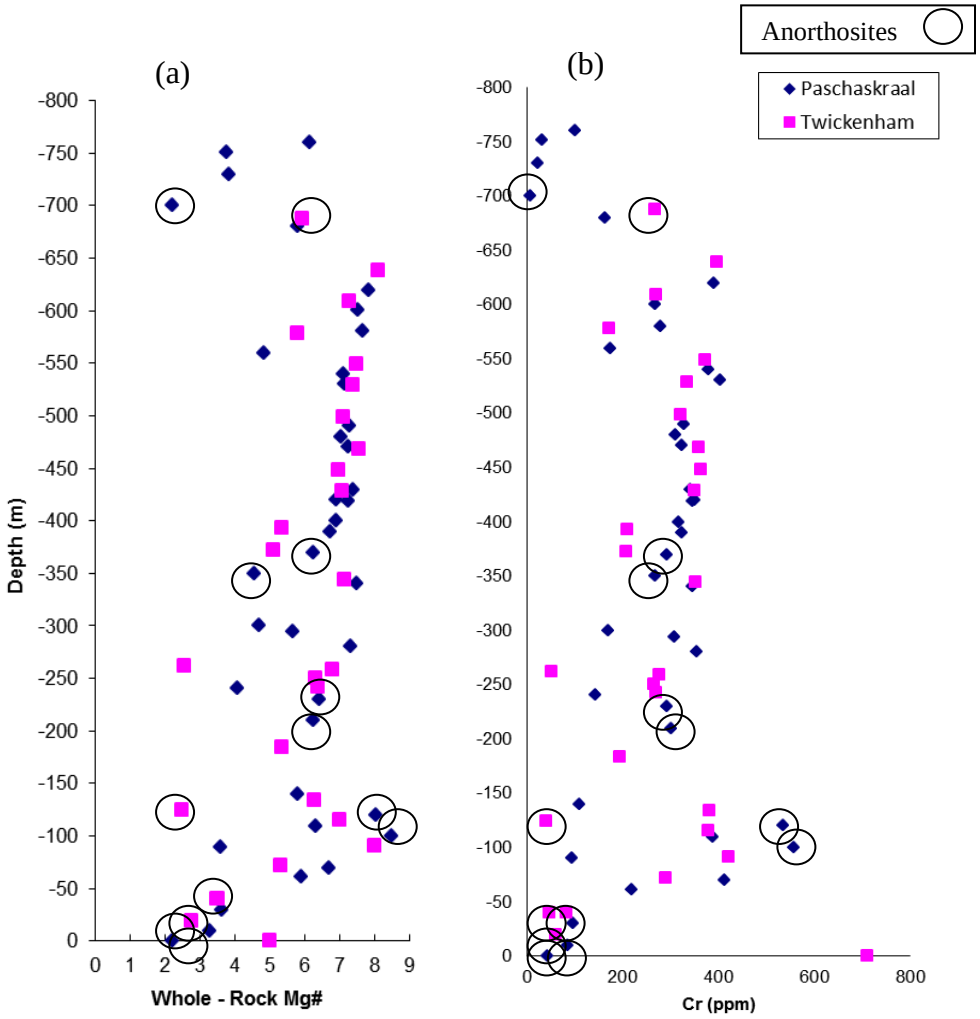

Figure 41: (a) Variation whole-rock Mg# with Depth (m) and (b) Variation Cr (ppm) with Depth (m).

(c) Cyclic units with phase, modal and cryptic basal reversals:

The cyclic units that display phase, modal and cryptic basal reversals are applied to megacyclic units such as the Penikat layered intrusion (Figure 42). Therefore this might rather be applied to the RLS than to explain the formation of a small unit such as the lower part of the MZ. This model proposed by Latypov et al., (2007) focuses on whole-rock Mg#, olivine, clinopyroxene and orthopyroxene concentrations, opx = (opx ÷ cpx) and whole-rock Cr_2O_3 (wt %). The megacycles all reflect well marked basal reversal as well as evolving magmas from the base of each unit towards the top of the units.

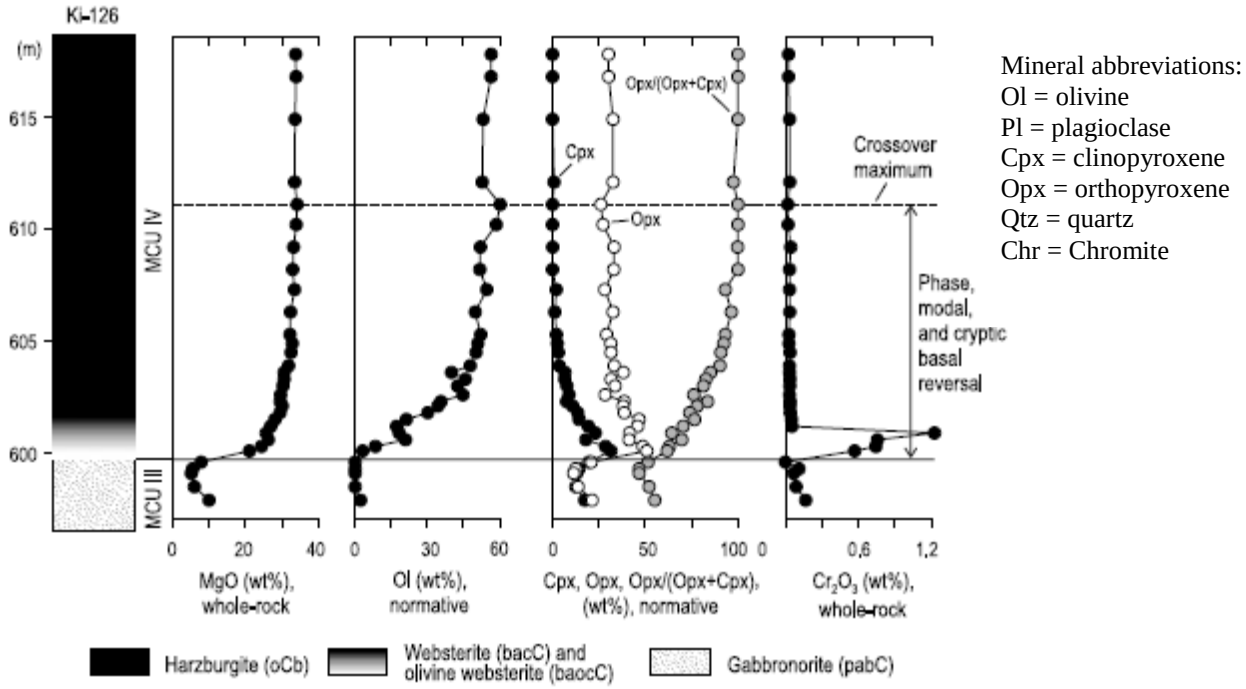

Mineral abbreviations:
Ol = olivine
Pl = plagioclase
Cpx = clinopyroxene
Opx = orthopyroxene
Qtz = quartz
Chr = Chromite

Figure 42: Variation in whole-rock MgO and Cr_2O_3 and normative olivine, opx, cpx and opx=(opx÷cpx) ratio with height through the Penikat layered intrusion (Latypov et al., 2007).

There is consensus that the Pyroxenite Marker of the Eastern and Western Limbs indicates an influx of new magma due to the distinct change in the initial Sr isotopic ratio (von Gruenewaldt, 1970 and Kruger et al., 1987). Cawthorn et al., (2005) proposed the new magma, entering the RLS between the CZ and the MZ was denser than the residual magma of the CZ. The new magma gave rise to the formation of the MZ; it flowed beneath the residual magma (CZ magma) and displaced it. The new magma did not mix (whatever the composition of the new magma) with the residual magma. All evidence obtained in this study reflects that the crystallisation of the subzone A of the MZ was not interrupted by an influx of new magma.

5.2. Mineralogical variation of the Main Zone

Variation of Al_2O_3 with depth (Figure 43a) indicates an overall decreasing trend from 0 m to -550 m and an increasing trend from -550 m to the bottom of the borehole. This variation is almost identical to the CIPW concentration of plagioclase (Figure 34 c). At specific depths (PAS 40, PAS 39, PAS 28, PAS 4, TW 27, TW 26, TW 25, TW 21 and TW 1) the Al_2O_3 concentration increases dramatically due to the presence of anorthosite

rocks. The anorthosites have lost most of their mafic components to the surrounding gabbronorites; this is evident by the plagioclase concentration of the anorthosites at the top of the boreholes. Al_2O_3 is compatible with plagioclase, therefore where Al_2O_3 increase the concentration of plagioclase increases.

Variations of CaO (Figure 43b) and Na_2O (Figure 43c) shows similar variations with depth as Al_2O_3 concentrations. Ca and Na are incorporated into plagioclase due to the higher affinity of Ca and Na for more felsic minerals.

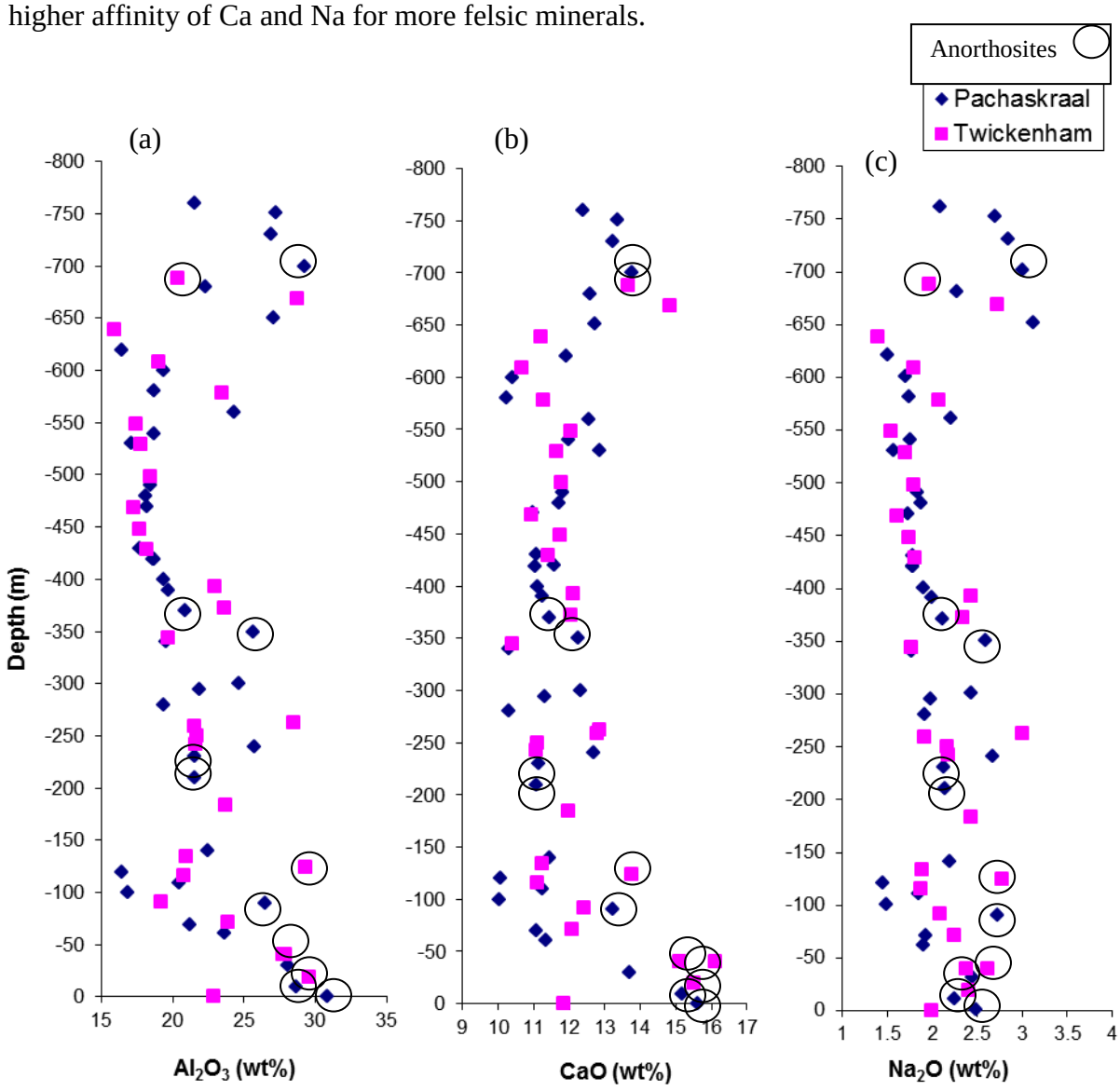

Figure 43: (a) Variation Al_2O_3 (wt %) with Depth (m), (b) Variation CaO (wt %) with Depth (m) and (c) Variation Na_2O (wt %) with Depth (m).

Plagioclase crystallises in the manner of a solid – solution series where two end – members can substitute for each other. Thus the variation of Na and Ca will be inversely proportional due to their ability to substitute for each other (Figure 44). The two end - members for plagioclase is albite (Na – end – member) and anorthite (Ca – end – member). The core plagioclase varies in composition ($(Na_{(0.227 - 0.353)}, K_{(0.012 - 0.046)} Ca_{(0.651 - 0.777)}) Al_{(1.630 - 1.752)} Si_{(2.183 - 2.345)}) O_8$ throughout the depth of the two boreholes (Figure 44).

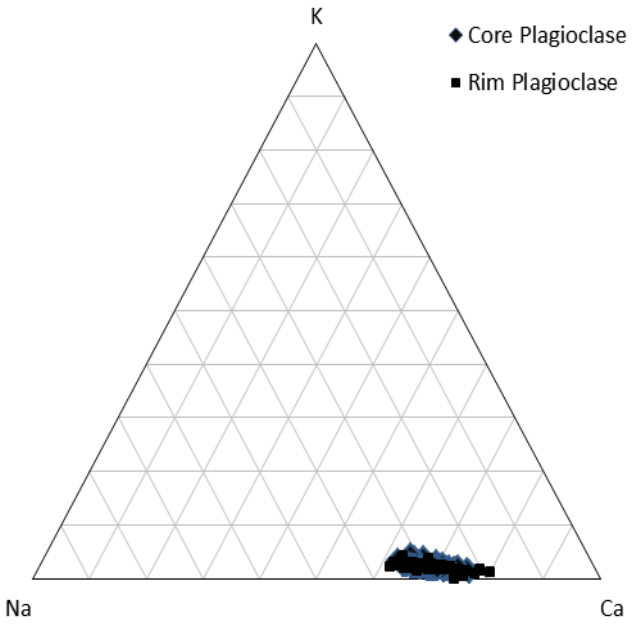

Figure 44: Triplot that shows compositional variation of the core and rim plagioclase crystals.

The plagioclase composition at the rim of the crystals have lower Na and similar Ca concentrations ($(Na_{(0.189 - 0.371)}, K_{(0.005 - 0.108)} Ca_{(0.651 - 0.777)}) Al_{(1.630 - 1.752)} Si_{(2.183 - 2.345)} O_8$). Na increases in concentration from 0m to -468.17 m within TW 632 and below this depth the Na concentration is relatively constant. In PK 206 the Na concentration is relatively constant throughout the whole borehole. The Ca concentration decreases from 0 m to -250 m. The Ca is relatively constant throughout the TW 632 below -250 m and constant throughout the PK 206 borehole (Figure 45b).

The concentration of K is very low due to the lower temperatures at which these minerals crystallise. The K_2O (wt %) vs. MgO (wt %) (Figure 22b) indicates a relatively constant concentration throughout the two boreholes.

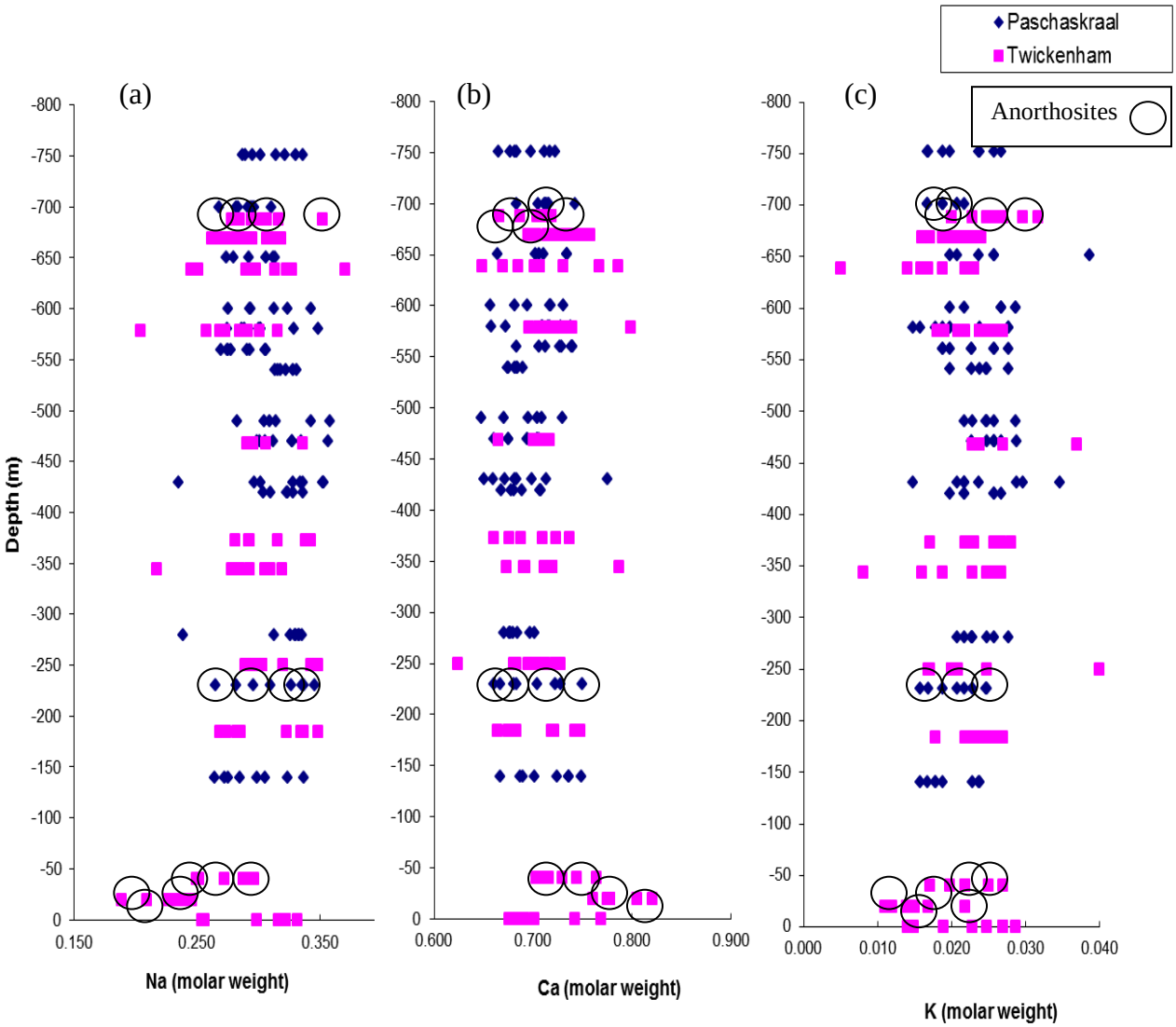

Figure 45: Microprobe recalculated data of the plagioclase crystals (a) Na (molar weight) variation with Depth (m), (b) Ca (molar weight) variation with Depth (m) and (c) K (molar weight) variation with Depth (m).

The Ca plagioclase is the major plagioclase throughout the subzone A of the MZ. The variation between the core and rim of the plagioclase crystals is too small to indicate a significant change in the processes that is responsible for the formation of plagioclase (Figure 44).

Variation of MgO (wt %) with depth (Figure 46a) indicates a large variation with depth. The MgO, Fe_2O_3 and CaO concentrations are obscured by the anorthosite rocks (PAS 40, PAS 39, PAS 35, PAS 28, PAS 4, TW 27, TW 26, TW 25, TW 21 and TW 1). The MgO concentration increases between 0 m to -428.72 m with relatively constant concentration between -428.72 m and -578.33 m. Below -578.33 m the MgO concentration decreases. The variation of MgO (wt %) with depth has a good correlation with the variation of pyroxene (wt %) with depth (Figure 35c).

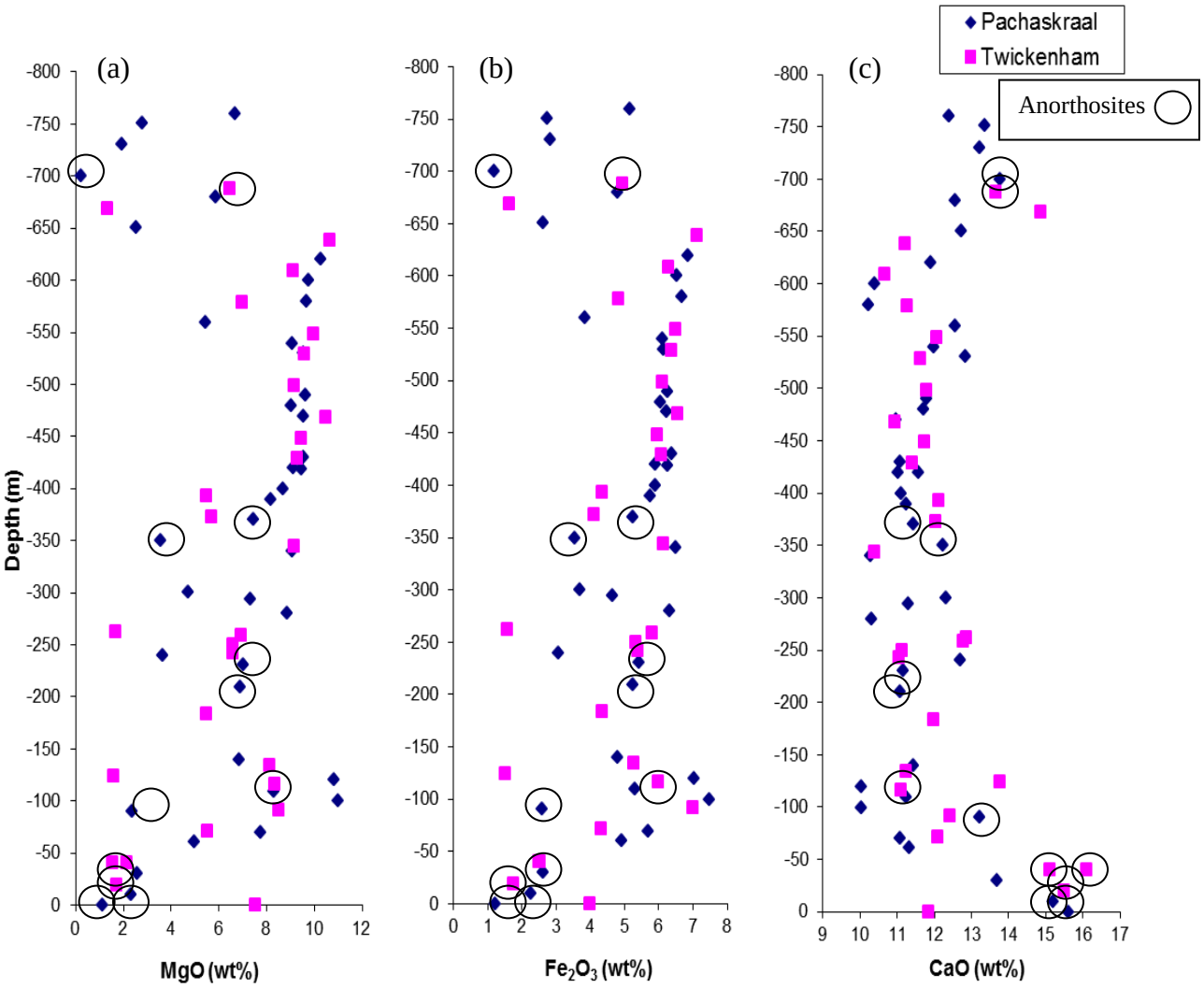

Figure 46: (a) Variation MgO (wt %) with Depth (m), (b) Variation Fe_2O_3 (wt %) with Depth (m) and (c) Variation CaO (wt %) with Depth (m).

Fe_2O_3 concentration has an identical variation as the variation of MgO (wt %) with depth throughout both boreholes (Figure 46b). The CaO concentration (Figure 46c) is inversely

proportional to Fe_2O_3 and MgO due to Ca affinity for plagioclase. The Ca concentration decreases from 0 m to -139.9 m, remaining relatively constant from -139.9 m to -489.98 m and increases below -489.98 m to -760.24 m. The pyroxene CIPW concentration increases between 0 m and -550 m, decreases below -550 m and increases form -700 m to -760.24 m (Figure 34c).

Pyroxenes have several different compositional and structural forms (Table 16). The composition of orthopyroxene crystals vary slightly ($(Mg_{(0.660 - 0.808)}, Fe_{(0.206 - 0.309)}, Ca_{(0.007 - 0.081)}) Si_{(0.960 - 1.037)} O_3$) throughout the different boreholes (Figure 47).

Table 16: Compositions and properties of natural pyroxenes (McBirney, 2007).

Mineral	Formula	Crystal System	MgO (wt %)	FeO_{tot} (wt %)	CaO (wt %)
Enstatite	$Mg_2Si_2O_6$	Orthorhombic (opx)	40	0	0
Ferrosilite	$Fe_2Si_2O_6$	Orthorhombic (opx)	0	55	0
Pigeonite	$(Mg,Fe,Ca)(Mg,Fe)Si_2O_6$	Monoclinic (cpx)	16	24	7
Augite	$Ca(Mg,Fe)Si_2O_6$	Monoclinic (cpx)	16	21	10
Diopside	$CaMgSi_2O_6$	Monoclinic (cpx)	19	0	26
Hypersthene	$(Mg,Fe)_2Si_2O_6$	Orthorhombic (opx)	23	19	2
Hedenbergite	$CaFeSi_2O_6$	Monoclinic (cpx)	0	29	23

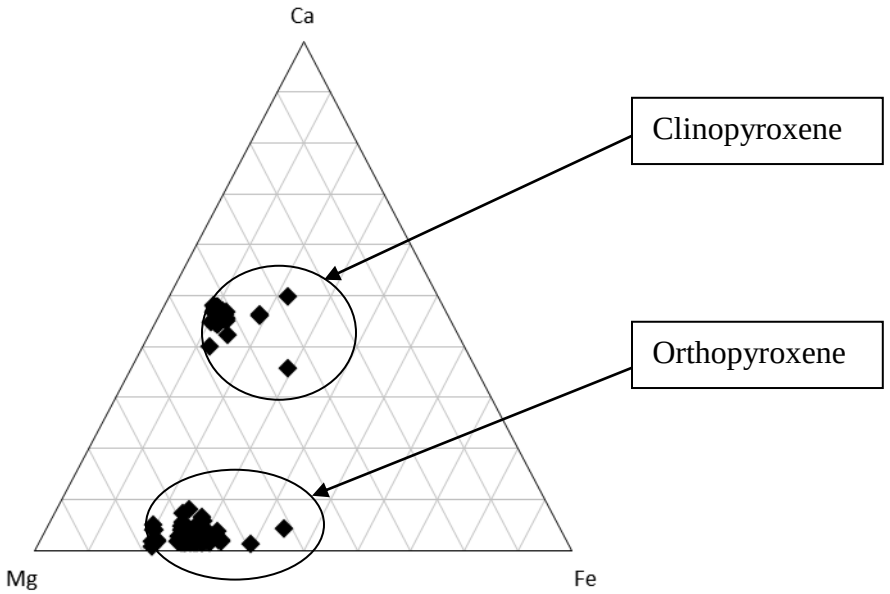

Figure 47: Triplot that shows compositional variation of the clinopyroxene and orthopyroxene crystals.

The orthopyroxene composition has more Mg and Ca concentrations; there are two different chemical compositions for the orthopyroxenes Mg - Fe series (hyperstene) and Mg – Ca (diopside) with small amount of Fe concentration (Figure 47).

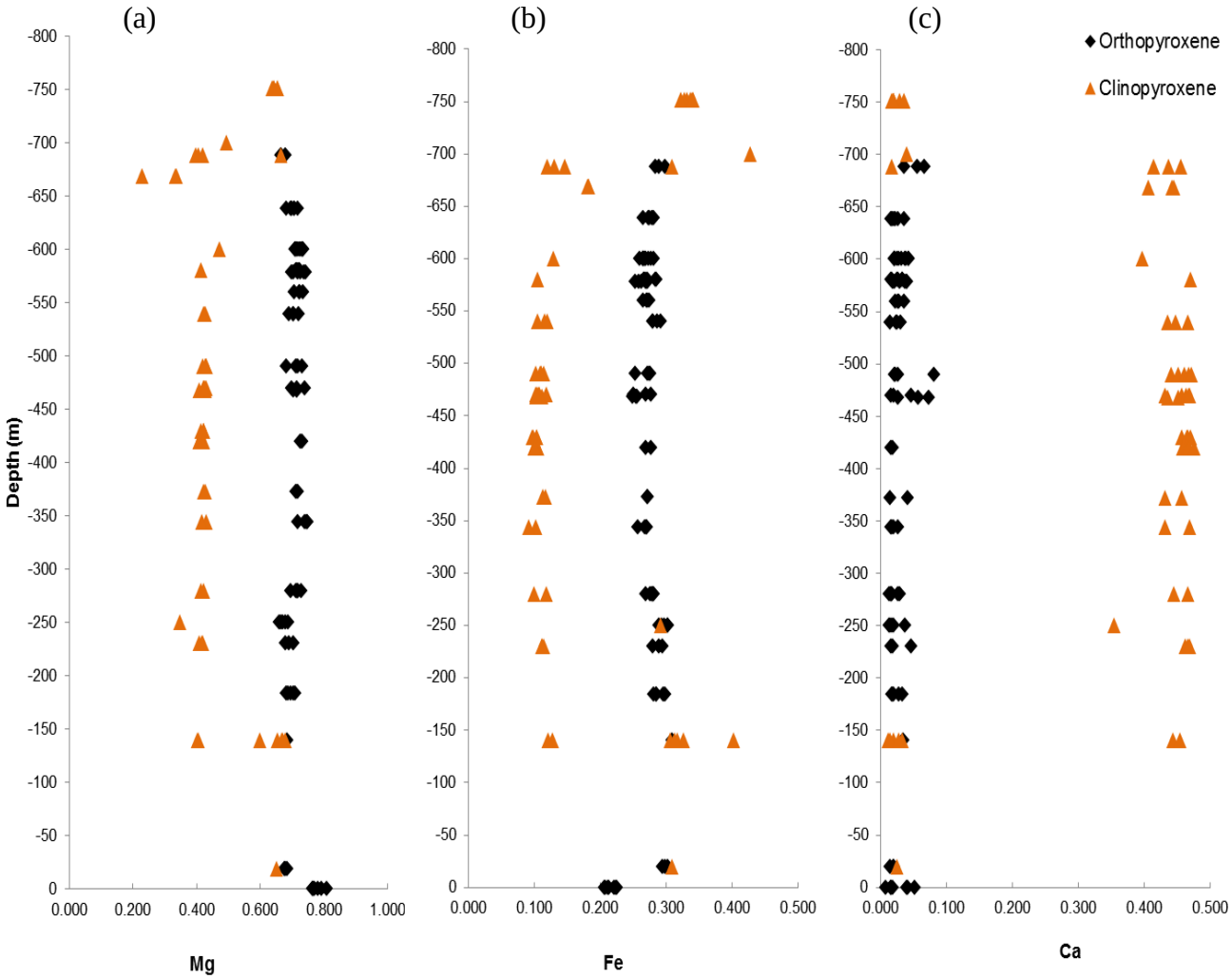

Figure 48: Microprobe recalculated data of the clinopyroxene and orthopyroxene crystals (a) Mg (molar weight) variation with Depth (m), (b) Fe (molar weight) variation with Depth (m) and (c) Ca (molar weight) variation with Depth (m).

The Mg concentration (Figure 48a) increases from -139 m to -230.32 m in the Paschaskraal. It then decreases from -230.32 m to -430 m, increases from -430 m to -600 m, decreases from -600 m to -700 m and increases below -700 m. In the Twickenham borehole the Mg (molar weight) decreases from 0 m to -262.32 m, remains relatively constant between -262.32 m and -638.7 m, decreases from -638.7 m to -668.74 m and increases below -668.74 m. The Fe (molar weight) (Figure 48b) variation with depth is

identical to the Mg (molar weight) throughout both the boreholes. The Ca (molar weight) (Figure 48c) is inversely proportional to the Mg and Fe concentrations due to Ca having more affinity for plagioclase.

The compositions of clinopyroxene varies slightly ($(Mg_{(0.229 - 0.678)}, Fe_{(0.092 - 0.427)}, Ca_{(0.012 - 0.475)}) Si_{(0.776 - 1.012)} O_3$) throughout the different boreholes (Figure 47). The composition of clinopyroxene varies between end members; Mg – Fe with small amounts Ca (pigeonite).The Mg and Fe concentrations are identical throughout the boreholes. The molar weight in PK 206 decreases from -139.9 m to -230.32 m, increases between -230.32 m to -280.11 m, decreases from -280.11 m to -429.96 m and increases from -429.96 m to -760.24 m. In the TW 632 borehole the concentrations decreases from 0 m to -250 m, increases from -250 m to -344 m, remains relatively constant from -344 m to -638.74 m and decreases below -638.74 m.

Al_2O_3 (Figure 43a) and CaO (Figure 43b) increases consistently with the decrease in MgO concentrations. The Al_2O_3 and CaO are less incompatible with pyroxene therefore their concentration increases with increasing plagioclase. The Al_2O_3 was removed by plagioclase and the CaO was removed from by the crystallisation of calcic plagioclase and clinopyroxene. The FeO_{tot} (Figure 20c) concentration increases with increasing MgO. These elements are incorporated into mafic minerals such as pyroxenes. These observations are correlated with the plagioclase (Figure 34c) and pyroxene (Figure 35c) variations with depth and therefore there is no remarkable change in composition throughout the two boreholes. There is no geochemical evidence of magma influx at the subzone A in the MZ. The plagioclase (wt %) increases where the pyroxene (wt %) decreases. This is reflected by the An# increasing with decreasing Mg#.

5.3. Trace element chemistry of the Main Zone

As in partial melting, trace-element partitioning during crystallisation depends on the proportions of liquid and crystals that equilibrate during magma cooling. This interaction can range between two limits, one in which crystals remain in the liquid and re-

equilibrate continuously as the liquid slowly crystallises and the other where crystals become separated as rapidly as they form and cannot equilibrate. Rayleigh fractionation is where the crystals are removed from the melt, and the melt becomes progressively depleted in those elements not consumed in crystal formation. As the composition of the melt changes, so do the minerals able to crystallise from it.

Mineral/melt partition coefficients for basaltic and basaltic andesite liquids show that trace elements favorably partition into specific minerals during the crystallisation of a liquid. The equation governing trace-element behavior (modified after White 1999), during fractional crystallisation accepts equilibrium either between the surface of the crystallising phases and the melt, or between the total solid and the melt. The equation describing trace-element behavior during fractional crystallisation may be written as:

$$C_L/C_i = F^{(D0-1)}$$

F is the fraction of liquid remaining, C_i is the concentration of the original melt, C_L is the concentration of the differentiated liquid, and D_0 is the bulk partition coefficient given by:

$$D_0 = W^{\alpha}K^{\alpha/L} + W^{\beta}K^{\beta/L} + \ldots$$

where W^{α} is the initial weight fraction of α in the precipitating phases, W^{β} the initial weight fraction of phase β, and $K^{\alpha/L}$ is the solid-liquid partition coefficient for phase α, $K^{\beta/L}$ the solid-liquid partition coefficient for phase β. When D_0 approaches zero,

$$C_L/C_i = 1/F$$

so that the concentration of an element depends only on the extent of solidification. The trace elements are subdivided into compatible, where the element has preference for the mineral phase and therefore has a partition coefficient >1, and incompatible, where the element has preference for the melt and a partition coefficient <1, although this can vary depending on the composition of the melt. Therefore, the abundance of trace elements should be controlled by the modal proportions of minerals present.

Most mathematical expressions used in modeling chemical processes assume that the partition coefficients remain constant throughout crystallisation (Blundy and Wood, (2003)). This raises two problems for geochemists: 1) to obtain the best conceivable partition coefficients for the process of interest, 2) to evaluate the degree to which these

partition coefficients vary in the course of the process and how to integrate this variability into a model. In this study, the partition coefficients D_{Zr} are experimental values for a basaltic liquid (White (1999)). During the modeling of Zr in the PK 206 and TW 632 we assume the partition coefficients remain constant throughout the fractional crystallisation process.

Table 17: The XRD data give modal concentrations and D_{Zr} according to White (1999).

Mineral	Modal Proportion	Modal Proportion	D_{Zr}[1.]
	Gabbronorite	**Anorthosite**	
Orthopyroxene	0.23	0.133	0.004
Clinopyroxene	0.118	0.067	0.195
Plagioclase	0.652	0.799	0.001

1. **Partition coefficient of Zr**

By calculating the bulk partition coefficient for Zr in gabbronorite and in anorthosite, we get D_{Zr} values of 0.025 and 0.014 respectfully. Two models are presented: 1) modeling C_S (ppm) using a proposed C_0 of 115 ppm for the trace element Zr (Cawthorn et al., (2005)), and 2) modeling C_S (ppm) using a proposed C_0 concentration of 20 ppm Zr (Sharpe (1981)).

Model 1: Original magma composition of 115 Zr (ppm):

Modeling $C_{S(Zr)}$, the gabbronorite has Zr concentrations between 3 ppm and 252 ppm and for anorthosite between 2 ppm and 155 ppm. The concentrations are very different than the PK 206 and TW 632 concentrations (12 ppm – 34 ppm Zr) measured in this study. In order to achieve the concentrations present in the real rocks, the model requires that only between 7.07 % and 23.98 % liquid remains for the gabbronorites and between 4.63 % and 13.52 % for the anorthosites. Thus, if Cawthorn's model liquid of $C_{0(Zr)}$ of 115 ppm is correct, and our D value is appropriate, the MZ gabbronorite would reflect 76.02 – 92.93 % crystallisation of the original liquid and the MZ anorthosite would reflect 86.00 – 95.00 % crystallisation of the liquid.

Table 18: Calculated Zr (ppm) using 115 ppm (Cawthorn et al., (2005)).

Gabbronorite		D=0.025		Anorthosite		D=0.014	
F	**C_L/C_0**	**C_L(ppm)**	**C_S (ppm)**	**F**	**C_L/C_0**	**C_L (ppm)**	**C_S (ppm)**
1	1	115	3	1	1	115	2
0.9	1.108	127	3	0.9	1.109	128	2
0.8	1.243	143	4	0.8	1.246	143	2
0.7	1.416	163	4	0.7	1.421	163	2
0.6	1.646	189	5	0.6	1.654	190	3
0.5	1.966	226	6	0.5	1.980	228	3
0.4	2.444	281	7	0.4	2.467	284	4
0.3	3.236	372	9	0.3	3.276	377	5
0.2	4.806	553	14	0.2	4.885	562	8
0.1	9.450	1087	27	0.1	9.674	1113	16
0.01	89.297	10269	252	0.01	93.585	10762	155

Table 19: Calculated PK 206 and TW 632 Zr (ppm) using 115 ppm (Cawthorn et al., (2005)).

Gabbronorite		D=0.025		Anorthosite		D=0.014	
1-F	**C_L/C_0**	**C_L (ppm)**	**C_S (ppm)**	**1-F**	**C_L/C_0**	**C_L (ppm)**	**C_S (ppm)**
0.103	9.197	1058	26	0.090	10.681	1228	18
0.128	7.429	854	21	0.135	7.188	827	12
0.086	10.966	1261	31	0.046	20.644	2374	34
0.095	9.905	1139	28	0.056	17.279	1987	29
0.128	7.429	854	21	0.099	9.763	1123	16
0.083	11.320	1302	32	0.052	18.262	2100	30
0.117	8.136	936	23	0.065	14.749	1696	24
0.099	9.551	1098	27	0.082	11.813	1359	20
0.159	6.014	692	17	0.050	19.329	2223	32
0.103	9.197	1058	26	0.055	17.544	2018	29
0.107	8.844	1017	25	0.067	14.256	1639	24
0.107	8.844	1017	25	0.096	10.038	1154	17
0.092	10.258	1180	29	0.099	9.804	1127	16
0.143	6.646	764	19	0.126	7.727	889	13

Model 2: Original magma composition of 20 Zr (ppm):

The $C_{S(Zr)}$ of gabbronorite is between 0 ppm and 44 ppm and for anorthosite between 0 ppm and 27 ppm. In order to achieve the concentrations present in the real rocks, the model requires that only between 1.17 % and 3.99 % liquid remains for the gabbronorites and between 0.78 % and 2.29 % liquid for the anorthosites. If Sharpe's model liquid of

$C_{0(Zr)}$ of 20 ppm is correct, and our D value is appropriate, the MZ gabbronorite would reflect 96.01– 98.83 % crystallisation of the liquid and the MZ anorthosite would reflect 97.71– 99.22 % crystallisation of the liquid.

Table 20: Calculated Zr (ppm) using 20 ppm (Sharpe (1981)).

Gabbronorite		D=0.025		**Anorthosite**		D=0.014	
F	**C_L/C_0**	**C_L (ppm)**	**C_S (ppm)**	**F**	**C_L/C_0**	**C_L (ppm)**	**C_S (ppm)**
1	1	20	0	1	1	20	0
0.9	1.108	22	1	0.9	1.109	22	0
0.8	1.243	25	1	0.8	1.246	25	0
0.7	1.416	28	1	0.7	1.421	28	0
0.6	1.646	33	1	0.6	1.654	33	0
0.5	1.966	39	1	0.5	1.980	40	1
0.4	2.444	49	1	0.4	2.467	49	1
0.3	3.236	65	2	0.3	3.276	66	1
0.2	4.806	96	2	0.2	4.885	98	1
0.1	9.450	189	5	0.1	9.674	193	3
0.01	89.297	1786	44	0.01	93.585	1872	27

Table 21: Calculated PK 206 and TW 632 Zr (ppm) using 115 ppm (Sharpe (1981)).

Gabbronorite		D=0.025		**Anorthosite**		D=0.014	
1-F	**C_L/C_0**	**C_L (ppm)**	**C_S (ppm)**	**1-F**	**C_L/C_0**	**C_L (ppm)**	**C_S (ppm)**
0.017	52.884	1058	26	0.015	61.413	1228	18
0.021	42.714	854	21	0.023	41.331	827	12
0.014	63.054	1261	31	0.008	118.700	2374	34
0.016	56.952	1139	28	0.009	99.355	1987	29
0.021	42.714	854	21	0.017	56.135	1123	16
0.014	65.088	1302	32	0.009	105.005	2100	30
0.019	46.782	936	23	0.011	84.806	1696	24
0.016	54.918	1098	27	0.014	67.927	1359	20
0.026	34.578	692	17	0.008	111.142	2223	32
0.017	52.884	1058	26	0.009	100.875	2018	29
0.018	50.850	1017	25	0.011	81.974	1639	24
0.018	50.850	1017	25	0.016	57.717	1154	17
0.015	58.986	1180	29	0.017	56.375	1127	16
0.024	38.216	764	19	0.021	44.429	889	13

Calculating $C_{s(Zr)}$ values for each proposed $C_{0(Zr)}$ the following possible fractionation trends are acquired.

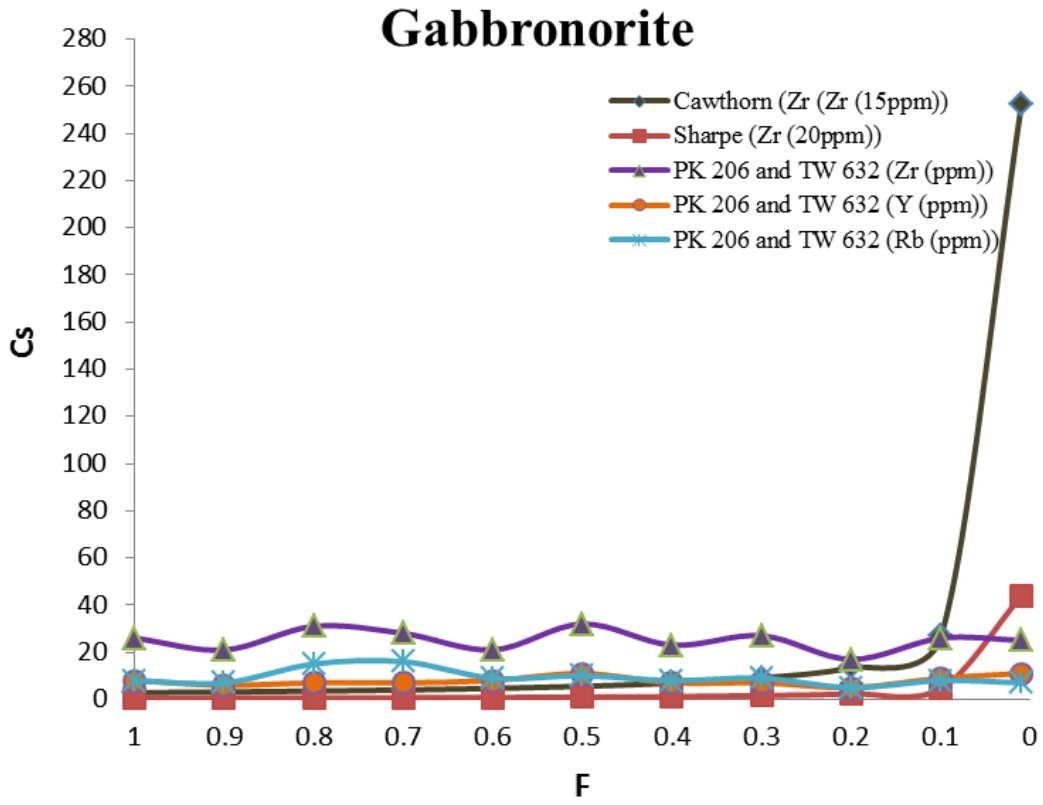

Figure 49: Melt composition $C_{s(Zr)}/C_{0(Zr)}$ as a function of melt fraction (F) in gabbronorite.

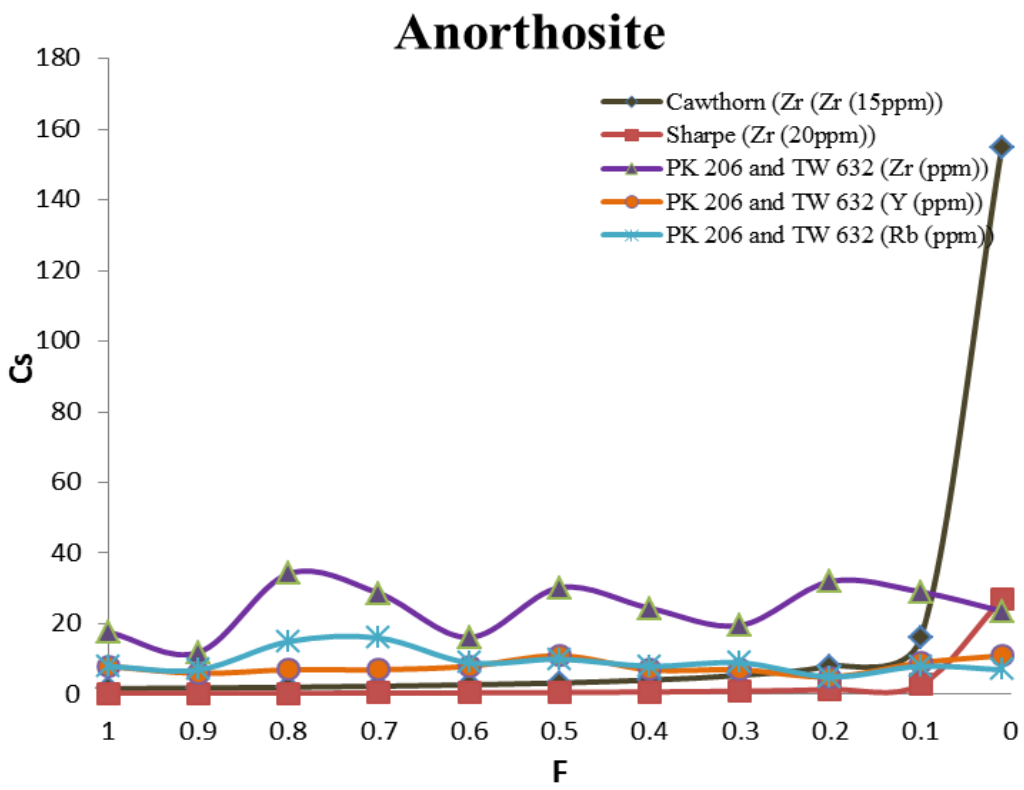

Figure 50: Melt composition $C_{s(Zr)}/C_{0(Zr)}$ as a function of melt fraction (F) in anorthosite.

There are several assumptions in these models which be considered. The model: 1) assume the starting compositions of 20 ppm and 115 ppm, 2) use fixed D values obtained from experimental data (White (1999)) for basaltic liquids, and 3) assume that the magma crystallised through pure fractional crystallisation.

The starting compositions of 20 ppm and 115 ppm are two extremes. The concentration of Zr in the initial magma that formed the MZ is unlikely to be higher than 115 ppm considering that the original liquid was a mantle-derived melt. Though contamination may have raised the Zr content somewhat, the volume of contaminant required to raise the Zr content of a basaltic liquid (generally between 20 and 40 ppm) above 115 ppm is extreme. Therefore the starting composition of between 20– 115 ppm covers all reasonable values for the real magma composition.

Trace element content of a liquid (or melt) is very sensitive to partition coefficients. This sensitivity varies with the absolute magnitude of the partition coefficient and with the style of crystallisation (fractional, batch, etc.).Two parallel approaches can be applied to obtain the right partition coefficient. The first approach involves experimental determination of the partition coefficients for all elements of interest under the exact conditions of pressure, temperature and composition for the process of interest. The second approach involves the development of predicted models of partitioning that can be applied over a wide range of conditions for a large number of elements (Blundy and Wood, (2003)). The problem in this study it is assumed that a pure basaltic liquid is the starting liquid, which is not the case owing to the MZ crystallising a higher amount of plagioclase than would be expected from a basaltic liquid. However, there are no specific studies done on parental liquids for the BIC, and the partition coefficients used in this study must be considered a "best guess", and the accuracy of these coefficients is impossible to evaluate.

It is also assumed that the concentration of plagioclase, orthopyroxene and clinopyroxene remains constant during crystallisation. This is definitely not the case; over the range of fractional crystallisation calculated in the different models (76- 99 %), it would be reasonable to expect that some change in the stabilities of the various minerals would have altered the proportions of the different minerals crystallising, and thus the partition coefficients. However, assuming a constant D is a standard approach to this type of modeling, even though it is inherently flawed.

The processes involved in the formation of magma may be a combination of different processes. The MZ may have formed from mixed processes wherein both equilibrium crystallisation and fractional crystallisation occurs at the same time. Fractional crystallisation and magma influxes cause very distinct geochemical behavior in a rock, which can be interpreted from bivariate diagrams comparing the behavior of different trace elements.

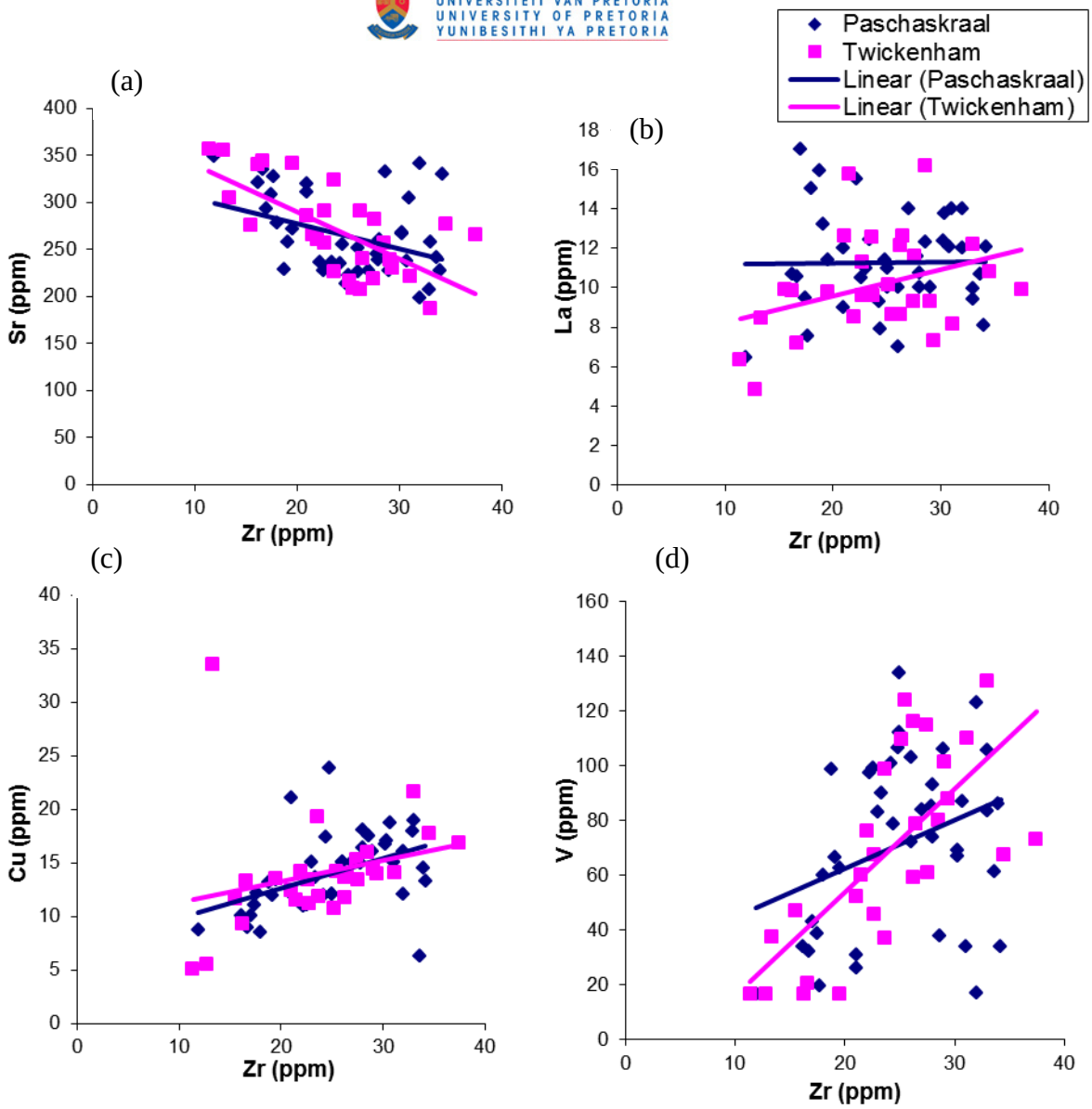

Figure 51: (a) Sr (ppm) vs. Zr (ppm), (b) La (ppm) vs. Zr (ppm), (c) Cu (ppm) vs. Zr (ppm) and (d) V (ppm) vs. Zr (ppm).

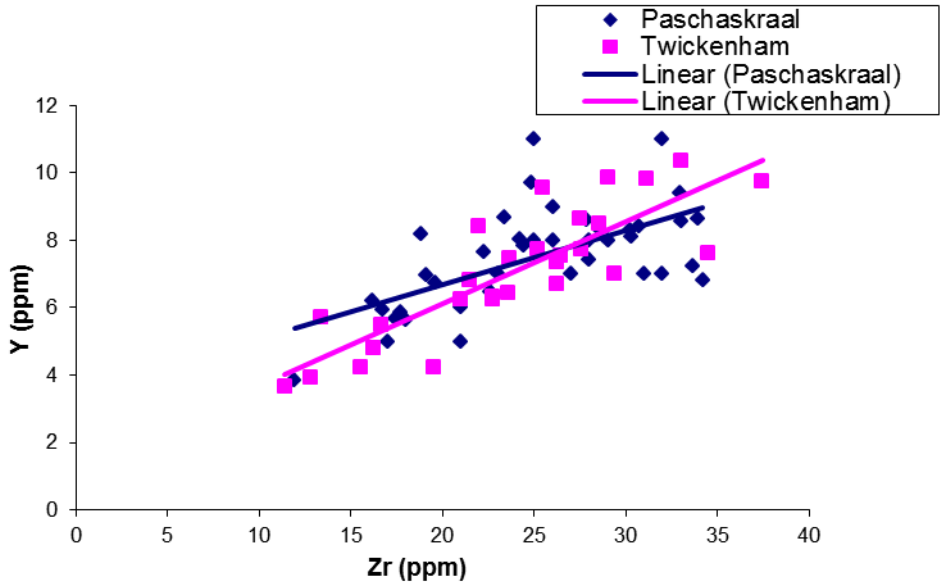

Figure 52: Y (ppm) vs. Zr (ppm).

Sr is a highly incompatible large ion lithophile (LIL) element which is plotted against compatible element Zr. Sr is inversely proportional to Zr (Figure 51 a). Sr concentrates in late liquids (in plagioclase) whereas Zr is incompatible with all minerals present. Thus, the Zr/Sr behavior indicates that the dominant process in the formation of the MZ is fractional crystallisation, and that the liquid is plagioclase dominated. Similarly, the bivariate plots of La, Cu, V (Figure 51b, c and d) and Y (Figure 52) against Zr shows a positive trend, where Zr increases as the concentrations of La, Cu, V and Y increase. This is because these trace elements are incompatible in both mafic minerals such as pyroxene and felsic minerals such as plagioclase. These strong correlations depicted in Figure 51 and Figure 52 show normal fractionation trends in mineral compositions. Thus, it appears reasonable to model the MZ as the result of a process dominated by fractional crystallisation.

Bearing in mind the limitation in the model as discussed above, the results of the modeling can be considered. The modeling indicates that a high initial Zr content (115 ppm) liquid which has already crystallised at least 75 % of its original volume and can crystallise the concentrations of Zr present in the rocks of the MZ. A liquid with a lower Zr content would require a much higher volume of crystallisation. These calculations are in agreement with those of Lundgaard et al., (2006), who calculated that the MZ formed

after 90 % crystallisation. Both sets of modeling thus indicate that the MZ formed from a liquid which had already undergone significant fractional crystallisation, not from a liquid freshly injected into the magma chamber as hypothesised by studies such as Kruger (1994).

5.4. Hypothesis for formation of the lower Main Zone

The formation of the MZ has long been discussed by various authors and most believe that the MZ crystallised from two magmas. The first magma according to Harmer and Sharpe (1985) is of tholeiitic nature with MgO concentrations of 9.21 wt% (Table 4). The major oxide concentrations (Table 4), obtained in this project, are similar to those proposed by Maier et al., (2001). Therefore the magma forming the lower MZ has lower silica and lower MgO concentrations than the CZ magma. The possibility of the subzone A in the MZ forming from a mixture of new magma and residual magma can only be determined if the parental magma to the MZ are accurately depicted but the amount of data needed are more significant than what we had in this project

Eales et al., (1986) suggested that the lower MZ formed by small injections of new magma. The mineralogy of the lower MZ indicates gradual changes throughout the PK 206 and TW 632 boreholes. These mineralogical changes are best described by the almost perfect linear relation in the Harker diagrams (Figure 20- 26) especially when looking at the elements which are associated with the plagioclase and pyroxene minerals. The plagioclase concentration plotted against depth (m) (Figure 34c) indicates no sharp reversals or distinct changes throughout the PK 206 and TW 632 boreholes. Investigating the variation of the An# and Mg#, throughout the two boreholes, indicates that the An# decreases when the Mg# is increasing and vice versa. This evidence confirms that all the mineralogical changes occurring in the lower MZ are related to normal fractional crystallisation and therefore the lower MZ formed from a single magma.

The magma forming the lower MZ must have intruded below the stratigraphy sampled in this project. If we assume that the new MZ magma entered the chamber at the level just

below the lower MZ, the decrease in temperature must have been sudden before the onset of crystallisation because there is no evidence of magma mixing in the lower MZ. But if we assume that the magma entered the chamber at the level of the MR; the crystallisation of the lower MZ would show no evidence of magma influx which is a better depiction due to the two magmas involved in forming the Merensky Reef (Maier et al., 2001).

No Sr isotopic data was obtained in this study but bulk trace element data was obtained which suggest that the lower MZ (subzone A) formed through fractional crystallisation of a single magma (Figure 51 and 52). As shown throughout this study the lower MZ has formed from a single magma (parental composition still unkown) but at the Pyroxenite Marker the decrease in initial Sr ratio (0.7073) (Kruger, 1994) is evidence of a new magma influx.

CHAPTER 6: CONCLUSION

This study's main aim was to investigate geochemical data throughout a large portion of the MZ as well as to review some of the ideas on how the lower MZ formed. Mineralogical data obtained from two boreholes of the Eastern Limb gave a comprehensive understanding of the processes involved in the formation of the MZ. Some major and trace elements plotted against height show variation, decreasing and increasing trends. This variation is caused by a change in magma composition (chemical composition or mineral composition).

Bivariate diagrams (Figure 20- 28), on which two selected variables are plotted, can give a good description of how the magma evolved. The major elements and trace elements plotted against each other show linear trends and the elements compare well with each other thus indicating differentiation by fractional crystallisation. Concentrations of TiO_2, FeO_{tot}, MgO, MnO, Cr_2O_3, NiO and V_2O_5 increases with increasing SiO_2 and MgO due to their compatibility with the pyroxene minerals. The Al_2O_3, CaO, Na_2O and ZrO_2 concentrations decreases with increasing SiO_2 and MgO concentrations, this relationship is due to the fractionation of Al, Ca, Na and Zr elements to the plagioclase minerals. The K_2O concentration is relatively constant in relation to the increase in SiO_2 (wt %) but the K_2O (wt %) decreases with increasing MgO (wt %) due to the fractionation of K into plagioclase minerals. P_2O_5 (wt %) increases with increasing SiO_2 concentration; this is directly correlated to the concentration of apatite throughout the MZ.

The modeling shows that a high initial Zr content (115 ppm) liquid which has already crystallised at least 75 % of its original volume and can crystallise the concentrations of Zr present in the rocks of the lower MZ. A liquid with a lower Zr content would require a much higher volume of crystallisation. These calculations are in agreement with those of Lundgaard et al., (2006), who calculated that the MZ formed after 90 % crystallisation. Both sets of modeling thus indicate that the MZ formed from a liquid which had already undergone significant fractional crystallisation, not from a liquid freshly injected into the magma chamber as hypothesised by studies such as Kruger (1994).

The bivariate plot of La, Cu, V (Figure 51b, c and d) and Y (Figure 52) against Zr shows a positive trend, where Zr increases the concentration of La, Cu, V and Y. This is because the trace elements are compatible in mafic minerals such as pyroxene. These strong correlations depicted in Figure 51 and Figure 52 show normal fractionation trends in mineral compositions.

The lower MZ (subzone A) has a broad mineralogical variation with depth (m), in the Paschaskraal borehole (PK 206) and Twickenham borehole (TW 632). The core plagioclase varies in composition ($(Na_{(0.227 - 0.353)}, K_{(0.012 - 0.046)} Ca_{(0.651 - 0.777)}) Al_{(1.630 - 1.752)} Si_{(2.183 - 2.345)}) O_8$ and the plagioclase composition at the rim of the crystals seems to have lower Na and similar Ca concentrations ($(Na_{(0.189 - 0.371)}, K_{(0.005 - 0.108)} Ca_{(0.651 - 0.777)}) Al_{(1.630 - 1.752)} Si_{(2.183 - 2.345)} O_8$) (Figure 44).

The composition of orthopyroxene crystals vary slightly ($(Mg_{(0.660 - 0.808)}, Fe_{(0.206 - 0.309)}, Ca_{(0.007 - 0.081)}) Si_{(0.960 - 1.037)} O_3$) throughout the different boreholes (Figure 47) and the compositions of clinopyroxene is ($(Mg_{(0.229 - 0.678)}, Fe_{(0.092 - 0.427)}, Ca_{(0.012 - 0.475)}) Si_{(0.776 - 1.012)} O_3$). The composition of clinopyroxene varies between end members; Mg – Fe with small amounts Ca (pigeonite).

The Mg# of the pyroxenes and An# of plagioclase show variation which is attributed by fractional crystallisation. The Mg# and An# varies with depth, where plagioclase increase in concentration the An# increases and the Mg# decreases. Al_2O_3 and Sr are compatible with plagioclase which is seen in their increase or decrease at certain depths corresponding to an increase or decrease in plagioclase at the same depths. MgO and Zr are compatible with pyroxene, and decreases at the depth where the lithology changes to anorthosite, a plagioclase – rich rock, and increases where the lithology changes to gabbronorite, which is a pyroxene – rich layer.

The mineralogy of PK 206 and TW 632 boreholes from base to top indicates compositional variations that purely formed by fractional crystallisation. These

compositional variations display no basal reversals in the MgO and Ni concentration or in the Mg #of the cumulus orthopyroxene.

The MZ formed through two magma influxes; one magma forming the lower MZ and a second forming the upper MZ. The magma forming the lower MZ intruded the RLS at the contact between the CZ and the MZ. The Merensky Reef is the transition zone between the CZ magma and the MZ magma (Maier et al., 2001). The second magma intruded the RLS at the level of the Pyroxenite Marker (Harris et al., 2005). There is no evidence that the lower MZ reflects magma mixing. The major and trace element variation are gradual and reflects mineralogical variation, the crystallisation formed through a process of normal magmatic differentiation. Therefore no evidence of new magma influx in the lower MZ; the MZ magma must have mixed with the CZ magma before the crystallisation of the lower MZ.

BIBLIOGRAPHY

Ariskin, A.A. and Yaroshevsky, A.A., (2006). Crystallization differentiation of intrusive magmatic melt: development of convection-accumulation model. Geochemistry international Vol. 44, pp 72-93.

Barnes, S.J., and Maier, W.D., (2002). Platinum-group elements and microstructures of normal Merensky Reef from Impala Platinum Mines, Bushveld Complex. Journal of Petrology Vol. 43, pp 103-128.

Barnes, S.J., Maier, W.D., Ashwal, L.D., (2004). Platinum-group element distribution in the Main Zone and Upper Zone of the Bushveld Complex, South Africa. Chemical Geology Vol. 208, pp 293-317.

Blundy, J., and Wood, B., (2003). Partitioning of trace elements between crystals and melts. Earth and Planetary Science Letters Vol. 219,pp 383-397.

Bowen, N.L., (1928). The evolution of igneous rocks. Princeton University Press, Prinston NJ.

Campbell, I.H., (1977). A study of macro-rhythmic layering and cumulate processes in the Jimberlana Intrusion, Western Australia. Part I: the upper layered series. Journal of Petrology Vol. 18, pp 83–215.

Cameron, E.N., (1978). The Lower Zone of the Eastern Bushveld Complex in the Olifants River trough. Journal of Petrology Vol. 19(3), pp 437-462.

Cawthorn, R.G. and McCarthy, T.S., (1981). Bottom crystallization and diffusion control in layered complexes: evidence from Cr distribution in magnetite from the Bushveld Complex. Transactions of the Geological Society of South Africa Vol. 84, pp 335-343.

Cawthorn, R.G., (1982). An origin for the small scale fluctuations in orthopyroxene composition in the Lower and Critical Zones of the Bushveld Complex, South Africa. Chem Geol Vol. 36, pp 227-236.

Cawthorn, R.G. and Molyneux, T.G., (1986). Vanadiferous magnetite deposits of the Bushveld Complex. In: Anhaeusser, C.R., Maske, S (Eds.), Mineral Deposits of Southern Africa. Geological. Society of South Africa, Johannesburg Vol. 2, pp 1251-1266.

Cawthorn, R.G. and Walsh, K.L., (1988). The use of phosphorus contents in yielding estimates of the proportion of trapped liquid in cumulates of the Upper Zone of the Bushveld Complex. Mineralogical Magazine Vol. 52, pp81-89.

Cawthorn, R.G. and Walraven, F., (1998). Emplacement and crystallization time for the Bushveld Complex. Journal of Petrology Vol. 9, pp 1669-1687.

Cawthorn, R.G. and Lee, C., (1998). Field excursion guide to the Bushveld Complex. 8'Th International Platinum Symposium. The Geological Society of South Africa and the South African Institute of mining and metallurgy, pp 113.

Cawthorn, R.G. and Webb, S.J., (2001). Connectivity between the Western and Eastern Limb of the Bushveld Complex. Tectonophysics Vol. 330, pp 195-209.

Cawthorn, R.G., Barnes, S.J., Ballhaus, C. and Malitch, K.N., (2005). Platinum-group element, chromium, and vanadium deposits in mafic and ultramafic rocks. Economic Geology, 100th Anniversary Volume, pp 215-249.

Cawthorn, R.G., (2007). Cr and Sr:Keys to parental magmas and processes in the Bushveld Complex, South Africa. Lithos Vol. 95, pp381-398.

Cawthorn, R.G. and Ashwal, L.D., (2009). Origin of anorthosite and magnetitite layers in the Bushveld Complex, constrained by major element compositions of plagioclase. Journal of Petrology. Vol. 50 no.9, pp 1607-1637.

Cheney, E.S and Twist, D., (1992). The conformable emplacement of the Bushveld mafic rocks along a regional unconformity in the Transvaal succession of South Africa. Precambrian Research Vol. 74, pp 203-223.

Coats, R.R., (1936). Primary banding in basic plutonic rocks. The Journal of Geology, pp 407.

Eales, H.V., Marsh, J.S., Mitchell, A.A., de Klerk, W.J., Kruger, F.J., Mathez, E.A., Hunter, R.H. and Kinzler, R., (1986). Some geochemical constraints upon models for the crystallization of the upper Critical Zone – Main Zone interval, north Western Bushveld Complex. Mineralogical Magazine Vol. 50, pp 567-582.

Eales, H.V. and Cawthorn, R.G., (1996). The Bushveld Complex; in layered intrusions. Ed: R.G. Cawthorn. Develop. Petrology Vol. 15 Elsevier, pp 531.

Eales, H.V. (2002). Caveats in defining the magmas parental to the mafic rocks of the Bushveld Complex, and the manner of their emplacement: review and commentary. Mineralogical Magazine Vol. 66, pp 815–832.

Hall, A.L., (1932). The Bushveld Igneous Complex of the central Transvaal Memoir. Geological Survey of South Africa Vol.28, pp 560.

Harker, A., (1909). The natural history of igneous rocks. Methuen & Co. London.

Harmer, R.E. and Armstrong, R.A., (2000). Duration of Bushveld Complex (sensu lato) magmatism: constraints from new SHRIMP zircon chronology. Workshop on the

Bushveld Complex Gethane Lodge, Burgersfort, University of the Witwatersrand, Johannesburg.

Harmer, R.E. and Sharpe, M.R. (1985). Field relations and strontium isotope systematics of the marginal rocks of the Eastern Bushveld Complex. Economic Geology Vol. 80, pp 813–837.

Harris, C., Pronost, J.J.M., Ashwal, L.D. and Cawthorn, R.G., (2005). Oxygen and Hydrogen Isotope Stratigraphy of the Rustenburg Layered Suite, Bushveld Complex: Constraints on crustal contamination. Journal of Petrology, Vol 46 no.3, pp579-601.

Irvine, T.N., (1980). Magmatic infiltration metasomatism, double diffusive fractional crystallization, and adcumulate growth in the Muskox Intrusion and other layered intrusions. In: Hargraves, R.B. (Ed.), Physics of magmatic processes, pp. 123–383. Princeton, New Jersey.

Irvine, T.N., (1982). Terminology for layered intrusions. Journal of Petrology Vol. 23, pp 127-162.

Jackson, E.D., (1961). Primary textures and mineral associations in the ultramafic zone of the Stillwater Complex: Montana, U. S. Geol. Survey Prof. Paper 358.

Kruger, F.J. and Marsh, J.S., (1982). Significance of $^{87}Sr/^{86}Sr$ ratios in the Merensky Cyclic Unit of the Bushveld Complex. Nature Vol. 298, pp 53-55.

Kruger, F.J., Cawthorn, R.G., Walsh, K.L., (1987). Strontium isotopic evidence against magma addition in the Upper Zone of the Bushveld Complex. Earth and Planetary Science Letters Vol. 84, pp 51-58.

Kruger, F.J., (1990). The stratigraphy of the Bushveld Complex: a reappraisal and the relocation of the Main Zone boundaries. South African Journal of Geology Vol. 93, pp 376-381.

Kruger, F.J., (1992). The origin of the Merensky cyclic unit: Sr- isotopic and mineralogical evidence for an alternative orthomagmatic model. Australian Journal of Earth Science Vol. 39, pp 255-261.

Kruger, F.J., (1994). The Sr-isotopic stratigraphy of the Western Bushveld Complex. South African Journal of Geology Vol. 97, pp 393-398.

Kruger, F.J., (2005). Filling the Bushveld Complex magma chamber: lateral expansion, roof and floor interaction, magmatic unconformities, and the formation of giant chromitite, PGE and Ti-V- magnetite deposits. Mineralium Deposita Vol. 40, pp 451-472.

Latypov, R.M., (2003). The origin of basic-ultrabasic sills with S-, D- and I-shaped compositional profiles by in situ crystallization of a single input of phenocryst-poor parental magma. J Petrol Vol. 44, pp 1619–1656.

Latypov, R.M., Chistyakova, S.Yu, Alapieti, T.T., (2007). Infiltration metasomatism in layered intrusions revisited: a reinterpretation of compositional reversals at the base of cyclic units. Mineralogy and Petrology Vol. 92, pp 243-258.

Lombard, B.V., (1934). On the differentiation and relationships of the rocks of the Bushveld Complex, Transactions of the Geological Society of South Africa Vol. 37, pp 5-52.

Lundgaard, K.T., Tegner, C., Cawthorn, R.G., Kruger, F.J., Wilson, J.R., (2006). Trapped intercumulus liquid in the Main Zone of the Eastern Bushveld Complex, South Africa. Contirbution to Mineral Petrology Vol. 151, pp 352-369.

Maier, W.D., Barnes, S.J. and van der Merwe, M.J., (2001). Platinum-group elements in the Pyroxenite Marker, Bushveld Complex: implications for the formation of the Main Zone. South African Journal of Geology Vol. 104, pp 301-308.

Maaloe, S., (1978). The origin of rhythmic layering. Mineralogical Magazine Vol. 42, pp 337-345.

Mathez, E.A., Hunter, R.H., Kinzler, R., (1997). Petrologic evolution of partially molten cumulate: the Atoc section of the Bushveld Complex. Contrib Mineral Petrol Vol. 129, pp 20–34.

McBirney, A.R., and Noyes, R.M., (1979). Crystallization and layering of the Skaergaard intrusion: Journal of Petrology, Vol. 20, pp 487–554.

McBirney, A.R., (1995). Mechanisms of differentiation in the Skaergaard Intrusion. Journal of the Geological society Vol.152, pp 421-435.

McBirney, A.R., (2007). Igneous Petrology. Jones and Bartlett. Canada. pp 128.

Mitchell, A.A., (1990). The stratigraphy, petrology and mineralogy of the Main Zone of the North-Western Bushveld Complex. South African Journal of Geology Vol. 93, pp 818-831.

Morse, S. A., (1984). Cation diffusion in plagioclase feldspar. Science Vol. 225, pp 504-505.

Naldrett, A.J., (1989). Stratiform PGE deposits in layered intrusions. Rev Econ Geol Vol. 4, pp 135–166.

Nelson, D.R., Trendall, A.F., Altermann, W., (1999). Chronological correlations between Pilbara and Kaapvaal Cratons. Precamb. Res. Vol. 97, pp 165–189.

Nex, P.A., Kinnaird, J.A., Ingle, L.J., van der Vyver, B.A., Cawthorn. R.G., (1998). A new stratigraphy for the Main Zone of the Bushveld Complex, in the Rustenburg area. South African Journal of Geology Vol. 98, pp 215-223.

Nex, P.A., Cawthorn, R.G. and Kinnaird, J.A., (2002). Geochemical effects of magma addition: compositional reversals and decoupling of trends in the Main Zone of the western Bushveld Complex. Mineralogical Magazine Vol. 66(6), pp 833–856.

Sharpe, M.R., (1981). The chronology of magma influxes to the eastern compartment of the Bushveld Complex as exemplified by its marginal border groups. Journal. Geological. Society. London Vol. 138, pp 307-326.

Sharpe, M.R., (1985). Strontium isotope evidence for preserved density stratification in the Main Zone of the Bushveld Complex. Nature Vol. 316, pp 199-126.

Sparks, R.S.J., Huppert, H.E., (1984). Density changes during the fractional crystallization of basaltic magmas: fluid dynamic implications. Contrib Mineral Petrol Vol 85, pp. 300-309.

Sparks, R.S.J., Huppert, H.E., Kerr, R.C., McKenzie, D.P., Tait, S.R., (1985). Post-cumulus processes in layered intrusions. Geological Magazine Vol. 122, pp 555–568.

Tait, S.R., Huppert, H.E., Sparks, R.S.J., (1984). The role of compositional convection in the formation of adcumulate rocks. Lithos Vol. 17, pp 139–146.

Tegner, C., Cawthorn, R. G., and Kruger F. J., (2006). Cyclicity in the Main and Upper Zones of the Bushveld Complex, South Africa: Crystallization from a zoned magma. Journal of Petrology. Vol.47, pp 2257–2279.

Van Zyl, J.P., (1970). The petrology of the Merensky Reef and the associated rocks on Swartklip 988 Rustenburg District. Geological Society of South Africa. Special Publication Vol. 1, pp 80-108.

Von Gruenewaldt, G., (1970). On the phase change orthopyroxene pigeonite and the resulting textures in the Main and Upper Zones of the Bushveld Complex in the eastern Transvaal. In: Visser, D. J. L. & von Gruenewaldt, G. (eds) Symposium on the Bushveld Igneous Complex and Other Layered Intrusions. Johannesburg: Geological
Society of South Africa, pp. 67-73.

Von Gruenewaldt, G., (1973). The Main and Upper Zones of the Bushveld Complex in the Roossenekal area eastern Transvaal. Transactions of the Geological Society of South Africa Vol. 76, pp 207-227.

Wager, L.R., (1959). Differing powers of crystal nucleation as a factor producing diversity in layered igneous intrusions. Geol. Mag, Vol. 96, pp 75-80.

Wager, L.R., Brown, G.M. and Wadsworth, W.J., (1960). Types of igneous cumulate. Journal of Petrology Vol. 1, pp 73-85.

Wager, L. R., (1963). The mechanism of adcumulus growth in the layered series of the Skaergaard intrusion. In: Fisher, D. J., Frueh, A. J., Hurlbert, C. S. & Tilley, C. E. (eds) Symposium on Layered Intrusions. Mineralogical Society of America, Special Paper 1, 1–9. Wager, L.R., and Brown, G.M., 1968, Layered igneous rocks: Edinburgh, Oliver and Boyd.

Winter, J.D., (2001). An introduction to igneous and metamorphic petrology. Prentice-Hall Inc. New Jersey.

White, W.M., (1999). Geochemistry. John-Hopkins University Press.

Appendix A: Major Element Data (XRF) *data given in weight percentage (wt %)*

Paschaskraal:

Depth (m)	-760.24	-751.29	-730.2	-700.11	-680.17	-650.87	-619.84	-600.16	-580.22	-560	-539.82	-530.2	-489.98	-479.8	-470.02
Rock Type	Gabbro - norite	Gabbro - norite	Gabbro - norite	Anorthosite	Gabbro - norite	Gabbro - norite	Gabbro – norite	Gabbro - norite	Gabbro - norite	Gabbro - norite	Gabbro - norite	Gabbro - norite	Gabbro - norite	Gabbro - norite	Gabbro - norite
Samples	**PAS 1**	**PAS 2**	**PAS 3**	**PAS 4**	**PAS 5**	**PAS 6**	**PAS 7**	**PAS 8**	**PAS 9**	**PAS10**	**PAS11**	**PAS12**	**PAS13**	**PAS14**	**PAS 15**
SiO_2	50.9	50.74	50.79	49.78	51.06	49.67	51.24	51.86	52.05	50.26	51.68	52.08	51.62	51.73	52.65
TiO_2	0.15	0.11	0.17	0.26	0.17	0.08	0.18	0.14	0.15	0.08	0.15	0.16	0.16	0.17	0.14
Al_2O_3	21.52	27.24	26.9	29.24	22.25	27.11	16.42	19.34	18.72	24.27	18.69	17.07	18.41	18.07	18.21
Fe_2O_3	5.14	2.75	2.83	1.2	4.79	2.63	6.84	6.51	6.66	3.84	6.12	6.14	6.27	6.04	6.24
MnO	0.1	0.05	0.05	0.02	0.09	0.03	0.14	0.12	0.13	0.08	0.12	0.13	0.13	0.12	0.13
MgO	6.7	2.84	1.96	0.26	5.92	2.59	10.32	9.81	9.72	5.5	9.1	9.6	9.68	9.06	9.59
CaO	12.39	13.35	13.21	13.77	12.57	12.73	11.9	10.4	10.22	12.56	11.99	12.84	11.8	11.71	10.98
Na_2O	2.09	2.7	2.84	3	2.27	3.12	1.5	1.71	1.75	2.21	1.76	1.57	1.84	1.88	1.74
K_2O	0.26	0.27	0.49	0.49	0.27	0.16	0.3	0.24	0.27	0.2	0.24	0.2	0.23	0.27	0.24
P_2O_5	0.01	0.01	0.03	0.09	0.01	LOD	0.02	0.01	0.01	LOD	0.01	LOD	0.01	0.01	0.01
Cr_2O_3	0.03	0.01	0.01	LOD	0.03	0.01	0.06	0.04	0.05	0.03	0.07	0.07	0.07	0.05	0.07
NiO	0.04	0.01	0.01	LOD	0.02	0.01	0.03	0.03	0.03	0.02	0.02	0.02	0.05	0.02	0.03
V_2O_5	0.01	0.01	0.01	LOD	0.01	LOD	0.02	0.01	0.01	0.01	0.02	0.02	0.02	0.02	0.02
ZrO_2	0.01	0.01	0.01	0.01	0.01	0.01	0.01	0.01	0.01	0.01	0.01	0.01	0.01	0.01	0.01
LOI	0.01	0.16	0.63	0.39	0.35	1.48	0.09	-0.12	-0.11	0.48	-0.05	-0.1	-0.11	-0.13	0.05
Total	99.35	100.24	99.94	98.51	99.81	99.65	99.07	100.12	99.67	99.54	99.93	99.81	100.2	99.03	100.09

LOD = Limit of detection

Depth (m)	-429.96	-419.69	-419.4	-399.95	-390.02	-369.99	-349.96	-340.08	-300.24	-294.12	-280.11	-240.22	-230.32	-209.8
Rock Type	Gabbro - norite	Gabbro - norite	Gabbro - norite	Gabbro - norite	Gabbro - norite	Anorthosite	Anorthosite	Gabbro - norite	Gabbro - norite	Gabbro - norite	Gabbro - norite	Anorthosite	Anorthosite	Gabbro - norite
Samples	**PAS16**	**PAS17**	**PAS18**	**PAS 19**	**PAS20**	**PAS21**	**PAS22**	**PAS23**	**PAS24**	**PAS25**	**PAS26**	**PAS27**	**PAS28**	**PAS29**
SiO_2	50.89	52.97	53	52.75	52.88	52.6	51.74	52.71	50.44	52.02	53.15	50.99	52.34	51.56
TiO_2	0.15	0.15	0.15	0.15	0.16	0.15	0.18	0.17	0.09	0.11	0.18	0.11	0.18	0.17
Al_2O_3	17.67	18.68	18.61	19.33	19.67	20.86	25.62	19.56	24.65	21.88	19.38	25.77	21.54	21.56
Fe_2O_3	6.38	5.89	6.26	5.89	5.75	5.24	3.56	6.5	3.69	4.66	6.31	3.07	5.41	5.23
MnO	0.13	0.12	0.12	0.11	0.11	0.1	0.06	0.12	0.07	0.1	0.12	0.06	0.1	0.1
MgO	9.58	9.15	9.49	8.74	8.2	7.47	3.59	9.1	4.76	7.36	8.92	3.7	7.05	6.95
CaO	11.08	11.58	11.02	11.09	11.23	11.43	12.23	10.29	12.31	11.29	10.3	12.7	11.15	11.09
Na_2O	1.78	1.78	1.79	1.9	2	2.12	2.6	1.78	2.43	1.98	1.92	2.67	2.12	2.14
K_2O	0.24	0.25	0.23	0.26	0.29	0.29	0.37	0.31	0.25	0.32	0.33	0.28	0.34	0.33
P_2O_5	0.01	0.01	0.01	0.01	0.01	0.01	0.03	0.01	LOD	LOD	0.01	0.01	0.02	0.02
Cr_2O_3	0.06	0.06	0.06	0.06	0.05	0.05	0.02	0.06	0.03	0.05	0.06	0.03	0.06	0.05
NiO	0.03	0.03	0.03	0.03	0.02	0.02	0.01	0.02	0.02	0.02	0.02	0.01	0.02	0.02
V_2O_5	0.02	0.02	0.02	0.02	0.02	0.01	0.01	0.01	0.01	0.01	0.01	0.01	0.01	0.01
ZrO_2	0.01	LOD	0.01	0.01	0.01	0.01	0.01	0.01	0.01	0.01	0.01	0.01	0.01	0.01
LOI	-0.06	0.02	-0.01	0.12	-0.06	0.1	0.17	0.05	0.03	0.82	-0.08	0.07	0.01	0.26
Total	97.97	100.88	100.87	100.57	100.37	100.47	100.45	100.74	98.8	100.62	100.64	99.48	100.36	99.48

LOD = Limit of detection

Depth (m)	-180.15	-139.9	-120	-109.77	-99.87	-90.05	-69.73	-60.84	-30.18	-9.91	0
Rock Type	Gabbro - norite	Anorthosite	Gabbro - norite	Gabbro - norite	Gabbro - norite	Anorthosite	Gabbro - norite	Gabbro - norite	Gabbro - norite	Anorthosite	Anorthosite
Samples	**PAS30**	**PAS31**	**PAS32**	**PAS33**	**PAS34**	**PAS35**	**PAS36**	**PAS37**	**PAS38**	**PAS39**	**PAS40**
SiO_2	51.15	52.37	51.6	51.17	51.44	49.94	51.92	49.73	50.03	48.82	48.43
TiO_2	0.2	0.12	0.19	0.11	0.17	0.17	0.18	0.19	0.09	0.07	0.04
Al_2O_3	18.39	22.46	16.45	20.47	16.87	26.51	21.2	23.61	28.09	28.69	30.87
Fe_2O_3	6.48	4.8	7.03	5.31	7.48	2.59	5.69	4.91	2.63	2.27	1.2
MnO	0.13	0.09	0.13	0.1	0.14	0.04	0.11	0.11	0.05	0.05	0.03
MgO	9.28	6.91	10.84	8.33	11.04	2.4	7.78	5	2.62	2.38	1.15
CaO	10.06	11.44	10.05	11.24	10.03	13.22	11.09	11.33	13.69	15.18	15.6
Na_2O	1.77	2.19	1.45	1.85	1.49	2.72	1.93	1.91	2.45	2.24	2.49
K_2O	0.31	0.25	0.28	0.19	0.22	0.42	0.32	0.24	0.25	0.17	0.15
P_2O_5	0.02	0.01	0.01	LOD	LOD	0.02	0.02	0.02	LOD	LOD	LOD
Cr_2O_3	0.07	0.05	0.09	0.07	0.09	0.02	0.07	0.03	0.02	0.02	0.01
NiO	0.03	0.03	0.03	0.02	0.03	0.01	0.02	0.01	0.01	0.01	0.01
V_2O_5	0.01	0.01	0.02	0.01	0.02	0.01	0.01	0.01	0.01	LOD	LOD
ZrO_2	0.01	LOD	0.01	0.01	LOD	0.01	0.01	0.01	0.01	0.01	0.01
LOI	0.11	0.04	0.04	-0.03	-0.16	0.11	0.09	3.08	0.06	0.19	0.13
Total	98.02	100.81	98.22	98.86	98.88	98.18	100.43	100.19	100	100.11	100.11

LOD = Limit of detection

Twickenham:

Depth(m)	-688.05	-668.74	-638.7	-608.6	-578.33	-548.57	-528.72	-498.59	-468.17	-448.42	-428.72	-392.68
Rock Type	Anorthosite	Gabbro - norite	Gabbro - norite	Gabbro - norite	Gabbro - norite	Gabbro - norite	Gabbro - norite	Gabbro - norite	Gabbro - norite	Gabbro - norite	Gabbro - norite	Gabbro - norite
Samples	**TW1**	**TW2**	**TW3**	**TW4**	**TW5**	**TW6**	**TW7**	**TW8**	**TW9**	**TW10**	**TW11**	**TW12**
SiO_2	51.67	49.72	52.41	51.59	51.97	52.47	52.49	53.23	52.09	51.56	51.48	52.12
TiO_2	0.17	0.09	0.19	0.16	0.09	0.16	0.16	0.18	0.15	0.15	0.14	0.14
Al_2O_3	20.4	28.77	15.93	19.05	23.45	17.47	17.77	18.46	17.26	17.71	18.15	22.92
Fe_2O_3	4.94	1.64	7.12	6.29	4.81	6.49	6.37	6.1	6.56	5.95	6.08	4.35
MnO	0.11	0.03	0.14	0.12	0.09	0.13	0.13	0.12	0.13	0.12	0.12	0.1
MgO	6.46	1.34	10.65	9.1	6.99	9.96	9.58	9.16	10.49	9.44	9.29	5.47
CaO	13.67	14.85	11.21	10.66	11.26	12.06	11.64	11.78	10.93	11.73	11.39	12.11
Na_2O	1.97	2.72	1.39	1.8	2.08	1.55	1.71	1.8	1.61	1.74	1.82	2.44
K_2O	0.31	0.3	0.32	0.29	0.2	0.22	0.26	0.31	0.25	0.26	0.24	0.34
P_2O_5	0.01	0.01	0.01	0.01	LOD	0.01	0.01	0.01	0.01	0.01	0.01	0.01
Cr_2O_3	0.05	0.01	0.07	0.04	0.04	0.06	0.06	0.06	0.06	0.06	0.06	0.04
NiO	0.02	LOD	0.03	0.02	0.02	0.03	0.03	0.03	0.03	0.03	0.02	0.01
V_2O_5	0.02	LOD	0.02	0.01	0.01	0.02	0.02	0.02	0.02	0.02	0.02	0.01
ZrO_2	0.01	0.01	0.01	0.01	LOD	0.01	0.01	0.01	0.01	0.01	0.01	0.01
LOI	0.12	0.24	0.38	-0.13	LOD	-0.11	-0.1	-0.07	-0.13	-0.07	-0.05	0.04
TOTAL	99.94	99.72	99.9	99.03	101.03	100.53	100.15	101.21	99.46	98.73	98.79	100.11

LOD = Limit of detection

Depth (m)	-372.41	-344.06	-262.32	-258.91	-249.89	-242.22	-183.9	-134.17	-124.2	-115.86	-91.26	-71.5
Rock Type	Gabbro - norite	Gabbro - norite	Gabbro - norite	Gabbro - norite	Gabbro - norite	Gabbro - norite	Gabbro - norite	Anorthosite	Anorthosite	Gabbro - norite	Gabbro - norite	Gabbro - norite
Samples	**TW13**	**TW14**	**TW15**	**TW16**	**TW17**	**TW18**	**TW19**	**TW20**	**TW21**	**TW22**	**TW23**	**TW24**
SiO_2	51.82	52.49	49.5	50.26	52.47	52.78	51.63	51.24	50.28	52.22	49.85	51.82
TiO_2	0.11	0.14	0.05	0.14	0.2	0.22	0.13	0.13	0.05	0.14	0.22	0.15
Al_2O_3	23.65	19.66	28.5	21.56	21.73	21.64	23.75	20.95	29.37	20.8	19.21	23.92
Fe_2O_3	4.1	6.13	1.57	5.8	5.33	5.39	4.33	5.27	1.5	6	6.99	4.31
MnO	0.08	0.12	0.04	0.1	0.1	0.1	0.08	0.1	0.03	0.11	0.12	0.08
MgO	5.69	9.15	1.67	6.94	6.57	6.61	5.49	8.13	1.6	8.34	8.5	5.53
CaO	12.04	10.4	12.86	12.78	11.12	11.06	11.99	11.23	13.76	11.12	12.42	12.09
Na_2O	2.34	1.77	3	1.92	2.17	2.18	2.43	1.89	2.78	1.87	2.09	2.25
K_2O	0.27	0.26	0.4	0.27	0.38	0.4	0.27	0.24	0.24	0.21	0.38	0.31
P_2O_5	0.01	0.01	LOD	LOD	0.03	0.03	0.01	0.01	LOD	LOD	LOD	0.01
Cr_2O_3	0.04	0.06	0.01	0.05	0.04	0.05	0.04	0.07	0.01	0.07	0.08	0.05
NiO	0.02	0.03	0.01	0.04	0.02	0.02	0.02	0.03	0.01	0.02	0.05	0.01
V_2O_5	0.01	0.01	LOD	LOD	0.01	0.01	0.01	0.01	LOD	0.01	LOD	0.01
ZrO_2	0.01	0.01	0.01	LOD	0.01	0.01	0.01	0.01	0.01	LOD	LOD	0.01
LOI	0.03	0.21	2.27	0.09	0.39	0.07	0.1	-0.03	0.05	-0.08	0.05	0.02
TOTAL	100.23	100.45	99.88	99.94	100.59	100.54	100.27	99.27	99.7	100.84	99.96	100.57

LOD = Limit of detection

Depth(m)	-40.23	-40.2	-19.34	0
Rock Type	Anorthosite	Anorthosite	Anorthosite	Gabbro - norite
Samples	**TW26**	**TW25**	**TW27**	**TW28**
SiO_2	49.59	48.78	48.62	50.64
TiO_2	0.12	0.08	0.08	0.08
Al_2O_3	27.9	27.77	29.58	22.88
Fe_2O_3	2.52	2.49	1.75	3.99
MnO	0.04	0.05	0.03	0.08
MgO	2.17	1.55	1.71	7.54
CaO	15.11	16.11	15.5	11.85
Na_2O	2.38	2.62	2.4	2
K_2O	0.25	0.32	0.19	0.16
P_2O_5	0.01	LOD	LOD	LOD
Cr_2O_3	0.02	0.02	0.01	0.12
NiO	0.01	0.02	LOD	0.02
V_2O_5	0.01	LOD	LOD	0.01
ZrO_2	0.01	LOD	0.01	0.01
LOI	0.16	0.15	0.17	0.07
TOTAL	100.28	99.95	100.06	99.46

LOD = Limit of detection

Standards of Deviation and limits of detection for the XRF data:

	Std. dev.(%)	**LOD**
SiO_2	0.4	0.02
TiO_2	0.03	0.0032
Al_2O_3	0.3	0.01
Fe_2O_3	0.3	0.0097
MnO	0.0065	0.0013
MgO	0.1	0.0118
CaO	0.07	0.01
Na_2O	0.11	0.0265
K_2O	0.06	0.005
P_2O_5	0.08	0.01
Cr_2O_3	0.0053	0.0006
NiO	0.01	0.0013
V_2O_5	0.0018	0.0008
ZrO_2	0.005	0.0009

Appendix B: Trace Element Data (XRF) *data given in parts per million (ppm)*

Paschaskraal:

Depth (m)	-760.24	-751.29	-730.19	-700.11	-680.17	-650.87	-619.84	-600.16
Rock Type	Gabbro - norite	Gabbro - norite	Gabbro - norite	Anorthosite	Gabbro - norite	Gabbro - norite	Gabbro - norite	Gabbro - norite
Samples	**PAS1**	**PAS2**	**PAS3**	**PAS4**	**PAS5**	**PAS6**	**PAS7**	**PAS8**
As	3	8	7	4	3	7	3	7
Cu	15	12	15	12	18	21	16	15
Ga	15	19	19	19	16	19	13	14
Mo	1	1	1	1	1	1	1	1
Nb	2	2	2	2	2	2	2	2
Ni	134	54	36	12	121	66	215	199
Pb	5	3	4	10	3	40	3	3
Rb	8	7	15	16	9	3	10	8
Sr	251	311	305	342	261	320	199	231
Th	3	3	3	3	3	3	3	3
U	3	3	3	3	3	3	3	3
W*	187	234	155	244	181	244	160	241
Y	8	6	7	7	8	5	11	7
Zn	40	25	27	18	41	71	52	50
Zr	26	21	31	32	28	21	32	23
Cl*	42	38	88	141	144	560	95	67
Co	54	46	34	37	50	47	62	72
Cr	100	33	23	7	164	54	391	267
F*	526	653	807	802	507	534	344	473
S*	16	16	16	16	31	51	27	21
Sc	11	4	5	1	15	3	23	16
V	72	31	34	17	74	26	123	83
Cs	9	9	9	9	9	9	9	9
Ba	104	111	164	141	110	83	100	93
La	10	9	14	12	10	12	14	11
Ce	5	5	8	8	5	5	5	5

Depth (m)	-580.22	-560	-539.82	-530.2	-489.98	-479.84	-470.02	-429.96
Rock Type	Gabbro - norite	Gabbro - norite	Gabbro - norite	Gabbro - norite	Gabbro - norite	Gabbro - norite	Gabbro - norite	Gabbro - norite
Samples	**PAS9**	**PAS10**	**PAS11**	**PAS12**	**PAS13**	**PAS14**	**PAS15**	**PAS16**
As	12	8	3	3	4	3	3	6
Cu	15	10	15	12	12	16	13	11
Ga	14	17	14	13	13	14	14	15
Mo	1	1	1	1	1	1	1	1
Nb	2	2	2	2	2	2	2	2
Ni	193	107	175	198	182	181	184	182
Pb	3	9	5	3	3	3	5	3
Rb	9	5	8	7	9	10	7	9
Sr	227	294	226	214	223	227	228	228
Th	3	3	3	3	3	3	3	3
U	3	3	3	3	3	3	3	3
W*	256	229	176	193	163	198	69	73
Y	7	5	9	11	8	8	8	6
Zn	51	32	41	42	42	43	43	46
Zr	27	17	26	25	25	29	19	23
Cl*	71	26	49	45	60	108	32	74
Co	76	54	60	62	59	63	55	51
Cr	279	175	379	403	329	310	325	341
F*	450	596	546	463	490	502	577	585
S*	16	16	16	16	19	24	16	16
Sc	14	7	17	23	16	19	18	18
V	84	43	103	134	112	106	99	99
Cs	9	9	9	9	9	9	9	9
Ba	103	90	97	82	92	100	90	98
La	14	17	7	10	11	10	16	11
Ce	5	5	5	5	5	5	5	5

Depth (m)	-419.69	-419.43	-399.95	-390.02	-369.99	-349.96	-340.08	-300.24
Rock Type	Gabbro - norite	Gabbro - norite	Gabbro - norite	Gabbro - norite	Anorthosite	Anorthosite	Gabbro - norite	Gabbro - norite
Samples	**PAS17**	**PAS18**	**PAS19**	**PAS20**	**PAS21**	**PAS22**	**PAS23**	**PAS24**
As	3	5	3	3	7	3	3	6
Cu	12	11	14	16	17	13	15	11
Ga	13	14	13	15	15	16	14	17
Mo	1	1	1	1	1	1	1	1
Nb	2	2	2	2	2	2	2	2
Ni	179	176	177	174	157	134	170	91
Pb	9	3	6	3	3	5	11	3
Rb	9	7	9	9	8	7	10	6
Sr	235	236	237	239	255	272	246	308
Th	3	3	3	3	3	3	3	3
U	3	3	3	3	3	3	3	3
W*	71	61	101	113	110	62	45	72
Y	8	8	9	7	8	7	9	6
Zn	53	43	46	47	42	36	45	29
Zr	24	22	23	28	24	20	28	17
Cl*	87	99	89	110	129	84	125	45
Co	47	47	51	52	48	37	46	31
Cr	350	346	317	324	292	268	346	170
F*	612	583	699	725	774	683	690	764
S*	16	16	16	20	17	16	16	16
Sc	17	17	15	17	14	12	15	7
V	101	97	90	93	79	63	85	39
Cs	9	9	9	9	9	9	9	9
Ba	101	97	95	98	93	101	119	97
La	9	15	12	11	8	11	12	9
Ce	5	5	5	5	5	5	5	5

Depth (m)	-294.12	-280.11	-240.22	-230.32	-209.84	-180.15	-139.9	-119.98
Rock Type	Gabbro - norite	Gabbro - norite	Anorthosite	Anorthosite	Gabbro - norite	Gabbro - norite	Anorthosite	Gabbro - norite
Samples	**PAS25**	**PAS26**	**PAS27**	**PAS28**	**PAS29**	**PAS30**	**PAS31**	**PAS32**
As	3	3	5	3	9	4	3	3
Cu	8	19	10	17	17	14	17	18
Ga	14	14	18	16	16	15	18	12
Mo	1	1	1	1	1	1	1	1
Nb	3	2	2	3	2	2	2	3
Ni	143	180	69	132	151	204	65	230
Pb	3	3	3	7	4	5	7	4
Rb	10	11	4	10	11	12	13	10
Sr	279	238	321	266	268	228	333	207
Th	3	3	3	3	3	3	3	3
U	3	3	3	3	3	3	3	3
W*	74	75	80	79	119	113	84	110
Y	6	8	6	8	8	9	8	9
Zn	38	47	25	38	46	63	29	50
Zr	18	31	16	30	30	34	29	33
Cl*	239	126	32	105	136	280	146	167
Co	47	47	26	43	45	52	30	56
Cr	309	354	143	293	301	403	109	534
F*	973	650	738	711	414	201	936	422
S*	16	16	16	16	1852	16	26	70
Sc	12	15	5	14	12	15	5	17
V	60	87	34	69	67	86	38	106
Cs	9	9	9	9	9	9	9	9
Ba	104	118	119	139	108	104	138	100
La	15	12	11	12	14	8	12	9
Ce	5	5	5	5	5	5	5	5

Depth (m)	-109.77	-99.87	-90.05	-69.73	-60.84	-30.18	-9.91	0
Rock Type	Gabbro - norite	Gabbro - norite	Anorthosite	Gabbro - norite	Gabbro - norite	Gabbro - norite	Anorthosite	Anorthosite
Samples	**PAS33**	**PAS34**	**PAS35**	**PAS36**	**PAS37**	**PAS38**	**PAS39**	**PAS40**
As	3	3	3	7	3	3	3	9
Cu	12	24	13	19	6	9	12	9
Ga	15	12	18	13	15	18	17	17
Mo	1	1	1	1	1	1	1	1
Nb	2	2	2	2	2	2	2	2
Ni	170	228	45	162	107	44	52	30
Pb	11	9	7	4	5	10	5	11
Rb	6	7	12	10	7	5	6	3
Sr	258	213	330	258	242	335	328	349
Th	3	5	3	3	3	3	3	3
U	3	3	3	3	3	3	3	3
W*	102	105	112	149	29	123	155	128
Y	7	10	7	9	7	6	6	4
Zn	38	55	25	47	36	24	24	20
Zr	19	25	34	33	34	17	18	12
Cl*	66	44	109	197	576	141	84	8
Co	46	57	26	51	29	31	34	23
Cr	388	557	95	412	218	97	87	42
F*	357	220	715	477	100	537	542	744
S*	74	115	16	63	83	16	772	126
Sc	11	17	5	13	9	2	3	1
V	67	107	34	84	61	32	20	17
Cs	9	9	9	9	9	9	9	9
Ba	86	89	162	111	82	106	88	84
La	13	11	12	10	11	11	8	6
Ce	5	5	5	5	5	5	5	5

Twickenham:

Depth (m)	-688.05	-668.74	-638.7	-608.6	-578.33	-548.57	-528.72
Rock Type	Anorthosite	Gabbro - norite	Gabbro - norite	Gabbro - norite	Gabbro - norite	Gabbro - norite	Gabbro - norite
Samples	**TW1**	**TW2**	**TW3**	**TW4**	**TW5**	**TW6**	**TW7**
As	9	3	3	3	3	6	3
Cu	14	14	22	14	12	14	15
Ga	14	21	12	14	16	13	13
Mo	1	1	1	1	1	1	1
Nb	2	2	4	2	2	3	2
Ni	134	29	231	199	135	208	198
Pb	7	3	13	4	3	3	3
Rb	9	7	12	10	5	7	10
Sr	239	342	187	231	275	209	218
Th	3	3	3	3	3	3	3
U	3	3	3	3	3	3	3
W*	102	269	121	227	139	200	148
Y	10	4	10	7	4	10	9
Zn	41	19	54	50	40	49	47
Zr	29	20	33	29	16	25	27
Cl*	65	40	495	45	8	37	47
Co	40	42	56	65	48	63	57
Cr	269	27	398	271	172	373	334
F*	536	832	604	467	666	493	452
S*	450	163	622	200	83	140	467
Sc	18	3	22	16	8	21	19
V	101	17	131	88	47	124	115
Cs	9	9	9	9	9	9	9
Ba	110	101	88	88	85	79	85
La	9	10	12	7	10	9	9
Ce	5	5	5	5	5	5	5

Depth (m)	-498.59	-468.17	-448.42	-428.72	-392.68	-372.41	-344.06	-262.32
Rock Type	Gabbro - norite	Gabbro - norite	Gabbro - norite	Gabbro - norite	Gabbro - norite	Gabbro - norite	Gabbro - norite	Gabbro - norite
Samples	**TW8**	**TW9**	**TW10**	**TW11**	**TW12**	**TW13**	**TW14**	**TW15**
As	3	3	3	6	7	4	3	6
Cu	14	12	11	12	13	12	14	5
Ga	14	12	13	14	16	16	14	17
Mo	1	1	1	1	1	1	2	1
Nb	2	3	2	2	2	2	2	2
Ni	187	228	201	188	112	119	188	41
Pb	3	3	3	4	6	7	7	5
Rb	8	9	9	9	10	7	8	9
Sr	221	208	216	226	281	286	240	356
Th	3	3	3	3	3	3	3	3
U	3	3	3	3	3	3	3	3
W*	196	247	210	102	121	170	73	113
Y	10	7	8	7	8	6	8	4
Zn	45	49	42	47	32	34	48	22
Zr	31	26	25	24	28	21	26	11
Cl*	83	40	40	27	107	27	68	289
Co	61	71	65	50	39	46	48	22
Cr	320	359	364	349	210	208	352	52
F*	539	427	491	456	668	648	410	540
S*	93	471	467	98	301	321	396	489
Sc	19	20	20	17	9	9	13	3
V	110	116	109	99	61	52	79	17
Cs	9	9	9	9	9	9	9	9
Ba	94	77	86	88	115	98	102	105
La	8	9	10	10	12	13	13	6
Ce	5	5	5	5	5	5	5	5

Depth (m)	-258.91	-249.89	-242.22	-183.9	-134.17	-124.2	-115.86	-91.26
Rock Type	Gabbro - norite	Gabbro - norite	Gabbro - norite	Gabbro - norite	Anorthosite	Anorthosite	Gabbro - norite	Gabbro - norite
Samples	**TW16**	**TW17**	**TW18**	**TW19**	**TW20**	**TW21**	**TW22**	**TW23**
As	3	3	3	3	8	7	10	3
Cu	12	18	17	13	11	6	14	16
Ga	15	15	15	17	16	18	14	16
Mo	1	1	1	1	1	1	1	1
Nb	2	2	2	2	2	2	2	2
Ni	140	130	127	105	160	28	159	160
Pb	3	5	8	3	3	3	5	9
Rb	7	12	14	6	7	4	6	10
Sr	266	277	266	291	257	356	260	257
Th	3	3	3	3	3	3	3	3
U	3	3	3	3	3	3	3	3
W*	87	89	96	82	81	102	99	61
Y	7	8	10	6	6	4	8	9
Zn	40	41	39	34	42	19	45	42
Zr	22	35	37	23	23	13	22	29
Cl*	39	133	159	48	20	8	24	106
Co	42	42	42	35	41	23	47	41
Cr	278	265	270	194	381	40	380	422
F*	369	712	576	660	409	776	440	574
S*	459	494	92	124	334	392	407	85
Sc	10	13	10	7	11	1	12	13
V	60	68	73	46	67	17	76	80
Cs	9	9	9	9	9	9	9	9
Ba	99	133	135	104	93	95	95	120
La	16	11	10	10	11	5	9	16
Ce	5	5	5	5	5	5	5	5

Depth (m)	-71.5	-40.23	-40.2	-19.34	0
Rock Type	Gabbro - norite	Anorthosite	Anorthosite	Anorthosite	Gabbro - norite
Samples	**TW24**	**TW26**	**TW25**	**TW27**	**TW28**
As	3	3	3	3	3
Cu	14	19	13	9	34
Ga	16	18	17	17	14
Mo	1	1	1	1	1
Nb	2	2	2	2	2
Ni	112	42	33	31	164
Pb	3	3	10	5	6
Rb	7	6	5	7	4
Sr	291	324	344	340	305
Th	3	3	3	3	3
U	3	3	3	3	3
W*	162	157	106	72	116
Y	7	6	5	5	6
Zn	35	23	22	17	30
Zr	26	24	17	16	13
Cl*	59	67	36	24	35
Co	44	34	26	20	43
Cr	290	84	48	62	711
F*	745	760	734	764	521
S*	397	95	243	67	499
Sc	9	6	4	1	10
V	59	37	21	17	38
Cs	9	9	9	9	9
Ba	112	119	111	105	88
La	12	13	7	10	8
Ce	5	5	5	5	5

Standards of Deviation and limits of detection for the XRF data:

	std dev.(ppm)	LOD (ppm)
As*	10	3
Cu	3	2
Ga	2	2
Mo	1	1
Nb	3	2
Ni	6	3
Pb	3	3
Rb	4	2
Sr	4	3
Th	2	3
U	2	3
W*	10	6
Y	4	3
Zn	4	4
Zr	6	10
Ba	14	5
Ce	14	6
Cl*	100	11
Co	6	3
Cr	40	15
F*	500	400
La	24	5
S*	300	40
Sc	5	1
V	10	1
Cs	5	10
Ba	14	5
La	24	5
Ce	14	6

Values for elements indicated with an * should be considered semi-quantitative.

Blank and certified reference materials are analysed with each batch of samples and the first two columns represent one of these. Results for elements indicated with an * was pressed in a powder briquette for trace element analyses

Appendix C: XRD Data *data given in weight fraction*

Paschaskraal:

Samples	PAS1	PAS2	PAS3	PAS4	PAS5	PAS6	PAS7	PAS8	PAS9	PAS10	PAS11	PAS12	PAS13	PAS14
Biotite	1.58	LOD	LOD	LOD	2.78	1.9	5.85	5.21	8.3	LOD	5.34	7.59	8.02	7.05
Calcite	1.91	2.2	1.64	2.27	2.24	2.99	2.52	1.93	1.83	2.53	1.6	2.55	1.46	1.72
Chlorite	LOD	3.15	1.92	LOD	2.59	4.6	LOD	LOD	LOD	LOD	LOD	LOD	LOD	LOD
Diopside	12.41	7.64	8.35	2.76	12.53	2.37	22.28	10.02	10.69	8.58	17.24	23.45	15.57	17.46
Enstatite	21.6	12.9	9.81	4.92	19.46	4.9	22.05	28.94	30.29	19.99	23.17	20.36	24.64	23.85
Magnetite	LOD	LOD	LOD	LOD	LOD	LOD	LOD	LOD	LOD	LOD	LOD	LOD	LOD	LOD
Hornblende	LOD	LOD	0.65	LOD	0.72	0.15	0.86	LOD	LOD	LOD	LOD	LOD	LOD	LOD
Microcline	2.78	2.72	2.09	1.86	2.29	2.28	2.8	2.14	1.97	2.07	2.25	2.95	1.97	0.79
Plagioclase	56	69.11	71.95	82.86	52.94	75.3	38.3	49.59	44.75	65.57	48.31	41.15	43.87	46.67
Quartz	2.3	2.28	3.58	5.33	2.45	5.62	2.07	2.17	2.17	1.27	2.08	1.96	1.87	2.47
Talc	1.42	LOD	LOD	LOD	2.01	2.91	3.26	LOD	LOD	LOD	LOD	LOD	2.61	LOD
Samples	**PAS15**	**PAS16**	**PAS17**	**PAS18**	**PAS19**	**PAS20**	**PAS21**	**PAS22**	**PAS23**	**PAS24**	**PAS25**	**PAS26**	**PAS27**	**PAS28**
Biotite	1.55	1.17	1.47	2.7	1.08	0.59	0.37	0.34	2.34	0.48	1.46	5.51	0.95	2.02
Calcite	2.04	1.23	1.95	1.77	1.41	1.49	LOD	2.4	2.05	1.91	3.18	1.55	2.1	2.19
Chlorite	LOD	LOD	LOD	LOD	LOD	LOD	LOD	LOD	LOD	LOD	3.09	LOD	LOD	LOD
Diopside	13.15	13.64	16.36	15.32	11.51	14.42	10.51	8.9	10.66	7.73	9.38	8.9	6.17	10.17
Enstatite	30.25	25.89	21.17	26.18	23.85	25.48	21.63	21.13	27.62	22.72	21.02	26.77	15.1	23.81
Magnetite	1.45	2.36	1.12	1.17	LOD	LOD	LOD	LOD	1.84	LOD	1.99	LOD	1.71	1.02
Hornblende	LOD	LOD	LOD	LOD	LOD	LOD	LOD	LOD	1.08	LOD	0.86	LOD	LOD	LOD
Microcline	2.98	2.12	2.68	2.27	1.62	1.06	2.71	0.61	1.91	1.8	3.54	1.95	1.77	1.5
Plagioclase	44.08	47.37	49.82	45.53	56.22	54.36	61.94	61.14	47.01	63.03	49.43	51.25	68.98	54.86
Quartz	2.71	2.34	2.65	2.71	2.13	2.59	2.84	3.3	3	2.32	4.24	2.6	3.22	4.43
Talc	1.77	3.88	2.77	2.37	2.18	LOD	LOD	2.18	2.5	LOD	1.79	1.47	LOD	LOD

LOD = Limit of detection

Samples	PAS29	PAS30	PAS31	PAS32	PAS33	PAS34	PAS35	PAS36	PAS37	PAS38	PAS39	PAS40
Biotite	1.53	1.83	1.79	1.19	LOD	1.22	0.87	1.52	3.55	0.66	LOD	LOD
Calcite	1.93	1.79	2.12	0.98	1.37	1.49	2.03	1.91	4.46	1.95	2.12	2.27
Chlorite	LOD	LOD	LOD	LOD	LOD	LOD	LOD	LOD	8.62	LOD	LOD	LOD
Diopside	9.22	11.37	5	10.9	13.23	13.15	6.04	10.26	2.82	5.48	3.46	2.51
Enstatite	23.89	27.79	17.36	31.37	26.36	32.72	13.68	25.96	1.7	13.04	14.2	8.81
Magnetite	LOD	1.8	LOD	2.11	1.97	2.88	LOD	1.77	1.9	2	1.44	0.91
Hornblende	LOD	LOD	LOD	LOD	LOD	LOD	LOD	LOD	2.11	LOD	LOD	LOD
Microcline	1.75	LOD	1.69	1.33	2.01	2.58	2.88	2.75	LOD	2.4	2.63	2.03
Plagioclase	57.05	48.18	68.26	46.12	53.28	41.96	70.1	50.85	54.64	72.91	73.18	82.46
Quartz	3.25	3.78	3.77	2.81	1.32	1.79	4.41	3.03	15.17	1.56	2.96	1.01
Talc	1.38	3.46	LOD	3.2	3.46	2.21	LOD	1.95	5.02	LOD	LOD	LOD

Twickenham:

Samples	TW1	TW2	TW3	TW4	TW5	TW6	TW7	TW8	TW9	TW10	TW11
Biotite	7.81	LOD	2.78	3.42	4.02	2.34	5.41	7.89	5.31	8.21	8.3
Calcite	2.52	2.73	1.77	1.47	1.75	1.29	1.33	0.96	1.38	0.95	1.53
Chlorite	LOD	LOD	LOD	LOD	LOD	LOD	LOD	LOD	LOD	LOD	LOD
Diopside	23.45	4.87	15.43	12.09	5.44	20.3	18.08	16.15	15.84	14.41	18.35
Enstatite	12.02	11.27	27.18	29.58	28.7	27.53	24.68	26.18	29.18	24.79	22.46
Hornblende	LOD	LOD	5.79	LOD	LOD	LOD	LOD	LOD	LOD	LOD	LOD
Lizardite	LOD	LOD	1.3	LOD	LOD	LOD	LOD	LOD	LOD	LOD	LOD
Microcline	2.64	1.22	2.13	1.11	2.76	1.19	1.51	1.07	1.09	1.53	3.42
Plagioclase	47.1	75.6	36.41	47.92	52.05	41.94	44.66	45.37	42.93	45.75	39.18
Prehnite	0.83	1.69	0.19	1.87	4.06	3.79	2.71	LOD	2.38	2.63	3.92
Quartz	2.54	2.62	2.9	2.55	1.22	1.61	1.63	2.38	1.9	1.72	1.52
Talc c-1	1.11	LOD	4.14	LOD	LOD	LOD	LOD	LOD	LOD	LOD	1.32

LOD = Limit of detection

Samples	TW12	TW13	TW14	TW16	TW17	TW18	TW19	TW20	TW21	TW22	TW23
Biotite	6.9	0.65	4.89	7.54	6.42	1.76	2.39	10.5	LOD	6.25	4.86
Calcite	2.37	1.67	1.84	2.3	1.79	2.17	1.87	1.25	2.47	1.95	2.53
Chlorite	LOD	LOD	LOD	LOD	LOD	LOD	LOD	LOD	1.44	LOD	LOD
Diopside	10.93	10	10.5	8.67	9.61	10.6	7.6	8.51	3.11	10.3	11.82
Enstatite	17.75	21.08	27.3	20.8	22.06	20.5	17	22.4	9.56	25.7	22.3
Hornblende	LOD	0.9	LOD	LOD	LOD	LOD	LOD	LOD	LOD	LOD	LOD
Lizardite	LOD	LOD	LOD	LOD	LOD	LOD	LOD	LOD	LOD	LOD	LOD
Microcline	1.76	0.92	1.47	LOD	2.12	1.69	LOD	1.39	2.34	1.71	1.6
Plagioclase	55.6	42.93	46.3	53.2	51.6	56.6	62.6	51.7	76.89	47	49.38
Prehnite	1.33	4.04	3.2	3.93	2.35	0.34	3.14	2.57	2.07	3.26	3.02
Quartz	3.06	2.22	2.23	2.51	2.6	4.62	2.24	1.67	1.33	1.39	2.16
Talc c-1	LOD	LOD	2.35	1.07	1.46	1.7	3.19	LOD	0.79	2.51	2.33

Samples	TW24	TW25	TW26	TW27	TW28
Biotite	4.28	2.52	0.82	0.79	LOD
Calcite	2.01	2.5	2.36	2.51	1.98
Chlorite	LOD	LOD	LOD	3.02	LOD
Diopside	9.88	3.58	6.16	3.92	7.93
Enstatite	20.5	11.2	7	9.5	28.3
Hornblende	LOD	LOD	1.06	LOD	LOD
Lizardite	LOD	LOD	LOD	LOD	LOD
Microcline	1.42	2.93	3.21	2.31	1.43
Plagioclase	56.7	71.1	71.62	70.8	59.9
Prehnite	3.29	3.8	5.24	4.48	LOD
Quartz	1.88	1.79	2.54	2.18	0.47
Talc c-1	LOD	0.6	LOD	0.49	LOD

LOD = Limit of detection

XRD Errors:

Paschaskraal:

Samples	PAS1	PAS2	PAS3	PAS4	PAS5	PAS6	PAS7	PAS8	PAS9	PAS10	PAS11	PAS12	PAS13	PAS14
Biotite	1.58	LOD	LOD	LOD	2.16	0.75	1.35	0.87	1.56	LOD	1.41	0.99	1.59	1.44
Calcite	0.39	0.48	0.39	0.54	0.42	0.54	0.42	0.39	0.36	0.51	0.36	0.45	0.36	0.33
Chlorite	LOD	0.78	0.57	LOD	0.96	3.9	LOD	LOD	LOD	LOD	LOD	LOD	LOD	LOD
Diopside	0.9	0.99	0.99	0.96	0.93	0.81	0.99	0.9	0.87	1.02	0.87	0.9	0.9	0.87
Enstatite	1.35	1.11	1.23	0.96	1.32	0.93	1.02	1.11	1.2	1.11	1.11	1.05	1.17	1.05
Magnetite	LOD	LOD	LOD	LOD	LOD	LOD	LOD	LOD	LOD	LOD	LOD	LOD	LOD	LOD
Hornblende	LOD	LOD	0.54	LOD	0.66	0.54	0.54	LOD	LOD	LOD	LOD	LOD	LOD	LOD
Microcline	0.84	0.93	0.93	1.05	0.78	0.9	0.72	0.72	0.75	0.84	0.69	0.66	0.72	0.6
Plagioclase	1.56	1.56	1.59	1.5	1.92	3.6	1.23	1.26	1.38	1.41	1.35	1.17	1.41	1.35
Quartz	0.33	0.36	0.45	0.51	0.3	0.57	0.3	0.29	0.28	0.29	0.33	0.26	0.29	0.3
Talc	1.23	LOD	LOD	LOD	0.96	1.68	0.78	LOD	LOD	LOD	LOD	LOD	1.26	LOD

Samples	PAS15	PAS16	PAS17	PAS18	PAS19	PAS20	PAS21	PAS22	PAS23	PAS24	PAS25	PAS26
Biotite	0.51	0.6	0.51	0.48	LOD	0.45	0.75	0.51	1.77	0.72	LOD	LOD
Calcite	0.54	0.42	0.36	0.3	0.36	0.36	0.48	0.39	0.63	0.48	0.48	0.51
Chlorite	LOD	LOD	LOD	LOD	LOD	LOD	LOD	LOD	1.77	LOD	LOD	LOD
Diopside	1.14	0.93	0.9	0.81	1.05	0.9	0.78	0.93	0.96	1.2	0.96	1.02
Enstatite	1.2	1.14	1.14	0.99	1.2	1.26	1.26	1.23	1.59	1.47	1.5	1.68
Magnetite	0.42	LOD	0.42	0.36	0.45	0.51	LOD	0.36	0.39	0.63	0.39	0.45
Hornblende	LOD	LOD	LOD	LOD	LOD	LOD	LOD	LOD	0.96	LOD	LOD	LOD
Microcline	0.9	0.75	LOD	0.6	0.81	0.96	1.02	0.87	LOD	0.96	1.05	1.05
Plagioclase	1.5	1.38	1.26	1.2	1.47	1.29	1.65	1.41	2.13	1.71	1.68	1.95
Quartz	0.42	0.36	0.36	0.3	0.27	0.3	0.48	0.33	1.08	0.33	0.39	0.33
Talc	LOD	0.81	1.05	0.84	1.38	0.99	LOD	0.93	1.44	LOD	LOD	LOD

LOD = Limit of detection

Twickenham:

Samples	TW1	TW2	TW3	TW4	TW5	TW6	TW7	TW8	TW9	TW10
Biotite	0.96	LOD	0.63	2.22	2.58	0.99	1.44	1.53	0.75	0.75
Calcite	0.42	0.54	0.36	0.33	0.39	0.3	0.3	0.3	0.3	0.3
Chlorite	LOD	LOD	LOD	LOD	LOD	LOD	LOD	LOD	LOD	LOD
Diopside	0.96	0.72	0.75	0.87	0.75	0.93	0.93	0.78	0.84	0.75
Enstatite	0.84	1.14	0.99	1.17	1.47	1.05	1.02	0.93	1.02	0.93
Hornblende	LOD	LOD	0.69	LOD	LOD	LOD	LOD	LOD	LOD	LOD
Lizardite	LOD	LOD	0.51	LOD	LOD	LOD	LOD	LOD	LOD	LOD
Microcline	0.84	0.87	0.6	0.57	0.87	0.57	0.57	0.54	0.54	0.57
Plagioclase	1.2	1.56	1.08	1.56	2.01	1.14	1.2	1.26	1.11	1.11
Prehnite	0.42	0.78	0.33	0.78	1.08	0.87	0.75	0	0.78	0.78
Quartz	0.29	0.36	0.26	0.29	1.63	0.21	0.22	0.29	0.24	0.24
Talc	0.66	LOD	0.72	LOD	LOD	LOD	LOD	LOD	LOD	LOD

LOD = Limit of detection

Samples	TW12	TW13	TW14	TW16	TW17	TW18	TW19	TW20	TW21	TW22
Biotite	1.38	1.53	0.36	0.99	1.65	1.26	0.54	1.23	1.83	LOD
Calcite	0.33	0.45	0.36	0.3	0.42	0.36	0.48	0.39	0.36	0.6
Chlorite	LOD	LOD	LOD	LOD	LOD	LOD	LOD	LOD	LOD	1.89
Diopside	0.87	0.93	0.99	0.81	0.93	0.9	1.08	1.08	0.96	1.05
Enstatite	1.11	1.14	1.02	1.14	1.08	1.14	1.26	1.47	1.14	1.35
Hornblende	LOD	LOD	0.63	LOD	LOD	LOD	LOD	LOD	LOD	LOD
Lizardite	LOD	LOD	LOD	LOD	LOD	LOD	LOD	LOD	LOD	LOD
Microcline	1.44	0.78	0.69	1.14	LOD	0.84	0.81	LOD	0.69	1.05
Plagioclase	1.32	1.53	1.53	1.38	1.56	1.47	1.47	1.77	1.62	2.43
Prehnite	0.63	0.57	0.93	0.63	1.05	0.69	0.6	1.08	0.87	0.87
Quartz	0.26	0.36	0.33	0.33	0.33	0.33	0.45	0.28	0.226	0.33
Talc	0.66	LOD	LOD	0.9	0.6	0.87	0.9	1.11	LOD	1.08

Samples	TW24	TW25	TW26	TW27	TW28	TW24	TW25
Biotite	1.5	0.78	1.14	0.84	0.6	0.69	0.99
Calcite	0.36	0.42	0.36	0.54	0.51	0.51	0.3
Chlorite	LOD	LOD	LOD	LOD	LOD	0.99	LOD
Diopside	0.84	0.84	0.87	1.05	0.6	1.26	0.81
Enstatite	1.26	1.08	1.08	1.35	0.9	1.59	1.14
Hornblende	LOD	LOD	LOD	LOD	0.63	LOD	LOD
Lizardite	LOD	LOD	LOD	LOD	LOD	LOD	LOD
Microcline	0.72	0.78	0.66	1.68	1.05	1.29	1.14
Plagioclase	1.5	1.35	1.47	2.19	1.77	2.4	1.38
Prehnite	1.02	0.63	0.87	1.05	1.32	1.47	0.63
Quartz	0.23	0.3	0.3	0.36	0.39	0.42	0.33
Talc	0.99	0.81	LOD	0.69	LOD	0.84	0.9

LOD = Limit of detection

Appendix D: CIPW Data *data given in weight percentage (wt %)*

Paschaskraal:

Depth (m)	-760.24	-751.29	-730.19	-700.11	-680.17	-650.87	-619.84	-600.16	-580.22	-560	-539.82	-530.2
Samples	**PAS1**	**PAS2**	**PAS3**	**PAS4**	**PAS5**	**PAS6**	**PAS7**	**PAS8**	**PAS9**	**PAS10**	**PAS11**	**PAS12**
Q	4.037	2.217	2.593	1.459	3.825	0.57	5.293	5.645	6.266	2.982	4.981	5.72
Or	1.548	1.596	2.919	2.949	1.607	0.963	1.791	1.418	1.602	1.194	1.418	1.182
Ab	17.82	22.83	24.209	25.876	19.326	26.908	12.836	14.453	14.859	18.886	14.909	13.31
An	48.928	61.374	59.637	66.119	50.02	60.632	37.614	44.321	42.56	56.275	42.45	39.023
Ne	LOD	LOD	LOD	LOD	LOD	LOD	LOD	LOD	LOD	LOD	LOD	LOD
Wo	LOD	LOD	LOD	0.098	LOD	LOD	LOD	LOD	LOD	LOD	LOD	LOD
Di(FS)	LOD	LOD	LOD	LOD	LOD	LOD	LOD	LOD	LOD	LOD	LOD	LOD
Di(MS)	9.964	3.553	4.503	1.424	9.663	2.779	17.043	5.54	6.405	5.189	13.233	19.276
Hy(MS)	12.193	5.422	2.829	LOD	10.356	5.287	18.1	21.831	21.318	11.433	16.564	15.025
Ol(MS)	LOD	LOD	LOD	LOD	LOD	LOD	LOD	LOD	LOD	LOD	LOD	LOD
Mt	LOD	LOD	LOD	LOD	LOD	LOD	LOD	LOD	LOD	0.03	LOD	LOD
Il	0.216	0.107	0.107	0.043	0.195	0.066	0.304	0.257	0.278	0.154	0.257	0.278
Hm	5.178	2.748	2.851	1.223	4.819	2.68	6.919	6.501	6.681	3.859	6.129	6.153
Tn	0.092	0.132	0.282	0.595	0.168	0.116	0.054	0.012	0.009	LOD	0.037	0.033
Pf	LOD	LOD	LOD	LOD	LOD	LOD	LOD	LOD	LOD	LOD	LOD	LOD
Ap	0.023	0.023	0.07	0.213	0.023	LOD	0.046	0.023	0.023	LOD	0.023	LOD

LOD = Limit of detection

Depth (m)	-489.98	-479.84	-470.02	-429.96	-419.69	-419.43	-399.95	-390.02	-369.99	-349.96	-340.08	-300.24
Samples	**PAS13**	**PAS14**	**PAS15**	**PAS16**	**PAS17**	**PAS18**	**PAS19**	**PAS20**	**PAS21**	**PAS22**	**PAS23**	**PAS24**
Q	4.054	5.115	6.677	5.041	6.465	6.627	6.387	6.44	5.747	4.464	6.992	3.086
Or	1.359	1.613	1.436	1.466	1.466	1.371	1.554	1.702	1.702	2.163	1.797	1.513
Ab	15.544	16.06	14.706	15.366	14.969	15.011	16.035	16.83	17.854	21.992	14.952	20.85
An	41.231	40.446	41.201	40.369	42.007	41.781	43.346	43.742	46.454	57.172	44.246	56.332
Ne	LOD	LOD	LOD	LOD	LOD	LOD	LOD	LOD	LOD	LOD	LOD	LOD
Wo	LOD	LOD	LOD	LOD	LOD	LOD	LOD	LOD	LOD	LOD	LOD	LOD
Di(FS)	LOD	LOD	LOD	LOD	LOD	LOD	LOD	LOD	LOD	LOD	LOD	LOD
Di(MS)	13.316	14.018	10.329	12.224	11.717	9.696	8.91	9.048	7.722	2.276	4.898	4.243
Hy(MS)	17.902	16.282	19.123	18.713	17.222	18.991	17.584	16.158	14.976	7.894	20.273	10.036
Ol(MS)	LOD	LOD	LOD	LOD	LOD	LOD	LOD	LOD	LOD	LOD	LOD	LOD
Mt	LOD	LOD	LOD	LOD	LOD	LOD	LOD	LOD	LOD	LOD	LOD	LOD
Il	0.278	0.259	0.269	0.28	0.257	0.261	0.246	0.24	0.218	0.133	0.259	0.148
Hm	6.261	6.097	6.241	6.521	5.859	6.217	5.879	5.728	5.231	3.556	6.461	3.736
Tn	0.033	0.088	0.005	0.004	0.027	0.033	0.048	0.091	0.076	0.278	0.093	0.045
Pf	LOD	LOD	LOD	LOD	LOD	LOD	LOD	LOD	LOD	LOD	LOD	LOD
Ap	0.023	0.023	0.014	0.016	0.014	0.014	0.014	0.023	0.021	0.074	0.032	0.012

LOD = Limit of detection

Depth (m)	-294.12	-280.11	-240.22	-230.32	-209.84	-180.15	-139.9	-119.98	-109.77	-99.87	-90.05	-69.73
Samples	**PAS25**	**PAS26**	**PAS27**	**PAS28**	**PAS29**	**PAS30**	**PAS31**	**PAS32**	**PAS33**	**PAS34**	**PAS35**	**PAS36**
Q	5.439	7.033	2.867	5.84	5.282	6.297	5.158	7.192	5.123	6.457	2.134	5.611
Or	1.915	1.927	1.69	1.986	1.974	1.844	1.448	1.672	1.158	1.294	2.518	1.873
Ab	16.822	16.136	22.745	17.93	18.235	15.358	18.421	12.557	15.849	12.726	23.464	16.255
An	50	43.032	57.847	48.114	48.686	42.25	50.4	38.302	47.566	39.157	60.091	48.158
Ne	LOD	LOD	LOD	LOD	LOD	LOD	LOD	LOD	LOD	LOD	LOD	LOD
Wo	LOD	LOD	LOD	LOD	LOD	LOD	LOD	LOD	LOD	LOD	LOD	LOD
Di(FS)	LOD	LOD	LOD	LOD	LOD	LOD	LOD	LOD	LOD	LOD	LOD	LOD
Di(MS)	4.809	5.841	4.165	5.237	5.045	6.578	4.574	9.587	6.916	8.644	4.831	4.964
Hy(MS)	16.143	19.365	7.34	15.077	15.111	20.583	14.974	23.101	17.796	23.812	3.863	17.034
Ol(MS)	LOD	LOD	LOD	LOD	LOD	LOD	LOD	LOD	LOD	LOD	LOD	LOD
Mt	0.003	LOD	LOD	LOD	LOD	LOD	LOD	LOD	0.006	LOD	LOD	LOD
Il	0.201	0.257	0.124	0.212	0.207	0.284	0.186	0.289	0.218	0.304	0.096	0.227
Hm	4.667	6.275	3.092	5.397	5.278	6.628	4.772	7.174	5.367	7.561	2.639	5.681
Tn	LOD	0.108	0.117	0.168	0.142	0.133	0.054	0.103	LOD	0.037	0.308	0.156
Pf	LOD	LOD	LOD	LOD	LOD	LOD	LOD	LOD	LOD	LOD	LOD	LOD
Ap	0.002	0.028	0.014	0.042	0.039	0.046	0.014	0.025	0.002	0.009	0.056	0.042

LOD = Limit of detection

Depth (m)	-60.84	-30.18	-9.91	0
Samples	**PAS37**	**PAS38**	**PAS39**	**PAS40**
Q	6.458	2.235	0.673	LOD
Or	1.43	1.477	1.034	0.875
Ab	16.619	20.773	19.005	20.244
An	56.858	64.958	67.771	72.674
Ne	LOD	LOD	LOD	0.434
Wo	LOD	LOD	LOD	LOD
Di(FS)	LOD	LOD	LOD	LOD
Di(MS)	0.545	2.199	5.892	3.679
Hy(MS)	12.577	5.514	3.201	LOD
Ol(MS)	LOD	LOD	LOD	0.815
Mt	LOD	LOD	LOD	LOD
Il	0.242	0.098	0.101	0.058
Hm	5.058	2.629	2.269	1.205
Tn	0.159	0.104	0.049	LOD
Pf	LOD	LOD	LOD	0.011
Ap	0.056	0.012	0.005	LOD

LOD = Limit of detection

Twickenham:

Depth (m)	-688.05	-668.74	-638.7	-608.6	-578.33	-548.57	-528.72	-498.59	-468.17	-448.42	-428.72	-392.68
Samples	**TW1**	**TW2**	**TW3**	**TW4**	**TW5**	**TW6**	**TW7**	**TW8**	**TW9**	**TW10**	**TW11**	**TW12**
Q	4.856	0.733	7.422	5.784	4.905	6.17	6.145	6.305	6.02	5.301	5.223	4.605
Or	1.814	1.767	1.909	1.732	1.176	1.3	1.548	1.802	1.46	1.548	1.448	2.015
Ab	16.746	23.143	11.863	15.383	17.397	13.023	14.453	15.053	13.699	14.935	15.553	20.613
An	46.036	65.761	36.489	43.452	53.573	39.853	39.986	40.913	39.338	40.265	41.196	50.6
Ne	LOD	LOD	LOD	LOD	LOD	LOD	LOD	LOD	LOD	LOD	LOD	LOD
Wo	LOD	LOD	LOD	LOD	LOD	LOD	LOD	LOD	LOD	LOD	LOD	LOD
Di(FS)	LOD	LOD	LOD	LOD	LOD	LOD	LOD	LOD	LOD	LOD	LOD	LOD
Di(MS)	16.897	6.283	14.996	7.608	1.375	15.267	13.672	12.955	11.776	14.471	12.447	7.22
Hy(MS)	8.309	0.437	19.732	19.353	16.621	17.609	17.494	16.551	20.801	17.125	17.675	10.277
Ol(MS)	LOD	LOD	LOD	LOD	LOD	LOD	LOD	LOD	LOD	LOD	LOD	LOD
Mt	LOD	LOD	LOD	LOD	0.039	LOD	LOD	LOD	LOD	LOD	LOD	LOD
Il	0.227	0.066	0.306	0.261	0.171	0.284	0.28	0.261	0.287	0.267	0.261	0.222
Hm	4.956	1.654	7.167	6.35	4.741	6.46	6.365	6.029	6.593	6.033	6.163	4.348
Tn	0.134	0.143	0.083	0.051	LOD	0.023	0.038	0.097	0.01	0.033	0.021	0.069
Pf	LOD	LOD	LOD	LOD	LOD	LOD	LOD	LOD	LOD	LOD	LOD	LOD
Ap	0.025	0.014	0.035	0.028	0.002	0.014	0.021	0.035	0.016	0.023	0.014	0.032

LOD = Limit of detection

Depth (m)	-372.41	-344.06	-262.32	-258.91	-249.89	-242.22	-183.9	-134.17	-124.2	-115.86	-91.26	-71.5
Samples	**TW13**	**TW14**	**TW15**	**TW16**	**TW17**	**TW18**	**TW19**	**TW20**	**TW21**	**TW22**	**TW23**	**TW24**
Q	4.276	6.717	0.651	3.381	6.224	6.527	3.982	4.882	1.607	5.811	1.196	4.656
Or	1.613	1.507	2.417	1.578	2.269	2.34	1.572	1.418	1.401	1.259	2.263	1.797
Ab	19.809	14.986	25.994	16.289	18.379	18.345	20.536	16.111	23.65	15.722	17.727	18.912
An	53.129	44.875	64.687	49.532	48.337	47.924	53.069	48.385	67.192	47.324	41.99	54.045
Ne	LOD	LOD	LOD	LOD	LOD	LOD	LOD	LOD	LOD	LOD	LOD	LOD
Wo	LOD	LOD	LOD	LOD	LOD	LOD	LOD	LOD	LOD	LOD	LOD	LOD
Di(FS)	LOD	LOD	LOD	LOD	LOD	LOD	LOD	LOD	LOD	LOD	LOD	LOD
Di(MS)	4.962	5.136	0.53	10.84	4.879	4.79	4.797	5.989	0.988	5.69	15.151	4.198
Hy(MS)	11.855	20.37	4.006	12.291	14.092	14.171	11.436	17.633	3.537	17.968	14.205	11.77
Ol(MS)	LOD	LOD	LOD	LOD	LOD	LOD	LOD	LOD	LOD	LOD	LOD	LOD
Mt	LOD	LOD	LOD	LOD	LOD	LOD	LOD	LOD	LOD	LOD	LOD	LOD
Il	0.169	0.257	0.09	0.212	0.21	0.21	0.175	0.218	0.06	0.233	0.25	0.165
Hm	4.098	6.121	1.609	5.817	5.325	5.366	4.329	5.312	1.509	5.952	7.01	4.287
Tn	0.059	0.014	0.012	0.063	0.21	0.259	0.085	0.04	0.058	0.033	0.209	0.146
Pf	LOD	LOD	LOD	LOD	LOD	LOD	LOD	LOD	LOD	LOD	LOD	LOD
Ap	0.03	0.019	0.005	LOD	0.074	0.07	0.019	0.014	LOD	0.009	LOD	0.025

LOD = Limit of detection

Depth (m)	-40.23	-40.2	-19.34	0
Samples	**TW26**	**TW25**	**TW27**	**TW28**
Q	1.423	LOD	LOD	3.014
Or	1.454	1.921	1.152	0.981
Ab	20.096	20.287	20.359	17.076
An	64.69	63.209	69.458	53.369
Ne	LOD	1.043	LOD	LOD
Wo	LOD	2.564	LOD	LOD
Di(FS)	LOD	LOD	LOD	LOD
Di(MS)	7.714	8.328	5.728	4.578
Hy(MS)	1.819	LOD	0.853	16.795
Ol(MS)	LOD	LOD	0.521	LOD
Mt	LOD	LOD	LOD	0.008
Il	0.094	0.113	0.068	0.161
Hm	2.52	2.491	1.753	4.019
Tn	0.175	LOD	0.098	LOD
Pf	LOD	0.031	LOD	LOD
Ap	0.014	LOD	0.009	LOD

LOD = Limit of detection

Appendix E: Electron Probe Microanalysis (EPM) *data given in weight percentage (wt %)*

Paschaskraal:

Depth (m)	DataSet/Point	Na_2O	MgO	Al_2O_3	SiO_2	K_2O	CaO	TiO_2	Cr_2O_3	MnO	FeO	BaO	Total	X	Y	Z
-751.29	-751.29 Plag 1 p1	3.28	0.01	31.69	50.08	0.2	14.81	0	0	0	0.31	0.02	100.39	-19939	-12016	308
-751.29	-751.29 Plag 1 p2	3.26	0	31.72	50.28	0.17	14.74	0.05	0	0.03	0.36	0.01	100.62	-19893	-12175	310
-751.29	-751.29 Plag 2 p1	3.74	0	31.07	50.83	0.24	13.97	0.05	0	0.01	0.32	0.01	100.24	-11257	-13535	340
-751.29	-751.29 Plag 2 p2	3.65	0.03	31.27	51.11	0.27	13.91	0.03	0	0	0.33	0.01	100.61	-11331	-13465	340
-751.29	-751.29 Plag 3 p1	3.42	0	31.33	50.53	0.17	14.3	0.03	0	0	0.33	0.02	100.14	-16721	-17540	342
-751.29	-751.29 Plag 3 p2	3.57	0.01	31.06	50.88	0.24	14.04	0.09	0	0.03	0.3	0.05	100.27	-16459	-17517	343
-751.29	-751.29 Plag 4 p1	3.81	0	30.94	51.01	0.26	13.63	0.03	0	0.03	0.3	0.02	100.02	-7738	-18925	341
-751.29	-751.29 Plag 4 p2	3.35	0.01	31.52	50.1	0.19	14.63	0.03	0	0	0.34	0	100.17	-7737	-19049	340
-700.11	-700.11 Plag 1 p1	3.34	0	31.41	49.46	0.21	14.68	0.04	0.02	0.01	0.37	0	99.56	19690	-32260	341
-700.11	-700.11 Plag 1 p2	3.04	0	31.71	48.94	0.19	15.26	0	0	0.02	0.41	0.03	99.59	20003	-32260	333
-700.11	-700.11 Plag 2 p1	3.3	0.01	31.57	50.37	0.22	14.62	0.03	0	0.01	0.37	0	100.5	4450	-28580	370
-700.11	-700.11 Plag 2 p2	3.2	0.02	31.67	50.44	0.19	14.69	0.03	0	0.03	0.34	0.02	100.62	4180	-28580	367
-700.11	-700.11 Plag 3 p1	3.52	0.02	30.92	50.74	0.19	14	0.07	0	0	0.42	0.02	99.9	6457	-18647	414
-700.11	-700.11 Plag 3 p2	3.37	0.02	31.31	50.12	0.17	14.49	0.03	0	0.01	0.28	0.04	99.83	6547	-19130	413
-700.11	-700.11 Plag 4 p1	3.33	0.03	31.39	50.45	0.21	14.6	0.02	0.02	0	0.34	0	100.37	6487	-9561	426
-700.11	-700.11 Plag 4 p2	3.22	0.01	31.91	50.46	0.17	14.62	0.06	0	0.01	0.4	0.01	100.88	6233	-9561	423
-650.87	127.47 Plag 1 p1	3.17	0	31.35	49.24	0.21	15.05	0.01	0.01	0.02	0.39	0	99.47	-9918	39130	344
-650.87	127.47 Plag 1 p2	3.11	0.02	31.65	49.13	0.26	15.09	0.1	0	0.02	0.39	0	99.78	-10203	39130	345
-650.87	127.47 Plag 2 p1	3.55	0.21	30.51	49.77	0.39	13.62	0.01	0.02	0.01	0.42	0.04	98.54	-7653	38059	334
-650.87	127.47 Plag 2 p2	3.54	0.01	31.14	50.09	0.24	14.43	0.03	0	0	0.35	0	99.82	-7731	38194	333
-650.87	127.47 Plag 3 p1	3.47	0	31.06	50.16	0.26	14.56	0.05	0.01	0	0.37	0	99.95	-19245	36795	396
-650.87	127.47 Plag 3 p2	3.32	0	31.6	49.96	0.2	14.5	0.05	0.05	0	0.31	0.04	100.04	-19064	36811	396

Depth (m)	DataSet/Point	Na_2O	MgO	Al_2O_3	SiO_2	K_2O	CaO	TiO_2	Cr_2O_3	MnO	FeO	BaO	Total	X	Y	Z
-600.16	-600.16 Plag 1 p1	3.54	0.01	31.34	50.52	0.27	14.22	0.03	0	0	0.26	0.03	100.22	-23266	-14990	299
-600.16	-600.16 Plag 1 p2	3.68	0.01	31.27	51.27	0.29	14.01	0.03	0.03	0.03	0.23	0.02	100.87	-23348	-14987	301
-600.16	-600.16 Plag 2 p1	3.33	0	31.48	50.1	0.2	14.69	0.04	0	0	0.28	0.02	100.14	-17271	-15606	301
-600.16	-600.16 Plag 2 p2	3.89	0.01	30.71	51.66	0.29	13.5	0.03	0	0	0.26	0.01	100.36	-17488	-15674	303
-600.16	-600.16 Plag 3 p1	3.12	0.01	31.54	49.6	0.22	14.98	0	0	0	0.24	0	99.72	-21672	-21391	303
-600.16	-600.16 Plag 3 p2	3.33	0.03	31.7	49.92	0.27	14.75	0	0	0.01	0.27	0.04	100.3	-21615	-21291	302
-580.22	-349.96 Plag 1 p1	3.27	0	31.39	49.72	0.24	14.66	0.06	0	0	0.26	0	99.61	5171	36936	407
-580.22	-349.96 Plag 1 p2	3.43	0.01	31.33	50.03	0.2	14.56	0.04	0.03	0	0.24	0	99.86	4862	36983	407
-580.22	-349.96 Plag 2 p1	3.73	0.01	30.85	50.77	0.28	13.79	0.01	0.02	0	0.29	0.04	99.79	6976	39360	379
-580.22	-349.96 Plag 2 p2	3.25	0	31.57	49.72	0.16	14.96	0	0.01	0	0.23	0	99.9	6757	39374	381
-580.22	-349.96 Plag 3 p1	3.11	0.02	31.23	48.69	0.15	15.13	0.03	0	0	0.26	0.01	98.64	9893	38665	371
-580.22	-349.96 Plag 3 p2	3.43	0.03	31.37	49.95	0.19	14.58	0.2	0	0.03	0.26	0	100.05	10151	38632	372
-580.22	-349.96 Plag 4 p1	3.4	0.01	31.54	50.16	0.18	14.69	0.02	0	0	0.32	0.01	100.34	5551	36454	411
-580.22	-349.96 Plag 4 p2	3.96	0.01	30.42	51.45	0.28	13.52	0.05	0	0.02	0.27	0	99.98	5555	36586	410
-560	-560 Plag 1 p1	3.46	0.01	30.8	50.18	0.19	14.48	0.05	0	0.04	0.3	0	99.51	-15738	29066	366
-560	-560 Plag 1 p2	3.3	0.03	31.55	50.11	0.26	14.94	0.05	0	0	0.26	0	100.5	-15645	29113	367
-560	-560 Plag 2 p1	3.32	0.02	31.17	49.88	0.26	14.6	0.14	0	0	0.41	0	99.8	-19091	25912	383
-560	-560 Plag 2 p2	3.13	0.01	31.65	49.31	0.19	15.2	0.02	0	0	0.25	0	99.75	-19206	26027	382
-560	-560 Plag 3 p1	3.11	0.03	31.76	49.64	0.28	15.14	0	0.02	0.01	0.28	0	100.26	-19519	22764	383
-560	-560 Plag 3 p2	3.48	0.02	31.42	50.49	0.23	14.05	0	0	0.01	0.27	0	99.96	-19659	22798	386
-560	-560 Plag 4 p1	3.05	0.01	31.99	49.26	0.2	15.17	0.03	0.01	0	0.26	0	99.99	-18063	14807	358
-560	-560 Plag 4 p2	3.15	0.02	32.08	49.91	0.23	14.97	0.05	0	0	0.3	0.01	100.72	-18185	14817	358
-539.82	-539.82 TS12 Plag 1 p1	3.58	0.02	31.11	50.5	0.2	14.13	0.02	0	0	0.21	0.02	99.81	15596	-32922	270
-539.82	-539.82 TS12 Plag 1 p2	3.66	0.02	30.79	50.67	0.28	14.06	0	0	0.02	0.26	0	99.76	15429	-32917	270
-539.82	-539.82 TS12 Plag 2 p1	3.6	0.01	31.08	50.76	0.25	14	0.02	0	0	0.23	0.04	99.99	9029	-31621	289
-539.82	-539.82 TS12 Plag 2 p2	3.56	0	31.02	50.63	0.23	14	0.01	0	0.01	0.24	0	99.69	8742	-31489	290
-539.82	-539.82 TS12 Plag 3 p1	3.72	0.03	30.93	50.92	0.24	13.83	0.01	0.03	0	0.2	0.02	99.93	9970	-30294	290

Depth (m)	DataSet/Point	Na_2O	MgO	Al_2O_3	SiO_2	K_2O	CaO	TiO_2	Cr_2O_3	MnO	FeO	BaO	Total	X	Y	Z
-539.82	-539.82 TS12 Plag 3 p2	3.76	0.02	30.9	50.75	0.25	13.85	0.07	0.01	0	0.25	0	99.87	10202	-30290	288
-489.98	-489.98 Plag 1 p1	3.56	0	31.27	50.52	0.23	14.24	0.04	0	0.01	0.23	0.04	100.15	-16607	-11265	322
-489.98	-489.98 Plag 1 p2	3.21	0.01	31.81	49.66	0.22	14.99	0.02	0	0.03	0.21	0.01	100.18	-16395	-11281	322
-489.98	-489.98 Plag 2 p1	3.5	0.01	31.26	50.69	0.25	14.44	0.05	0	0.01	0.26	0.01	100.49	-17976	-14504	332
-489.98	-489.98 Plag 2 p2	3.89	0.02	30.76	51.11	0.25	13.78	0.01	0	0	0.25	0	100.07	-18333	-14519	334
-489.98	-489.98 Plag 4 p1	3.45	0.01	31.4	50.43	0.26	14.52	0.05	0	0	0.25	0	100.37	-18721	-19083	334
-489.98	-489.98 Plag 4 p2	4.07	0.01	30.63	51.84	0.29	13.32	0.04	0	0	0.24	0.01	100.44	-18931	-19123	334
-470.02	PK 1 plag 1 p1	3.79	0.03	30.94	51.15	0.29	13.84	0.02	0	0.01	0.25	0.02	100.34	18114	-11801	270
-470.02	PK 1 plag 1 p2	3.72	0	30.87	50.03	0.26	14.26	0.03	0.01	0.02	0.33	0.01	99.55	18260	-11781	269
-470.02	PK 1 Plag 2 p1	3.46	0.02	31.15	50.32	0.26	14.44	0.03	0	0.02	0.26	0	99.96	9539	-14006	263
-470.02	PK 1 Plag 2 p2	4.05	0	30.7	50.11	0.26	13.57	0.01	0	0.02	0.26	0	98.97	9541	-13891	262
-470.02	PK 1 Plag 3 p1	3.71	0.02	30.55	50.97	0.46	13.84	0.02	0	0.01	0.22	0.04	99.84	19602	-13972	276
-470.02	PK 1 Plag 3 p2	3.39	0.03	31.05	49.86	0.23	14.48	0.04	0.01	0	0.26	0.01	99.35	19353	-13955	276
-470.02	PK 1 Plag 4 p1	3.41	0	31.26	50.29	0.25	14.48	0.01	0.02	0	0.25	0.05	100.02	9935	-20220	273
-470.02	PK 1 Plag 4 p2	3.54	0.01	31.1	50.43	0.27	14.27	0.02	0	0.01	0.32	0	99.98	10200	-20217	273
-429.96	PK 2 Plag 1 p1	3.81	0.02	30.71	50.91	0.29	13.76	0.03	0	0.01	0.21	0.01	99.76	-12536	24940	313
-429.96	PK 2 Plag 1 p2	3.79	0.01	30.72	50.9	0.3	14	0.05	0.02	0.02	0.24	0.04	100.08	-12292	24941	314
-429.96	PK 2 Plag 2 p1	3.72	0.01	30.91	51.18	0.22	14	0.05	0	0.05	0.2	0.01	100.36	-11442	22007	302
-429.96	PK 2 Plag 2 p2	3.37	0.02	31.46	50.04	0.21	14.65	0.03	0	0.02	0.21	0	100.01	-11616	22007	302
-429.96	PK 2 Plag 3 p1	4	0.02	30.38	51.48	0.35	13.34	0.04	0	0	0.24	0	99.85	-12257	20036	300
-429.96	PK 2 Plag 3 p2	2.67	0.01	32.54	48.3	0.15	15.93	0.06	0.04	0	0.24	0.02	99.95	-12353	20010	299
-429.96	PK 2 Plag 4 p1	3.42	0	31	49.97	0.22	14.32	0.05	0.02	0.01	0.25	0	99.28	-12428	15809	284
-429.96	PK 2 Plag 4 p2	4	0.02	30.34	51.47	0.24	13.55	0.04	0	0	0.24	0.07	99.98	-12536	15813	284
-419.69	Pk 3 Plag1 p1	3.51	0	31.24	50.16	0.26	14.49	0.04	0	0	0.25	0	99.94	5270	29959	411
-419.69	Pk 3 Plag1 p2	3.73	0.01	30.87	50.84	0.22	13.92	0.03	0.01	0.01	0.24	0	99.9	5304	30061	411
-419.69	Pk 3 Plag 2 p1	3.44	0.01	31.14	50.04	0.22	14.5	0	0	0.02	0.3	0	99.67	7389	27633	422
-419.69	Pk 3 Plag 2 p2	3.68	0.02	30.95	50.67	0.2	14.15	0.03	0	0.03	0.22	0	99.95	7502	27641	421

Depth (m)	DataSet/Point	Na_2O	MgO	Al_2O_3	SiO_2	K_2O	CaO	TiO_2	Cr_2O_3	MnO	FeO	BaO	Total	X	Y	Z
-419.69	Pk 3 Plag 3 p1	3.66	0.03	30.79	50.77	0.26	13.94	0.04	0.01	0	0.27	0.01	99.79	5886	21309	441
-419.69	Pk 3 Plag 3 p2	3.82	0	30.7	51.11	0.27	13.72	0	0	0.04	0.26	0	99.92	5944	21311	443
-280.11	PK 14 Plag 1 p1	3.74	0.01	30.47	50.93	0.25	13.75	0.02	0.01	0.01	0.24	0.03	99.46	-20995	33509	440
-280.11	PK 14 Plag 1 p2	3.55	0	31.43	50.28	0.23	14.42	0.01	0.01	0	0.28	0	100.2	-20793	33534	441
-280.11	PK 14 Plag 2 p1	3.8	0.01	30.86	50.77	0.21	13.88	0.05	0	0.04	0.24	0	99.86	-13847	27750	418
-280.11	PK 14 Plag 2 p2	2.71	0.01	31.53	49.07	1.09	14.33	0.01	0.02	0	0.57	0.03	99.37	-13754	27783	419
-280.11	PK 14 Plag 3 p1	3.78	0.04	30.56	51	0.28	14.02	0.04	0	0	0.28	0	100.02	-14720	18744	396
-280.11	PK 14 Plag 3 p2	3.78	0.02	30.77	51	0.26	13.89	0.06	0.03	0	0.26	0	100.06	-14560	18763	397
-280.11	PK 14 Plag 4 p1	3.69	0.02	31.2	50.01	0.23	13.93	0.09	0	0	0.23	0.01	99.4	-12327	16681	367
-280.11	PK 14 Plag 4 p2	3.74	0.01	30.47	50.2	0.22	13.91	0.01	0	0	0.27	0.01	98.83	-12447	16685	369
-230.32	Pk 15 Plag 1 p1	3.19	0	31.65	49.45	0.19	14.92	0.01	0.01	0	0.27	0	99.68	9111	32679	372
-230.32	Pk 15 Plag 1 p2	3.81	0.03	30.54	50.42	0.25	14.04	0.02	0	0	0.31	0	99.42	9253	32687	370
-230.32	Pk 15 Plag 2 p1	3.35	0.01	31.5	49.83	0.17	14.81	0.04	0.04	0.01	0.32	0	100.07	19112	34461	306
-230.32	Pk 15 Plag 2 p2	3.83	0.04	30.78	50.96	0.21	13.7	0.01	0	0	0.27	0.01	99.81	18886	34450	307
-230.32	Pk 15 Plag 2 p1	3.7	0.05	30.93	50.82	0.23	13.95	0.04	0	0	0.26	0.02	100	12131	33697	356
-230.32	Pk 15 Plag 2 p2	3.52	0.02	31.12	50	0.22	14.47	0	0.01	0	0.28	0.02	99.66	12057	33690	355
-230.32	Pk 15 Plag 3 p1	3.92	0.01	30.61	51.12	0.25	13.54	0.06	0.01	0	0.22	0	99.73	8550	33829	378
-230.32	Pk 15 Plag 3 p2	3.01	0.01	31.61	48.64	0.16	15.41	0	0	0.02	0.29	0	99.16	8514	33794	378
-139.9	PK 17 Plag 1 p1	3.67	0	31.34	51.4	0.24	14.08	0.06	0	0.02	0.29	0.07	101.19	-20450	-14528	298
-139.9	PK 17 Plag 1 p2	3.83	0	31	51.78	0.24	13.71	0.03	0.01	0.03	0.22	0.01	100.86	-20219	-14515	300
-139.9	PK 17 Plag 2 p1	3.46	0.02	31.23	50.61	0.23	14.37	0.03	0	0	0.28	0.05	100.28	-14669	-11005	360
-139.9	PK 17 Plag 2 p2	3	0.01	32.3	49.28	0.16	15.38	0.03	0.02	0	0.27	0	100.45	-14667	-10878	360
-139.9	PK 17 Plag 3 p1	3.12	0.01	32.09	49.76	0.18	15.09	0.01	0	0.02	0.31	0	100.58	-16649	-18653	327
-139.9	PK 17 Plag 3 p2	3.09	0.01	32.01	49.82	0.17	15.13	0.01	0	0	0.32	0	100.54	-16899	-18752	325
-139.9	PK 17 Plag 4 p1	3.23	0.01	31.87	50.02	0.18	14.84	0.02	0	0	0.28	0.06	100.51	-12288	-27416	319
-139.9	PK 17 Plag 4 p2	3.74	0	31.03	51.47	0.23	13.67	0.06	0	0	0.4	0	100.6	-12482	-27402	315

Depth (m)	DataSet/Point	Na_2O	MgO	Al_2O_3	SiO_2	K_2O	CaO	TiO_2	Cr_2O_3	MnO	FeO	BaO	Total	X	Y	Z
-429.96	PK 2 Opx 2 p1	0.29	14.93	1.23	52.27	0	23.33	0.39	0.2	0.19	6.2	0	99.04	-11604	16807	283
-419.69	Pk 3 Opx 1 p1	0.34	14.77	1.53	51.96	0.01	23.3	0.37	0.26	0.16	6.77	0.01	99.48	19648	29990	332
-419.69	Pk 3 Opx 2 p1	0.29	14.75	1.26	51.94	0	23.39	0.26	0.24	0.19	6.36	0.01	98.69	9600	31950	379
-419.69	Pk 3 Opx 1 p2	0.29	14.98	1.34	52.38	0	22.94	0.38	0.21	0.21	6.77	0	99.49	19593	30423	335
-419.69	Pk 3 Opx 1 p3	0.34	15	1.43	52.18	0	23.46	0.44	0.21	0.21	6.57	0	99.85	19560	29579	335
-280.11	PK 14 Opx 1 p1	0.01	25.65	0.78	53.94	0.01	0.8	0.26	0.13	0.39	17.93	0.06	99.97	-15368	33542	432
-280.11	PK 14 Opx 2 p1	0.32	14.88	1.43	52.05	0	23.39	0.27	0.28	0.17	6.4	0.03	99.23	-5458	20599	299
-280.11	PK 14 Opx 3 p1	0.02	25.83	0.71	53.86	0	0.64	0.2	0.1	0.33	17.84	0.01	99.54	-7228	20604	328
-280.11	PK 14 Opx 4 p1	0.01	25.06	0.63	51.53	0	0.85	4.77	0.11	0.34	17.25	0	100.54	-5404	18392	285
-230.32	Pk 15 Opx 1 p2	0.01	24.83	0.75	53.5	0	0.88	0.17	0.12	0.34	18.51	0	99.11	7792	32429	378
-230.32	Pk 15 Opx 2 p1	0.04	24.5	0.77	53.33	0	2.33	0.28	0.11	0.33	17.92	0.07	99.68	7898	31883	377
-139.9	PK 17 Opx 1 p1	0.02	24.07	0.73	53.69	0	0.98	0.23	0.08	0.43	20.38	0	100.62	-16936	-13482	339
-139.9	PK 17 Opx 1 p2	0.03	23.59	0.72	53.76	0.01	1.67	0.12	0.12	0.41	19.7	0.02	100.15	-16888	-13394	337
-139.9	PK 17 Opx 2 p1	0.34	14.52	1.52	52.18	0	22.25	0.35	0.24	0.21	8.19	0	99.82	-14646	-22170	331
-139.9	PK 17 Opx 3 p1	0.02	21.6	0.43	45.81	0.01	0.6	8.26	0.12	0.44	25.86	0	103.13	-11862	-31065	287

Depth (m)	DataSet/Point	Na_2O	MgO	Al_2O_3	SiO_2	K_2O	CaO	TiO_2	Cr_2O_3	MnO	FeO	BaO	Total	X	Y	Z
-751.29	-751.29 Cpx 2 p1	0.01	23.23	0.79	53.22	0.02	0.97	0.25	0.05	0.44	21.49	0	100.48	-14217	-16452	225
-751.29	-751.29 Cpx 3 p1	0	22.81	0.62	53.16	0	0.97	0.19	0.02	0.46	21.56	0	99.8	-6243	-17668	236
-600.16	-600.16 Cpx 1 p1	0.24	16.76	1.13	52.79	0	19.63	1.24	0.19	0.22	8.12	0.05	100.38	-25033	-15229	272
-600.16	-600.16 Cpx 2 p1	0.01	26.03	0.74	54.31	0	1.06	0.16	0.09	0.37	17.52	0	100.3	-23793	-14576	380
-600.16	-600.16 Cpx 3 p1	0.02	25.44	0.78	53.93	0	2.1	0.2	0.1	0.3	16.8	0.03	99.7	-22480	-15028	334
-600.16	-600.16 Cpx 4 p1	0.01	26.02	0.81	54.16	0.01	1	0.25	0.09	0.39	17.77	0	100.53	-17363	-14661	336
-600.16	-600.16 Cpx 5 p1	0.04	25.3	0.88	53.86	0	2.11	0.15	0.14	0.38	16.74	0.01	99.6	-12426	-15054	330
-600.16	-600.16 Cpx 6 p1	0.03	25.98	0.8	54.56	0.01	1.86	0.21	0.12	0.36	16.97	0.03	100.92	-25300	-21391	303
-580.22	-349.96 Cpx 1 p1	0	25.71	0.82	53.77	0.02	0.79	0.3	0.12	0.38	18.04	0	99.95	6274	34996	333
-580.22	-580.22 Cpx 1 p2	0.02	25.57	0.7	54.1	0	0.86	0.23	0.05	0.37	17.92	0	99.82	6688	35189	223
-580.22	-580.22 Cpx 2 p2	0.28	14.75	1.51	51.73	0	23.25	0.45	0.22	0.17	6.64	0	99	8646	33858	235
-580.22	-580.22 Cpx 3 p1	0.02	25.43	0.77	53.8	0	1.65	0.45	0.09	0.32	17.03	0.02	99.6	8609	32949	376
-560	-560 Cpx 1 p1	0.01	25.64	0.74	53.82	0	1.38	0.2	0.12	0.35	17.07	0.03	99.38	-19592	27062	395
-560	-560 Cpx 1 p2	0.01	25.7	0.75	54.11	0	1.31	0.19	0.08	0.34	17.23	0	99.72	-19270	27054	351
-560	-560 Cpx 2 p1	0.02	26.06	0.8	54.24	0	1.1	0.22	0.1	0.38	17.33	0.02	100.25	-16806	23731	342
-539.82	-539.82 TS12Cpx 1 p1	0.3	15.12	1.23	52.2	0	22.11	0.47	0.21	0.18	7.35	0.03	99.19	13180	-34144	364
-539.82	-539.82 TS12 Cpx 3 p1	0.29	15.05	1.35	52.33	0	23.04	0.32	0.25	0.2	6.62	0	99.46	6846	-30006	319
-539.82	-539.82 TS12 Cpx 4 p1	0.01	25.6	0.67	54.14	0	0.7	0.2	0.1	0.35	18.45	0	100.23	5655	-23590	327
-489.98	-489.98 Cpx 1 p1	0.29	15.16	1.35	52.82	0.02	23.3	0.3	0.2	0.24	6.44	0.01	100.12	-23880	-10994	324
-489.98	-489.98 Cpx 2 p1	0.28	15.22	1.27	52.63	0	23.12	0.4	0.19	0.22	6.89	0.03	100.24	-23328	-12017	328
-489.98	-489.98 Cpx 3 p1	0.32	14.93	1.42	51.97	0	22.8	0.42	0.18	0.2	6.96	0.02	99.21	-13168	-14179	419
-489.98	-489.98 Cpx 4 p1	0.01	25.97	0.8	53.96	0	1.29	0.21	0.09	0.37	17.41	0.02	100.13	-19561	-17268	418
-470.02	PK 1 Cpx 1 p2	0.33	15.01	1.57	52.34	0	23.07	0.37	0.21	0.25	6.53	0	99.67	17978	-12746	312

Depth (m)	DataSet/Point	Na_2O	MgO	Al_2O_3	SiO_2	K_2O	CaO	TiO_2	Cr_2O_3	MnO	FeO	BaO	Total	X	Y	Z
-470.02	PK 1 Cpx 2 p1	0.31	15.29	1.37	52.39	0	22.89	0.42	0.21	0.19	6.78	0	99.85	16122	-14397	391
-470.02	PK 1 Cpx 3 p1	0.31	15.06	1.45	52.21	0	23.16	0.42	0.23	0.18	6.48	0	99.51	8399	-20168	337
-470.02	PK 1 Cpx 4 p1	0	26.29	0.61	54.21	0.01	0.76	0.24	0.15	0.37	17.5	0	100.15	18529	-21784	355
-429.96	PK 2 Cpx 1 p1	0.31	14.96	1.29	52.07	0	23.24	0.46	0.22	0.22	6.52	0.02	99.32	-11170	21388	301
-429.96	PK 2 Cpx 2 p1	0.31	14.98	1.27	52.54	0	23.02	0.42	0.21	0.17	6.54	0	99.47	-7911	18684	371
-419.69	Pk 3 Cpx 1 p1	0	25.99	0.8	54.12	0	0.91	0.21	0.11	0.36	16.98	0	99.48	7733	32365	380
-419.69	Pk 3 Cpx 2 p1	0.32	14.86	1.47	52.27	0	23.47	0.44	0.24	0.21	6.39	0	99.67	19692	27636	371
-419.69	Pk 3 Cpx 2 p2	0.33	14.96	1.57	52.13	0	23.07	0.44	0.22	0.22	6.63	0	99.57	19693	26948	288
-419.69	Pk 3 Cpx 3 p1	0.03	25.76	0.62	53.61	0.03	0.77	0.29	0.06	0.38	17.52	0.02	99.09	22322	17814	294
-280.11	PK 14 Cpx 1 p1	0.32	14.97	1.38	52.32	0	22.01	0.47	0.25	0.21	7.49	0	99.41	-11343	33560	295
-280.11	PK 14 Cpx 2 p1	0.02	25.47	0.89	54.18	0	1.44	0.21	0.15	0.34	17.77	0	100.5	-13480	27741	412
-280.11	PK 14 Cpx 3 p1	0.02	25.4	0.84	53.94	0.03	1.31	0.29	0.11	0.35	17.48	0	99.78	-4293	27711	410
-280.11	PK 14 Cpx 4 p1	0	25.92	0.84	54.01	0.01	0.8	0.23	0.15	0.38	17.7	0	100.05	-18336	15956	396
-230.32	Pk 15 Cpx 1 p2	0.36	14.48	1.51	52	0	22.86	0.45	0.24	0.2	7.24	0	99.32	9417	33563	270
-230.32	Pk 15 Cpx 1 p2	0.31	14.85	1.28	51.99	0	23.14	0.44	0.23	0.17	7.09	0	99.5	9230	33744	305
-230.32	Pk 15 Cpx 2 p1	0.37	14.86	1.57	52.01	0	23.04	0.37	0.24	0.16	7.04	0.01	99.66	6531	33786	330
-139.9	PK 17 Cpx 1 p1	0.02	24.08	0.76	53.59	0.01	0.67	0.15	0.1	0.46	20.66	0	100.5	-10651	-7831	298
-139.9	PK 17 Cpx 2 p1	0.02	23.84	0.81	53.59	0	1.37	0.16	0.09	0.38	19.79	0	100.07	-14323	-16025	335
-139.9	PK 17 Cpx 3 p1	0.03	24.31	0.88	53.76	0	1.69	0.14	0.15	0.43	19.57	0.04	101.02	-9188	-26217	272
-139.9	PK 17 Cpx 4 p1	0.31	14.39	1.89	51.51	0.08	22.44	1.28	0.27	0.16	7.62	0	99.97	-17294	-26922	277

Twickenham:

Depth (m)	DataSet/Point	Na_2O	MgO	Al_2O_3	SiO_2	K_2O	CaO	TiO_2	Cr_2O_3	MnO	FeO	BaO	Total	X	Y	Z
-688.05	-688.05 Plag 1 p1	3.35	0.02	31.89	50.36	0.23	14.6	0.04	0	0	0.32	0	100.81	5450	35048	290
-688.05	-688.05 Plag 1 p2	3.43	0.01	31.31	49.94	0.2	14.66	0.05	0	0	0.26	0	99.87	5281	35032	285
-688.05	-688.05 Plag 2 p1	3.24	0	31.45	49.85	0.25	14.78	0.07	0.01	0	0.23	0.01	99.9	10973	34936	297
-688.05	-688.05 Plag 2 p2	3.42	0.01	31.6	50.38	0.2	14.66	0.06	0.03	0	0.21	0.01	100.59	11041	34782	298
-688.05	-688.05 Plag 3 p1	3.6	0.03	31.27	50.63	0.3	14.15	0	0.01	0.05	0.29	0.03	100.36	10945	33106	301
-688.05	-688.05 Plag 3 p2	3.97	0.01	30.78	51.63	0.26	13.58	0.05	0	0	0.3	0	100.57	10545	33109	301
-688.05	-688.05 Plag 4 p1	3.17	0.03	31.59	49.23	0.32	14.63	0.03	0	0.03	0.26	0.01	99.29	10573	31917	303
-688.05	-688.05 Plag 4 p2	3.46	0.01	31.41	50.32	0.27	14.35	0.03	0	0	0.33	0	100.17	11003	31917	301
-668.74	-668.74 Plag 1 p1	3.57	0	31.25	50.3	0.21	14.32	0.03	0.03	0.02	0.33	0	100.07	-18627	21720	334
-668.74	-668.74 Plag 1 p2	2.99	0	31.94	49.02	0.17	15.33	0.05	0.02	0	0.31	0.02	99.85	-18365	21720	333
-668.74	-668.74 Plag 2 p1	3.03	0.01	31.79	49.14	0.17	15.33	0.02	0.02	0	0.33	0.01	99.85	-10962	26250	320
-668.74	-668.74 Plag 2 p2	3.59	0	30.97	50.54	0.2	14.34	0.02	0	0.02	0.41	0.05	100.14	-11195	26260	320
-668.74	-668.74 Plag 3 p1	3.3	0.02	31.38	49.73	0.19	14.9	0.05	0	0.01	0.36	0.01	99.95	-13342	11445	313
-668.74	-668.74 Plag 3 p2	3.27	0	31.44	49.93	0.24	14.95	0.06	0.03	0.01	0.26	0	100.19	-13211	11505	314
-668.74	-668.74 Plag 4 p1	3.06	0.01	31.96	49.61	0.21	15.31	0.06	0.04	0.02	0.35	0	100.64	-13732	31872	327
-668.74	-668.74 Plag 4 p2	2.95	0.01	31.6	48.02	0.22	15.46	0.01	0	0	0.32	0.06	98.64	-13911	31876	325
-668.74	-668.74 Plag 5 p1	3.49	0.02	31.14	49.94	0.23	14.71	0.02	0	0	0.36	0.08	99.98	-6050	19347	288
-668.74	-668.74 Plag 5 p2	3.18	0.01	31.61	49.32	0.16	15.28	0.08	0.02	0	0.37	0	100.05	-5998	19144	288
-668.74	-668.74 Plag 6 p1	3.36	0.01	31.09	49.59	0.23	14.36	0.03	0	0.01	0.36	0	99.04	-4957	32677	283
-668.74	-668.74 Plag 6 p2	3.09	0	31.71	49.13	0.19	15.14	0.04	0	0.03	0.38	0	99.71	-4990	32827	285
-638.7	-638.7 Plag 1 p1	2.86	0.01	32.15	48.88	0.19	15.8	0.01	0	0.03	0.23	0.02	100.17	-18122	-9875	336
-638.7	-638.7 Plag 1 p2	3.53	0.1	31.04	49.93	0.23	13.65	0.04	0.01	0	1.02	0.01	99.56	-18354	-9875	335
-638.7	-638.7 Plag 2 p1	3.68	0.02	30.68	50.87	0.22	14.12	0.04	0	0.01	0.26	0.01	99.91	-23807	-14060	319

Depth (m)	DataSet/Point	Na_2O	MgO	Al_2O_3	SiO_2	K_2O	CaO	TiO_2	Cr_2O_3	MnO	FeO	BaO	Total	X	Y	Z
-638.7	-638.7 Plag 2 p2	4.18	0.01	30.33	52.19	0.23	13.22	0.02	0	0	0.2	0	100.38	-23393	-14060	321
-638.7	-638.7 Plag 3 p1	3.39	0	31.39	50.04	0.16	14.56	0.05	0.03	0	0.22	0.04	99.88	-10955	-18916	299
-638.7	-638.7 Plag 3 p2	2.76	0	32.94	48.47	0.05	16.03	0.04	0	0	0.22	0.01	100.52	-11098	-18789	299
-638.7	-638.7 Plag 4 p1	3.3	0	31.4	49.8	0.17	15.05	0.02	0	0	0.22	0.01	99.96	-6088	-28288	250
-638.7	-638.7 Plag 4 p2	3.69	0.01	31.05	50.09	0.14	14.31	0.02	0	0	0.28	0	99.58	-5929	-28288	249
-578.33	-578.33 Plag 1 p1	3.24	0.02	31.46	49.31	0.26	15.03	0.02	0	0	0.29	0	99.63	14898	-6721	256
-578.33	-578.33 Plag 1 p2	3.23	0	31.55	50.37	0.26	14.69	0.03	0	0	0.24	0.08	100.46	14673	-6721	255
-578.33	-578.33 Plag 2 p1	3.32	0.03	31.37	49.81	0.24	14.54	0.03	0.03	0	0.3	0.02	99.69	15491	-8395	257
-578.33	-578.33 Plag 2 p2	3.39	0.01	31.08	50.05	0.25	14.51	0.06	0	0	0.3	0.04	99.69	15677	-8395	257
-578.33	-578.33 Plag 3 p1	3.11	0.03	31.66	49.4	0.24	14.87	0.04	0.03	0	0.28	0.01	99.65	16255	-11958	257
-578.33	-578.33 Plag 3 p2	3.07	0.01	31.96	49.47	0.19	15.08	0.03	0	0	0.23	0	100.04	16724	-11958	257
-578.33	-578.33 Plag 3 p1	3.06	0.04	31.7	49.45	0.22	15.18	0	0.02	0.02	0.35	0	100.03	7910	-12200	251
-578.33	-578.33 Plag 3 p2	3.56	0.02	30.84	50.48	0.27	14.19	0.06	0	0.04	0.29	0	99.74	8128	-12200	251
-578.33	-578.33 Plag 4 p1	2.93	0.09	31.18	49.17	0.21	15.03	0.04	0.01	0.02	0.32	0.02	99	9306	-24256	240
-578.33	-578.33 Plag 4 p2	2.3	0.02	32.79	48.18	0.18	16.29	0.02	0.02	0.01	0.29	0	100.1	9108	-24256	240
-468.17	-468.17 Plag 1 p1	3.83	0.02	30.74	51.1	0.24	13.69	0.01	0	0	0.26	0	99.89	5020	38950	336
-468.17	-468.17 Plag 1 p2	3.28	0.01	31.21	50.11	0.37	14.29	0.03	0	0	0.27	0	99.58	4955	38950	337
-468.17	-468.17 Plag 2 p2	3.45	0	31.05	50.31	0.27	14.62	0	0.01	0	0.26	0	99.96	10320	37444	302
-468.17	-468.17 Plag 2 p1	3.37	0.02	31.25	49.98	0.23	14.57	0.02	0	0.02	0.25	0	99.7	10568	37430	298
-468.17	-468.17 Plag 3 p1	3.37	0.02	31.57	49.98	0.24	14.59	0.03	0	0	0.25	0	100.07	4510	36665	340
-372.41	-372.41 Plag 1 p1	3.33	0.01	31.57	50.01	0.22	14.61	0.04	0	0	0.31	0.03	100.11	-12929	37435	305
-372.41	-372.41 Plag 1 p2	3.3	0.02	31.7	49.92	0.23	14.75	0.03	0	0	0.29	0	100.23	-13081	37435	305
-372.41	-372.41 Plag 2 p1	3.59	0.02	30.8	50.27	0.27	14.17	0.07	0.02	0.04	0.26	0	99.49	-4153	35810	280
-372.41	-372.41 Plag 2 p2	3.86	0.02	30.19	50.46	0.28	13.79	0.01	0.02	0	0.31	0.02	98.97	-3859	35826	277
-372.41	-372.41 Plag 4 p1	3.85	0.02	30.79	51.16	0.26	13.61	0.01	0	0	0.27	0	99.98	-21197	35967	320
-372.41	-372.41 Plag 4 p2	3.17	0	31.72	49.79	0.17	15.03	0.02	0	0	0.25	0	100.15	-21372	35967	321
-344.06	-344.06 Plag 1 p1	3.24	0.01	31.76	50.14	0.19	14.66	0.07	0.02	0.03	0.27	0	100.4	10955	-34357	211

Depth (m)	DataSet/Point	Na_2O	MgO	Al_2O_3	SiO_2	K_2O	CaO	TiO_2	Cr_2O_3	MnO	FeO	BaO	Total	X	Y	Z
-344.06	-344.06 Plag 1 p2	3.3	0	31.75	50.23	0.16	14.68	0.02	0	0	0.29	0	100.43	10757	-34357	210
-344.06	-344.06 Plag 2 p1	3.17	0.01	31.73	50.18	0.25	14.82	0.06	0.02	0	0.27	0.01	100.53	7979	-33152	194
-344.06	-344.06 Plag 2 p2	2.45	0.07	32.57	47.6	0.08	16.04	0	0	0	0.28	0.02	99.11	7962	-33066	194
-344.06	-344.06 Plag 3 p1	3.53	0.02	31.36	51.76	0.27	13.87	0.02	0.03	0	0.24	0	101.1	4409	-20535	205
-344.06	-344.06 Plag 3 p2	3.6	0.02	31.25	51.24	0.26	14.07	0.02	0.01	0.01	0.25	0.03	100.74	4582	-20511	208
-344.06	-344.06 Plag 4 p1	3.48	0.04	31.14	50.61	0.23	14.26	0.01	0.01	0	0.25	0	100.04	8247	-17627	240
-249.89	-249.89 Plag 1 p1	3.45	0.01	31.53	49.71	0.17	14.68	0.02	0	0	0.27	0	99.84	-3953	-15862	250
-249.89	-249.89 Plag 1 p2	3.86	0.03	30.45	50.63	0.2	13.93	0.04	0.01	0	0.28	0	99.44	-3806	-15869	248
-249.89	-249.89 Plag 2 p1	3.29	0.01	31.36	49.96	0.25	15	0.01	0	0.02	0.29	0	100.19	-10998	-21202	242
-249.89	-249.89 Plag 2 p2	3.61	0.07	28.75	48.55	0.4	12.73	0.01	0	0.02	0.33	0.02	94.48	-10387	-21083	246
-249.89	-249.89 Plag 3 p1	3.45	0.04	30.99	50.02	0.41	14.31	0.11	0.02	0	0.41	0.01	99.76	-3192	-20798	235
-249.89	-249.89 Plag 3 p2	3.35	0	31.35	49.48	0.17	14.72	0.09	0.02	0	0.24	0	99.42	-2968	-20936	233
-249.89	-249.89 Plag 4 p1	3.38	0.02	31.38	50.14	0.21	14.48	0.02	0.01	0	0.28	0	99.93	-12034	-28329	226
-249.89	-249.89 Plag 4 p2	3.93	0.01	30.89	51.21	0.2	13.87	0.05	0	0.01	0.29	0	100.46	-11821	-28450	224
-183.9	-183.9 Plag 1 p1	3.25	0.02	31.67	49.61	0.22	14.8	0.04	0.02	0	0.26	0	99.89	-7910	39971	336
-183.9	-183.9 Plag 1 p2	3.09	0.01	31.94	49.15	0.23	15.24	0.03	0	0.02	0.28	0.01	99.99	-7668	39971	335
-183.9	-183.9 Plag 2 p1	3.06	0.01	31.64	48.96	0.18	15.3	0.04	0	0	0.28	0	99.48	-14839	37211	398
-183.9	-183.9 Plag 2 p2	3.77	0.02	30.54	50.99	0.27	13.76	0.02	0	0	0.29	0.03	99.7	-15041	37495	397
-183.9	-183.9 Plag 3 p1	3.68	0	30.94	50.8	0.24	14.08	0	0.03	0.01	0.25	0.01	100.03	-17624	27055	406
-183.9	-183.9 Plag 3 p2	3.93	0	30.66	51.71	0.25	13.54	0.04	0	0	0.2	0.03	100.36	-17959	27049	408
-183.9	-183.9 Plag 4 p1	3.22	0	31.65	49.6	0.25	14.87	0.04	0.02	0.01	0.3	0.02	99.98	-9721	19532	347
-183.9	-183.9 Plag 4 p2	3.8	0.01	30.68	50.78	0.26	13.83	0.05	0	0	0.28	0.03	99.73	-9452	19536	342
-40.23	-40.23 Plag 1 p1	2.87	0.01	32.57	49.4	0.2	15.33	0.1	0	0.01	0.38	0.06	100.93	5735	22676	355
-40.23	-40.23 Plag 1 p2	2.81	0.02	32.51	49.3	0.17	15.59	0.03	0	0.01	0.34	0	100.8	5648	22680	353
-40.23	-40.23 Plag 2 p1	3.28	0.06	31.88	50.71	0.22	14.49	0.04	0	0	0.49	0	101.17	3648	24390	328
-40.23	-40.23 Plag 2 p2	3.29	0.05	31.63	50.29	0.27	14.6	0.06	0	0.01	0.29	0.05	100.55	3765	24397	329

Depth (m)	DataSet/Point	Na_2O	MgO	Al_2O_3	SiO_2	K_2O	CaO	TiO_2	Cr_2O_3	MnO	FeO	BaO	Total	X	Y	Z
-40.23	-40.23 Plag 3 p1	3.38	0	31.19	49.45	0.22	14.61	0.03	0	0.04	0.26	0	99.18	8164	27861	348
-40.23	-40.23 Plag 3 p2	3.07	0.75	31.07	48.98	0.25	14.87	0.03	0.01	0.02	0.84	0.02	99.88	8159	27704	348
-19.34	-19.34 Plag1 p1	2.58	0.01	32.81	48.59	0.12	16.01	0.02	0.01	0.01	0.26	0	100.42	9040	-36312	247
-19.34	-19.34 Plag1 p2	2.62	0.01	32.75	48.7	0.15	15.86	0.02	0.01	0.02	0.32	0.03	100.47	9469	-36252	249
-19.34	-19.34 Plag2 p1	2.62	0.02	32.38	48.18	0.14	16	0.05	0.02	0.02	0.34	0.01	99.78	19125	-35851	250
-19.34	-19.34 Plag2 p2	2.13	0.02	32.91	46.78	0.11	16.73	0.02	0	0.02	0.33	0.05	99.1	19364	-35854	249
-19.34	-19.34 Plag 3 p1	2.65	0.01	32.28	48.45	0.17	15.96	0.04	0	0	0.3	0.01	99.86	21152	-33447	256
-19.34	-19.34 Plag 3 p2	2.71	0.02	32.05	48.01	0.14	15.86	0.02	0	0	0.31	0.03	99.15	20783	-33470	256
-19.34	-19.34 Plag 4 p1	2.8	0.01	32.34	48.78	0.22	15.67	0.04	0.04	0	0.31	0.04	100.26	19070	-25592	294
-19.34	-19.34 Plag 4 p2	2.36	0.01	33.05	47.92	0.14	16.41	0.03	0	0.01	0.31	0	100.25	18927	-25569	296
0	0 Plag 1 p1	2.89	0.03	32.24	49.15	0.15	15.29	0	0	0.05	0.21	0	100.02	-15843	-8121	338
0	0 Plag 1 p2	2.89	0.01	32.21	49.12	0.14	15.68	0.01	0.01	0.01	0.24	0	100.31	-15870	-8214	338
0	0 Plag 2 p1	3.6	0	31.28	50.56	0.23	14.12	0.06	0.02	0	0.24	0	100.12	-16707	-11455	340
0	0 Plag 2 p2	3.39	0.03	31.39	50.24	0.19	14.17	0.07	0.01	0	0.28	0	99.77	-16450	-11464	341
0	0 Plag 3 p2	3.74	0.03	30.94	51.25	0.27	13.79	0.03	0	0	0.27	0.04	100.36	-19283	-12055	338
0	0 Plag 3 p1	3.67	0.01	30.83	51.14	0.25	13.95	0.05	0	0	0.28	0.01	100.2	-18945	-12078	339
0	0 Plag p1	3.62	0.02	30.78	50.31	0.29	14.24	0.02	0	0	0.34	0.04	99.67	-4070	-20588	271
0	0 Plag p2	3.63	0.03	31.07	50.59	0.27	14.31	0.01	0	0	0.31	0	100.23	-4290	-20556	274

Depth(m)	DataSet/Point	Na2O	MgO	Al_2O_3	SiO_2	K_2O	CaO	TiO_2	Cr_2O_3	MnO	FeO	BaO	Total	X	Y	Z
-688.05	-688.05 Opx 1 p1	0.02	24.15	0.7	53.4	0	0.87	0.29	0.08	0.37	20.06	0.01	99.94	17642	35157	267
-688.05	-688.05 Opx 2 p1	0.28	14.42	1.44	52.36	0.01	23.02	0.28	0.19	0.19	7.78	0.02	99.98	12232	31841	298
-688.05	-688.05 Opx 3 p1	0.25	14.75	1.35	52.17	0.02	22.12	0.46	0.17	0.26	8.46	0.01	100.02	10564	16340	300
-668.74	-668.74 Opx 1 p1	0.17	8.33	9.85	44.29	0	20.56	0.21	0.04	0.23	11.81	0	95.5	-8818	8723	286
-668.74	-668.74 Opx 2 p1	0.27	12.26	1.3	51.25	0	22.5	0.28	0.1	0.28	11.81	0	100.04	-9742	12662	304
-668.74	-668.74 Opx 4 p1	0.27	12.2	1.34	51.28	0.03	22.37	0.24	0.03	0.27	11.76	0	99.76	-13249	5986	300
-638.7	-638.7 Opx 1 p1	0.01	25.43	0.82	54.18	0	0.84	0.21	0.08	0.37	17.74	0.04	99.72	-19024	-9875	336
-638.7	-638.7 Opx 2 p1	0.02	25.39	0.73	53.91	0.01	0.77	0.21	0.08	0.42	17.99	0.01	99.53	-14464	-14590	320
-638.7	-638.7 Opx 3 p1	0.02	25.72	0.73	53.8	0.02	0.93	0.29	0.06	0.34	17.74	0.04	99.69	-8757	-17784	299
-638.7	-638.7 Opx 4 p1	0.01	25.28	0.67	53.89	0	1.33	0.23	0.13	0.34	17.68	0.03	99.59	-21577	-23505	287
-638.7	-638.7 Opx 5 p1	0.04	24.77	0.71	53.7	0	1.82	0.22	0.09	0.34	17.19	0	98.87	-3740	-28297	245
-578.33	-578.33 Opx 1 p1	0.04	25.42	0.78	53.77	0	1.89	0.2	0.11	0.34	16.74	0	99.29	18007	-7682	251
-578.33	-578.33 Opx 3 p1	0.03	25.6	0.84	53.51	0.01	2.01	0.16	0.1	0.34	16.42	0	99.01	7576	-10042	246
-468.17	-468.17 Opx 1p1	0.02	25.96	0.84	54.39	0	1.32	0.26	0.1	0.34	16.55	0.01	99.79	14536	36594	270
-468.17	-468.17 Opx 2 p1	0.3	14.87	1.41	52.48	0	22.87	0.37	0.2	0.2	6.61	0.01	99.33	4230	36665	341
-468.17	-468.17 Opx 3 p1	0.29	15.6	1.39	52.76	0	22.03	0.35	0.18	0.23	7.23	0	100.06	2348	36002	353
-372.41	-372.41 Opx 1 p1	0.32	15.38	1.45	52.18	0	21.83	0.42	0.29	0.21	7.55	0.03	99.67	-5906	35461	288
-372.41	-372.41 Opx 3 p1	0.01	25.92	0.81	54.08	0	0.75	0.23	0.14	0.41	17.58	0.01	99.95	-20534	31920	322
-344.06	-344.06 Opx 1 p1	0.28	15.18	1.34	52.82	0	23.69	0.24	0.24	0.13	5.96	0	99.89	9057	-31251	209
-344.06	-344.06 Opx 2 p1	0.01	26.1	0.74	54.26	0	1.3	0.15	0.12	0.38	16.67	0.03	99.77	11577	-27584	240
-344.06	-344.06 Opx 3 p1	0.34	15.67	1.45	52.92	0	21.83	0.31	0.33	0.21	6.66	0.02	99.75	12803	-20535	265
-249.89	-249.89 Opx 1 p1	0.02	24.2	0.97	52.91	0	0.82	0.26	0.08	0.39	19.56	0	99.22	-8633	-17641	251
-249.89	-249.89 Opx 2 p1	0.04	24	0.77	53.07	0	1.85	0.41	0.09	0.35	18.7	0	99.28	-17673	-21501	240
-249.89	-249.89 Opx 3 p1	0.01	24.42	0.67	53.74	0	0.67	0.1	0.11	0.36	19.59	0	99.67	-6657	-24299	232
-249.89	-249.89 Opx 4 p1	0.01	24.69	0.79	53.83	0	1	0.18	0.08	0.33	19.21	0	100.13	-10607	-27995	224

Depth(m)	DataSet/Point	Na_2O	MgO	Al_2O_3	SiO_2	K_2O	CaO	TiO_2	Cr_2O_3	MnO	FeO	BaO	Total	X	Y	Z
-249.89	-249.89 Opx 4 p1	0.02	24.96	0.91	53.59	0	0.74	0.2	0.13	0.36	19	0	99.89	-12882	-31480	215
-183.9	-183.9 Opx 1 p1	0.01	24.83	0.66	53.65	0.01	1.65	0.2	0.14	0.39	18.16	0.03	99.74	-18430	37217	404
-183.9	-183.9 Opx 2 p1.	0.01	24.96	0.86	53.78	0	1.39	0.18	0.14	0.37	18.47	0.04	100.18	-15980	23093	393
-183.9	-183.9 Opx 3 p1.	0.01	25.32	0.79	53.77	0	0.99	0.22	0.1	0.4	18.45	0	100.03	-14290	21696	382
-230.32	Pk 15 Opx 1 p1	0.02	25.36	0.78	53.64	0	0.75	0.16	0.07	0.4	18.85	0	100.04	7789	31911	377
-19.34	-19.34 Opx 1 p1	0.02	24.84	0.82	53.62	0	1.01	0.15	0.15	0.35	19.3	0	100.26	6269	-21110	256
-19.34	-19.34 Opx 1 p2	0.02	23.66	0.63	50.17	0	1.24	3.63	0.16	0.37	19.98	0.02	99.89	6196	-20902	255
-19.34	-19.34 Opx 1 p3	0.01	24.64	0.89	53.51	0	0.97	0.18	0.17	0.34	19.06	0.08	99.86	6001	-20991	253
-19.34	-19.34 Opx 2 p1	0.01	24.54	0.74	53.7	0.01	0.75	0.24	0.14	0.39	19.62	0	100.13	8985	-21466	272
-19.34	-19.34 Opx 3 p1	2.2	0.02	33.1	47.1	0.1	16.51	0	0	0.02	0.26	0	99.31	17527	-14447	299
0	0 Opx1 p1	0.01	27.81	0.97	54.73	0	0.78	0.21	0.34	0.29	14.47	0	99.6	-2934	-9538	274
0	0 Opx2 p1	0.01	27.88	1.05	54.58	0	0.91	0.27	0.35	0.23	14.32	0	99.6	-12165	-9852	337
0	0 Opx 2 p1	0.03	27.76	1.25	54.84	0.01	2	0.15	0.45	0.25	13.44	0.01	100.19	-11076	-14510	329
0	0 Opx 4 p1	0.01	28.01	1.5	54.29	0.1	0.8	0.2	0.39	0.3	13.76	0.01	99.39	-19006	-24342	298

Depth(m)	DataSet/Point	Na_2O	MgO	Al_2O_3	SiO_2	K_2O	CaO	TiO_2	Cr_2O_3	MnO	FeO	BaO	Total	X	Y	Z
-688.05	-688.05 Cpx 1 p1	0.25	14.91	1.41	51.56	0	20.47	0.43	0.19	0.25	9.25	0.03	98.75	19071	35182	331
-688.05	-688.05 Cpx 2 p1	0.04	23.58	0.82	53.76	0	3.27	0.21	0.09	0.37	17.97	0	100.11	6187	28735	305
-688.05	-688.05 Cpx 3 p1	0.04	23.58	0.83	53.32	0	2.77	0.19	0.06	0.39	18.3	0	99.49	15699	23296	326
-688.05	-688.05 Cpx 4 p1	0.02	24.15	0.84	53.16	0	1.76	0.16	0.11	0.43	18.85	0.04	99.52	15936	17035	310
-638.7	-638.7 Cpx 1 p1	0.02	25.45	0.75	54.09	0	1.06	0.26	0.09	0.37	17.74	0	99.84	-8807	-11244	208
-638.7	-638.7 Cpx 3 p1	0.02	25.13	0.64	53.97	0.03	1.07	0.3	0.08	0.35	17.68	0	99.26	-4381	-28288	322
-578.33	-578.33 Cpx 1 p1	0.02	25.77	0.73	53.79	0	0.9	0.24	0.09	0.36	16.98	0.01	98.9	13478	-12592	309
-578.33	-578.33 Cpx 2 p1	0.02	26.15	0.72	54.13	0	1.03	0.23	0.12	0.36	17.15	0	99.92	4710	-24095	318
-578.33	-578.33 Cpx 2 p1	0.02	25.5	0.77	54.13	0	1.95	0.2	0.07	0.35	16.6	0.01	99.61	8723	-25814	291
-578.33	-578.33 Cpx 3 p1	0.01	26.37	0.71	54.31	0	1.41	0.22	0.07	0.35	17.11	0.02	100.58	3193	-27315	257
-468.17	-468.17 Cpx 1 p1	0.04	25.37	0.82	53.88	0	2.81	0.29	0.15	0.36	16.13	0	99.85	7671	38931	333
-468.17	-468.17 Cpx 3 p1	0.04	25.01	0.74	53.86	0	3.6	0.19	0.12	0.32	15.72	0	99.61	5331	21798	336
-372.41	-372.41 Cpx 1 p1	0.33	15.17	1.41	52.43	0	22.6	0.41	0.26	0.18	7.16	0.01	99.95	-19864	37133	333
-372.41	-372.41 Cpx 2 p1	0.02	25.46	0.64	53.94	0	2.04	0.17	0.11	0.32	17.17	0	99.86	-14862	36193	291
-344.06	-344.06 Cpx 1 p1	0.01	26.5	0.74	54.39	0.02	0.84	0.24	0.16	0.42	16.97	0	100.28	8528	-35052	373
-344.06	-344.06 Cpx 2 p1	0	26.57	0.87	54.81	0	0.79	0.17	0.12	0.36	17.14	0	100.84	6405	-32687	388
-344.06	-344.06 Cpx 2 p1	0.01	26.29	0.81	54.27	0	0.95	0.22	0.13	0.36	17.09	0	100.13	16532	-17805	382
-249.89	-249.89 Cpx 3 p1	0.26	12.33	1.05	41.09	0	17.52	11.44	0.42	0.66	18.49	0.04	103.3	-16451	-31573	293
-183.9	-183.9 Cpx 1 p1	0.01	25.03	0.75	54.11	0	0.88	0.17	0.08	0.33	18.84	0	100.2	-12750	26632	396
-183.9	-183.9 Cpx 2 p1.	0.01	25.15	0.78	53.83	0	0.84	0.25	0.13	0.36	18.69	0	100.04	-8080	20226	299
0	0 Cpx 1 p1	0	28.7	1.13	54.82	0	0.36	0.17	0.27	0.31	14.2	0	99.96	-13962	-8218	384
0	0 Cpx 2 p2	0.02	28.12	1.13	54.49	0	2.02	0.58	0.4	0.24	13.36	0	100.35	-10224	-11019	336
0	0 Cpx 4 p1	0.02	27.72	1.16	54.9	0	2.54	0.16	0.36	0.25	13.04	0.03	100.19	-12545	-12892	307